Microstructure and texture evolution during hot deformation of AZ80 magnesium alloy

by

Paresh Prakash

A thesis

presented to the University of Waterloo

in fulfillment of the

thesis requirement for the degree of

Doctor of Philosophy

in

Mechanical and Mechatronics Engineering

Waterloo, Ontario, Canada, 2019

Examining Committee Membership

The following served on the Examining Committee for this thesis. The decision of the Examining Committee is by majority vote.

External Examiner	BRADLEY DIAK Professor, Department of Mechanical and Materials Engineering Queen's University, Kingston, ON
Supervisor	MARY WELLS Professor, Department of Mechanical and Mechatronics Engineering University of Waterloo, Waterloo, ON
Internal Member	HAMID JAHED Professor, Department of Mechanical and Mechatronics Engineering University of Waterloo, Waterloo, ON
Internal Member	ADRIAN GERLICH Professor, Department of Mechanical and Mechatronics Engineering University of Waterloo, Waterloo, ON
Internal-External Member	SUSAN TIGHE Professor, Department of Civil and Environmental Engineering University of Waterloo, Waterloo, ON

Author's Declaration

I hereby declare that I am the sole author of this thesis. This is a true copy of the thesis, including any required final revisions, as accepted by my examiners.

I understand that my thesis may be made electronically available to the public.

Abstract

Magnesium alloys offer tremendous weight saving potential in automotive applications, owing to their significantly lower densities, and superior specific strength and stiffness values, compared to traditional structural materials. However, the current use of Mg alloys in the automotive industry, particularly in wrought form, such as forged Mg alloy components, is rather low, owing to difficulties associated with forging them under ambient conditions. These stem from an almost ideal hexagonal close packed (HCP) crystal structure of the Mg lattice, which results in a lack of easily activated slip systems for low temperature deformation, and also in anisotropic deformation along and perpendicular to the c-axis of the HCP unit cell. Mg alloys also have a tendency to develop sharp deformation textures, which aggravate the problem of anisotropy, as well as make any subsequent deformation very difficult. High temperature deformation can improve the formability, by activating higher order slip systems, as well as promoting dynamic recrystallization (DRX).

The current research is part of a Natural Sciences and Engineering Research Council of Canada's Automotive Partnership Canada project, aimed at forging an industrial scale control arm for a Ford Fusion car using three potential Mg alloys: AZ31, AZ80 and ZK60. This research is experimental in nature and focuses on exploring the hot deformation behaviour of cast and extruded AZ80 alloys under typical industrial forging conditions. In particular, the role of the following process and material parameters are explored: deformation conditions (temperatures of 300 – 400 °C, and strain rates of 0.001 – 0.1 s^{-1}), the presence or absence of precipitates during deformation, and the processing history of the starting material (cast/extruded). Additionally, the hot deformation behaviour of cast AZ31 and AZ80 alloys are compared to explore the role of Al (in solid solution) on the deformation behavior of the AZ alloys. The hot deformation behaviour was studied by conducting uniaxial compression tests done using a Gleeble™ 3500 thermal-mechanical simulator available at the University of Waterloo. Material characterization on undeformed and deformed samples was performed using a variety of techniques, including: optical, and scanning electron microscopy, energy dispersive X-ray spectroscopy, electron back scatter diffraction microtexture analysis, X-ray diffraction (XRD) macrotexture analysis, and XRD phase identification analysis.

The results indicate that DRX, through different mechanisms, took place under all investigated deformation conditions in the AZ80 alloy. For deformation at 300 °C, DRX took place via particle stimulated nucleation (PSN) at $Mg_{17}Al_{12}$ lamellar discontinuous precipitates, and via the grain boundary bulging mechanism. For deformation at 400 °C, the $Mg_{17}Al_{12}$ precipitates dissolved, and DRX took place through the grain boundary bulging mechanism. DRX at 300 °C resulted in texture randomization, which was attributed to its occurrence through the PSN mechanism, while at 400 °C, DRX led to the preservation of the deformation texture. The DRX grain size was found to be dependent on the deformation conditions (viz. the temperature and strain rate), but not on the processing history of the starting material (cast/extruded), its starting texture, initial grain size, or the deformation strain level. Deformation at lower temperature/and or higher strain rates resulted in a finer DRX grain size, and a more pronounced grain refinement of the microstructure relative to the as-received state. In addition to DRX, continuous dynamic recrystallization (CDRX), via grain fragmentation and recovery, also contributed to grain refinement for all deformation conditions.

The forgeability of various starting materials was judged in terms of their ability to forge at high strain rates, without cracking, and development of a homogeneous and fine grained microstructure, and a random texture, in them, as a result of deformation. In this regards, extruded AZ80 was found to show all these desired features, except for a random texture, for deformation at 400 °C, 0.1 s^{-1}. Cast AZ80, on the other hand, showed cracking at higher strain rates, while cast AZ31, showed development of a bimodal microstructure.

Acknowledgements

Journey to a doctorate is very difficult. In most cases it is not possible to make it without adequate support, both technical, as well as moral, and was certainly the case for me. I would like to gratefully acknowledge all those who made this journey possible for me.

Firstly, I would like to thank my supervisor, Prof. Mary Wells, for giving me a chance to work in her research group. I am thankful to her for her guidance, and letting me pursue my research freely. Most importantly, I am eternally grateful to her for the time when she showed faith in me, when I was not getting any results, and had hit a particularly rough patch in my research. Her encouragement and support made me make a complete turnaround and made this work possible. It has been a tremendous learning experience, and I will cherish my memories with her as my guide.

I would like to gratefully acknowledge NSERC APC grant APCPJ 459269-13, and the cooperation I received from the project partners: University of Waterloo (UW), Multimatic Inc., Ford Motor Company, CenterLine (Windsor) Ltd, and CanmetMATERIALS laboratory, which has made this work feasible.

I am thankful to my examination committee members: Prof. Brad Diak, Prof. Hamid Jahed, Prof. Adrian Gerlich, and Prof. Susan Tighe, for their valuable feedback during my PhD defense examination, and my draft thesis document, which has helped me improve upon it. I am thankful to Dr. Amir Hadadzadeh, and Rick Wong, for their help with some experiments, and development and proof reading of my comprehensive exam proposal.

I would like to thank Prof. Jean-Pierre Hickey for giving me the opportunity to work for him as a Teaching Assistant. This was the first time I worked as a TA, and was a great learning experience under his guidance.

I would like to thank my long-time friend, Indranil Basu, for his mentorship during my studies. I have greatly benefited from his expertise on the Mg alloys.

I would like to thank Rick Forgett, Mark Kuntz, and their team at the Engineering Machine Shop, for the supply of test samples in a timely manner, and at sometimes even on an urgent basis. I highly appreciate their support. Special thanks to Jorge

Cruz, for simply being there, and helping me with random stuff at the machine shop, anytime I approached him. I would also like to thank Mark Griffet, of the microscopy lab, for his help with different stuff, and specially, which I will remember the most, for the countless number of times he opened the Gleeble room for me. I would like to thank Martha Morales of the IT support for keeping my computer system up and running.

I would like to thank all those who helped me with experiments and gathering the data. Special thanks to Mark Whitney, for the countless number of samples he *squeezed* for me in the Gleeble. Special thanks to him also for his friendship and mentorship. Thanks to Dr. Sugrib Kumar Shaha, for doing XRD texture measurements and phase identification tests for my innumerable samples. I would also like to thank him for his friendship. I would like to thank Amir Yazdanmehr and Sasan Faghih for help with some XRD measurements, and their friendship. I would like to thank Dwayne Toscano, for helping me with SEM/EDS data collection at the WATLAB, and also for his friendship. I would like to thank Hugo, Talal and Tharindu for help with running some DEFORM 3D simulations, and their friendship. I would also like to thank Prof. Hamid Jahed and Prof. Steve Lambert, for letting me work freely with their students, and Prof. Jahed also for letting me use his research equipment for my tests freely.

I would like to thank my colleagues at Canmet Materials, where I did all of metallography, EBSD, and even some SEM/EDX work. Special thanks to my supervisor there, Dr. Bruce Williams, for letting me be part of the Canmet team, and letting me pursue my research freely. I highly appreciate his help on random stuff, and also him sharing his knowledge, particularly on CP-FEM, freely. Special thanks to Dr. Jian Li, for sharing his knowledge on EBSD freely, and helping me with some of the measurements. Special thanks to Cathy Bibby, for being there, and helping me with random stuff. Also thanks to Pei Liu, Mehdi Mehdi, Joe Pezze, and James Saragosa for their help at different times. Special thanks to Yuna Xue and Liting Shi, for their friendship, and the innumerable times they helped me with the Metlab bookings. Special thanks to Waqas Muhummad, for helping me with the EBSD analysis software, and more importantly for his friendship, and mentorship. I would also like to thank Christopher Butcher and Yuan Hui of McMaster University (CCEM) for their help with

some of the EBSD measurements (not included in the current thesis) and their advice in general on the best practises on EBSD sample preparation and equipment handling.

Very very special thanks to Renata Zavadil, of Canmet Materials. Metallography of Magnesium is very hard, but she made me master it, and guided me throughout that process. It won't be an overstatement to say that the thesis would not have been possible in the present format had it not been for her timely help. I am also thankful to her for her friendship, and mentorship.

I would like to thank my *doctoral brothers*: Massimo Di Ciano, Michael Benoit, Daniel Odoh and Yu Wang for their friendship, mentorship, and the general twaddle. I will cherish my memories with them.

I would also like to thank my friends, colleagues, and well-wishers in Waterloo (in alphabetical order): Abhishek, Ali K, Amir Y, An Nguyen, Andrew G, Anindya, Ankur, Apratim, Archisman, Arshad, Arti, Behzad, Dan Walsh, Daniel, Dwayne, Ekta, Gitanjali, Glenn, Huangrui Mo, Hugo, Jalaj, Jie Wang, Karen, Kevin, Khaled Younes, Lokesh, Luqman, Mark W, Massimo, Mike B, Nitin, Pranav, Raj, Ranga Rajan, S Jeyaparathi, Saber, Sasan, Saurabh, Shitikanth, Shivam, Shivang, Shrinu, Talal, Tharindu, Vinit, Waqas, Yahya, and Yuna. Thank you guys for being there, and making my journey a pleasant one!

Lastly, and most importantly, I would like to thank my family for their continued love, support and encouragement. Special thanks to my parents, for nurturing me, inculcating good habits, encouraging a sense of curiosity in me and letting me explore the world freely. I am thankful to them for being always there for me, their continued belief in me, and their love, which keeps me going. Special thanks my brother, Ken, for his love, support and general goofing around. I love my conversations with him on varied subjects, and I know we have got each other's back! Special thanks to my grandparents for their love and blessings. Special thanks to my in-laws, for giving me their wonderful daughter/sister, in a land very far away from their home, and at a time when I still was a student.

Most importantly, I would like to thank to my wife, Shivangi Bansal. Initially when I used to see people acknowledging their spouses in their PhD theses, I used to consider it just a goodwill gesture. But going through the PhD process myself, as a

married man, I now realize how significantly mentally and emotionally draining this can be on one’s spouse, and how much sacrifice this entails from them. I am truly grateful that I have a wonderful wife, who not only made a lot of sacrifices so that I can be successful, but also stood as a pillar of strength for me, providing constant love, encouragement and support.

Dedication

To the Guru .. who guides us

To the Family .. which nurtures us

To the 10,000 hours .. that define us

Table of Contents

List of Figures

List of Tables

List of Abbreviations

AHSS	Advanced High Strength Steels
AR	Anisotropy Ratio
BSE	Backscatter Electron
CAFÉ	Corporate Average Fuel Economy
CD	Compression Direction
CDRX	Continuous Dynamic Recrystallization
CH	Cast-homogenized
CP	Continuous Precipitates
CRSS	Critical Resolved Shear Stress
DDRX	Discontinuous Dynamic Recrystallization
DP	Discontinuous Precipitates
DRX	Dynamic Recrystallization
EBSD	Electron Backscatter Diffraction
ED	Extrusion Direction
EDX	Energy Dispersive X-Ray Spectroscopy
F-E	Friedel-Escaig
FEM	Finite Element Model
GB	Grain Boundary
GOS	Grain Orientation Spread
GS	Grain Size
HCP	Hexagonal Closed Packed
IPF	Inverse Pole Figure
IQ	Image Quality
KAM	Kernel Average Misorientation
LAB	Low Angle Boundary
ND	Normal Direction
ODF	Orientation Distribution Function
PF	Pole Figure
PID	Proportional–Integral–Derivative
PSN	Particle Stimulated Nucleation
Py2	Second Order Pyramidal

RD	Radial Direction
RDRX	Rotational Dynamic Recrystallization
RSS	Resolved Shear Stress
SE	Secondary Electron
SEM	Scanning Electron Microscopy
SF	Schmid Factor
TD	Transverse Direction
TDRX	Twin induced Dynamic Recrystallization
XRD	X-Ray Diffraction

1 Introduction

1.1 Magnesium alloys for lightweight automotive applications

Over the past few decades, greenhouse gas emissions, global warming, and climate change have become some of the most important and challenging concerns in Canada, and the world. Automotive exhaust gas emissions are one of the major sources of greenhouse gases (mainly in the form of carbon dioxide, but also as nitrous oxide and methane). As a result, various national governments and regulators have come up with emission standards for the vehicles manufactured and operating in their respective jurisdictions. The amount of exhaust gas emissions are directly related to the fuel economy of the vehicle, and therefore these standards are typically implemented in the form of minimum requirements on the fuel economy of the vehicles, and are set in a graduated manner (increasing fuel economy requirements for a model for every subsequent model year). An example is given here in Figure 1-1 (a) of the CAFE (Corporate Average Fuel Economy) Standards, which are the most important standards the vehicles produced for sale in the United States must comply by, and the targets set under it, for passenger cars and light trucks to 2025 [1].

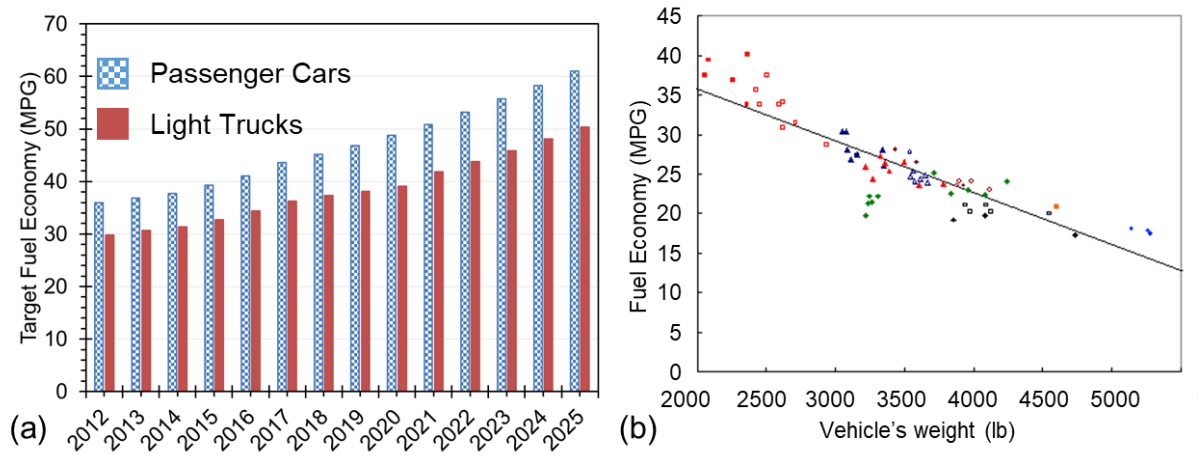

Figure 1-1 (a) CAFE Standards for vehicles with footprint ≤ 41 ft² [1], (b) Vehicle's fuel economy as a function of its weight

A vehicle's weight is one of the major contributing factor towards its fuel consumption, with heavier vehicles having a lower fuel economy, and vice versa. Figure 1-1 (b) represents this for a large amount of data, including cars, sport utility vehicles, and light trucks (different model years). It is apparent that light weighing forms an important near term solution we have at our disposal to improve the fuel efficiencies of vehicles.

This has spurred research activities in lightweight component design for various automotive applications worldwide. On one hand this has led to the development of advanced high strength steels (AHSS) [2], and on the other, this has led to an interest in the use of alternative lightweight materials, such as polymers, composites, and non-ferrous alloys, among others, for various automotive applications [3]. Magnesium (Mg), being the lightest structural material, is an important contender in this space. Some of the desirable properties of Mg-based alloys include: high specific stiffness and strength, good machinability, weldability, castability, vibration damping capacity, low melting temperature and melting energy [4, 5]. Table 1-1 compares some of the important mechanical properties of magnesium alloys, to alloys based on steels, titanium and aluminum. Considering the data in the table, it is evident that Mg is a viable alternative to the conventional heavier alloys for various structural automotive applications.

Table 1-1 Comparison of the mechanical properties of some major structural metallic alloys [6]

		Units	Steel	Titanium	Aluminum	Magnesium
ρ	Density	g/cm^3	7.83	4.5	2.8	1.74
E	Elastic Modulus	MPa	210	110	70	45
R_m	Tensile Strength	MPa	300-1200	910-1190	150-680	100-380
R_m/ρ	Specific Strength	10^6 $Nmmkg^{-1}$	38-153	202-264	54-243	57-218
E/ρ	Specific Stiffness	10^9 $Nmmkg^{-1}$	26.8	24.4	25	25.9
$\sqrt{R_m}/\rho$	Dent Resistance	10^6 $N^{0.5}mm^2kg^{-1}$	4.4	7.7	9.3	11.2
$\sqrt[3]{E}/\rho$	Shell Stiffness	10^7 $N^{1/3}mm^{7/3}kg^{-1}$	7.6	10.6	14.7	20.4

It is worth mentioning that owing to their tremendous light weighing potential, Mg alloys were already in use in various automotive components during the 1940s - 1970s, but were not able to compete with the increasing performance requirements of the newer generation vehicles, especially with regards to high temperature operation and corrosion stability, and thereby went out of favour [7]. However, in recent years, a renewed interest in Mg has led to the development of newer (high performance) alloys, and better and more efficient fabrication processes. A growing number of automotive parts are now manufactured using Mg-based alloys. Figure 1-2 shows a concept car, with a range of Mg alloys based components and the respective weight savings achieved (by replacing the original component with the Mg-based component) [8]. The data in Figure 1-2 is from 2008, and the use of Mg in automobiles has grown

significantly since then [7]. It is noteworthy that the North American automobile industry has set for itself a target of using around 160 kg of Mg per vehicle by the year 2020 [9].

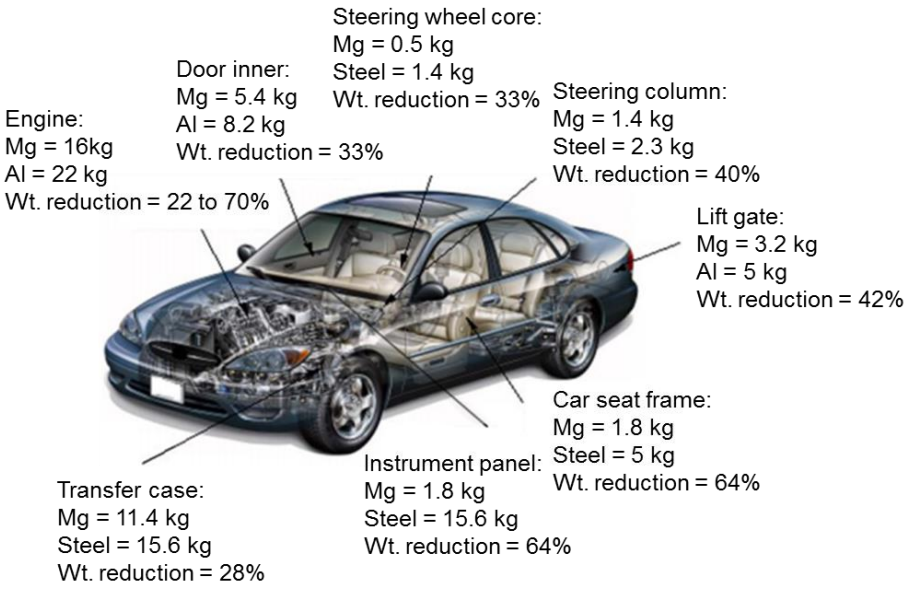

Figure 1-2 A concept car, showing the use of Mg alloys in various automotive components, and the resultant weight savings [8]

1.2 Forging of Mg alloys

With the multi-material vehicle architecture concept emerging in automotive design, lightweight materials such as Mg are gaining increased attention as structural materials. However, despite the many advantages that magnesium has from a weight savings perspective, the use of magnesium in automotive applications is still very limited. The vast majority of the Mg components are die-cast, which makes them ineligible for high-performance structural applications because of their relatively poor microstructure, and correspondingly poor structural properties [10, 11, 12, 13, 14, 15, 16, 17, 18]. Wrought processed alloys have superior microstructure and mechanical properties [12], but the formability of Mg alloys itself is very low, particularly so at temperatures lower than about 225 °C [19], which is attributed to few easy to activate slip systems, anisotropy in deformation, and the development of strong textures (which makes further deformation difficult) during deformation. These issues can generally be mitigated by forging the material at elevated temperatures, which helps in the activation of higher order slip systems, and also leads to the activation of the microstructural restoration phenomena of dynamic recrystallization (DRX). Activation

of DRX is very desirable as it restores the ductility of the material to a certain extent [20], as well as can potentially cause texture randomization [21, 22, 23, 24], which makes for a more isotropic deformation of the material, and can also results in lower forging loads.

Together, these factors (i.e. activation of higher order slip systems and DRX), can result in an enhanced forgeability of the material, which is defined in the present work as the ability of the material to be deformed at high strain rates to large strains, without showing any cracking, and development of a fine grained and homogeneous microstructure, and a random texture distribution, as a result of deformation. A random texture distribution provides for lower flow stress values and isotropic material flow during the forging itself; while a homogeneous, fine grained, and crack free microstructure is desirable for superior in-service performance of the forged part such as its fatigue life [11, 12, 13, 14, 15, 16, 17, 18].

1.3 Overview of the current research

The current research is part of a Natural Sciences and Engineering Research Council of Canada's Automotive Partnership Canada (NSERC APC) grant. The project includes the following industry and government partners: University of Waterloo (UW), Multimatic Inc., Ford Motor Company, CenterLine (Windsor) Ltd, and CanmetMATERIALS laboratory. The project aims to design and forge an industrial scale control arm using Mg alloy that is slated for use in the Ford Fusion car. Three commercially relevant magnesium alloys are examined throughout the project as potential candidates and include: AZ31, AZ80 and ZK60, and a weight saving of at least 35 wt.% over the benchmark component made using A356 aluminum alloy is targeted. The current research investigates the hot deformation behaviour of the AZ80 alloy, with special emphasis on obtaining the flow stress data for a variety of deformation conditions based on uniaxial compression tests, and studying how the microstructure and texture of the material evolves with deformation temperature, strain rate and strain. The flow stress data generated during this research was used as part of a finite element model (FEM) that was developed by another student at the University of Waterloo to simulate forging of magnesium. The microstructure and texture results from this research also provide scientific insights into how deformation

of magnesium occurs. These results also help us to determine the forgeability for each magnesium alloy.

2 Hot deformation behaviour of AZ alloys

2.1 Hot deformation fundamentals

2.1.1 Deformation modes

Magnesium (Mg) has a hexagonal closed packed crystal (HCP) structure. The dominant deformation modes in Mg alloys are crystallographic slip and deformation twinning [25, 26]. The major slip and twin systems in Mg alloys are presented in Figure 2-1 - Figure 2-3. With reference to Figure 2-1, the slip planes are highlighted in blue, while the slip directions are marked by red arrows.

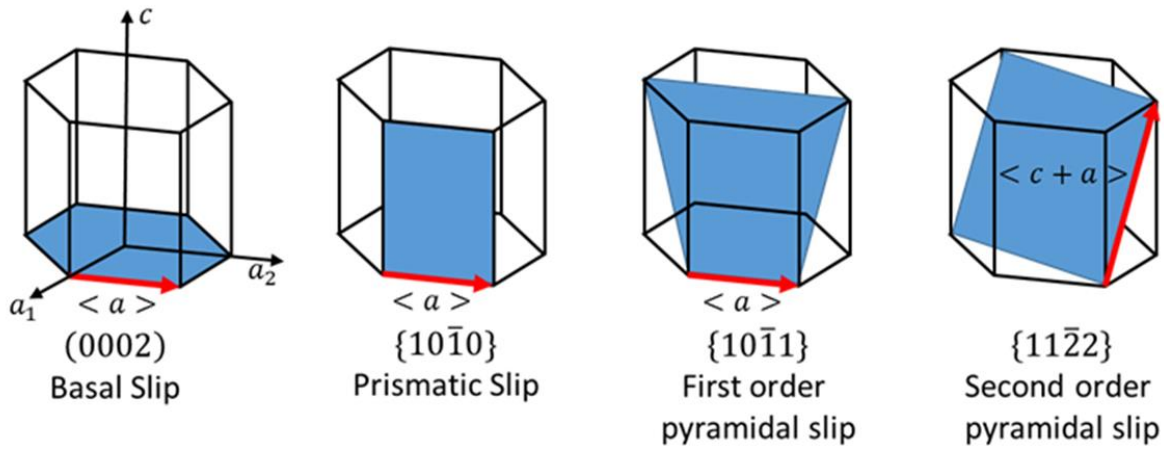

Figure 2-1 Major slip systems in Mg alloys

Referring to Figure 2-1, basal, prismatic and first-order pyramidal slip systems have slip directions along $< 11\bar{2}0 >$ direction ($< a >$), and have no slip component along the $< c >$ axis, and thereby cannot accommodate any deformation along it. These slip systems provide a total of 4 independent slip modes (2 each for basal slip and prismatic slip, while the slip through the first order pyramidal slip system is not considered independent of these two former slip systems [27]). As such, none of these slip systems, or any combination thereof, can provide for five independent slip modes, required for a homogeneous deformation of a polycrystalline material by the Taylor's criteria [28]. The second order pyramidal $< c + a >$ slip system, henceforth referred to as the Py2 slip system, can accommodate deformation along the c-axis, and also provides a total of 5 independent slip systems [27], and thereby its activation is of special interest for an enhanced forgeability of the material.

Deformation twinning is another major deformation mechanism for Mg alloys. Twinning involves strain accommodation by rapid reorientation of part of the grain about a fixed axis and amount (with respect to the non-twinned part of the same grain). This misorientation angle and axis is characteristic of the particular twin system involved. The major twin modes observed in Mg, are shown in Figure 2-2 and Figure 2-3. $\{10\bar{1}2\}$ tensile and $\{10\bar{1}1\}$ compression twins are named as such because the matrix reorientation associated with them is such that it supports deformation only in tension or compression along the c-axis, respectively [29, 30, 31]. $\{10\bar{1}1\}$-$\{10\bar{1}2\}$ double twinning involves $\{10\bar{1}2\}$ tensile twinning of a region that has already undergone $\{10\bar{1}1\}$ compression twinning. The sequence of twinning, and the reorientations involved, in $\{10\bar{1}1\}$-$\{10\bar{1}2\}$ double twinning, are schematically illustrated in Figure 2-3 [32, 33]. All these twins show a matrix reorientation about the $< 1\bar{2}10 >$ axis, of ~ 86°, 56° and 38°, for tension twins, compression twins, and double twins, respectively [34].

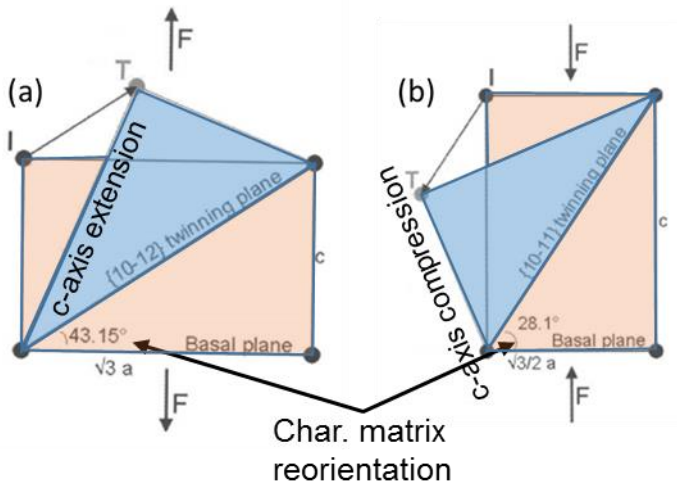

Figure 2-2 Major twin systems in Mg alloys and the matrix reorientations associated with them: (a) $\{10\bar{1}2\} < 10\bar{1}1 >$ *tension twin, (b)* $\{10\bar{1}1\} < 10\bar{1}2 >$ *compression twin. Orange areas represent prior grain, while the blue areas represent the twinned region. Adapted from [31]*

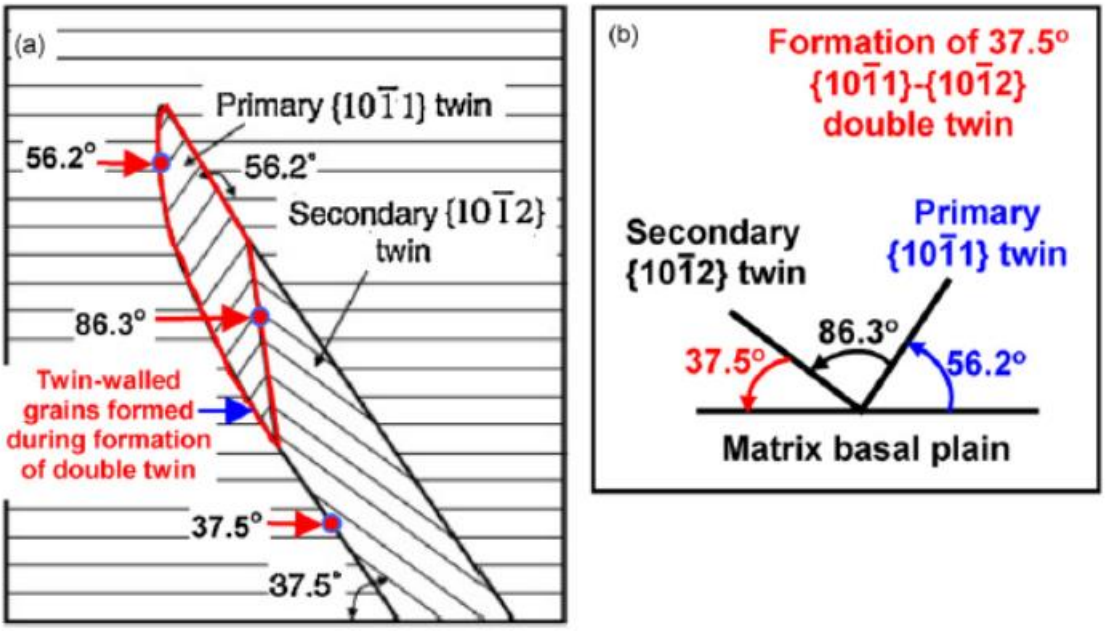

Figure 2-3 Schematic of occurrence of $\{10\bar{1}1\}$-$\{10\bar{1}2\}$ *double twinning in Mg [32, 33]*

It is noteworthy that other than the Py2 slip system, deformation twinning can also accommodate deformation along the c-axis. However, the role of twinning in accommodating deformation is limited by the directional nature of twinning, as well as limited strain accommodated by them [31]. In contrast, deformation through slip, does not have any limitation on the strain that can be accommodated through it. Additionally, twinning only provides additional ½ independent slip systems, owing to its polar nature (i.e. unidirectional activation) [27], and Taylor's criteria can still not be met if the Py2 slip system is not activated.

It is noteworthy that twins are also found to promote the occurrence of dynamic recrystallization in the material [20, 33, 35, 36]. This is explained in more detail in section 2.1.3.

2.1.2 Activation criteria for various deformation modes

A particular deformation mode becomes active when the value of the resolved shear stress on that slip/twin system becomes greater than a critical value. This critical value, also referred to as critical resolved shear stress (CRSS), is a characteristic of the particular deformation mode. CRSS of Mg alloys has historically been determined based on experiments using single crystals, with the test specimens oriented (with respect to the loading direction) to activate single deformation mode in the crystal

during the deformation. A comprehensive list of references for these studies can be found in [37, 38, 39]. CRSS values for individual deformation modes show significant variations among these different publications, and it is also found that the values from single crystal experiments are very different from those determined for polycrystalline material (of similar alloys), based on crystal plasticity simulations [38]. The latter can be attributed to grain boundary effects in polycrystals [40], and to other effects constituting additional hardening of individual deformation modes [38].

Recently Chapuis et al. determined the CRSS of various deformation modes in pure Mg single crystals using plane strain compression tests, and reported values which are very close to those published for a polycrystalline AZ31 sample [39, 41]. The CRSS values, as a function of deformation temperature, from the study by Chapuis et al. are presented in Figure 2-4. It is noteworthy that over the temperature range ~ 25 °C to 450 °C, CRSS for basal slip and $\{10\bar{1}2\}$ tensile twinning are found to be essentially athermal, while those for other deformation modes decrease with increasing temperature.

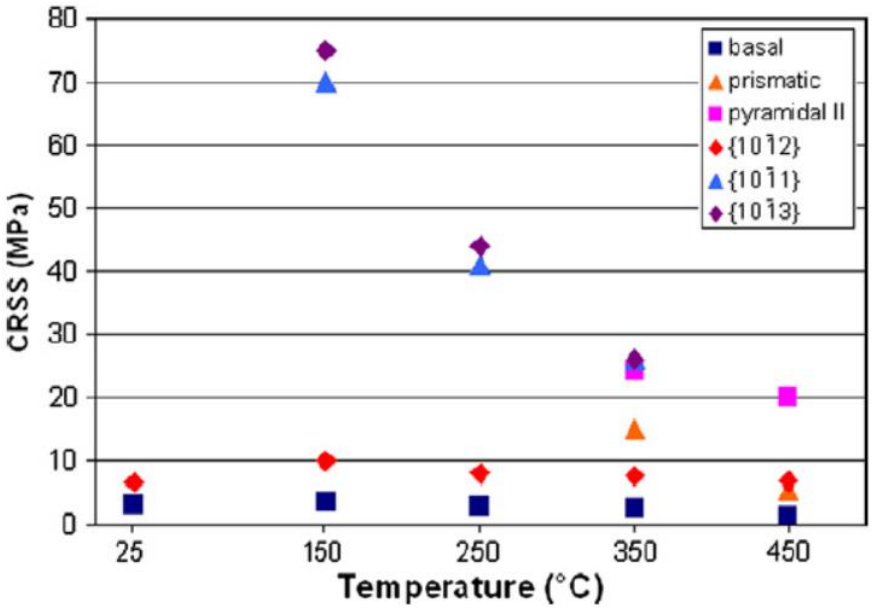

Figure 2-4 CRSS variation with temperature for different deformation modes in pure Mg single crystals [39]

As can be seen from Figure 2-4, at lower temperatures, basal slip and tensile twinning systems have by far the lowest CRSS values, and therefore form the dominant deformation modes, while at higher temperatures the CRSS values for other deformation modes fall rapidly, facilitating their activation. Of particular interest is the

activation of Py2 slip system (because of its ability to provide five independent slip modes). In their study, Chapuis et al. reported that for samples oriented for compression along the c-axis, Py2 slip became the dominant deformation mode at temperatures above 350 °C (and therefore the corresponding CRSS values in Figure 2-4 are only presented for temperatures of 350 °C and above). It is found that CRSS of slip systems is sensitive to deformation strain rate, while that of twinning is not [39], however suitable quantitative information in this regards is currently not available in the literature. Higher twinning activity is reported to take place at higher deformation strain rates [42, 43]. CRSS is also sensitive to the grain size, substitutional solid solutioning, and presence of precipitates in the material. These are described in more detail in section 2.2.1, 2.2.3, and 2.2.4.2, respectively.

2.1.3 Dynamic recrystallization

Dynamic recrystallization (DRX) refers to the phenomenon of nucleation and growth of new stress-free grains in a material by the generation and movement of high angle grain boundaries during deformation [26]. This conventional occurrence of recrystallization is generally called discontinuous dynamic recrystallization (DDRX) because nucleation and growth processes takes place only in localized regions in the microstructure [26]. The driving force for DRX is the stored energy of excess dislocations in the material. DRX nuclei gets generated in the material during deformation as a result of recovery related processes, resulting in formation of cell and subgrain structure in the material. This nuclei can grow (as a new grain) if there is a mechanical driving force (owing to dislocation stress field, or grain boundary surface tension), at a site of high strain energy (i.e. dislocation density, which provides driving force for DRX) and orientation gradient (which provides for a boundary with high mobility) [26, 44]. A defining feature of DRX is the movement of a high angle boundary, which absorbs any excess dislocation density it encounters.

Generation of new grains in the material during deformation can also take place by the rearrangement of dislocations into dislocation cells and subgrains. Further deformation can lead these subgrain boundaries to migrate locally to coalesce and develop into high angle grain boundaries [45], or alternatively, the development of high angle grain boundary can take place through continuous absorption of dislocations into the subgrain structure [46]. This mechanism of new grain formation involves a

minimal movement of high angle boundaries and since it proceeds through continuous absorption of dislocations in the subgrain structure during deformation, it is generally referred to as continuous dynamic recrystallization (CDRX), to distinguish it from the DDRX mechanism. It is noteworthy that CDRX is essentially a recovery phenomenon [26]. In the subsequent text, the terminology “DRX” is specifically used for true recrystallization phenomena, i.e. DDRX, which results in a significant reduction of the excess dislocation density in the material as a result of their absorption in moving high angle grain boundaries, while recovery based continuous dynamic recrystallization is referred to as “CDRX”.

Occurrence of DRX and CDRX in AZ alloys has been found to be associated with certain microstructure features, and the same is reviewed briefly in the following:

1) Grain boundaries

Deformation strain incompatibility at the grain boundaries can result in the development of dislocation pile ups, which create localized stress concentrations on the grain boundary. These stresses can be relaxed in one of the two ways [31]:

i) Rearrangement of dislocations close to the grain boundaries into subgrain structure. These subgrains can rotate (with respect to each other) with continued deformation, followed by coalesce of adjacent low angle boundaries, resulting in the formation of high angle boundaries. This is a type of CDRX mechanism, and was first identified by Ion et al. in Mg-0.8 wt.% Al alloy, and is commonly referred to as **rotational dynamic recrystallization (RDRX) mechanism** [45].

ii) Localized part of the grain boundary can itself move to consume the excess dislocations [31]. This movement of grain boundary typically manifests in form of grain boundary serrations and bulging. The bulged region eventually gets cut off from the parent grain by development of a high angle boundary, resulting in formation of a new recrystallized grain [47]. Since the new grain is formed behind a moving grain boundary, which consumes away excess dislocations in the material, the resultant grain is softer (than the non-recrystallized grains) and deformation preferentially gets localized in it, resulting in its work hardening. The bulged grain boundary continues to move until the work hardening rate balances the driving force for growth, and this determines the DRX grain size of the material

[48]. This mechanism is referred to as the **grain boundary bulging mechanism**, and is a type of the DDRX mechanism. This mechanism is illustrated in in Figure 2-5 for ZK60 alloy deformed in uniaxial compression at 350 °C, at a strain rate of 2.8 x 10^{-3} s^{-1} [47]. In the case shown, the bulged region gets separated from the parent grain by the development of a low angle boundary.

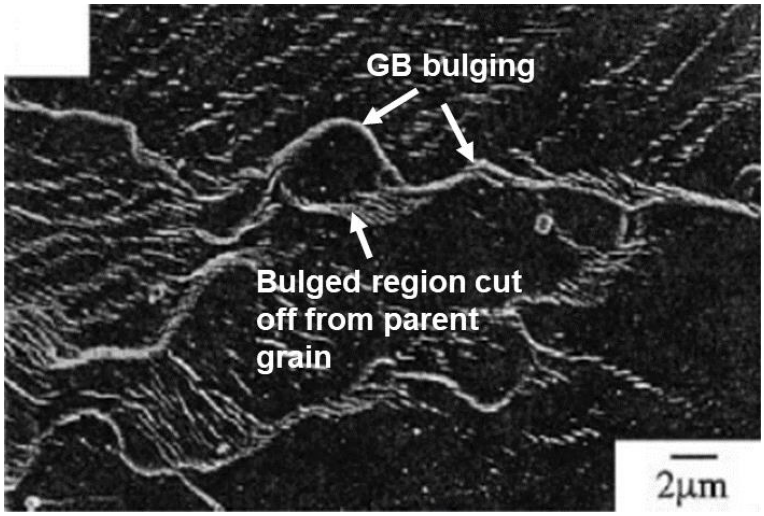

Figure 2-5 ZK60 alloy deformed in uniaxial compression at 350 °C, 2.8 x 10^{-3} s^{-1}, to a strain of 12% [47]

2) Kink bands

Kink bands are intragranular features, and are finite bands of constant misorientation with respect to the grain in which they occur [49]. They typically manifest in the microstructure as bands of finite width and parallel edges, spanning the entire width of the grain in which they occur. Their formation takes place due to activity of different deformation modes in different regions of the same grain, which results in the formation of orientation gradients within the grain. Criss-crossing of individual kink bands leads to the formation of subgrains in the deforming material, which convert into grains with progressive deformation, by continuous absorption of dislocations [46]. This is a type of the CDRX mechanism. Since this mechanism advances by fragmentation of original grain by low angle boundaries, this is referred to as the **grain fragmentation mechanism** in the subsequent text. It is noted that observing kink bands necessitates the use of some misorientation based technique, such as the EBSD. Figure 2-6 shows an example of extensive kink band formation in extruded AZ31 alloy during hot compression at 400 °C, 0.003 s^{-1}, which led to extensive CDRX

in the material [46]. The mechanism has been reported in AZ61 and AZ91 alloys as well [33, 50].

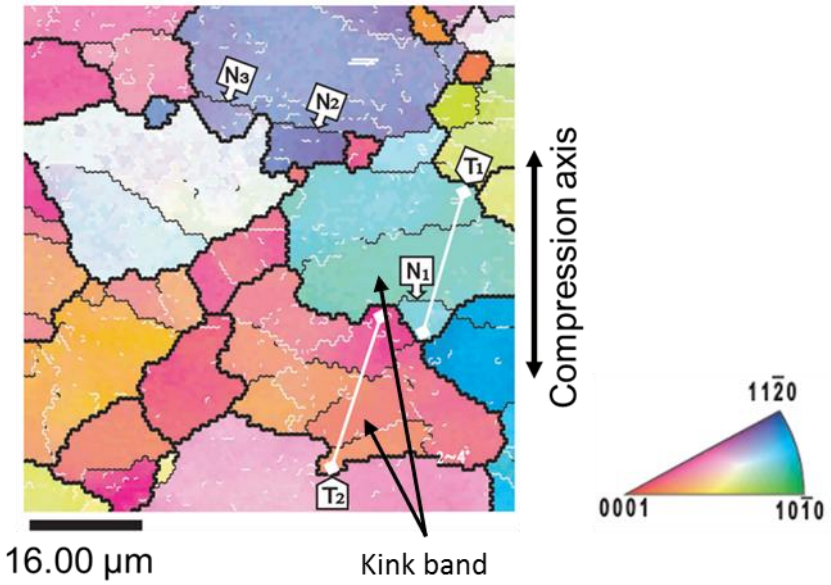

Figure 2-6 Inverse pole figure map of extruded AZ31 deformed in uniaxial compression at 400 °C, 0.003 s^{-1}, to a strain of 0.1. Thin white lines correspond to boundaries with misorientation > 2° thin black line > 4° and thick black lines > 15°, respectively. Colors correspond to crystallographic orientations indicated in the inverse pole figure. Some kink bands are marked in the figure. N1-N3, and T1-T2 are not relevant for the present description. [46]

3) Second phase particles

Second phase particles (> 1µm) are found to aid in DRX through a mechanism referred to as the particle stimulated nucleation (PSN) mechanism [51]. Deformation strain incompatibility near the particles leads to development of deformation heterogeneities. These are highly misoriented regions with respect to the surrounding matrix, and also show much higher dislocation densities, both of which are conducive for DRX [51]. Figure 2-7 shows an example for PSN at a cluster of coarse precipitate particles in a Mg - 0.77 at.% Mn - 0.19 at.% Fe - 0.04 at.% Si alloy [52].

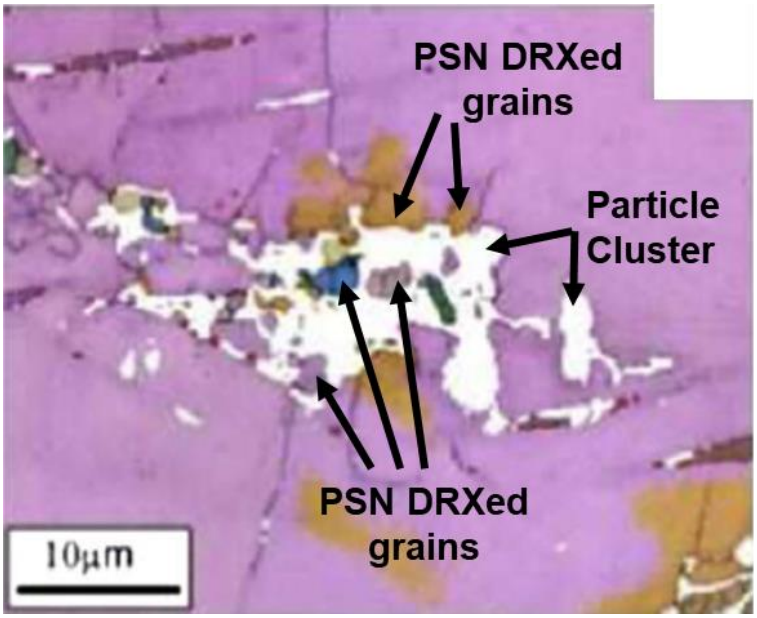

Figure 2-7 PSN of multiple grains at a cluster of coarse precipitate particles in a Mg - 0.77 at.% Mn - 0.19 at.% Fe - 0.04 at.% Si alloy [52]

Work by Xu et al. [33] on PSN in cast AZ91 alloy show that deformation heterogeneities take the form of kink bands in this material, which criss-cross each other at higher deformation strains, leading to the development of a subgrain structure. Further deformation leads to gradual absorption of dislocations by these subgrain boundaries, increasing their misorientation, and eventually converting them into high angle grain boundaries. This seems more like a CDRX type of mechanism, but it is noted that other literature indicates that DRX through PSN can also involve movement of the high angle boundaries [53].

An interesting aspect of DRX through PSN is that owing to large misorientation gradients and multiple nucleation events associated with coarse particles, the DRXed grains typically show a wide scatter in orientations with respect to the parent grains, and thereby can potentially randomize the texture in the material [51]. Prior research on high Al content AZ alloys (AZ61 and AZ91) indicate that PSN at coarse eutectic $Mg_{17}Al_{12}$ particles, and at lamellar discontinuous precipitates, results in DRX texture randomization [22, 23, 24].

4) Shear bands

Shear bands refer to special features in the microstructure wherein the crystallographic planes align themselves with the macroscopic shear plane, with easy

slip taking place within these bands. In AZ alloys, clustering of $\{10\bar{1}1\}$ compression twins and $\{10\bar{1}1\} - \{10\bar{1}2\}$ double twins play an important role in shear banding, owing to easier basal slip in these twinned regions [54, 55]. Once a shear band is formed, deformation becomes highly localized in it, resulting in macroscopically observable strain softening with continued deformation. Owing to localization of deformation in the shear zones, they are frequently associated with the occurrence of DRX [55, 56]. Alternatively, it is also found that RDRX (described earlier) can itself aid in formation of shear bands in Mg alloys, [45]. More recently, Sun et al. have reported that a preferential occurrence of DRX along certain directions (depending on the stress state) can also eventually develop into a shear band, with continued deformation [57]. It is noteworthy that shear bands are considered undesirable for bulk forgeability as localization of deformation in them can lead to shear crack nucleation and fracture [45].

5) Twins

DRX preferentially takes place at regions of high misorientations from surrounding regions, and thereby, twin boundaries, and twin-twin and twin-grain boundary intersections, are found to be among the preferred nucleation sites for DRX. Additionally, the twinned region itself, in many cases, is found to be associated with DRX (or CDRX). In this regards the following mechanisms are found to be relevant for AZ alloys:

a. CDRX in the interior of $\{10\bar{1}2\}$ twins and $\{10\bar{1}1\}$-$\{10\bar{1}2\}$ double twins

Various authors have reported formation of new grains in AZ alloys within $\{10\bar{1}2\}$ tension twins [20], and $\{10\bar{1}1\}$-$\{10\bar{1}2\}$ double twins [33], by initial development of a low angle boundary structure within the twins (aided by basal slip), and its subsequent conversion into high angle boundaries by progressive absorption of dislocations with progressive deformation. Figure 2-8 illustrates this for an AZ91 alloy sample, deformed in uniaxial compression at 300 °C, 0.2 s^{-1}, to a strain of 5% [33].

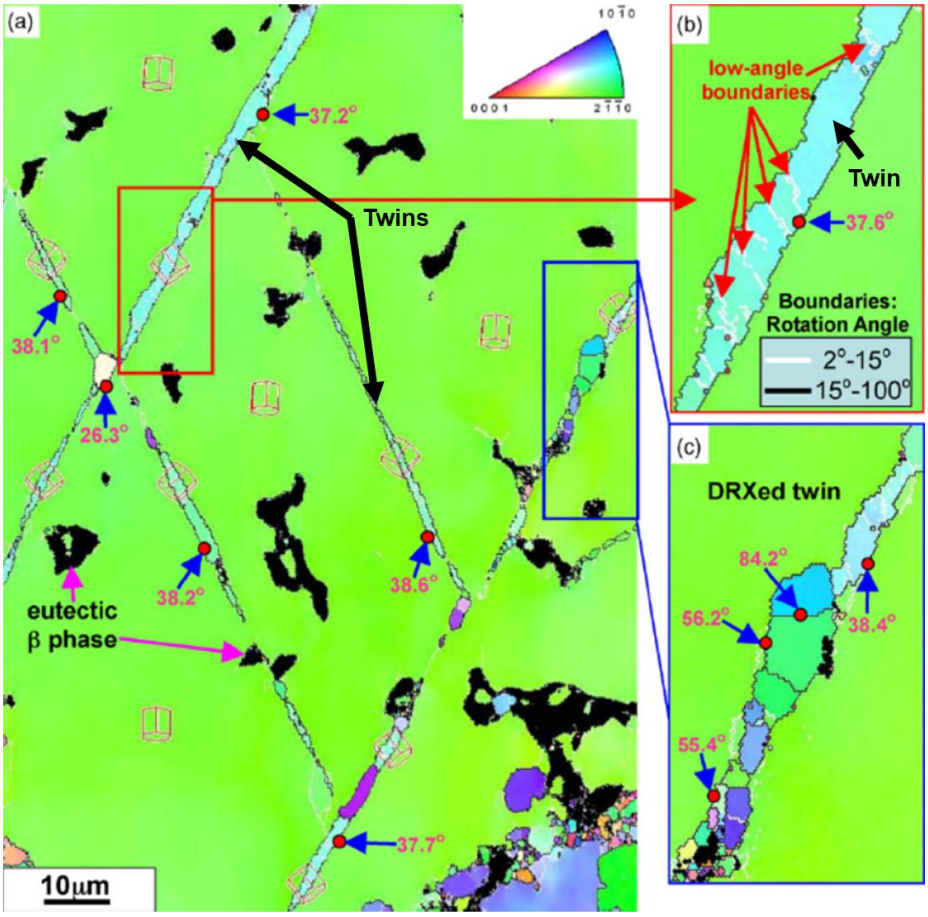

Figure 2-8 DRX within twins by the CDRX mechanism in AZ91 alloy deformed in uniaxial compression at 300 °C, 0.2 s^{-1}, to a strain of 5% [33]

b. Twin-twin intersections and double-twinning

A high propensity of twinning during deformation at low temperatures and/or high strain rates can result in mutual criss-crossing of twins, leading to formation of twin walled grains. Additionally, double twinning also leads to formation of twin-walled grains. These twin-walled grains can grow into the surrounding non-twinned matrix region during further deformation, and thereby act as nuclei for DRX [35, 36].

In this research, the occurrence of DRX within twins, via either of the mechanisms described above, is referred to as twin related DRX (or TDRX).

2.1.4 Deformation texture evolution

2.1.4.1 Texture sharpening

The grains in a deforming material tend to rotate as the deformation progresses, leading to a change of the texture from the starting state. During twinning, the

reorientation of the twinned region takes place rapidly with deformation strain, while for crystallographic slip, the deforming region rotates gradually. The grain rotation due to slip in uniaxial compression is always such that it tends to make the active slip plane perpendicular to the applied loading direction [58]. This is shown schematically for the occurrence of basal slip (which is the dominant slip mode in Mg alloys) in Figure 2-9.

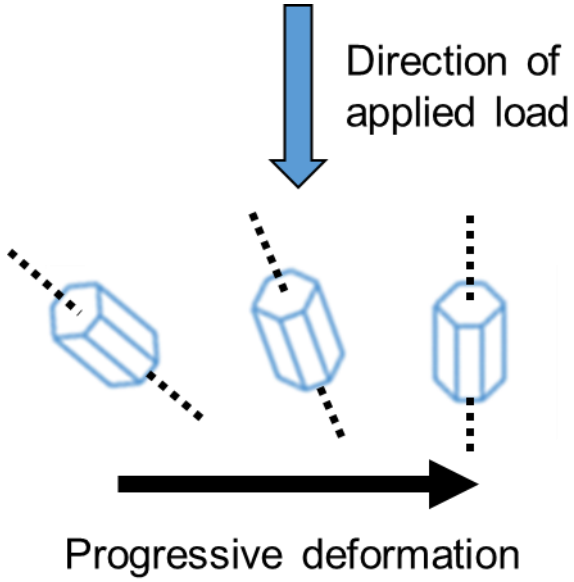

Figure 2-9 Grain rotation due to basal slip during deformation. Dashed lines represents the c-axes of the HCP unit cells.

The rotation of the grains due to various slip and twinning based deformation modes for compressive loading was investigated in detail by Agnew et al., for polycrystalline pure Mg, and Mg-Li and Mg-Y based binary alloys (maximum of 5 wt.% alloying in Mg), aided by crystal plasticity simulations [59]. Their main findings are summarised in the following:

i) Basal slip and $\{10\bar{1}2\}$ tensile twinning reorients the grains so as to align their c-axis parallel to the direction of the applied load. This results in a sharp basal texture along the loading direction. Note that tensile twinning gets activated only if the c-axis of the grain is approximately perpendicular to the compression direction, and since tensile twinning reorients the twinned region by ~ 86°, it results in the formation of basal texture.
ii) Prismatic slip produces crystal rotation around the c-axis, without reorienting it.
iii) Py2 slip accommodates deformation along both $< a >$ and $< c >$ axes. In accommodating deformation along the $< c >$ axis, it rotates the grains away from

the $< c >$ axis, which has the effect of splitting the basal texture developed along the compression direction due to the occurrence of basal slip. The amount of this split depends on the relative activity of Py2 slip and basal slip, with a higher activity of Py2 slip resulting in a more pronounced split from an ideal basal texture.

It is noteworthy that multiple deformation modes can be active in a deforming material (and even within the same grain) simultaneously, and the overall rotation of individual grains is thereby affected by this. Since for low temperature deformation, the CRSS for basal slip and tensile twinning is by far the lowest, and since both of them results in the development of a basal texture along the compression direction, it is easy to see why sharp basal textures typically develop during low temperature forging operations (a type of compressive loading).

2.1.4.2 Texture weakening

A random texture is desirable for better formability of Mg alloys. This is because basal slip, which has the lowest CRSS of any deformation mode, can be easily activated, and also because a more random texture in the deforming material results in more uniform deformation of the material. Previously it has been reported that a more homogeneous partitioning of slip into multiple slip systems can result in a weakening of the texture during deformation [60], and directly relates to the fact that a dominant prevalence of a single deformation mode causes texture sharpening. Additionally, DRX can result in texture randomization during deformation. In this regards, the following studies are found to be of particular interest for the present research:

i) Backx, et al. tested extruded AZ31 rod in compression along the extrusion direction, and showed that the DRXed grains had much weaker texture than the non-DRXed grains [21]. Their results can be best summarized through Figure 2-10.

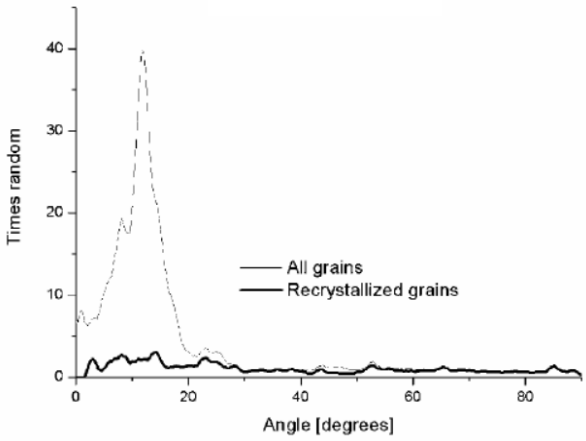

Figure 2-10 (0002) *pole plot of extruded AZ31 sample compressed along the prior extrusion axis at 250 °C, 0.01 s^{-1} to a strain of 0.2. Alignment closer to 0° indicate c-axis of grain being approximately parallel to the compression direction [21].*

The authors further reported that DRX texture randomization took place under all investigated deformation conditions (200 °C – 300 °C, 0.001 s^{-1} – 0.1 s^{-1}), however, was more pronounced at higher deformation temperatures and/ or lower strain rates. The authors reported that grain boundary bulging induced DDRX was the operative DRX mechanism.

ii) Works by Li et al. [22] and Xu et al. [23, 24] have shown DRX texture randomization due to PSN at coarse eutectic $Mg_{17}Al_{12}$ particles, and $Mg_{17}Al_{12}$ lamellar discontinuous precipitates, respectively, in AZ alloys. The role of $Mg_{17}Al_{12}$ precipitates on DRX behaviour of AZ alloys is described in more detail in section 2.2.4.2.

iii) Grains recrystallizing (via CDRX) within the interiors of $\{10\bar{1}2\}$ twins were reported to be randomly oriented with respect to compression direction for AZ31 alloy deformed in uniaxial compression (c-axis lying in a range of 30-70° with respect to the compression direction) [20]. It is noteworthy that CDRX by grain fragmentation approach generally preserves the deformation texture [61].

2.2 Effect of material parameters on hot deformation behaviour

2.2.1 Grain size

It is found that the yield strength of polycrystalline metallic materials follows an inverse dependence on its grain size, with a finer grained material requiring higher stress to yield, compared to a coarser grained material of the same alloy. The underlying reason for inverse dependence of flow stress on the grain size relates to the inverse

dependence of stress required and the space available for dislocation sources to operate. The dependence is traditionally captured through the well-known Hall-Petch equation (equation 2.1), which is found to be applicable for the AZ alloys as well [62].

$$\sigma_Y = \sigma_0 + k_{HP} d^{-1/2} \quad (2.1)$$

In equation 2.1, σ_0 is a materials constant and corresponds to the stress required to initiate dislocation motion in the material, k_{HP} is the strengthening coefficient, σ represents the yield stress, and d represents the effective grain diameter. It is noteworthy that k_{HP} is found to be dependent on the active deformation mode, among other factors, such as, alloying content in the material, and its processing history (e.g. rolling, extrusion, etc.) [62].

A more fundamental way of looking at the effect of grain size on the flow stress values is through its effect on the CRSS values [63, 64]. This is shown in Figure 2-11 (a) for deformation of pure Mg polycrystals at room temperature. The y-axis of the plot shows the yield stress of the material, which also happens to represent the CRSS for individual deformation modes, because of the way the experiments were designed [63]. Considering the figure, different deformation modes have different Hall-Petch slopes, k, with that of the prismatic slip being the highest. Though the corresponding data for Py2 slip system is not included in Figure 2-11, Raeisinia et al. have shown that its slope is slightly higher than that of the prismatic slip [65]. Difference in slopes indicate that the sensitivity of CRSS to grain size for different deformation modes varies, which results in variations in the relative ratios of CRSS of non-basal deformation modes to that of the basal slip. This is shown for the data presented in Figure 2-11 (a) in Figure 2-11 (b), in terms of variation of $CRSS_{Prismatic}/CRSS_{Basal}$ and $CRSS_{Tensile\ Twinning}/CRSS_{Basal}$ with grain size. The plot indicates that at very coarse grain size, the $CRSS_{Prismatic}/CRSS_{Basal}$ approaches that of the single crystals [38], while with grain refinement it lowers substantially, indicating that it becomes progressively easier to activate prismatic slip in the material with grain refinement (and likewise an ease in the activation of Py2 slip with grain refinement is expected). Previous results by Koike, et al. [40], on room temperature deformation of a fine grained AZ31 alloy (initial grain size ~ 6.5 µm), whereby the authors reported activity of Py2 slip near the

grain boundaries, validates the prediction of these crystal plasticity based simulations. It is noted that these studies on the effect of grain size on the CRSS values were mainly limited to room temperature deformation, however, considering that Barnett et al. have reported for AZ31 alloy that k_{HP} (with reference to equation 2.1) for slip and twinning were different, at least till 200 °C [62], it is reasonable to assume that the effect of grain size on CRSS for different deformation modes persist even for high temperature deformation.

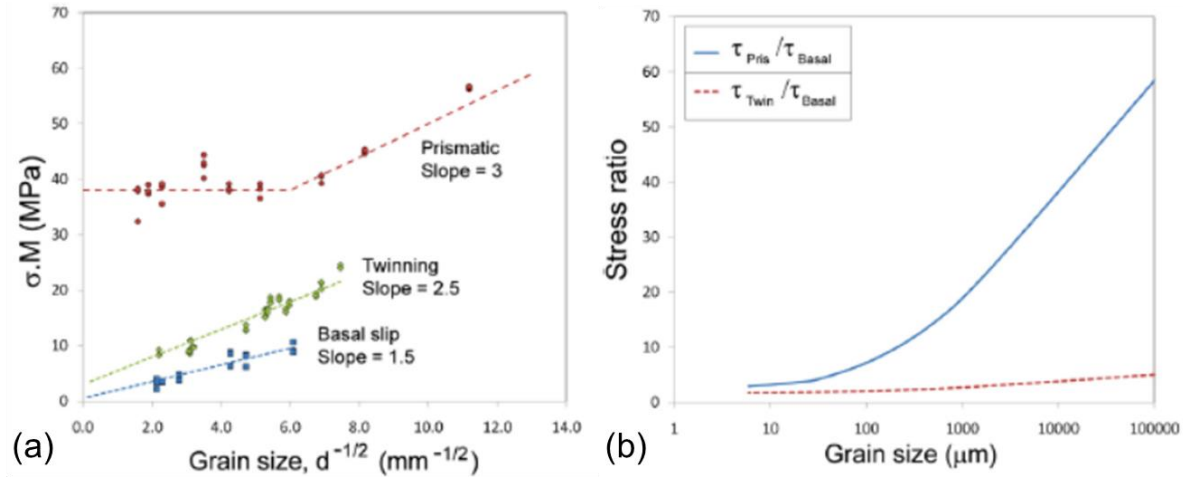

Figure 2-11 Effect of grain size on the CRSS for various deformation modes in pure Mg polycrystals for deformation at the room temperature: (a) Yield stress (indicative of CRSS in the present case), (b) relative CRSS ratio (lower values indicate an ease in activation with reference to the basal slip) [63]

Grain boundaries form a preferred nucleation site for DDRX to occur, and because of this, grain refinement, which increases the grain boundary area per unit material's volume, is found to enhance the DRX kinetics in the material [66, 67]. This is shown in graph in Figure 2-12 for extruded AZ31 alloy [66].

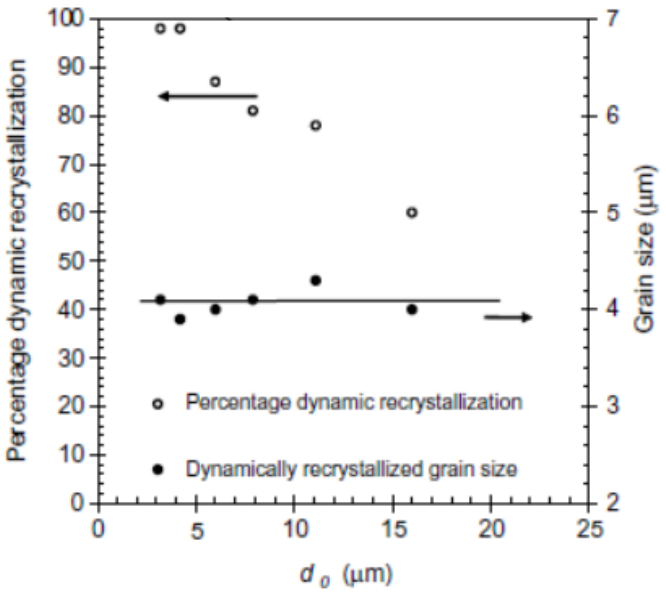

Figure 2-12 Effect of starting grain size on DRX fraction and DRX grain size in an extruded AZ31 alloy deformed in uniaxial compression at 300 °C, 0.01 s^{-1} to a strain of 0.5. Adapted from [66].

The graph also shows the effect of initial grain size on the DRX grain size, whereby it can be seen that the DRX grain size does not depend on the grain size of the starting material. The finding is in line with prior work by Sellars on other materials, whereby the author noted that the DRX grain size depends on deformation conditions (temperature and strain rate), and not on the prior grain size or the deformation strain level [68]. It is important to highlight here that few authors have reported for some AZ alloys that a finer initial grain size results in a finer DRX grain size [67, 69]. Considering this discrepancy, there is currently a lack of clarity regarding the effect of prior grain size on the DRX grain size for these alloys.

2.2.2 Texture

Orientation of the grains determine the resolved shear stress acting on various deformation modes, thereby controlling their activation and determining the flow stress values during deformation [25]. Texture affects both strength and ductility of a material, and various authors have extensively studied this relationship for various AZ alloys [19, 70, 71]. A particularly noticeable way the effect of starting texture manifests is the way the material flows during deformation. Various authors have reported for AZ alloys that applying loads, which lead to asymmetric activation of various deformation modes with respect to the loading axis, can result in preferred material flow in specific

directions [42, 72, 73, 74]. Figure 2-13 shows such a situation when a (sharp textured) extruded AZ31 plate was deformed in compression parallel and perpendicular to the extrusion direction. The starting texture of the cylindrical compression test samples (with respect to the loading direction) is also provided. It can be seen that deformation of the sample for which the compression direction was symmetric with respect to the starting texture resulted in symmetric shape (circular) of the final deformed sample (Figure 2-13 (a)), while for the sample for which the starting texture was asymmetric with respect to the compression direction, preferential material flow took place along ND, resulting in an oval shaped cross-section (Figure 2-13 (b)). Material flow anisotropy has also been reported for extruded AZ80 rod deformed in uniaxial compression along and perpendicular to the prior compression axis [75].

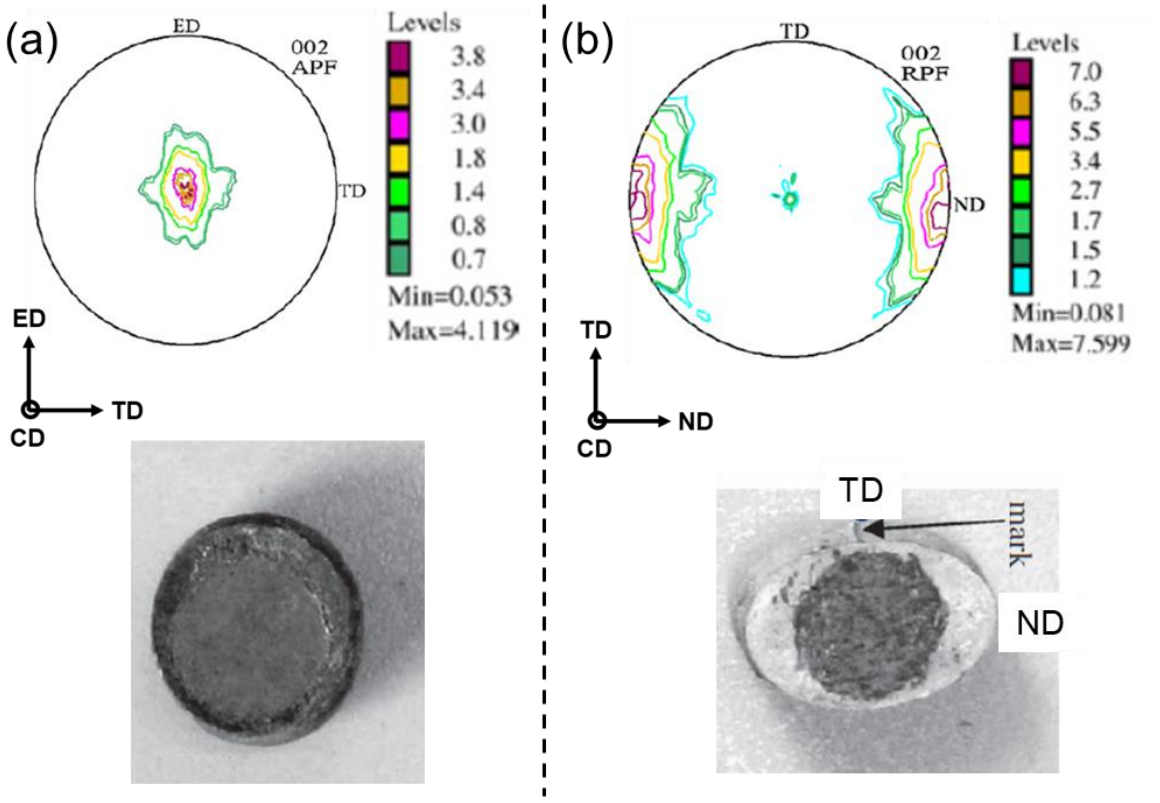

Figure 2-13 Effect of initial texture on material flow (a) symmetric distribution of the starting texture results in a symmetric material flow during deformation, (b) asymmetric distribution of starting texture with respect to compression direction (CD) results in a preferred material flow along ND. Deformation was done using symmetrical cylindrical samples (with cylindrical axis along the CD). CD: Compression direction, ND: Normal direction, TD: Transverse direction, ED: Extrusion direction. Adapted from [42]

The starting texture was found to affect the DRX behaviour of the material as well. Various authors have reported that the texture effect on DRX is based on the activation

of different deformation mechanisms (i.e. the slip/twin systems) depending on the starting texture of the material, with the overall result that DRX initiation and propagation is favored for certain orientations more than others [61, 76, 77, 78, 79]. A common observation from most of these studies is that DRX is promoted for starting textures which promote multiple slip activity [61, 76, 79]. Of special importance is activation of Py2 slip, since it offers 1) five independent slip systems, and also, 2) owing to a high stacking fault energy on the Py2 slip plane (~ 452 mJ/m^2), also promote cross-slip and climb, both of which aid in DRX [79]. Additionally, it is reported that starting texture also affects the DRX mechanism (including the possibility of CDRX) in the material [79].

An example is given in Figure 2-14 regarding the effect of the starting texture on DRX fraction and DRX grain size in a wrought AZ31 alloy deformed in plane strain compression [77]. Z in Figure 2-14 refers to the Zener-Hollomon parameter, which is a parameter that combines the effect of the deformation strain rate and temperature, and is also sometimes referred to as the temperature corrected strain rate. Z is calculated based on the following equation:

$$Z = \dot{\varepsilon} * \exp\left(Q/_{RT}\right) \tag{2.2}$$

where Q refers to the activation energy of deformation, R is the universal gas constant, while $\dot{\varepsilon}$ and T represent the deformation strain rate and temperature, respectively. Higher deformation temperatures and lower strain rates results in lower Z values, and vice versa.

With regards to the Figure 2-14 (a), the author explained a lower DRX fraction in case of the c-axis constraint samples to an ease in prismatic slip (i.e. prevalence of single slip conditions). With regards to the DRX grain size (Figure 2-14 (b)), on the other hand, the starting texture did not have any noticeable effect. In both cases (i.e. Figure 2-14 (a) and (b)) the sensitivity of DRX fraction and DRX grain size to the starting texture is much less compared to that to the deformation conditions. Similar results have been reported by other authors as well on low Al content AZ alloys [20, 45, 61, 77], while for high Al content AZ alloys, such studies are altogether lacking.

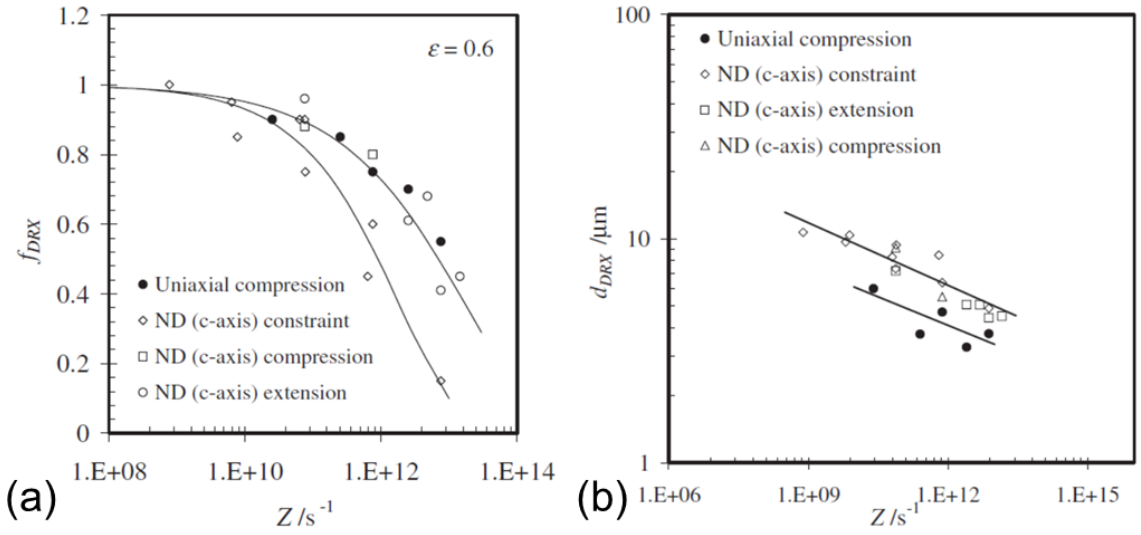

Figure 2-14 Effect of starting texture on (a) DRX fraction, (b) DRX grain size. AZ31 alloy deformed in plane strain compression, in temperature range of 300 °C– 400 °C, and strain rate range of 0.001 s^{-1} – 1 s^{-1}. Adapted from [77]

2.2.3 Alloying

Alloying elements effect the deformation behaviour in both solid solution, as well as by formation of secondary phases. The current section describes the effect of solid solutioning on hot deformation behaviour of the Mg alloys, while the next section describes the same for the effect of the precipitates. Since one of the objectives of the present research is to compare hot deformation behaviours of AZ31 and AZ80 alloys, which mainly differ in terms of the Al content, the literature specifically pertaining to Al in Mg is explored in more detail in the following.

The alloying element induces misfit strains (due to its different atomic size) in the base material, as well as alter the stacking fault energy on various crystallographic planes. As such, the effect manifests in terms of varied activity of various slip systems. Some authors have explored the effect of Al alloying in terms of its effect on the CRSS values for various deformation modes [80, 81, 82]. Mahato has recently systemically studied the effect of Al alloying in polycrystalline Mg, in a range of 0.2 – 5 wt.% Al content, and temperatures ranging from -78 °C to 200 °C, on the deformation and recrystallization behaviour of the binary Mg-Al alloys [82]. The author's results pertaining to the effect of alloying on CRSS are presented in Figure 2-15. The results indicate that Al in Mg increases the CRSS, with different deformation modes having different sensitivity to the Al content. Based on the results presented in Figure 2-15, basal slip seems to be

relatively insensitive to the Al content, although it is noteworthy that previously few other authors have shown that for both single crystals, and polycrystalline material, CRSS for basal slip increases with an increase in the Al content [80, 81].

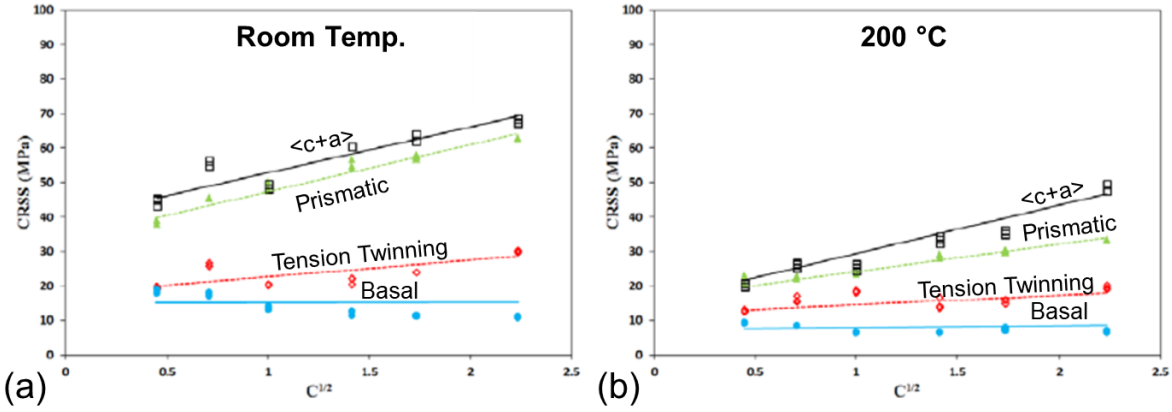

Figure 2-15 Effect of Al alloying in polycrystalline Mg on the CRSS for various deformation modes at: (a) Room temperature, (b) 200 °C. Twinning refer to $\{10\bar{1}2\}$ *tensile twinning. X-axis shows concentration of Al in square root of wt.% [82].*

The alloying elements also have a tendency to segregate to the grain boundaries (in order to reduce the misfit strain energy), which causes a dragging force on the latter's movement (also referred to as solute drag) [83]. This reduces the mobility of the boundaries, and thereby also affects the DRX behaviour of the material [82, 83]. This aspect had, however, not been very systematically studied for the Mg-Al system until very recently [82, 84]. Mahato studied the effect of Al content (in the range of 0.2 – 5 wt.%) in binary Mg-Al alloys [82], and reported that increasing the Al content in Mg reduced both, DRX fraction, as well as the DRX grain size, and attributed this to an increase in the solute drag pressure on the grain boundaries with an increased Al content, which restricted the growth of the DRXed grains. For polycrystals oriented for easy basal slip and deformation at 200 °C, the author reported that the DRX fraction decreased from 70% to 10% on increasing the Al content in the material from 0.5 to 5 wt.%, while at the same time, the DRX grain size got reduced from ~ 5 µm to ~ 1 µm. Mahato did not investigate the role of alloying on the texture evolution.

Guo et al., on the other hand, compared the microstructure and texture evolution during hot rolling of wrought AZ31, AZ61 and AZ91 alloys at 450 °C [84]. Similar to Mahato's work, they reported a decrease in the DRX grain size with an increase in the Al content in the material ($d_{DRX.\ AZ31}$ ~ 8 µm, while $d_{DRX.\ AZ91}$ ~ 2 µm). It is noteworthy

that that they attributed the finer DRX grain size in the AZ91 alloy to pining of the boundaries of the DRXed grains by fine $Mg_{17}Al_{12}$ particles, that got dynamically precipitated during the deformation itself (even at a high deformation temperature of 450 °C) [85]. As such, though the results seem comparable to those of Mahato, the underlying reason behind the DRX grain refinement in the two cases is very different. Guo et al. further reported a decrease in the twin/shear band activity in the material with an increase in the Al content, and a change in the dominant twin type from $\{10\bar{1}2\} - \{10\bar{1}1\}$ double twins in AZ31 to mainly the $\{10\bar{1}2\}$ tension twins in the AZ91 alloy. The authors even investigated the effect of alloying on texture evolution, and while their interpretation of the DRX texture results seem subjective, their work conclusively established that the texture of the non-recrystallized grains was shaper in the AZ91 alloy, compared to the AZ31 alloy, which they attributed to a lowering of prismatic slip activity in the material with an increase in the Al content.

2.2.4 Precipitate state

2.2.4.1 Types of precipitates in AZ alloys

The current work focuses on the AZ80 magnesium alloy, so the precipitates relevant to it are described in this section. The equilibrium phase diagram for this alloy is presented in Figure 2-16. It shows that depending on the temperature, different secondary phases can be present in the material, along with the α-Mg matrix. In addition to these, some non-equilibrium phases involving Mg-Zn and Mg-Al-Zn elements, are also reported in these alloys, since the material rarely shows an equilibrium microstructure [86, 87, 88]. It is noteworthy that only the $Mg_{17}Al_{12}$ phase (also known as the γ phase) occurs in any significant amount. Also, the amount, morphology and distribution of $Mg_{17}Al_{12}$ phase is also found to be amenable to heat treatment in the usual heat treatment and hot working temperature regime of these alloys (250 °C – 450 °C) [89, 90, 91, 92].

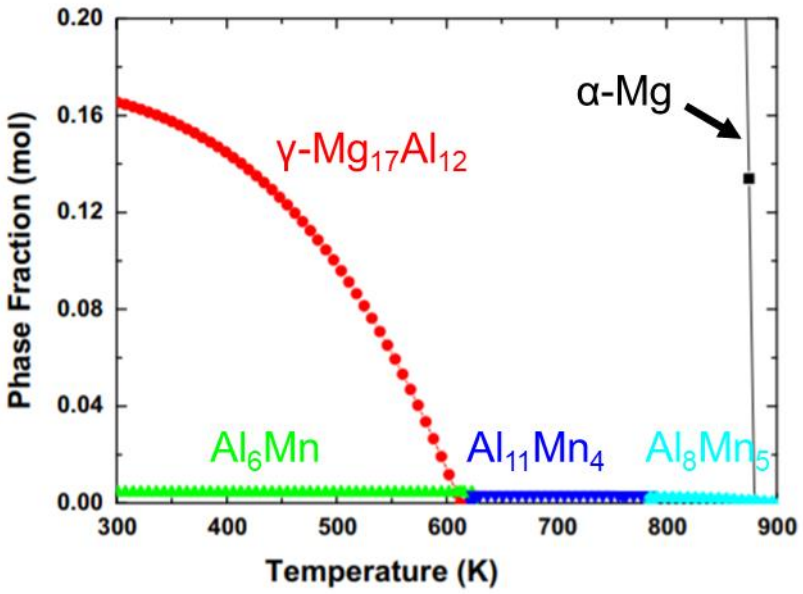

Figure 2-16 Equilibrium phase fraction map of AZ80 alloy [93]

In AZ alloys γ-$Mg_{17}Al_{12}$ can occur in different morphologies. One type of morphology is related to eutectic solidification after casting, while the other morphologies are related to solid state phase transformation taking place during heat treatment. During solid state phase transformation, γ-$Mg_{17}Al_{12}$ phase can precipitate in various morphologies: lath form, irregular slab form, lamellar form, globular form, and intergranular form [89, 90, 92, 94, 95, 96]. The first two are forms of continuous precipitates (CP), so called because they occur more or less uniformly throughout the grain's volume and are related to volume diffusion of Al in the Mg matrix. The latter three are forms of discontinuous precipitates (DP), so called because they nucleate only at the grain boundaries, and their formation is aided by grain boundary diffusion [90, 94]. Among DP, lamellar form and globular form are the dominant morphologies. All these precipitate forms, except the lamellar form, are very fine (typically less than 1 μm) [91, 92, 95]. Figure 2-17 shows some of the $Mg_{17}Al_{12}$ precipitate morphologies found relevant for the present work.

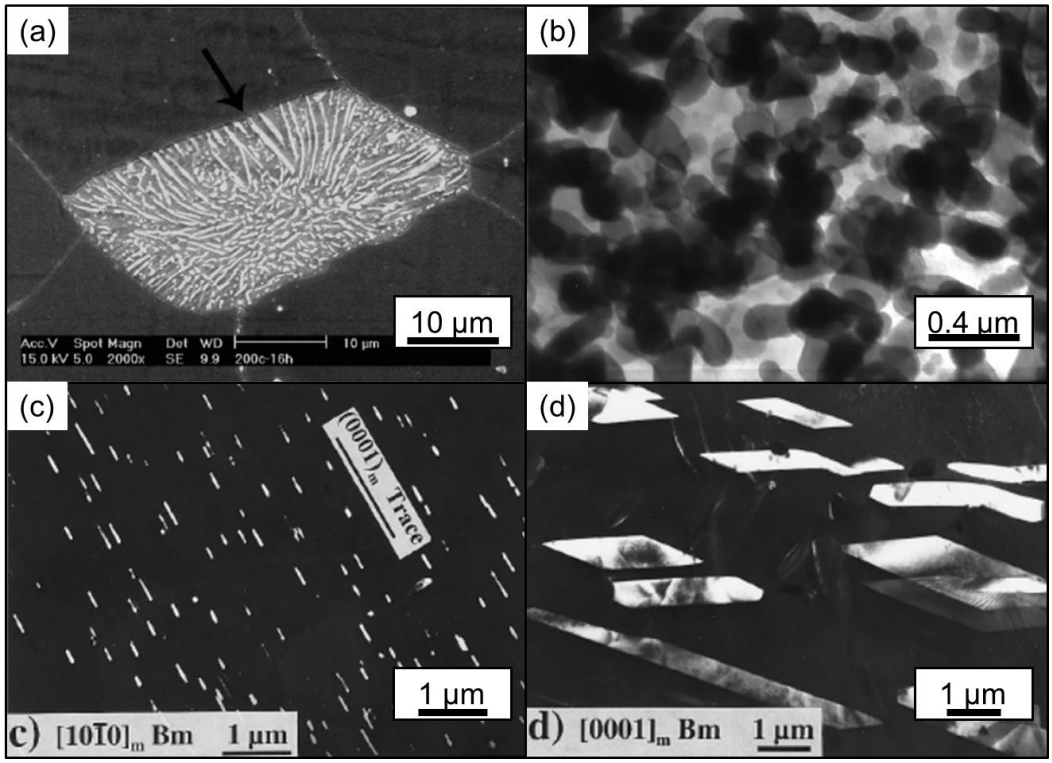

Figure 2-17 Different $Mg_{17}Al_{12}$ precipitate morphologies in AZ alloys: (a) DP in lamellar form, (b) DP in ellipsoidal particle (globular) form, (c) CP in form of laths, and (d) CP in form of irregular plates. (a) and (b) are for AZ80 [92], while (c) and (d) are for AZ91 [91].

Through extensive heat treatment studies on various Mg-Al and AZ alloys, various authors have reported temperature windows where a particular type of precipitate is dominant, and their results show that it is even possible to obtain only continuous or discontinuous type of precipitates in the material by aging it under specific temperature regimes [89, 90, 92, 96]. In addition to the CP and DP morphologies described above, γ-$Mg_{17}Al_{12}$ is also found to precipitate in another form: as fine submicron sized particles, during hot deformation itself, whereby the precipitation takes place at grain boundaries and within grains [85]. This phenomenon is also referred to as dynamic precipitation, since the precipitation is induced by deformation. Other authors have reported this phenomena in other AZ alloys as well, including AZ81 [23, 69, 97].

2.2.4.2 Effect of precipitates on hot deformation behaviour

Shear-resistant (i.e. non-deformable) precipitates can block the movement of dislocations on various slip/twin planes, and result in hardening of the deformation modes by the Orowan strengthening mechanism [53]. The hardening effectively takes place by an increase in the CRSS for various slip/twin modes (by differing amounts)

and results in an alternation of their relative activities. This has been explored for various Mg based alloys, including for AZ91, both experimentally (in some cases also aided by crystal plasticity simulations) [98, 99, 100], as well as based on theoretical calculations [98, 101, 102].

Precipitates, depending on their size, can also affect the recrystallization behaviour of the material by either promoting DRX via PSN (for precipitates coarser than 1 µm), or by pinning the growth of the newly DRXed grains (for precipitates finer than 1 µm) [51]. Prior literature on AZ91 alloy indicates that **coarse eutectic $Mg_{17}Al_{12}$ particles** lead to PSN, as well as to DRX texture randomization [22, 33].

The role of **CP and DP** on DRX, however, is less clear, as only one research group has previously reported on this, and their results are seemingly contradictory [23, 24]. In some research involving cast AZ91 alloy, Xu et al. showed clear evidence of DRX taking place only in previously DP precipitated area, and not in the CP precipitated area (shown in Figure 2-18 (a-c)), while in other research, their results indicate that substantial amount of DRX took place even in the CP precipitated area (shown in Figure 2-18 (d-f)). While the authors do not point out the apparent discrepancy, or provide any explanation, it is noteworthy that the deformation conditions (i.e. temperature and strain rate) in the two cases were very different, which could have affected the deformation and recrystallization mechanisms in the material.

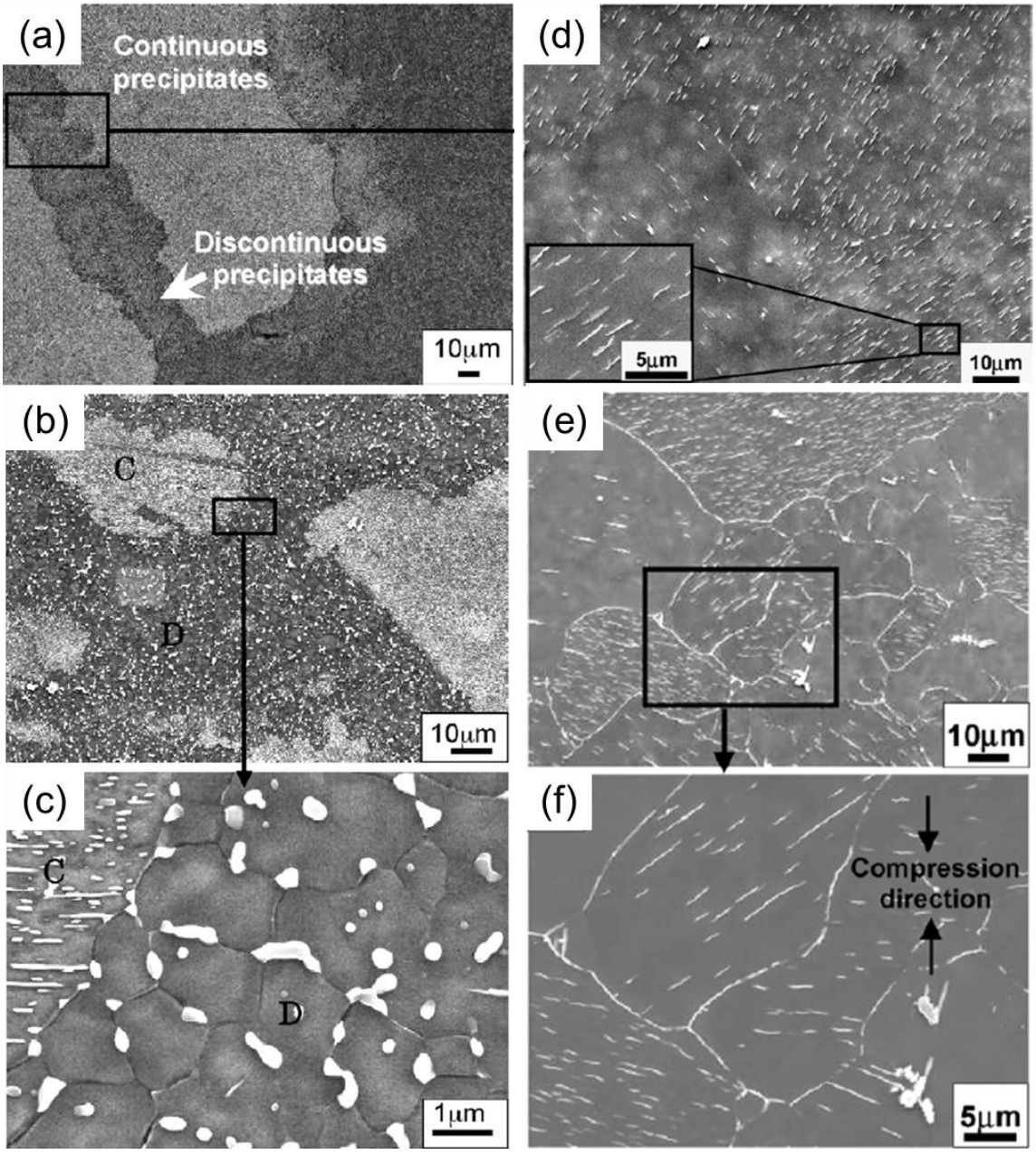

Figure 2-18 (a-c) hot deformation of a cast-homogenized and pre-aged AZ91 sample at 300 °C, 0.2 s^{-1}, showing the occurrence of DRX only in regions previously occupied by DP [24]; (d-f) hot deformation of a cast-homogenized AZ91 sample at 400 °C, 0.2 s^{-1}. At 400 °C, CP got precipitated in the homogenized material during heating to and holding at the test temperature. (e-f) shows extensive DRX occurred in the material in this case as well [23]. (a) and (d) correspond to non-deformed samples, while (b, c, e, and f) correspond to deformed samples. C and D in (b) and (c) refer to continuous precipitates and discontinuous precipitates, respectively.

Second phase particles of size less than 1 μm are generally associated with the grain boundary pinning phenomenon. When a grain boundary comes in contact with a particle, its effective boundary area is reduced, and hence its energy reduces.

However, when the boundary moves (for grain growth), this grain boundary area needs to be regenerated, thereby requiring energy, and therefore resulting in generation of a drag force on movement the boundary [26]. This drag force is commonly referred to as the Zener drag force. For spherical, uniformly distributed particles, the Zener drag force is given by,

$$p_R = -\frac{3}{2}\gamma\frac{f}{R_P} \tag{2.3}$$

where, p_R is the Zener drag force, γ is the grain boundary energy, and f and R_P are the volume fraction of the second phase particles, and their radius, respectively. The negative sign implies a retarding force. Equation 2.3 suggests that a higher fraction of particles with a lower particle size are more effective in pinning the grain boundaries.

Previous research on DRX in high Al content AZ alloys show that grain refinement is promoted by pinning of the DRXed grains by fine $Mg_{17}Al_{12}$ precipitate particles [23, 24, 33, 85, 97, 103]. Specifically, it is found that fine $Mg_{17}Al_{12}$ precipitates get distributed at the boundaries of the newly recrystallized grains during deformation, and the pinning effect caused by them restricts the growth of these grains, resulting in a finer DRX grain size. Xu et al. have reported that these pinning precipitates are in size range ~ 0.3 - 0.8 μm [24], and reported a DRX grain size of 0.2–1 μm in more heavily pinned regions, while of 2–5 μm in less pinned regions [33]. Pinning of DRXed grains by fine $Mg_{17}Al_{12}$ precipitates can be seen in Figure 2-18 (c). Work by Guo et al. has shown that these precipitates get dynamically precipitated directly in this morphology during the hot deformation itself [85]. Additionally, shearing of large lamellar precipitates (i.e. DP) during deformation and DRX might also contribute to formation of these fine pinning precipitates as Xu et al. have proposed [33].

2.3 Effect of deformation parameters on hot deformation behaviour

2.3.1 Temperature and strain rate

Various studies on AZ alloys have established that the formability of the material is enhanced at higher deformation temperatures and lower strain rates. While the role of temperature is related to the lowering of CRSS for non-basal slip systems (especially the Py2 slip) which significantly enhances the material's workability at higher deformation temperatures, the effect of strain rate is related to the time available for

various microstructure phenomenon like restoration process (recovery, recrystallization), grain growth, and dynamic precipitation to take place. Also, higher strain rates may not allow enough time for diffusion based deformation modes (i.e. crystallographic slip) to accommodate the deformation fully, and thereby shear based mechanisms (i.e. twinning) are promoted. Flow stress evolution (with deformation strain) is found to be dependent on the Z values (i.e. the Zener-Hollomon parameter, as defined in equation 2.2), with deformation at high Z values resulting in flow curves with distinct work hardening and work softening regimes, while deformation at low Z values resulting in more of a steady state flow stress curve throughout the deformation.

Hot deformation also promotes the occurrence of DRX in the material. The deformation conditions are found to affect both, the DRX fraction, as well as the DRX grain size. Results from Beer et al. for hot uniaxial compression of cast and extruded AZ31 alloys are presented in Figure 2-19, and show the variation in DRX% and DRX grain size with Z values (deformation temperature in the range of 300 °C – 450 °C, and strain rates in the range of 0.01 s^{-1} - 1 s^{-1}) [67]. The results show that lowering the Z value promotes occurrence of DRX, as well as increase the DRX grain size. Similar results have been reported by other authors as well [20, 48, 77].

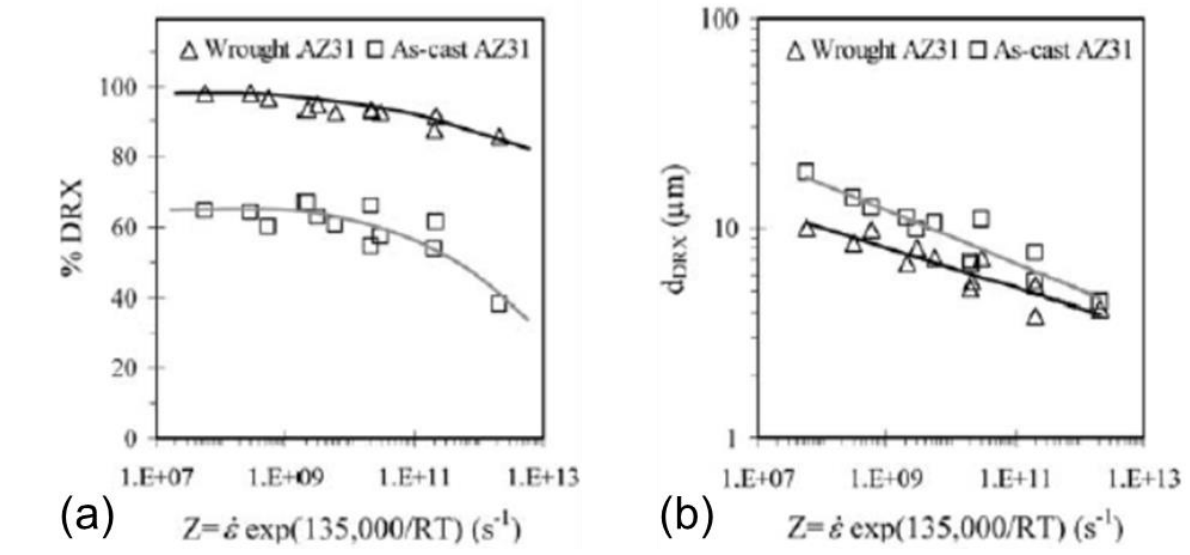

Figure 2-19 Variation in (a) DRX ratio and (b) DRX grain size, with the Z parameter. Cast and extruded AZ31 alloys deformed in uniaxial compression for temperatures in the range of 300 - 450 °C, and strain rates in the range of 0.01 – 1 s^{-1}. For the data presented in the graphs, DRXed grains were distinguished from the parent grains based on their size and shape [67].

Change in deformation conditions can alter the mechanism by which DRX is taking place in the material [35, 47, 48]. Figure 2-20 illustrates this for the case of hot deformation of pure Mg [35]. As is evident, the DRX mechanism is strongly dependent on the deformation conditions (in this case, the deformation temperature), as well as the deformation strain level. The map also indicates that for certain conditions it is possible for multiple DRX mechanism to be simultaneously active.

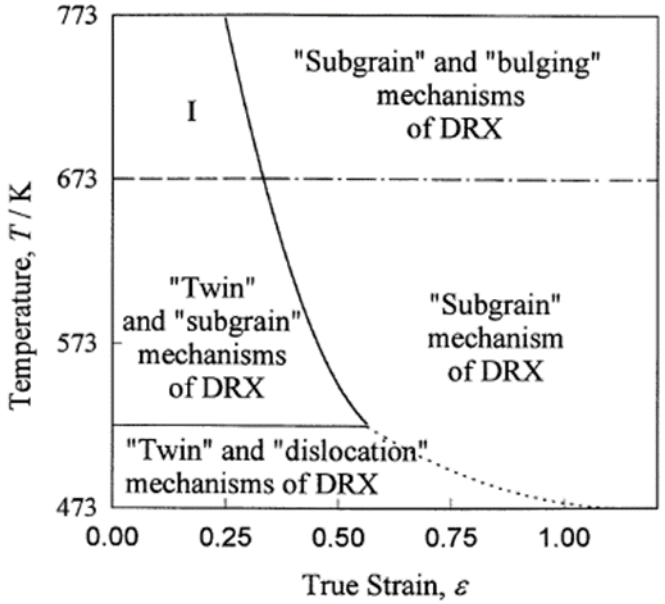

Figure 2-20 Change of DRX mechanism with deformation conditions for deformation of pure Mg. In area marked as I, DRX takes place via the twinning mechanism [35]

For high Al content AZ alloys, such studies investigating the role of deformation conditions on DRX behaviour are comparatively few [22, 23, 24, 97], and leaves much to be explored, particularly with regards to studying simultaneously, the evolution of flow stress, microstructures and texture, with deformation conditions and strain.

2.3.2 Strain

DRX is a dynamic softening mechanism, which gets activated in the material to compensate for work hardening and dislocation accumulation. The driving force for DRX is the accumulated deformation energy [26]. As such, DRX is typically reported to initiate only when there is already some critical buildup of deformation energy in the material. Poliak and Jonas, based on principles of irreversible thermodynamics, determined that DRX initiates in the material before the peak strain (i.e. the strain corresponding to peak stress) is achieved, and this strain can be determined based

on the inflection point in the work hardening vs flow stress curve (i.e. Θ – σ curve) [104, 105]. Since then, many authors have successfully used this technique for various materials, including Mg alloys, to determine the critical strain required to initiate DRX in the material for various deformation conditions [106, 107, 108, 109, 110]. Some studies reveal that DRX initiates approximately at some constant fraction of the peak strain level, with many authors using a value of 0.8 times the peak strain as the critical strain [111, 112], and the same has been found to be appropriate for the AZ31 alloy as well [113]. After the initiation, DRX progresses rapidly to consume more of the deformed microstructure, with the recrystallization kinetics typically captured by the Johnson-Mehl-Avrami-Kolmogorov (JMAK) equation [26, 108]. DRX grain size is typically reported to be independent of the deformation strain level [48, 67, 114].

The results pertaining to evolution of DRX% and DRX grain size by Beer et al. in cast and extruded AZ31 alloy deformed in uniaxial compression at 350 °C, 0.01 s^{-1}, are presented in Figure 2-21, and validate the above description [67].

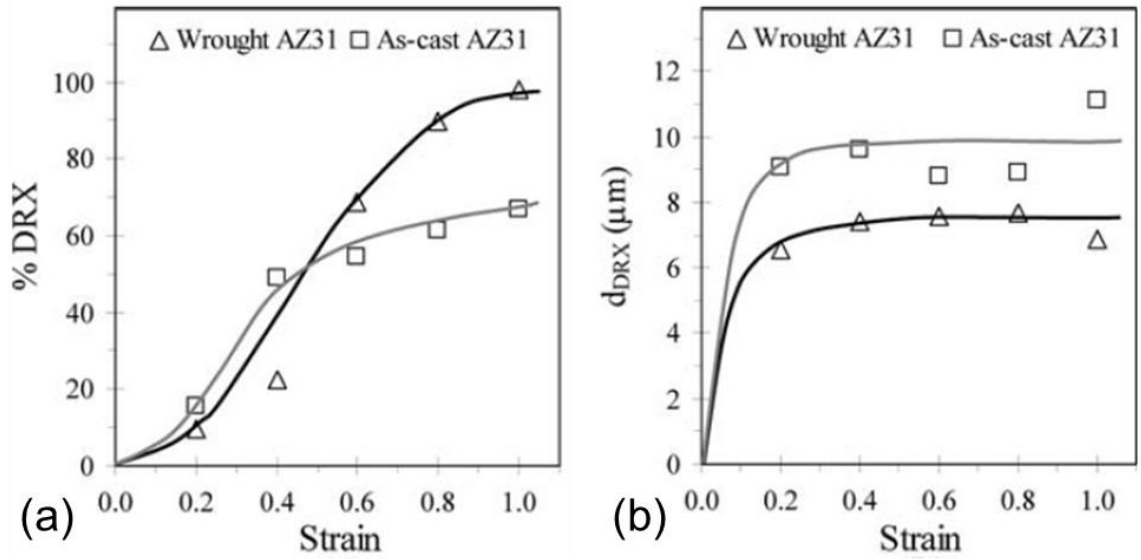

Figure 2-21 Progress of DRX with deformation strain for deformation of cast and extruded AZ31 alloys at 350 °C, 0.01 s^{-1}: (a) DRX%, (b) DRX grain size. Lines are drawn to guide the eye. For the data presented in the graphs, DRXed grains were distinguished from the parent grains based on their size and shape [67]

The progress of DRX in the deforming material is also reflected in the evolution of the flow stress curves. DDRX, owing to rapid absorption of dislocations by the moving grain boundaries, results in a pronounced work softening following the peak flow stress [48, 67, 115]. CDRX, on the other hand, being essentially a strong recovery

phenomenon, with no drastic reduction in the dislocation density in the material involved, typically results in a steady state flow stress curve [106, 116].

2.4 Summary

High Al content AZ alloys (in the range of ~ 6 - 9 wt.% Al), such as the AZ80 alloy, are of special interest for structural applications since they show an optimum combination of castability and forgeability, and are also amenable to heat treatment (based on the $Mg_{17}Al_{12}$ precipitates). However, most of our understanding on the hot deformation behaviour of the AZ alloys is still based on research studies done primarily on the AZ31 alloy as it is the most important alloy from a commercial perspective. In order to be able to use AZ80 for industrial forging applications, we need to have a better understanding of the *starting material-forging process-final properties* relationship. Considering this, specific knowledge gaps in the literature have been identified and summarized below:

1) The effect of deformation conditions on the hot deformation behaviour, particularly with regard to DRX and texture evolution, has not be explored systematically for AZ80 alloy.
2) The role different morphologies of $Mg_{17}Al_{12}$ precipitates play during hot deformation of AZ alloys with a high aluminium content, such as AZ80 and AZ91 is not clear.
3) The role of starting texture on the hot deformation behaviour, including on microstructure evolution and DRX, and material flow anisotropy, have been mainly explored for AZ31 alloy, while no comparable study exist for AZ alloys with higher Al content.
4) Prior literature indicates that Al content in solid solution in Mg has a significant effect on the hot deformation behaviour of the material, including on microstructure evolution, dynamic recrystallization, and texture evolution. It is therefore of interest to compare the hot deformation behaviour of the present material being investigated (i.e. AZ80), with the most studied alloy in the same alloy series, viz. AZ31.

3 Objectives

The objective of the current research is to contribute to the fundamental level knowledge on the thermomechanical behaviour of the AZ80 alloy, particularly in the range of industrial forging conditions, and determine the conditions for which the material shows an enhanced forgeability. To this end, the effect of the following material and process parameters on the evolution of microstructure and texture in conjunction with the associated material flow stress was studied in the present work:

- Effect of deformation parameters
    - Temperature (300 °C – 450 °C)
    - Strain rate (0.001 s^{-1} – 1 s^{-1})
    - Strain (up to 1.0)
- Effect of $Mg_{17}Al_{12}$ precipitates
- Effect of processing history of the starting material (cast vs extruded)
- Effect of texture of the starting material

Additionally, it was of academic interest to compare the hot deformation behaviour of the AZ80 alloy with that of the AZ31 alloy, so it has also been studied as part of the present work.

The entire study has been designed such that the knowledge that is generated fills some of the gaps in the current literature on the hot deformation behaviour of these alloys, and perhaps, more importantly, experimentally measured data such as the flow stress curves, as well as the scientific insights from the observed microstructure and texture for each hot deformation condition, can be used to guide our decision making in the APC project as to how best to forge this material.

4 Methodology

This chapter describes the starting materials, and the experimental methodology and techniques, used in the present work.

4.1 Starting materials

The materials used in the present work were commercial grade AZ31B and AZ80A-F alloys, obtained from Magnesium Elektron North America Inc. The alloys are henceforth referred to as AZ31 and AZ80, respectively. Cast alloys were obtained in the form of billets (Ø 300 mm x 500 mm), while the extruded alloy was obtained in the form of rods (Ø 63.5 mm x 65 mm). The chemical composition of the starting materials is reported in Table 4-1.

Table 4-1 Chemical composition (in wt.%) of the materials used in the present study, as determined using SEM-EDX analysis

	Al	**Mn**	**Zn**	**Mg**
AZ31 (Cast)	2.94	0.44	0.85	rest
AZ80 (Cast)	8.45	0.22	0.46	rest
AZ80 (Extruded)	8.17	0.31	0.42	rest

Detailed characterization results on the starting materials are presented in the following sections. It is noted that cast AZ alloys are prone to inverse segregation during solidification [117], and also a change in microstructure (including grain size) and texture is expected along the cast billet/extruded rod cross-section. Considering these variations, the characterization (including chemical analysis in Table 4-1) was performed on the as-received material in the same region from where samples for hot deformation tests were machined. These locations are illustrated in Figure 4-10.

4.1.1 Cast AZ31

The microstructure of the as-cast AZ31 is presented in Figure 4-1 (a-b), and is a dendritic microstructure, with a relatively coarse grain size of 483.7 ± 52.2 μm (based on the line intercept method using optical micrographs, as described in Appendix B). The starting material also showed some porosity, which is a typical defect in the as-cast microstructure.

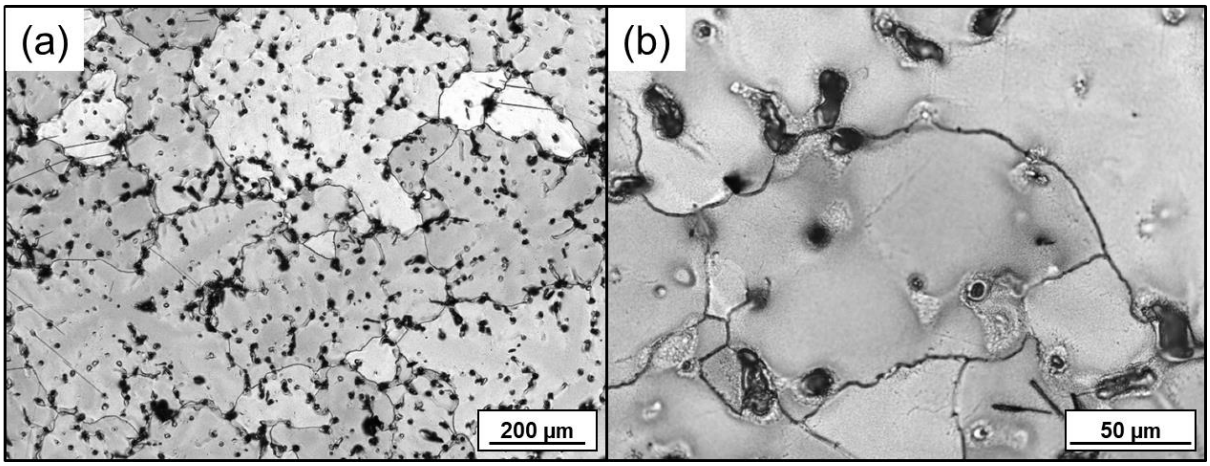

Figure 4-1 Microstructure of the as-cast AZ31 alloy: (a) and (b) are micrographs at low and high magnifications, respectively.

Some precipitates can also be seen in the microstructure. Phase fraction maps developed using FactSage® thermodynamic database (taken from a study on the same alloy, recently published by some of my research group members [86]) were used to estimate the composition of these precipitates. These maps are presented in Figure 4-2, and indicate that γ-$Mg_{17}Al_{12}$ should be the dominant second phase in the material. Additionally, precipitates based on Mg-Al-Zn, Mg-Zn and Mn-Al phases are also likely to be present in some minor quantities.

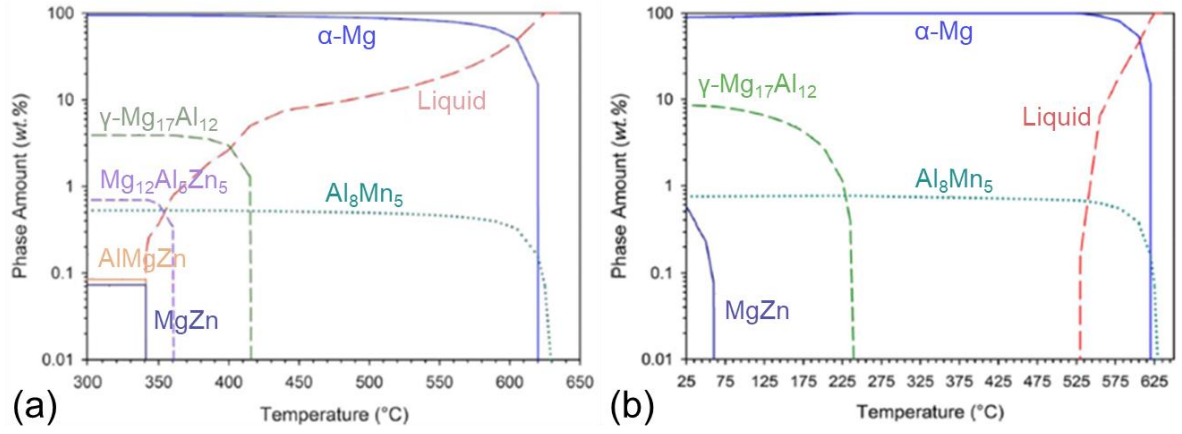

Figure 4-2 Phase fraction map of cast AZ31 alloy developed using FactSage® thermodynamic database: (a) Scheil solidification condition (relevant to the as-cast material), and (b) Equilibrium solidification condition [86]

These predictions from the phase fraction maps were verified by conducting scanning electron microscopy - energy dispersive X-ray spectroscopy (SEM-EDX) and X-Ray diffraction (XRD) phase identification analysis on the samples. The results of SEM-

EDX are presented in Figure 4-3, in terms of elemental maps, and verify that phases based on multiple constituents were indeed present in the material as precipitate particles. The XRD phase identification results are presented in Appendix A, and confirm the presence of γ-$Mg_{17}Al_{12}$ phase in the material. It is noteworthy that though SEM-EDX and XRD phase identification techniques were used to ascertain the presence of various alloying elements in the precipitates, they could not be used to precisely determine the chemical composition of these precipitates (except for the γ-$Mg_{17}Al_{12}$ phase, based on the XRD phase identification analysis) because of a relatively high interaction volume of the incident beam (electrons or X-rays) with the α-Mg matrix, and low precipitate content of phases other than γ-$Mg_{17}Al_{12}$.

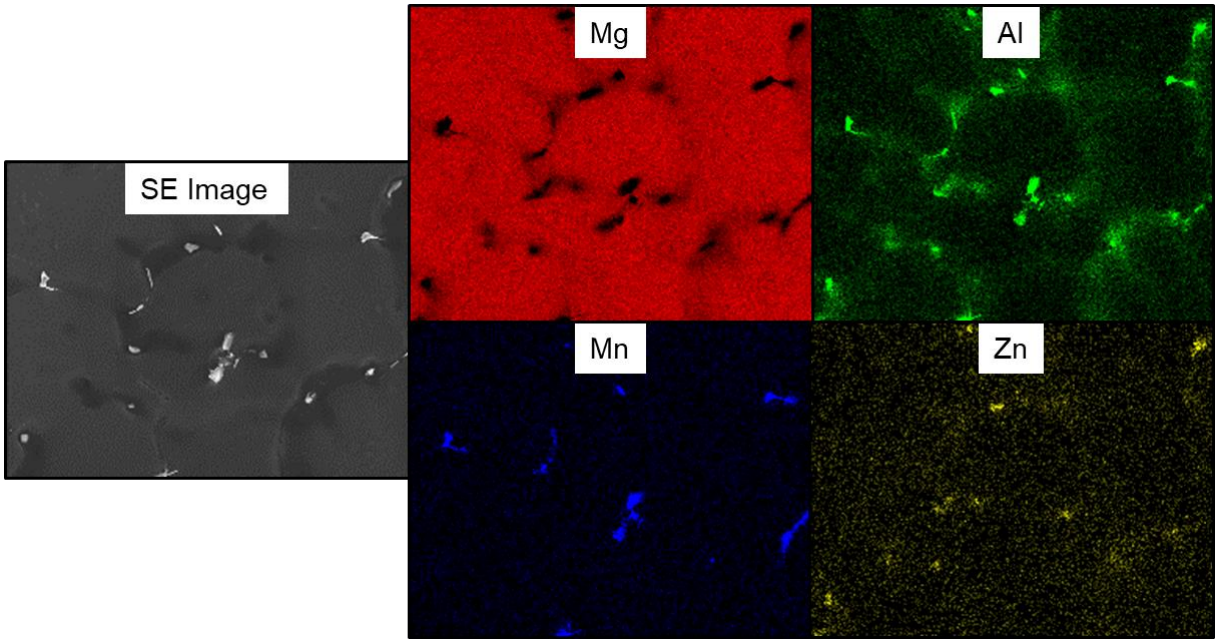

Figure 4-3 SEM micrograph of as-cast AZ31 alloy, and the corresponding EDX area maps showing the distribution of the major alloying elements in the matrix and precipitates.

The macrotexture of the starting material is presented in terms of (0002) and $(10\bar{1}0)$ pole figures (Figure 4-4). Because of the coarse grain size of the cast material, and limited area scanned for the macrotexture determination, the texture is dominated by a few coarse grains. However, since these grains seem to be randomly oriented with respect to the casting direction (referring to pole figures in Figure 4-4), a random texture distribution in the starting cast material can be inferred.

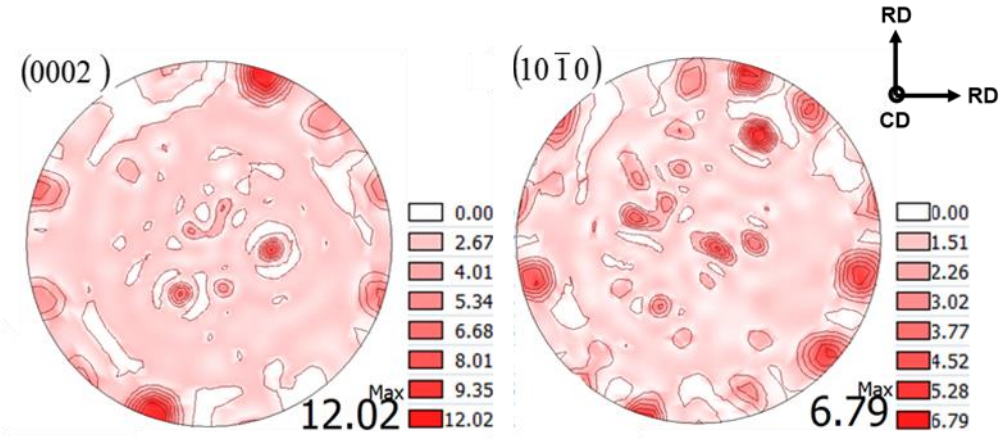

Figure 4-4 XRD macrotexture of the as-cast AZ31 alloy. The unit of texture intensity is "Multiples of Random Distribution (MRD)". Orientation legend: CD – Compression direction, RD – Radial direction.

4.1.2 Cast AZ80

The microstructure of the as-cast material is presented in Figure 4-5 (a-c). As in the case of the cast AZ31 alloy, the microstructure is dendritic, and shows presence of some porosity. The grain size of the as-received material was measured to be 311.3 ± 116.6 µm. Scheil solidification phase fraction map (Figure 4-6 (a)) predicted a large amount of γ-$Mg_{17}Al_{12}$ phase and a minor amount of Mn-Al based phases, in the as-cast state, both of whose presence was confirmed in the material using EDX (Figure 4-5 (c-d)). The corresponding XRD phase identification results are presented in Appendix A. γ-$Mg_{17}Al_{12}$ precipitates occurred in various morphologies in the as-cast material – lath, intergranular and lamellar forms, as is evident from Figure 4-5 (b-c), while Mn-Al based phases mainly occurred as irregularly shaped coarse particles.

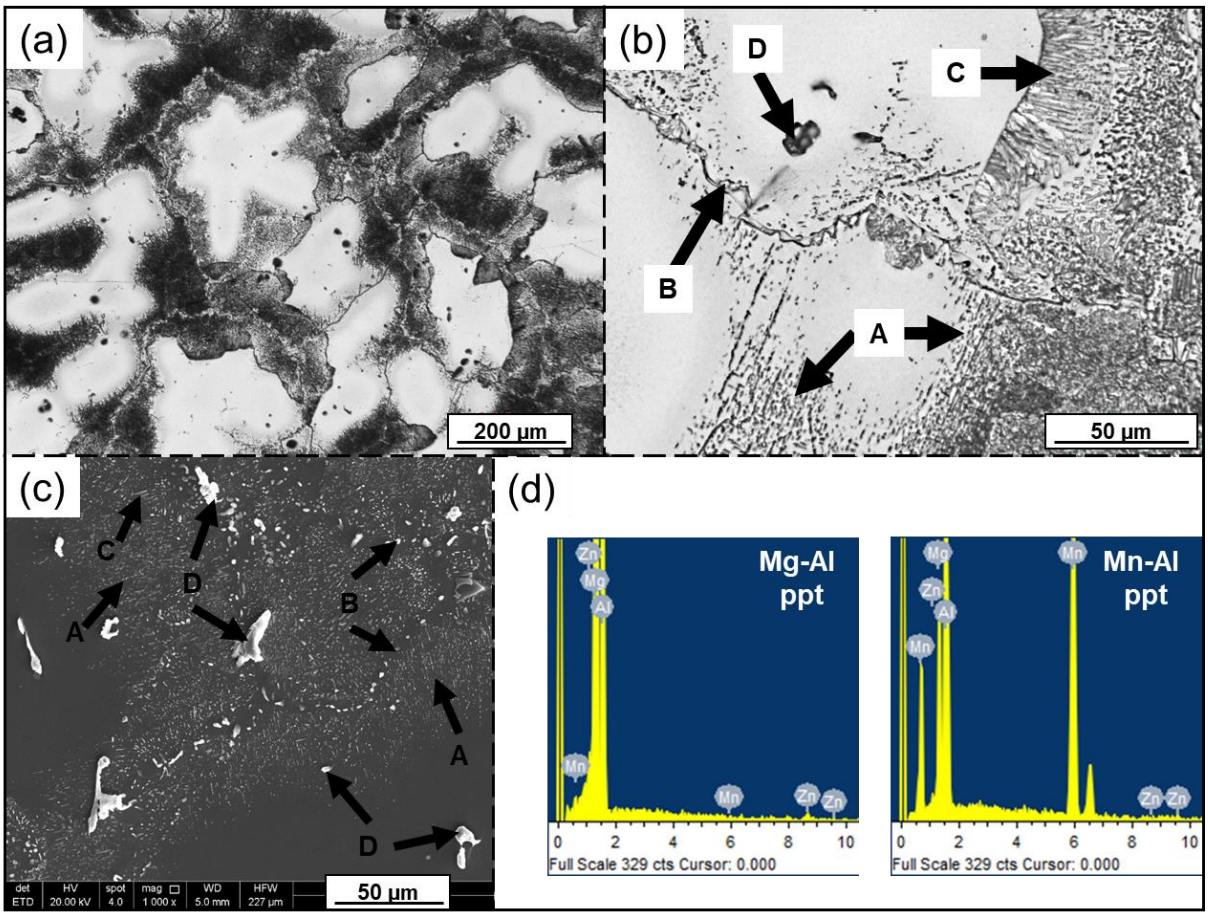

Figure 4-5 Microstructure of the as-cast AZ80 alloy: (a) and (b) Optical micrographs, (c) SEM micrograph and (d) EDX peaks for the major secondary phases in the material. A: $Mg_{17}Al_{12}$ in lath form; B: $Mg_{17}Al_{12}$ at grain boundaries in intergranular form; C: $Mg_{17}Al_{12}$ in lamellar form; D: Mn-Al based coarse precipitate particles.

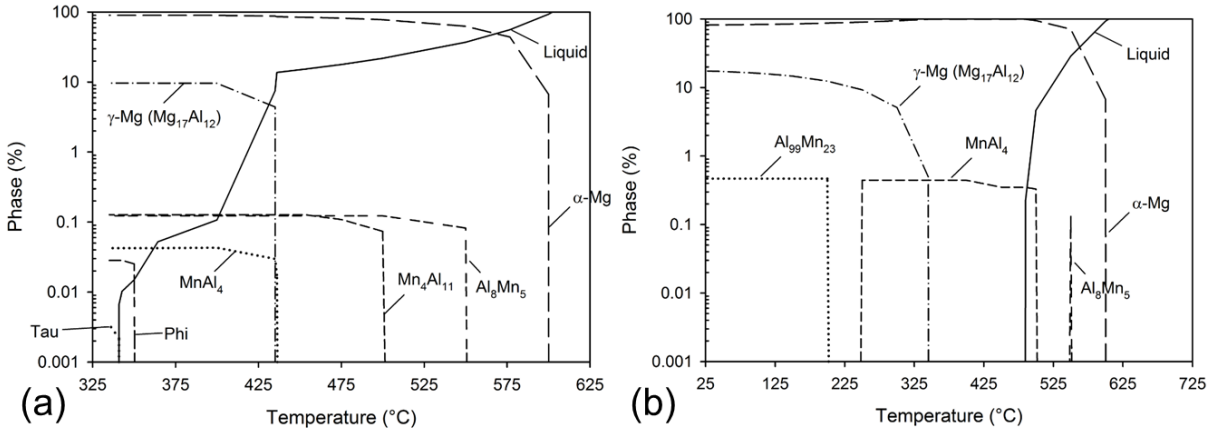

Figure 4-6 Phase fraction map of cast AZ80 alloy developed using FactSage® thermodynamic database: (a) Scheil solidification condition, (b) equilibrium solidification condition

The macrotexture of the starting material is presented in Figure 4-7, and shows a random texture distribution.

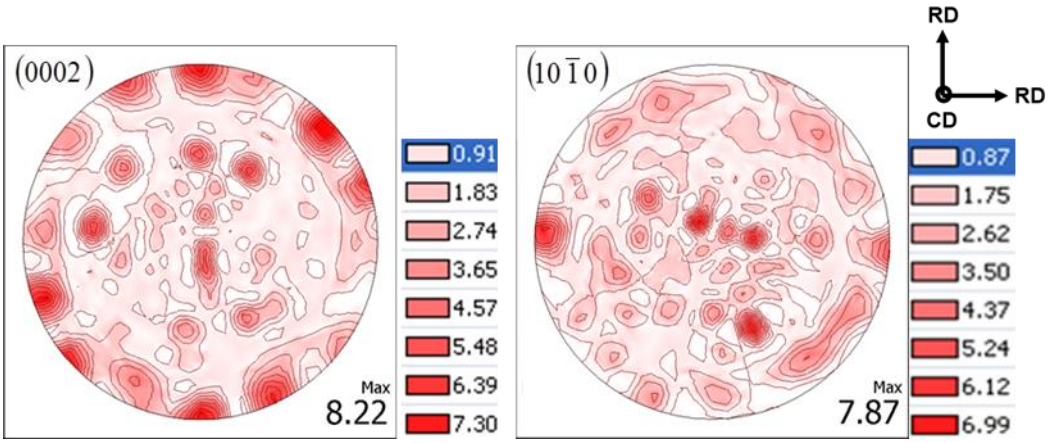

Figure 4-7 XRD macrotexture of the as-cast AZ80 alloy. The unit of texture intensity is "Multiples of Random Distribution (MRD)". Orientation legend: CD – Compression direction, RD – Radial direction.

4.1.3 Extruded AZ80

The micrograph of the as-extruded material is presented in Figure 4-8, and shows an equiaxed, fully recrystallized microstructure, with an average grain size of 34.8 ± 4.7 µm. The composition of the extruded AZ80 alloy was comparable to that of the cast AZ80 alloy, and therefore similar secondary phases in it were expected, and also verified using SEM-EDX and XRD phase identification analysis. The corresponding SEM-EDX results are presented in Figure 4-8 (b), while the XRD phase identification results are presented in Appendix A. It is noted that the γ-$Mg_{17}Al_{12}$ phase in the extruded material was mainly present in lamellar and intergranular forms.

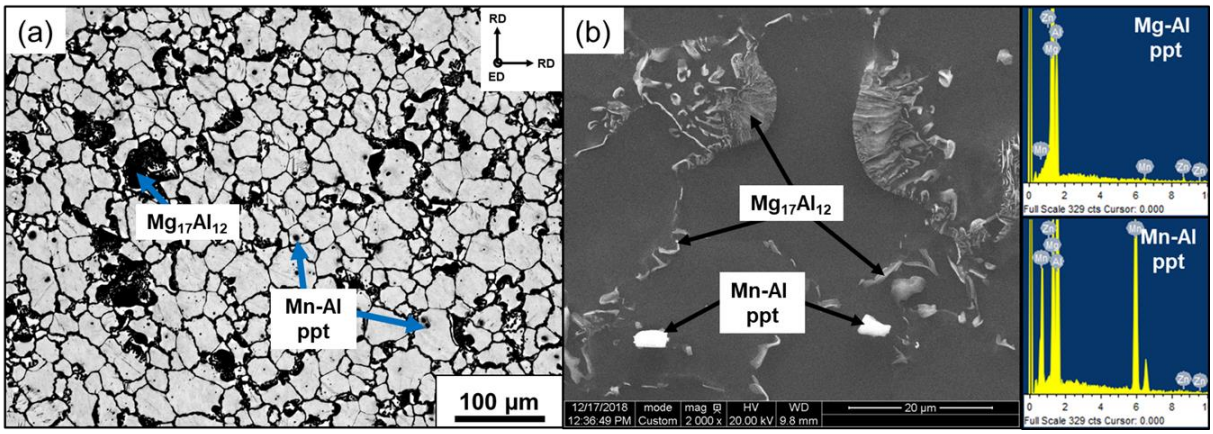

Figure 4-8 Microstructure of the as-extruded AZ80 alloy: (a) Optical micrograph, (b) SEM micrograph and EDX peaks for the major secondary phases in the material. γ-$Mg_{17}Al_{12}$ mainly occurred in the lamellar and intergranular forms.

The macrotexture of the starting material is shown in Figure 4-9 and showed a typical magnesium extrusion texture, with basal poles mainly aligning perpendicular to the prior extrusion axis. Additionally, the current material also showed a minor basal peak aligning parallel to the prior extrusion axis. The material is considered to show sharp texture because of these preferential distributions of the basal poles.

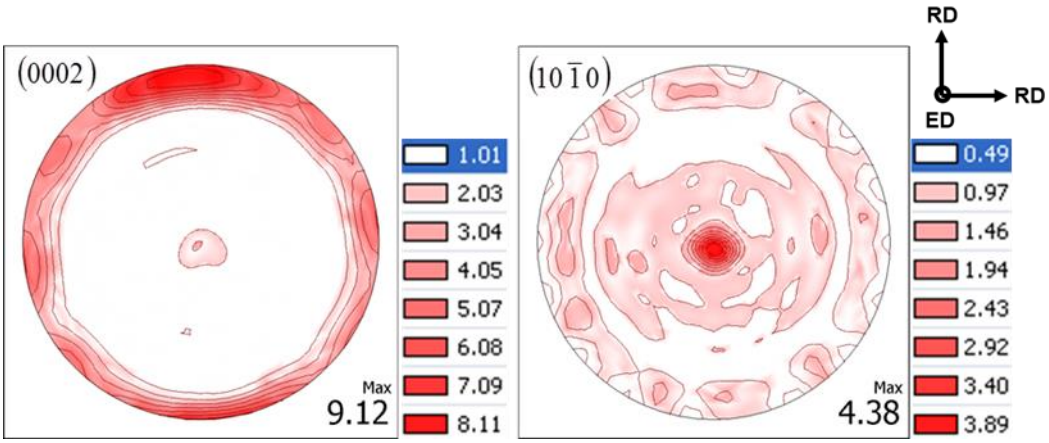

Figure 4-9 XRD macrotexture of the as-extruded AZ80 alloy. The unit of texture intensity is "Multiples of Random Distribution (MRD)". Orientation legend: ED – Extrusion direction, RD – Radial direction.

4.2 Uniaxial hot compression tests

Hot deformation was studied by means of uniaxial compression tests. The particular test method was chosen because of the symmetrical nature of the deformation process, which helps in the interpretation of the texture results. The process also efficiently simulates open die forging process, and the obtained flow stress data can

be used for crystal plasticity and finite element modelling of more intricate closed-die forgings. The following describes the sample geometry and the testing procedure for the uniaxial compression tests.

4.2.1 Test sample geometry and their extraction scheme from the starting materials

Uniaxial compression tests were conducted on cylindrical test samples of dimensions Ø 10 x 15 mm. The samples were extracted from the starting materials according to the schematic shown in Figure 4-10. For the cast alloys, the longitudinal direction of the test samples was kept parallel to the prior casting direction of the billet, while for the extruded alloy, the samples were extracted with their longitudinal axis in two orientations: one parallel to the prior extrusion direction (ED), and the other along the prior radial direction (RD). The starting extruded material was sharply textured, and extracting the samples from the starting extruded rod in two mutually perpendicular orientations thereby facilitated studying the effect of starting texture on the deformation behaviour of the material.

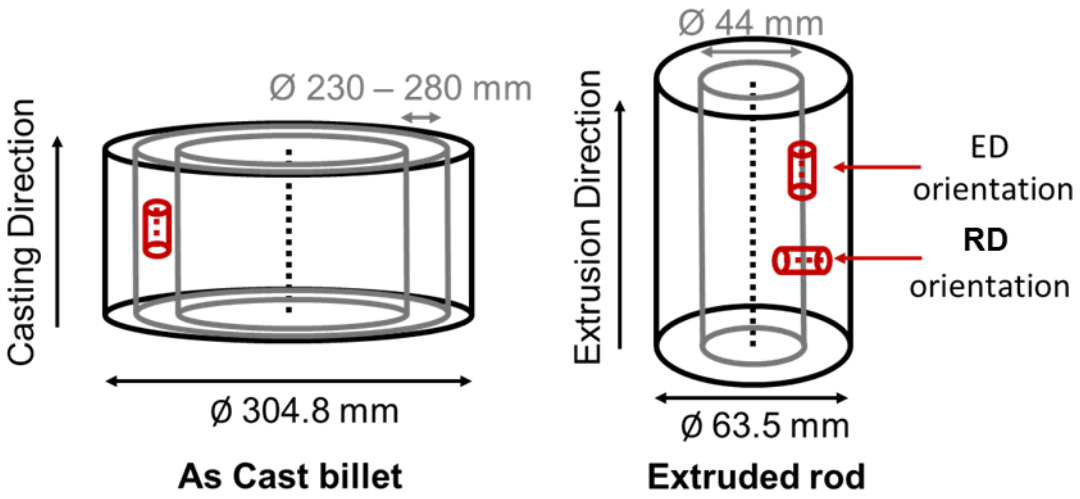

Figure 4-10 Sample extraction scheme from the as-received materials for hot compression tests

4.2.2 Test apparatus and procedure

The tests were conducted using a Gleeble™ 3500 thermal-mechanical simulator that is available at the University of Waterloo. Gleeble™ 3500 is a fully integrated hydraulic servo system, can provide for up to 10 ton of tensile/compressive load, and allow for

ram displacement rates of up to 1000 mm/s. It allows for flexible control of the temperature and the ram displacement during the tests, and it is possible to do tests at constant deformation temperatures and true strain rates. Additionally, it provides for quenching of the deformed samples using various media, including air and water [118].

The compression test chamber of the Gleeble™ 3500 is shown in Figure 4-11. A compression test sample can be seen sitting between two hardened steel anvils (sample is marked by a white arrow). Prior to the compression tests, the lateral surfaces of the samples were sprayed with a graphite based lubricant, to reduce friction and barrelling effects during deformation. The samples were heated at a rate of 5 °C.s^{-1} to the test temperature, held for 60 seconds to equilibrize the temperature throughout the sample's volume, and then compressed at the desired strain rate. The Proportional–Integral–Derivative (PID) controller settings for the Gleeble™ 3500 that were used in the present work are presented in Appendix F. The samples were heated during the tests via the Gleeble direct resistance heating technology, while the temperature during the duration of the test was controlled via feedback from the sample through two k-type thermocouples welded at its surface at the mid height level. The temperature was controlled within ± 3 °C of the target test temperature in all the cases except for deformation at the highest strain rate (viz. 1 s^{-1}), where the temperature controls were unable to cope up with the rapid rise in the sample's temperature due to deformation heat, and a rise in temperature of up to 23° above the desired test temperature was observed. After compressing the samples to the desired strain level (upto a true strain of 1.0), they were immediately quenched in water (within 1 s the temperature of the samples fell below 80 °C, as determined using the data from the thermocouples) to preserve their as-deformed microstructures. Load - stroke data was collected during the tests and converted to true stress - true strain data.

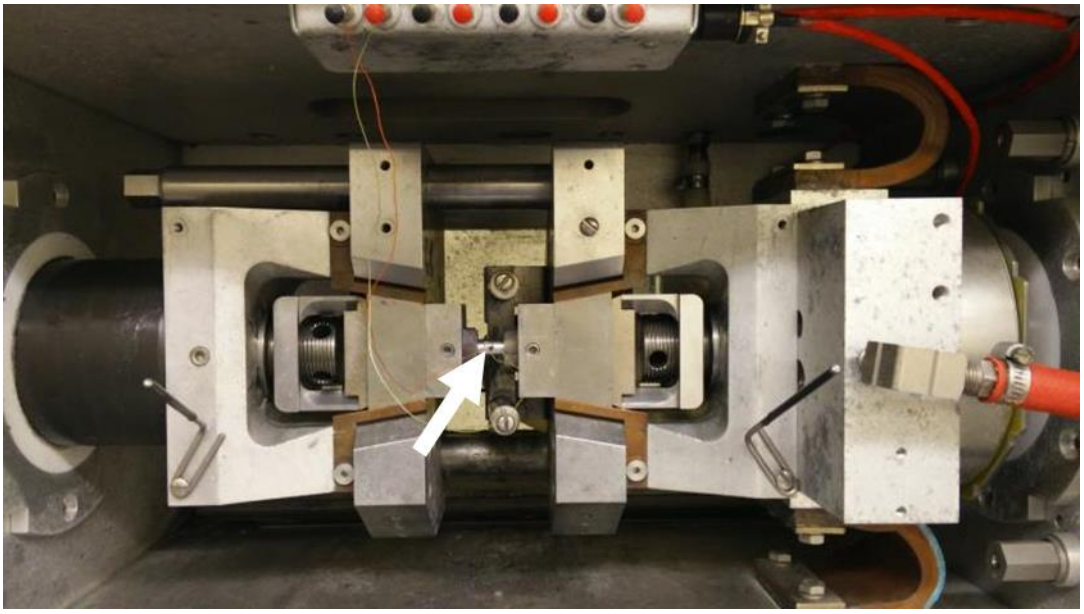

Figure 4-11 Compression test chamber of Gleeble™ 3500 thermal-mechanical simulator. The sample is marked by a white arrow.

Samples were hot compressed for the test matrix presented in Table 4-2. It is noted that detailed material characterization of the deformed samples for various studies was done only on a subset of the test conditions presented in Table 4-2.

Table 4-2 Test matrix for uniaxial compression tests for various starting materials

	300 °C	350 °C	400 °C	450 °C
1 s^{-1}	■ ●	■ ●	■ ● ◆	■ ●
0.1 s^{-1}	■ ●	■ ●	■ ● ◆	■ ●
0.01 s^{-1}	■ ●	■ ●	■ ● ◆	■ ●
0.001 s^{-1}	■ ●	■ ●	■ ● ◆	■ ●

■ Cast AZ80 ● Extruded AZ80 ◆ Cast AZ31

The process of converting the load-stroke data to the stress-strain curve is illustrated in Figure 4-12, using the example of compression test data for extruded AZ80 alloy, compressed along prior extrusion direction, at 400 °C, 0.1 s^{-1}. Initially, the load-stroke

data is obtained from the machine (Figure 4-12 (a)), which is then converted into True Stress-True Strain data (Figure 4-12 (b)) based on the following equations:

$$\varepsilon = \ln\left(\frac{L_0+\Delta L}{L_0}\right) \tag{4.1}$$

$$\sigma = \frac{Force}{\frac{\pi.(d_0)^2.L_0/_4}{[L_0+\Delta L]}} \tag{4.2}$$

where, L_0 is the initial length of the test samples (i.e. 15 mm), d_0 is their initial diameter (i.e. 10 mm), ΔL is the change in length of the sample due to deformation (which is a negative value in compression tests) and is calculated from the stroke data, while Force is the corresponding load value. Both true strain (ε) and true stress (σ) values come out to be negative for compression tests, while the negative sign is dropped when plotting the flow stress curves. It is noted that no corrections for temperature change, and friction and barrelling effects, were made to the presented flow stress data.

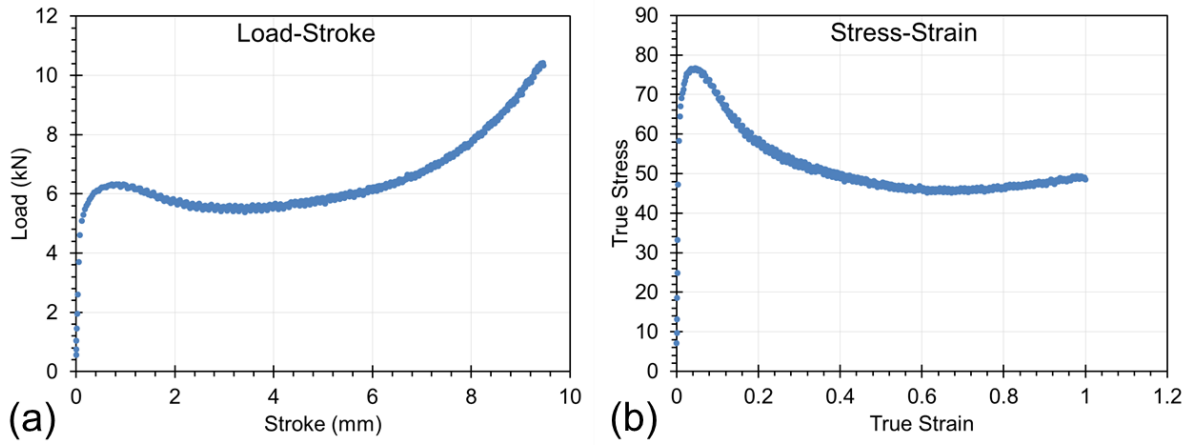

Figure 4-12 Processing of the load-stroke data for analysis: Extruded AZ80 hot compressed along the prior extrusion direction at 400 °C, 0.1 s^{-1}

4.3 Material Characterization

4.3.1 Metallographic sample preparation

The compressed samples were sectioned longitudinally along the compression axis (Figure 4-13), cold mounted in epoxy, and prepared using standard metallographic procedures [119]. Grinding was done using 400, 600, 800 and 1200 grit Silicon

Carbide (SiC) papers manually on a hand grinder. Flowing water was used as the lubricant for all the grinding steps, and after each step, the samples were washed with soapy water. After the final grinding step, only uniform deformation lines on the sample surface along the last grinding direction remained. Samples were washed in ultrasonic ethanol bath for about 30 seconds before the subsequent polishing steps. Polishing was performed on a rotatory disc Struers autopolisher using diamond pastes of 9 µm, 3 µm and 1 µm particle size, at loads of 10-20 N, and a polishing time of 5 min at 150 rpm. An ethanol-based lubricant was used for polishing at 9 µm, while an oil-based lubricant was used for polishing at 3 and 1 µm. Samples were thoroughly cleaned after each polishing step using soap water and ultrasonic ethanol bath. Final polishing was performed using a 0.05 µm colloidal silica solution (50% diluted) at 5-10 N for 30-60 s at 150 rpm. Distilled water was used as the lubricant, and samples were immediately washed under flowing water following the polishing in order to avoid chemical reaction between colloidal silica and the sample surface. The final polished sample was cleaned in an ultrasonic ethanol bath, and dried. Samples for electron backscatter diffraction (EBSD) were further polished chemically using a 10 vol.% Nital solution for 30-60 seconds using cotton balls. It is noteworthy that concentrated Nital solution is unstable and needs to be diluted below 5 vol.%, in case if it is unused, or below 2.5 vol.%, in case it has already been used for polishing purposes, for storage/disposal. Samples for optical microscopy and scanning electron microscopy (SEM) were etched. For AZ80, a solution of 90 ml ethanol, 10 ml acetic acid, and 5 g picric acid was used, while for AZ31, a solution of 70 ml ethanol, 10 ml water, 10 ml acetic acid, and 4.2 g picric acid was used. It is noteworthy that picric acid is highly explosive when dry, so caution must be exercised while preparing the etchant and storing it (especially with regards to potential spills on the side of the glass storage bottles while pouring out the etchant). Various microstructural analyses were performed on the central region of the prepared section, unless otherwise specified in the text.

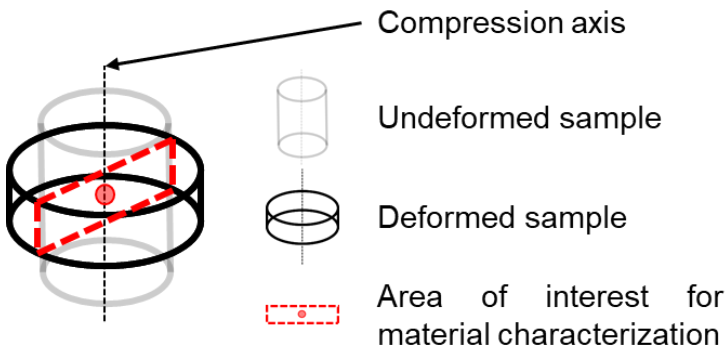

Figure 4-13 Sectioning scheme of the compressed samples for metallography and characterization

4.3.2 Microstructure analysis

The microstructures of the samples were examined using optical microscopy, SEM and EBSD inverse pole figure (IPF) maps. Samples for optical and SEM microscopy were etched to reveal the grain boundaries. In case of the EBSD IPF maps, grain boundaries are defined by the analysis software (TSL OIM 8.0) based on the provided grain tolerance angle (10° in the present work), which essentially defines the minimum misorientation between two adjoining pixels in the map, above which a high angle boundary is considered to be present between them. It is noted that using a specific misorientation limit (i.e. the grain tolerance angle) to define the high angle boundary is subjective, with different authors choosing typically either 10° or 15°. In either case, the basic idea is to have a conformity between the optical microstructures and the microstructures developed based on the misorientation data. Reducing this misorientation limit will result in under prediction of the actual grain size values, while using a higher misorientation limit will result in its over prediction.

Optical microscopy was done using an Olympus microscope, and micrographs were obtained at 50x to 1000x magnifications. SEM was done using two different equipment: 1) FEI Nova NanoSEM-650 and 2) FEI Quanta field-emission-gun 250 Environmental SEM. An operating voltage of 20 kV was used in each case. Micrographs were taken in both secondary electrons (SEs), and backscatter electrons (BSEs) mode, and for magnifications ranging from 200x to 8000x. EBSD was done at CanmetMaterials, Hamilton, ON, while SEM was done at both CanmetMaterials, Hamilton, ON (using the Nova NanoSEM-650), and the University of Waterloo at the WATLab (using the Quanta field-emission-gun 250 Environmental SEM).

4.3.3 Second phase chemical characterization

The starting materials and deformed materials both showed the presence of different precipitates in the microstructure, which were analyzed using a combination of various characterization techniques as described in the following.

4.3.3.1 Thermodynamic calculations

Thermodynamic calculations were done using FactSage® thermodynamic database to develop phase diagrams and phase fraction maps. These were used to predict the phases developed in the material under various conditions, including during Scheil solidification, and equilibrium solidification conditions.

4.3.3.2 Energy dispersive X-ray spectroscopy (EDX)

EDX analysis is done in conjunction with a focused electron source, such as a SEM, whereby focused electron beam on a targeted area causes emission of characteristic X-rays from individual chemical elements in the material in that area, which are then captured using an EDX detector. These characteristic X-rays are used to reveal the identity of the underlying chemical constituents present in the targeted microstructural feature (e.g. in a precipitate). It is even possible to determine the precise chemical composition of the phase based on the relative intensities of the emitted X-rays from different elements making up that phase. It is noteworthy that a precise determination of the composition in this manner requires that the incident electron beam is localized to the targeted phase only, such that the beam do not cause emission of X-rays from the surrounding phases as well.

In the present work, EDX data was collected using two equipment: 1) an FEI Nova NanoSEM-650 (FEG-SEM), equipped with an EDAX EDX detector, and 2) an FEI Quanta field-emission-gun 250 Environmental SEM (FEG-ESEM), equipped with an Oxford Systems EDX detector. An operating voltage of 20 kV was used in each case. The distribution of alloying elements in matrix and precipitates was determined based on area scan, spot scan, and in few cases, elemental distribution maps were also created. The precipitates were generally observed to be too small to be accurately characterized using EDX because of a relatively large interaction volume of the incident electron beam, and therefore the utility of EDX in the present work was limited to identifying the different chemical elements present in the individual precipitates.

4.3.3.3 X-ray diffraction (XRD) phase identification

Similar to EDX, XRD can be used for chemical analysis. The technique differs from EDX on three major counts:

1) Incitation of the target material (whose chemical characterization needs to be done) is through X-rays, instead of electron beam used in EDX
2) In the case of XRD phase identification, the signals are produced due to diffraction of incident X-rays from individual crystallographic planes, based on the crystal structure of the target material and the Bragg diffraction condition. In the case of EDX, on the other hand, the characteristic X-ray signal is produced due to a jump of electrons in the inner shells of the individual elements.
3) In case of XRD phase identification, the chemical compound (as opposed to elements in a compound), and the phase in which it occurs, is identified based on the position and nature of its diffraction peaks. In the case of EDX, on the other hand, the individual chemical elements within a compound are identified (though as described earlier it is possible to identify the compound by determining its chemical formula).

It is noted that using XRD to identify precipitates in the material require them to be present in sufficient quantity (> 3 vol.%) so that their diffraction signals are at least reasonably stronger than the background noise level. In the present work, only $Mg_{17}Al_{12}$ occurred in any substantial content to be identifiable using the XRD phase identification technique.

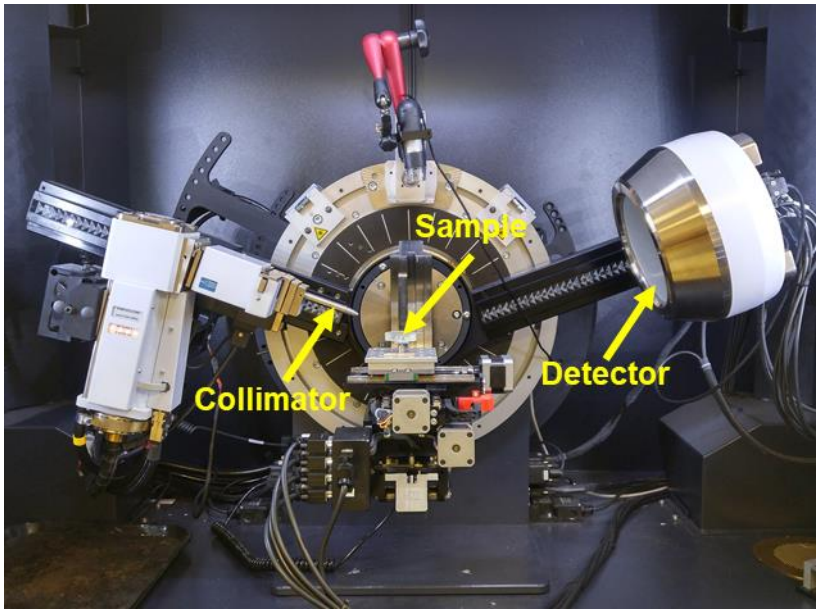

Figure 4-14 Test setup inside Bruker D8-Discover XRD machine used in the present work

In the present work, the XRD macrotexture measurements were performed using a Bruker D8-Discover machine, equipped with a VÅNTEC-500 area detector, using Cu K_α radiation at 40 kV and 40 mA. A collimator of Φ 1 mm was used. The experimental setup is shown in Figure 4-14. The diffraction data for phase identification for individual samples was collected in θ/2θ mode, with 2θ varying from 20 to 110°, with a step size of 15° (note that an **area** detector was used, which collected data at a resolution of 0.005° for a spread of ±12.5° at each 2θ angle), and a measurement time of 60 s/ step. Afterward, the data was plotted in terms of intensity vs 2θ X-Y plots, and peaks corresponding to α-Mg phase, and $Mg_{17}Al_{12}$ phase were manually identified (based on literature values) and labelled.

4.3.4 Texture analysis

The texture of the samples was measured using both X-Ray diffraction (XRD), for macro texture analysis, as well as electron back scatter diffraction (EBSD), for microtexture analysis.

4.3.4.1 Macrotexture measurements

Texture measurements using XRD involve incidence of monochromatic X-rays on a polished sample surface, while the sample is rotated with respect to the incident X-ray beam in a controlled way, and the diffracted rays from the atomic planes near the surface (based on Bragg's diffraction law) on the sample are collected by a detector,

and mapped with the orientation of the sample with respect to the global coordinate system. The data is later post-processed, based on standard mathematical procedures (typically done automatically by custom software these days), and analyzed in terms of Pole Figures (PFs), Inverse Pole Figures (IPFs), or Orientation Distribution Functions (ODFs).

In the present research, the same XRD setup, as is described in section 4.3.3.3, was used. For collecting an adequate grain statistics, an area of ~ 1.5 x 2.5 mm was scanned for each sample. The incident beam and the detector were placed at a fixed 2θ angle of 40° for texture measurements. For Ψ-scan, the sample was tilted between 0° and 75°, with a step of 15° (note that an **area** detector was used, so measurements at even finer step sizes were not required). For Φ-scan, the sample was rotated between 0° and 360°, with a step size of 5°. Measurements were performed for 20 seconds at each orientation. Afterward, the diffraction data was processed using DIFFRAC.Suite:Texture software to calculate the completed pole figures. The texture results are presented and analysed in terms of the (0002) pole figures. It is noted that because of the nature of the technique, no separate calibration file, to define perfect random texture, was required.

4.3.4.2 Microtexture measurements

EBSD measurements were conducted to obtain the microtexture of the samples. In microtexture measurements, the orientation of each individual pixel in the microstructure is determined (with respect to some fixed reference frame) by raster scanning electron beam on the sample surface using a focused electron beam source, such as a SEM [120]. The microtexture data is obtained from the backscatter electrons (BSE), which are typically released from the top few atomic layers (tens of nm thickness) of the sample's surface. Because of the low surface depth from which the BSEs are emitted, a highly polished and un-etched sample surface is desirable for generating good quality EBSD data. In order to maximize the collection of the BSEs, the sample is positioned such that its surface normal is at 70° to the incident electron beam. The data is obtained in the form of diffraction patterns (Kikuchi bands), which are then converted into orientation maps based on a standard mathematical procedure [120]. The current state of technology allows automatic acquisition of the data and

conversion of the Kikuchi bands into orientation data. Data acquisition via EBSD (using a SEM) is schematically presented in Figure 4-15.

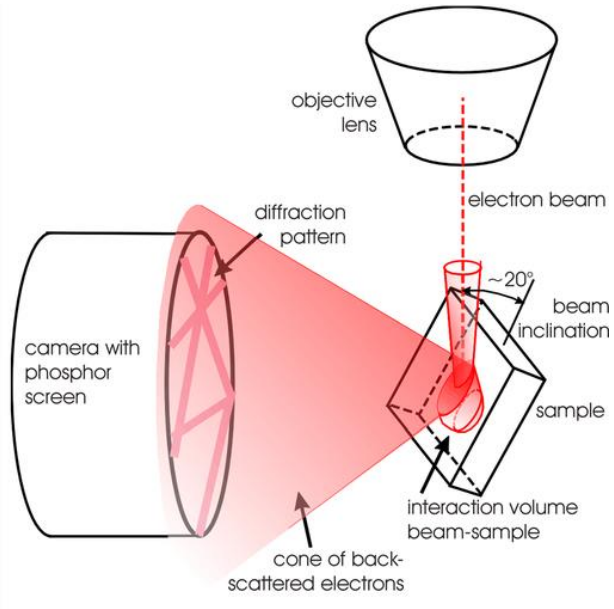

Figure 4-15 Schematic of EBSD data acquisition in a SEM [121]

For the current research, EBSD was done at Canmet Materials in Hamilton, ON, using an EDAX EBSD detector, mounted to a FEI Nova NanoSEM-650 (FEG-SEM). An operating voltage of 20 kV was used. EBSD scans on the starting materials were performed using a step size of 4 µm and 0.75 µm, for the cast and extruded materials, respectively. For the deformed samples, step sizes according to Table 4-3 were used. The step sizes were based on preliminary DRX grain size calculations from the optical micrographs, and were chosen so as to have a minimum of 16 measurements points per grain. It is noted that the DRX grain size at 300 °C, 0.001 s^{-1}, was low (~ 5.6 µm), and the microstructure showed substantial presence of $Mg_{17}Al_{12}$ precipitates, which affected the indexing rate, and thereby, to be able to more accurately post-process the raw scan data, a finer step size of 0.25 µm, and a minimum of 36 pixels per grain (equivalent to a minimum grain size of 1.5 µm) were used.

Table 4-3 Step size used for various deformation conditions

	300 °C	**400 °C**
0.1 s^{-1}		0.5 µm
0.001 s^{-1}	0.25 µm	0.75 µm

Due to a relatively coarse grain size of the as-received cast material (compared to the starting extruded material), a larger area needed to be scanned for the cast-deformed samples, to be able to capture enough grains to produce statistically relevant results. Details of the area scanned for cast and extruded-deformed samples at various strain levels are provided in Figure 4-16. Note that for the sample deformed to the strain of 1.0, the scan area was limited to 0.75 x 0.6 mm even for the cast material, in order to avoid an overlap of the scan area with the dead metal zone (refer to Figure 4-16 (c) and (d)). As the results in later text show, hot deformation resulted in a considerable grain refinement in both cast and extruded materials, and this relatively small scan area was still found to adequately capture statistically relevant amount of data.

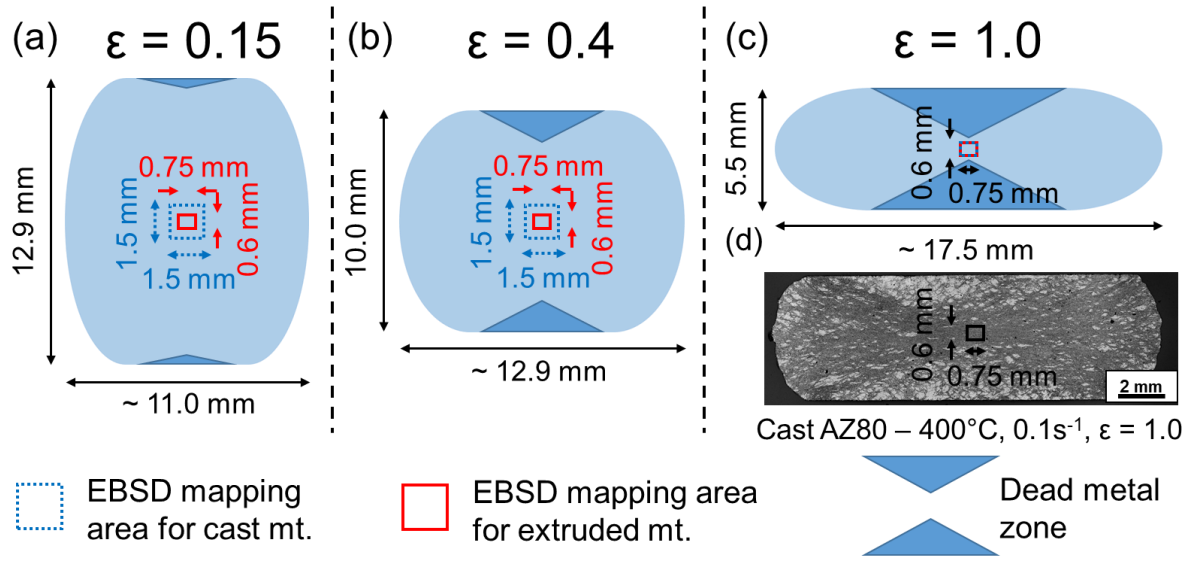

Figure 4-16 Location and size of EBSD scan for cast and extruded compressed samples. Sample size and the scan area are proportionally scaled. The dead metal zone location and extent is a simple schematic (and not to scale) and just for illustrative purposes. The true extent of the dead metal zone for one of the samples can be visualized from (d).

The scanned data was processed and analysed using TSL OIM 8.0 software. The data was cleaned using standard data cleaning techniques [122]. This is illustrated through Figure 4-17 and Figure 4-18 for an extruded AZ80 sample deformed at 400 °C, 0.1 s^{-1} to a strain of 1.0. Initially, based on Image Quality (IQ) map and distribution, it was observed that areas with precipitates showed much lower IQ values. Therefore, the data pertaining to the precipitates could be filtered away from the data pertaining to the actual grains, using a lower threshold on the IQ values. For the case presented in Figure 4-17, an IQ value of 550 was found to be appropriate, though it should be noted

that this value needs to be determined for individual samples on a case by case basis. With reference to the shape of the precipitate particles in Figure 4-17 (b), the particles appear more elongated along the vertical axis than they actually are, and is due to the fact that some part of the matrix immediately below the precipitates (i.e. in negative y-direction) fall under the shadow of the precipitates (generated because of the incident electron beam), which results in lower IQ values in these regions.

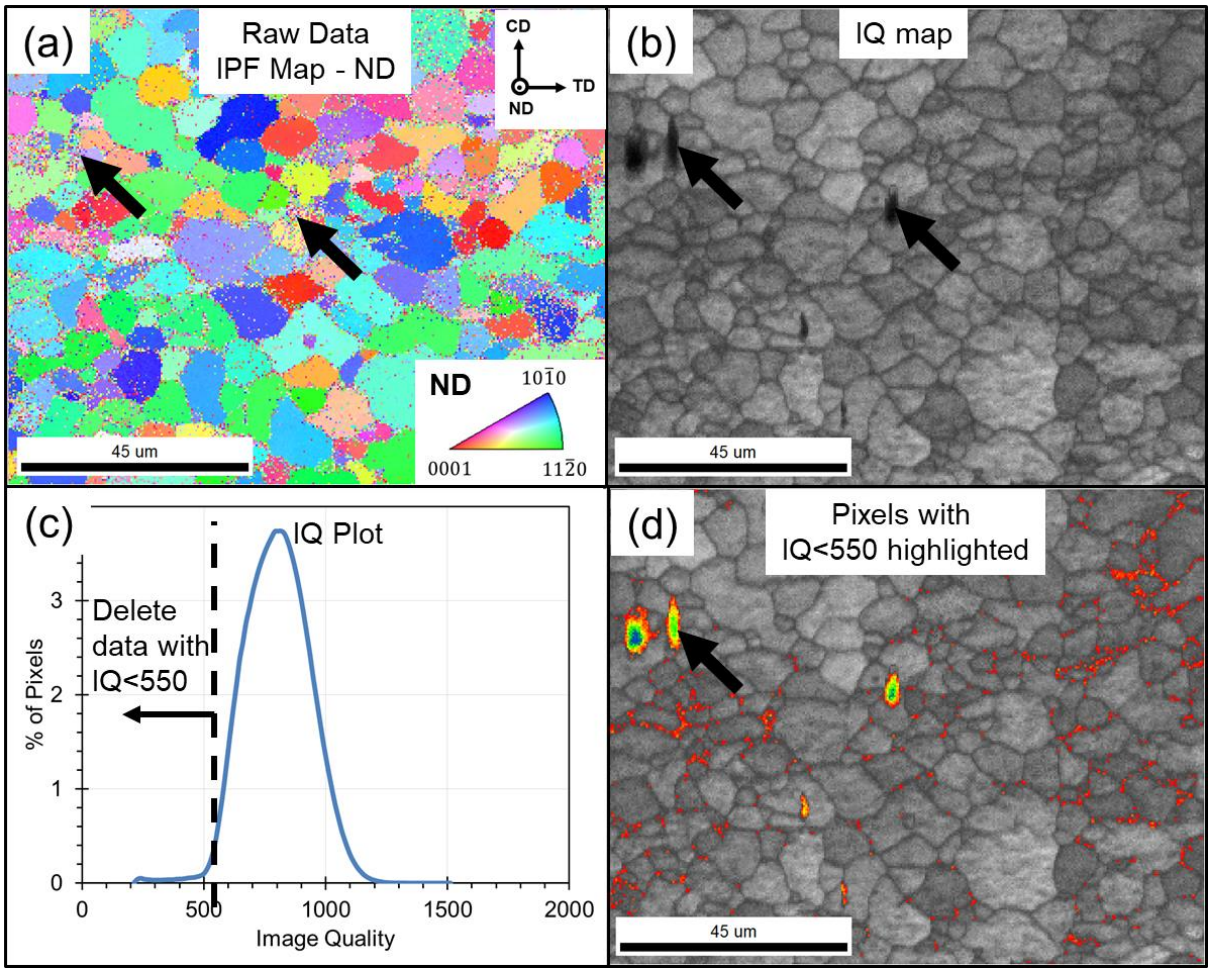

Figure 4-17 Identifying pixels associated with the precipitates in the microstructure. Data is of extruded AZ80 sample, compressed along prior extrusion direction at 400 °C, 0.1 s^{-1}, to a strain of 1.0. CD, ND, and TD refer to Compression direction, Normal direction, and Transverse direction, respectively.

Further data cleaning steps are illustrated in Figure 4-18. The objective was to correctly index the mis-indexed and non-indexed points, but avoid over cleaning of the data so as to introduce artifacts. With respect to the figure, the steps are in the sequence (a) through (f). The data was cleaned using a standard *Grain dilation* cleaning approach. For this purpose, a grain tolerance angle of 10° (to define the grain

boundaries) and a minimum grain size of 16 pixels were used. After the grain dilation cleaning step, a Kernel Average Misorientation (KAM) filter, with a maximum misorientation of 10° and Kuwahara filtering using the 3rd nearest neighbour, was used to reduce the orientation noise, in order to correctly delineate the low angle boundaries in the microstructure. This step is shown in Figure 4-18 (c) and (d). Afterward, the anti-grains (i.e. clusters of still non-indexed neighbouring points in the data) were removed (Figure 4-18 (e)). Subsequently, the orientation data was rotated with respect to the horizontal axis, so as to make the colouring in the IPF map reflect the orientation of the grains with respect to the compression direction (vertical). Grain boundaries and low angle boundaries were superimposed on the resultant IPF map (Figure 4-18 (f)).

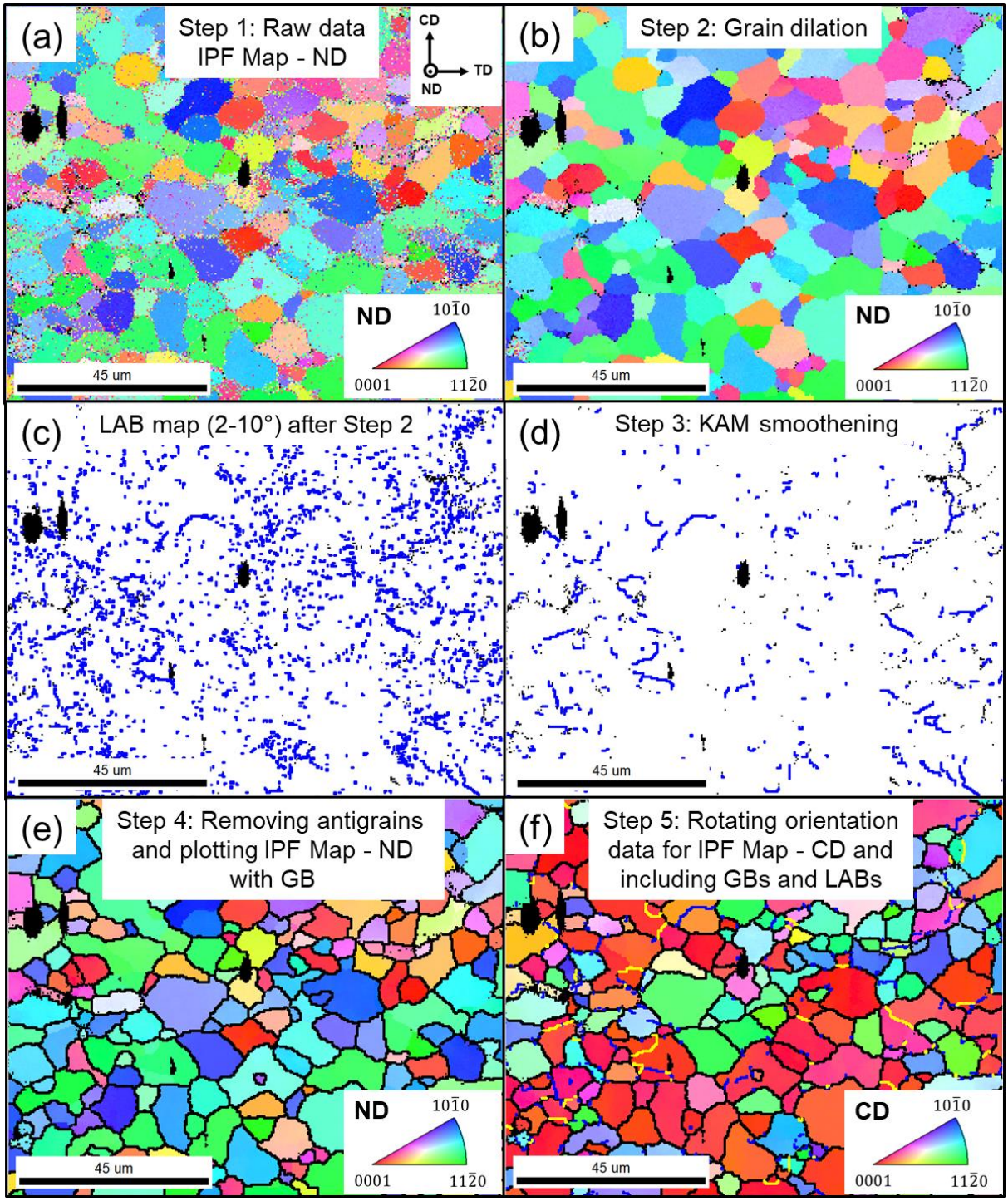

Figure 4-18 Preparing raw data for analysis. Cleaning steps are in sequence (a) through (f). Data from Figure 4-17 is used after removing pixels with IQ < 550. Blue lines/points in (c) and (d) are low angle boundaries (LABs) with misorientation of 2-10°. Black lines in (e) and (f) are grain boundaries with misorientation greater than 10°, while blue lines and yellow lines are LABs with misorientations of 2-5°, and 5-10°, respectively. CD, ND, and TD refer to Compression direction, Normal direction, and Transverse direction, respectively.

5 Results and Discussion

5.1 Typical flow stress curve

This section describes the analysis of a typical flow stress curve, by taking the example of the flow curve of cast AZ80 alloy sample deformed at 300 °C, 0.001 s^{-1} (Figure 5-1 (a)). The flow curve shows that the material experienced rapid work hardening during the initial phase of deformation, reaching a peak stress, and subsequently showed gradual softening to a steady state flow stress at higher strains. Characteristic strain levels pertaining to the flow stress curve are also marked in the figure. With regards to these strain levels, ε_C refers to the critical strain, and is the minimum strain that is required to initiate DRX in the material; ε_P refers to the peak strain, which is the strain required to achieve the peak in the flow stress curve; and ε_{SS} refers to the steady state strain, which is the strain beyond which the material exhibits a steady state flow stress value. It is noted that the flow curve presented in Figure 5-1 (a) shows slight increase in the flow stress values at high strain levels (beyond the ε_{SS} marked in the figure). The reason behind this is not known, but is likely related to an increase in the friction at the contact between the sample surface and the anvils (due to an increase in the contact area as a result of deformation). As mentioned earlier in the thesis, the flow stress curves presented in the present thesis were not corrected for friction and barrelling effects.

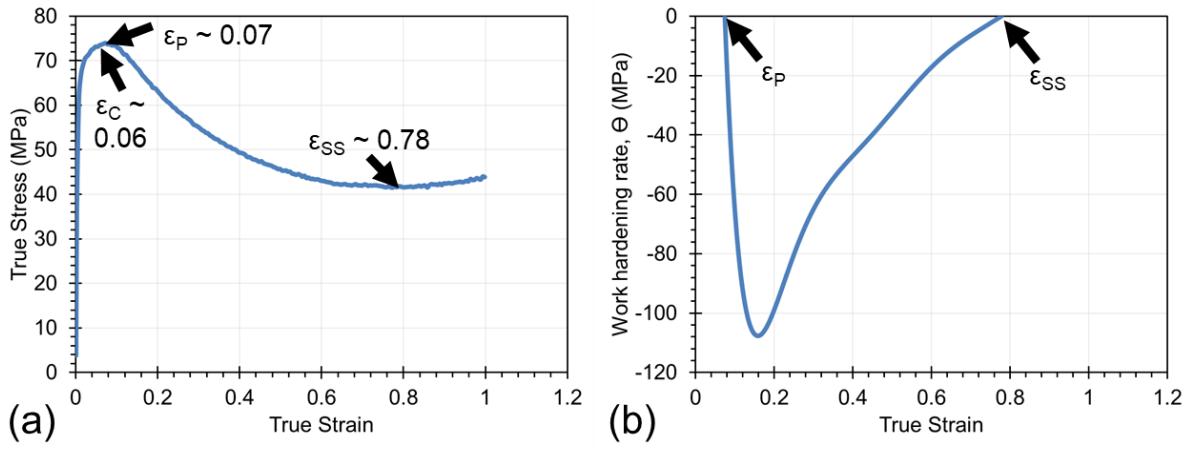

Figure 5-1 (a) Flow stress curve of the cast AZ80 sample deformed at 300 °C, 0.001 s^{-1}, (b) work hardening rate plot of the flow stress curve in (a). ε_C, ε_P, ε_{SS} refer to critical strain, peak strain, and steady state strain, respectively.

This flow softening is typically attributed to the occurrence of DRX in the material [20, 67, 115, 123]. DRX initiates in the material at strains slightly lower than the peak strain, and a value of $\varepsilon_C \approx 0.8 * \varepsilon_P$ is found to be reasonable for various metallic alloys, including AZ31 [20, 113]. The peak strain (ε_P) and steady state strain (ε_{SS}) can be identified based on a work hardening rate of 0 (illustrated in Figure 5-1 (b)). The work hardening rate is determined by taking the derivative of the stress strain curve and then plotting it as a function of strain. Work hardening rate curves also provide information about the DRX kinetics in the material, with a more rapid work softening rate following the peak strain typically indicating a faster DRX kinetics in the material [106].

It is noted that under certain deformation conditions, the material showed virtually no initial work hardening regime, and the peak strain closely coincided with the initiation of the plastic flow in the material. It is not known if critical strain analysis, as described above, is valid in such cases. Also, for such flow curves, it is difficult to determine the derivative of the stress strain curve just prior to the peak stress, and as such the peak is typically identified visually from the flow stress curve itself, while the corresponding work hardening rate plots are drawn from peak strain onwards.

In the present work, microstructure and texture evolution with strain in various starting materials, and for various deformation conditions, was studied by stopping the compression tests at various strain levels: 0.15, 0.4 and 1.0. In all the cases, the lowest tested strain of 0.15 was found to be higher than the corresponding ε_P values, and therefore the deformed samples are expected to show at least some occurrence of DRX in these samples. Additionally, in some cases, compression tests were also conducted to a strain of 0.05, which fell below the critical strain for the DRX to occur, in order to examine the microstructure just prior to the initiation of DRX in the material.

In the following sections, the effect of various deformation parameters, and material related parameters, on the hot deformation behaviour of AZ80 alloy is explored systematically.

5.2 Effect of temperature

This section explores the role of deformation temperature on the hot deformation behaviour of cast AZ80 alloy. A temperature range of 300 °C to 400 °C was selected for this study, which also marks the temperature range over which a transition from $Mg_{17}Al_{12}$ precipitation in the material to its dissolution occurs (the transition point being 350 °C, based on the equilibrium phase fraction map presented in Figure 4-6). The microstructure and texture results are presented only for deformation at the strain rate of 0.001 s^{-1}, and a strain of 1.0.

5.2.1 Flow stress curves

The flow stress curves at the strain rate of 0.001 s^{-1}, and temperatures of 300 °C - 400 °C, are presented in Figure 5-2. The flow stress curve at 300 °C shows a clear work hardening regime during the initial phase of deformation, followed by the achievement of a distinct peak in flow stress, and eventually work softening, until a steady-state flow stress value is reached. The flow curves shifted to lower stresses, as the deformation temperature increased, which is attributed to both, a decrease in the CRSS on non-basal slip systems, and also increasing DRX grain sizes at higher deformation temperatures. Samples deformed at 350 °C and 400 °C showed very little to no initial work hardening (before the peak), with the peak roughly coincided with the initiation of the plastic flow in the material. With progressive deformation, the flow stress decreased, and eventually reached a steady state at high strain levels. The strain to reach the steady state decreased as the deformation temperature increased.

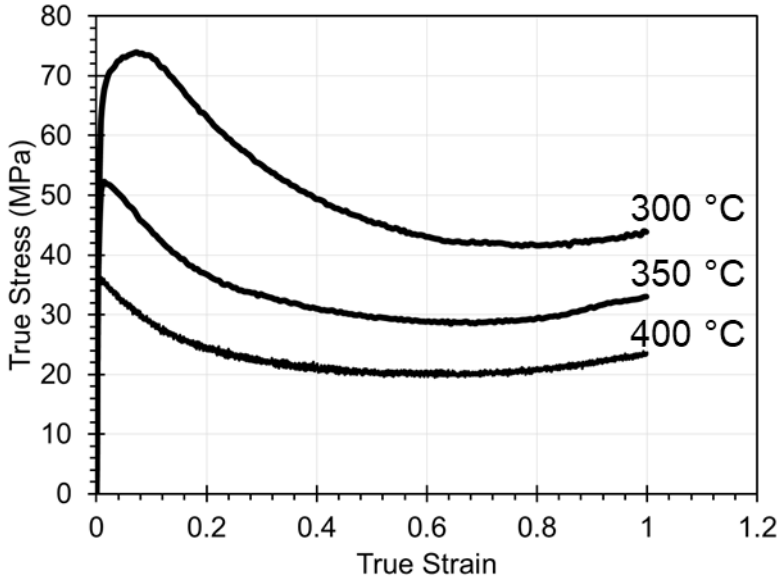

Figure 5-2 Flow stress curves of the cast AZ80 samples deformed at a strain rate of 0.001 s^{-1} at different temperatures

The flow stress values can be used to determine the stress exponent, n (where $n = 1/m$ in $\sigma = k\dot{\epsilon}^m$), and the apparent activation energy (Q) of deformation, at various temperatures, both of which relate to the active deformation mechanism in the material at that temperature [47, 124, 125, 126].

In calculating the stress exponent, n, initially the m values were calculated at individual temperatures by determining the slope of the best linear fit to $log\ \dot{\epsilon}$ - $log\ \sigma$ plots, for a fixed strain, and averaging over all four strain rates (0.001 – 1 s^{-1}). The average of m values determined in this fashion for strains of 0.15, 0.4 and 1.0 was calculated, and inverted to get the value of n (for that particular deformation temperature). The calculated n values at different temperatures of interest are presented in Table 5-1.

Table 5-1 Calculated values of the stress exponent, n, at different deformation temperatures

300 °C	**350 °C**	**400 °C**
7.78	5.95	5.42

The Q values can be calculated using the following equation [71],

$$Q = R\left(\partial \ln \dot{\epsilon} \Big/ \partial \ln\left(1/T\right)\right)|_{\sigma} \tag{5.1}$$

where, R is the universal gas constant. Use of equation 5.1 is based on identifying the deformation conditions which result in approximately overlapping flow stress curves. Some such flow curves are presented in Figure 5-3 (a). Any pair of the curves from Figure 5-3 (a) can be used in equation 5.1, which would give the Q value at the average deformation temperature for the two curves. For example, considering the curves (1) and (2) in Figure 5-3 (a), the Q determined using equation 5.1 corresponds to a deformation temperature of 325 °C. The Q values calculated using equation 5.1 and the current experimental data are provided in Figure 5-3 (b). A dashed line showing the best linear fit is also provided. Calculations indicate that the Q values increased from about 123 kJ/mol at 300 °C, to about 174 kJ/mol at 400 °C, and are pretty consistent with those reported earlier by Barnett on a wrought AZ31 alloy, deformed under comparable deformation conditions (the corresponding data is also included in Figure 5-3 (b)) [71].

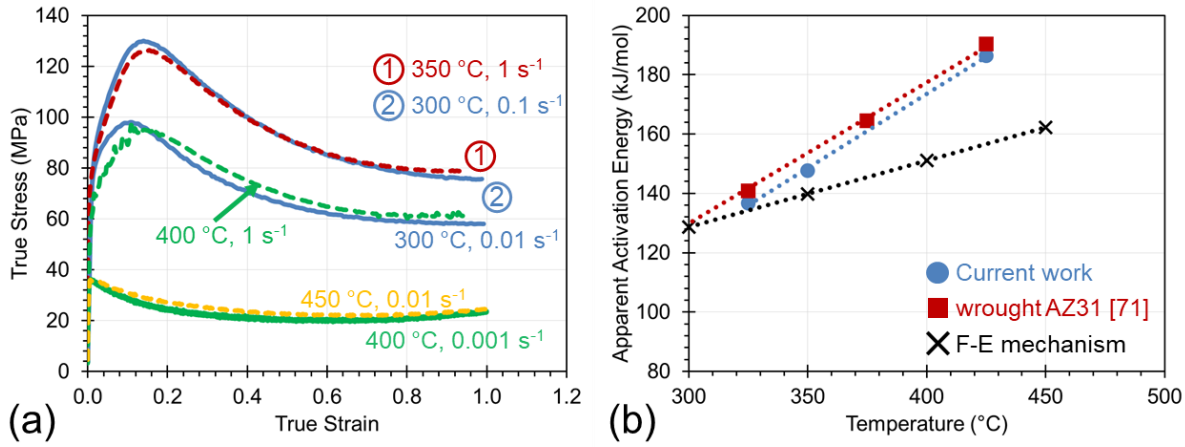

Figure 5-3 Apparent activation energy of deformation, Q: (a) Some of the flow stress curves that coincided, and were used to determine the Q as a function of deformation temperature, (b) Calculated values of Q as a function of deformation temperature. Data from [71] *for AZ31 alloy is included for comparison. Also included is calculated activation energy values for Friedel-Escaig (F-E) cross-slip mechanism. In (b), the dotted lines show the best linear fit to the experimental data points.*

Figure 5-3 (b) also includes a curve that shows the estimated value of the activation energy of the Friedel-Escaig (F-E) cross-slip mechanism (which involves cross-slip of $< a >$ dislocations from the basal plane to the prismatic plane [47]), based on the formula $Q_{\mathrm{F-E}} \approx 27RT$ [71]. Previously Galiyev et al. have reported a transition in deformation mechanism from cross-slip (by F-E mechanism) at intermediate deformation temperatures (200 - 250 °C), involving a Q of 92 kJ/mol ($Q_{\mathrm{F-E}}$ estimated

at 106 kJ/mol, based on the equation provided above) and n of 7, to climb at higher deformation temperatures (300 – 450 °C), involving a Q of 135 kJ/mol ($Q_{F\text{-}E}$ estimated at 128-162 kJ/mol) and n of 5, for deformation of a cast-homogenized ZK60 alloy [47]. In the current work, it can be seen that for deformation at 300 °C, besides an n of 7, which relates to the occurrence of cross-slip mechanism as reported by Galiyev et al., the Q value was also comparable to that of the F-E mechanism ($Q_{deformation} \approx 123$ kJ/mol, while $Q_{F\text{-}E} \approx 128$ kJ/mol), both of which strongly suggests that at 300 °C cross-slip of $< a >$ dislocations from basal planes to prismatic planes by the F-E mechanism was the rate-controlling step. The Q data has been similarly interpreted previously by Barnett et al. on wrought AZ31 alloy [71]. At higher temperatures, n was reduced to about 5, while the Q value increased much above that of the F-E mechanism (Figure 5-3 (b)), suggesting a shift in deformation mechanism to climb controlled dislocation creep [47]. It is noteworthy that the above description should be treated as a qualitative analysis only, based purely on the flow stress curves, as a precise analysis of the deformation mechanism necessitates visualizing the dislocation structure in the material, and is beyond the scope of the present research. It is also noted that the calculated Q values at 300 °C are very close to that of volume self-diffusion in Mg (~ 135 kJ/mol [127]), as well as to that of diffusion of Al in Mg (~ 143±10 kJ/mol [128]). It was found in a separate analysis that solution treated cast AZ80 alloy in undeformed state shows precipitation of (mainly) lath continuous precipitates during aging at 300 °C. The precipitation takes place throughout the grain's volume, and is related to diffusion of Al in Mg matrix. Since the activation energy of deformation at 300 °C, and that for Al's diffusion in Mg, were found to be quite comparable in the present work, this suggests that deformation and precipitation might be linked at 300 °C, however the specifics were not investigated in this research.

5.2.2 Microstructure evolution

The micrographs of the samples deformed at 300 °C and 400 °C to a strain of 0.15 are presented in Figure 5-4. It can be seen that for deformation at 300 °C, $Mg_{17}Al_{12}$ precipitates from the starting material mostly remained intact by this deformation level, while for the sample deformed at 400 °C, the precipitates had already dissolved. The latter observation is attributed to the fact that 400 °C falls in the solutionizing regime of the alloy, and also some of our other results (presented in section 5.4.1) suggest

that the deformation and DRX assisted in the dissolution of the $Mg_{17}Al_{12}$ precipitates at this temperature.

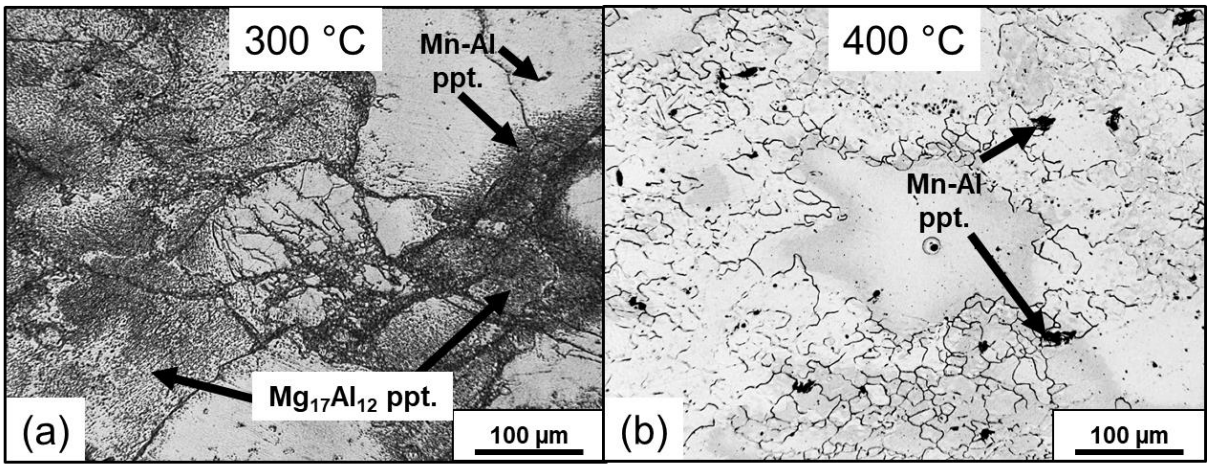

Figure 5-4 Micrographs of the samples deformed to a strain of 0.15 at (a) 300 °C, and (b) 400 °C, and a strain rate of 0.001 s^{-1}. A considerable amount of $Mg_{17}Al_{12}$ precipitates were present in the material after deformation at 300 °C, while they were not present after deformation at 400 °C.

The mechanisms by which DRX took place at different deformation temperatures are illustrated through the micrographs in Figure 5-5 and Figure 5-6. It was found that deformation at 300 °C resulted in the occurrence of twinning at low strain levels, and based on EBSD misorientation angle analysis, these twins were determined to be almost exclusively the $\{10\bar{1}2\} < 10\bar{1}1 >$ tensile twins. DRX was observed within some of these twins (i.e. TDRX) at low strain levels, while samples deformed to a strain of 1.0, showed no presence of twins, which implied that twinning took place only during the initial phase of deformation, and by higher strain levels, either those twins were fully recrystallized, or alternately, entire grains in which twins were nucleated, were fully twinned. At 300 °C, the material also showed DRX through particle stimulated nucleation at lamellar discontinuous precipitates (DP), while lath continuous precipitates were found to block the progress of the advancing DRX front into the non-recrystallized regions. The effect of $Mg_{17}Al_{12}$ precipitates on the hot deformation behaviour of cast AZ80 alloy is described in more detail in a separate section (section 5.5), while it is noted that the results are consistent with those reported previously on cast AZ91 alloy [24]. DRX was also found to take place at the prior grain boundaries, independently of the presence of precipitates. The results suggest a grain boundary bulging mechanism for DRX at the prior grain boundaries, however, the same could

not be ascertained owing to the very fine-grained and heavily precipitated nature of the microstructure. For deformation at 400 °C, twinning did not occur, even at low strain levels, and DRX only took place through the grain boundary bulging mechanism (Figure 5-6). In addition to DRX as a grain refinement mechanism, continuous dynamic recrystallization (CDRX), through kink banding and grain fragmentation in the material during deformation, was also found to contribute to it at all temperatures. This is shown in Figure 5-7.

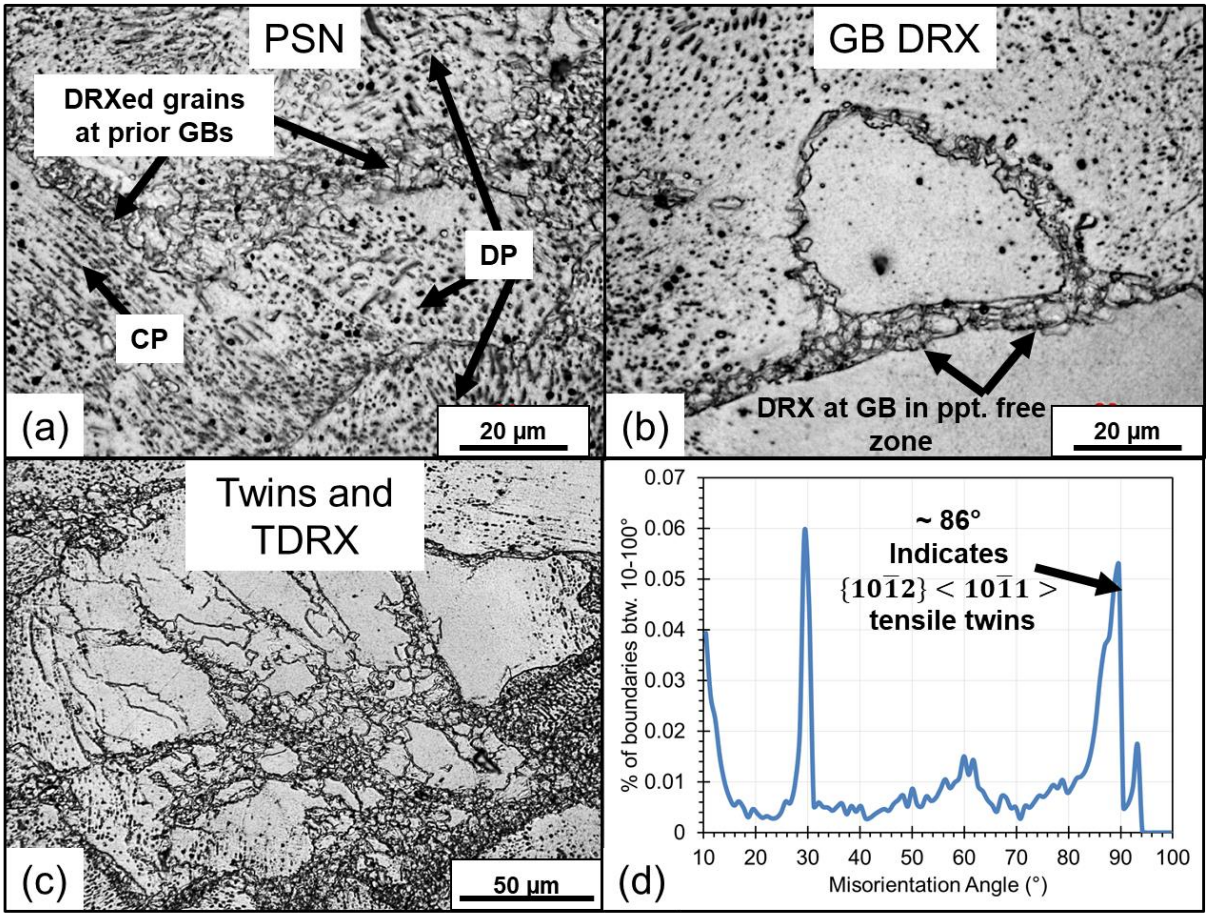

Figure 5-5 Micrographs showing DRX mechanism for the cast AZ80 sample deformed at 300 °C, 0.001 s^{-1}, to a strain of 0.15: (a) Particle stimulated nucleation (PSN) at lamellar discontinuous precipitates (DP), (b) Grain boundary (GB) DRX, (c) A particularly intensely twinned grain, also showing DRX within twins (i.e. TDRX), (d) Misorientation angle plot for the entire scanned area (1.5 x 1.5 mm), developed using the EBSD data. CP refers to lath continuous precipitates.

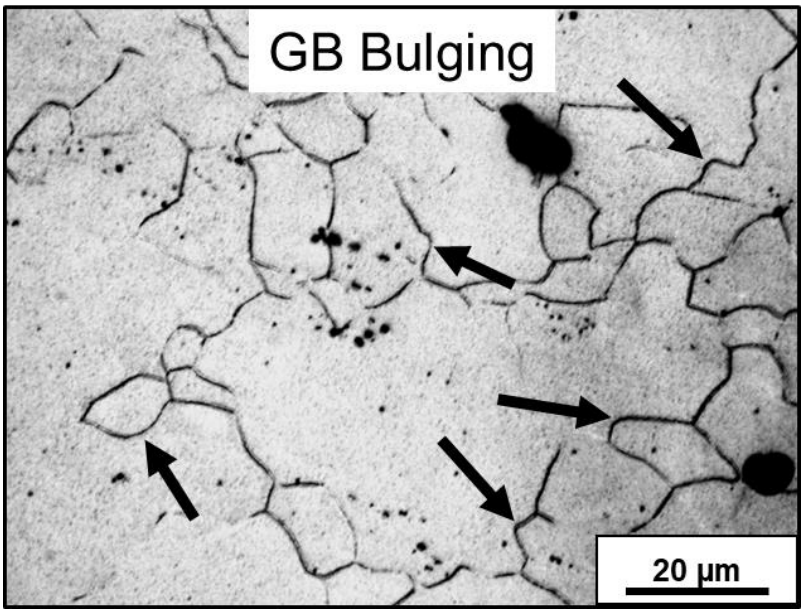

Figure 5-6 Micrograph of the cast AZ80 sample deformed at 400 °C, 0.001 s^{-1}, to a strain of 0.15, showing DRX by the grain boundary bulging mechanism. Arrows mark some of the bulged grain boundaries.

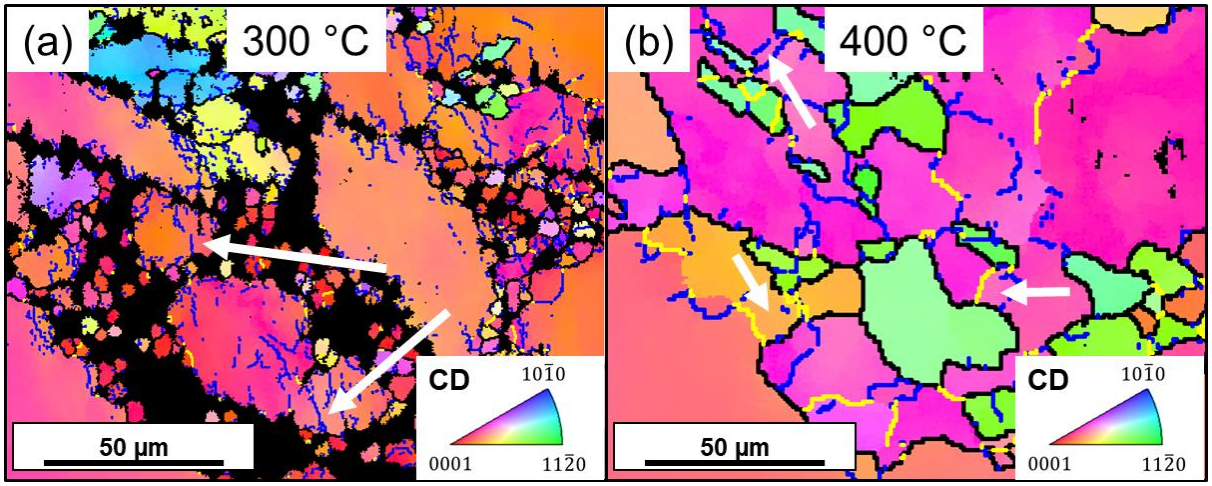

Figure 5-7 Continuous dynamic recrystallization (CDRX) via kink banding and grain fragmentation, in the samples deformed at: (a) 300 °C, and (b) 400 °C, at a strain rate of 0.001 s^{-1}, to a strain of 0.15. Compression direction is vertical, while the colouring in IPFs is w.r.t. the compression direction. Blue lines and yellow lines mark the low angle boundaries, with misorientations in range of 2-5° degrees, and 5-10°, respectively, while black lines mark the grain boundaries. Arrows mark some of the kink bands observed in the microstructure.

The micrographs of the samples deformed to the strain of 1.0 at various temperatures and strain rate of 0.001 s^{-1} are presented in Figure 5-8. Considering the micrographs, the $Mg_{17}Al_{12}$ precipitate content in the microstructure can be seen to decrease with an

increase in the deformation temperature. Another interesting observation is that for deformation at 300 °C, the microstructure was bimodal, with the presence of both coarse and fine grains, while with an increase in deformation temperature, the homogeneity of the microstructure increased. The sample that was deformed at 400 °C showed a reasonably homogeneous microstructure.

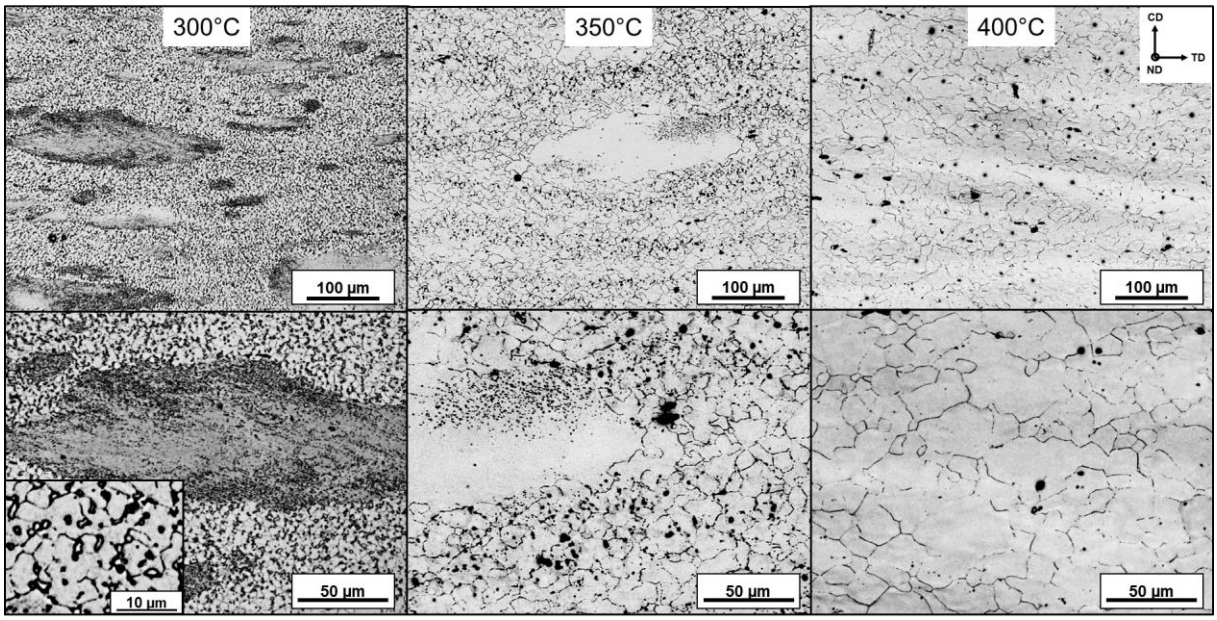

Figure 5-8 Microstructures of the samples compressed at a strain rate of 0.001 s^{-1}, to a strain of 1.0, at various temperatures. The top row shows lower magnification micrographs, while the bottom row shows the corresponding higher magnification micrographs.

It is of interest to quantify the grain size to see how it varied with a change in the deformation temperature. Considering the bimodal microstructure shown by the samples deformed at lower temperatures, it makes sense to just focus on the grain size of the DRXed grains. In order to determine the DRX grain size, EBSD data, and a grain orientation spread (GOS) criterion was used. EBSD software allows for direct export of the GOS values, as well as creating various data subsets based on the provided GOS range. DRXed grains typically show GOS less than 2°, while deformed grains show much higher GOS values [129]. The exact value to distinguish between the DRXed and non-DRXed grains is typically obtained by plotting the GOS distribution for all the grains in a deformed material, and identifying specific GOS range which correspond to the DRXed grains for that material [129]. In the present work, a GOS ≤ 2° was found to be appropriate, for the samples deformed to a strain of 1.0, and the

same has been illustrated for the cast AZ80 alloy deformed at 300 °C, 0.001 s^{-1} in Figure 5-9.

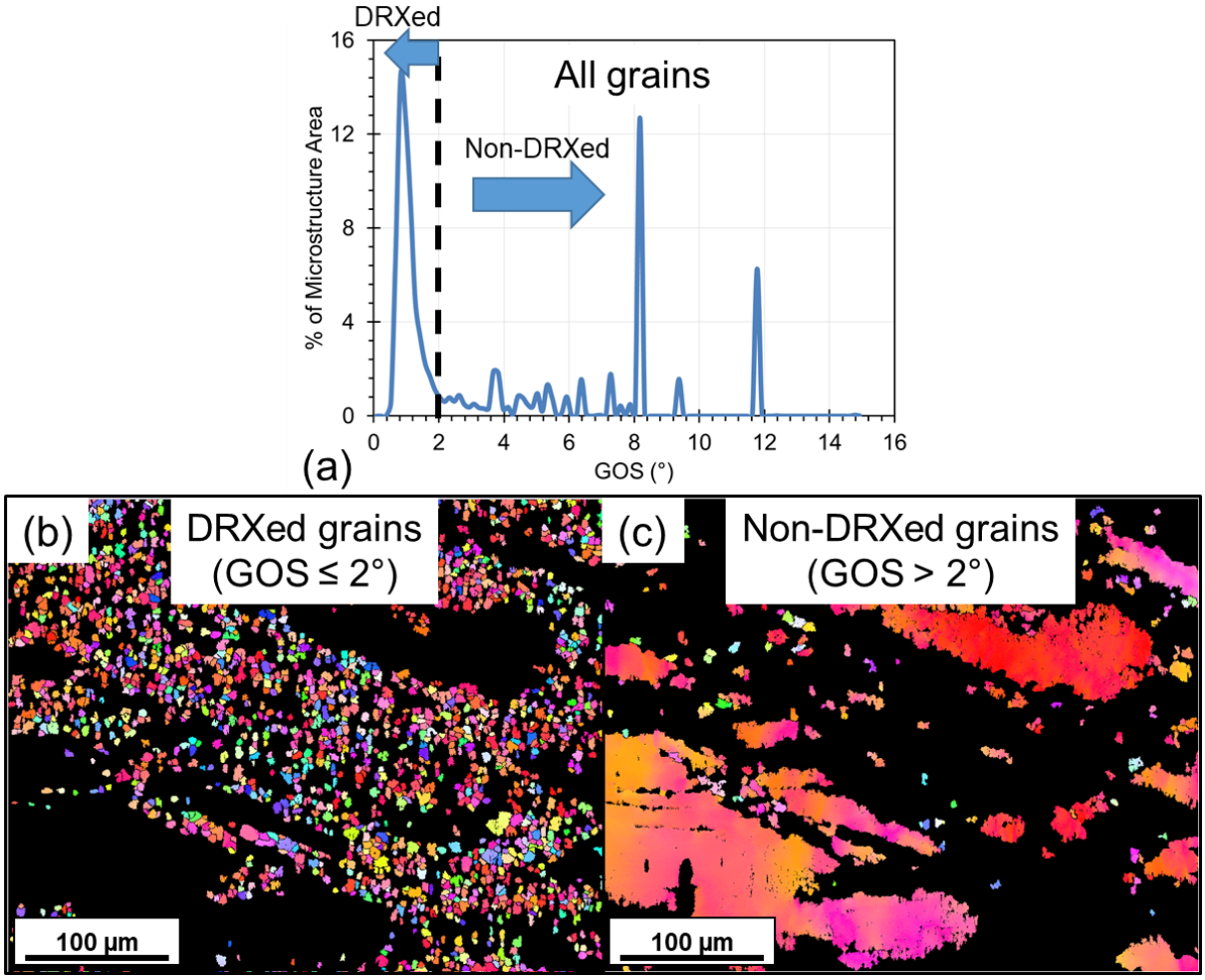

Figure 5-9 Cast AZ80 sample deformed at 300 °C, 0.001 s^{-1}, to a strain of 1.0: (a) GOS distribution of all the grains, (b) IPF map of dataset created by applying a GOS ≤ 2° filter, and (c) IPF map of dataset create by applying a GOS > 2° filter.

The DRX grain size values at 300 °C and 400 °C are presented in Figure 5-10. An average value of ~ 6 µm and ~ 24 µm were determined for deformation at these respective temperatures, and indicate that the DRX grain size increased with the deformation temperature. A lower DRX grain size value at 300 °C is attributed to an availability of less thermal energy for the DRXed grains to grow, and also to the pinning of the boundaries of the DRXed grains by finely distributed $Mg_{17}Al_{12}$ particles (corresponding results are presented in section 5.5.3). For deformation at 400 °C, much more thermal energy for growth was available, and no pinning precipitates were

present, and as such, the corresponding DRX grain size was much larger. At either temperatures, DRX resulted in an outstanding grain refinement from the as-cast state.

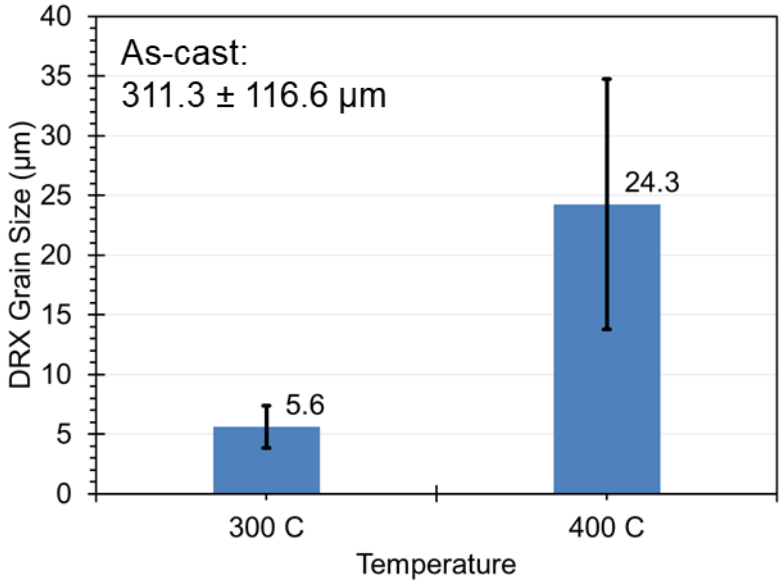

Figure 5-10 DRX grain size in the cast AZ80 alloy samples deformed at 0.001 s^{-1} at different temperatures. DRX grain sizes were determined using the EBSD data. Grain size of as-cast material was determined manually using optical micrographs.

5.2.3 Texture evolution

The texture results of samples deformed to the strain of 1.0 at various temperatures and a strain rate of 0.001 s^{-1}, are presented in Figure 5-11. It can be seen that the texture of the deformed samples, regardless of the deformation temperature, is comparable, in both distribution and intensity. From an initial random texture, deformation at all temperatures led to formation of a predominantly basal texture (i.e. with basal poles mainly aligning closely to the compression direction).

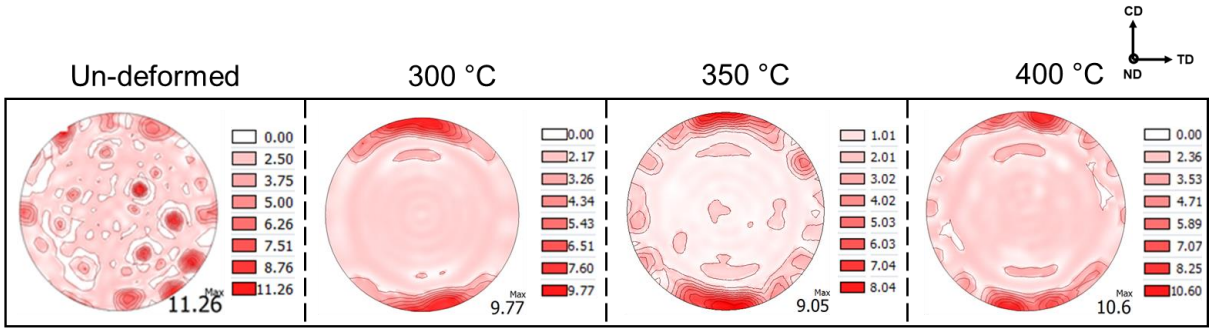

Figure 5-11 XRD macrotexture of the samples deformed to a strain of 1.0, at a strain rate of 0.001 s^{-1} and different temperatures. Texture of as-cast material is also provided for reference. The unit of texture intensity is "Multiples of Random Distribution (MRD)". Orientation legend: CD – Compression direction, ND – Normal direction, TD – Transverse direction.

The bulk texture is made up of texture contributions from the DRXed grains and non-DRXed grains (deformed grains that have not recrystallized, original undeformed grains, and CDRXed grains). Typically it is found that a basal texture develops in the material with deformation (due to predominance of basal slip and tensile twining), while DRXed grains can potentially have a different texture than the parent grains from which they nucleate (refer to section 2.1.4.2). To analyze this for the present material, the textures of DRXed and non-DRXed grains were separately plotted (using the EBSD data) and compared (Figure 5-12). It can be seen that for deformation at 300 °C the DRXed grains had much lower texture intensity compared to the surrounding non-DRXed grains. This strongly suggests that the DRXed grains were randomly oriented, and is attributed to DRX taking place through the PSN mechanism (corresponding results are presented in section 5.5.1). For deformation at 400 °C, the textures of the DRXed and non-DRXed grains were both sharp basal, indicating that the DRXed grains preserved the deformation texture.

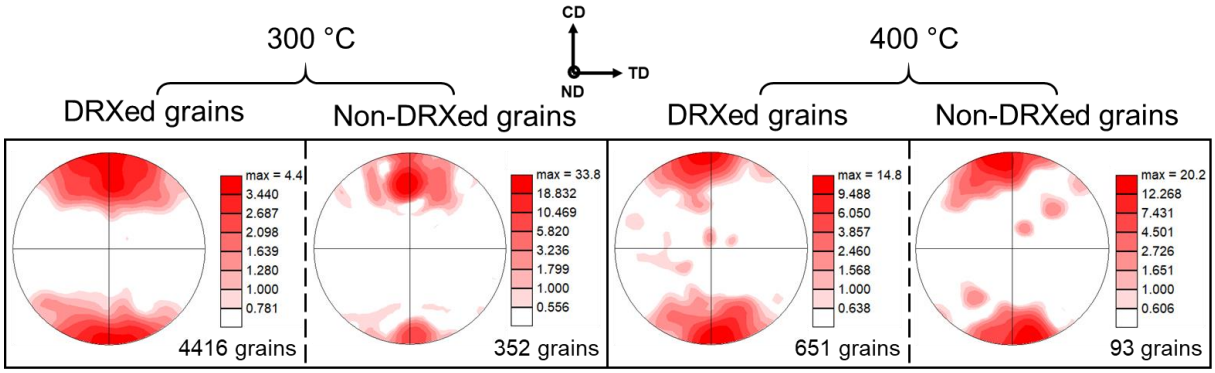

Figure 5-12 Texture of DRXed and non-DRXed grains for the samples deformed to a strain of 1.0 at 300 °C and 400 °C, at a strain rate of 0.001 s^{-1}. The texture plots were developed using the EBSD data, and a GOS ≤ 2° filter to identify the DRXed grains. The number of grains in each subset are also provided. The unit of texture intensity is "Multiples of Random Distribution (MRD)". Orientation legend: CD – Compression direction, ND – Normal direction, TD – Transverse direction.

It is also of interest to investigate if CDRX, which took place under all the investigated conditions as a mechanism of recovery and grain refinement, can cause texture randomization. This is illustrated in Figure 5-13 by taking the example of cast AZ80 alloy deformed at 400 °C, 0.001 s^{-1}, to a strain of 0.15. The figure shows the grain boundary map of the deformed sample, with the orientation of individual fragmented regions indicated by the orientation of the HCP unit cell in it. It can be seen that though the individual fragmented regions within individual grains had some misorientation with

respect to each other (which results in the formation of the low angle boundaries (LABs)), their orientations were still closely related, and comparable to that of the parent grain as a whole. This indicates that the CDRXed grains preserved the texture of the parent grains. Similar observations were made for the sample deformed at 300 °C as well.

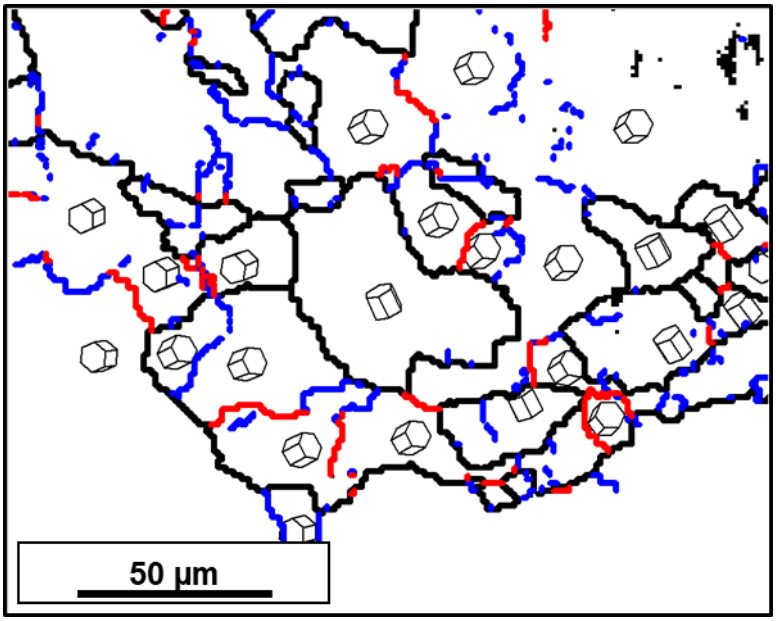

Figure 5-13 Grain fragmentation due to kink banding and development of low angle boundaries (LABs) in the material. The HCP unit cells mark the orientation of individual fragmented regions. The compression direction is vertical.

5.2.4 Summary

The effect of deformation temperature on the hot deformation behavior of cast AZ80 alloy was studied for temperatures ranging from 300 °C to 400 °C, at a strain rate of 0.001 s^{-1}. The main findings of the study are summarized in the following:

1) The analysis of stress exponent, n, and apparent activation energy of deformation, Q, suggested a shift in deformation mechanism from cross-slip of $< a >$ dislocations from basal planes to prismatic planes by Friedel-Escaig mechanism at 300 °C, to a climb controlled dislocation creep at 400 °C.
2) $Mg_{17}Al_{12}$ precipitate content in the deformed material decreased with increasing deformation temperatures. At 400 °C there were no $Mg_{17}Al_{12}$ precipitates present in the material after the deformation.

3) At 300 °C, DRX occurred through PSN (at lamellar DP), grain boundary bulging, and TDRX, while at 400 °C, DRX occurred through the grain boundary bulging mechanism alone. DRX resulted in grain refinement under all conditions, with DRX grain size increasing with an increase in the deformation temperature (d_{DRX} ~ 6 µm at 300 °C, while d_{DRX} ~ 24 µm at 400 °C). Additionally, CDRX, occurring via grain fragmentation, also contributed to grain refinement at all the test temperatures.
4) The microstructure transitioned from being bimodal for deformation at 300 °C, to a homogeneous microstructure for deformation at 400 °C.
5) Bulk textures of the samples deformed to a strain of 1.0 at various temperatures were comparable, though the textures of the sub-components (viz. the DRXed and the non-DRXed grains) were very different. Specifically, the DRXed grains at 300 °C had random texture, while at 400 °C, the DRXed grains preserved the texture of the deformed grains from which they developed. CDRXed grains were found to preserve the deformation texture under all investigated conditions.

5.3 Effect of strain rate

This section explores the role of deformation strain rate on the hot deformation behaviour of cast AZ80 alloy. Uniaxial compression tests were conducted at 400 °C, and strain rates ranging from 0.001 – 0.1 s^{-1}.

5.3.1 Flow stress curves

The flow curves for cast AZ80 alloy at different strain rates at 400 °C are presented in Figure 5-14. It can be seen that as the strain rate increased, entire flow curves shifted to higher stress values. Initial work hardening regime became more pronounced at higher strain rates, while the peak and steady state strains shifted to higher strain levels. An increase in the flow stress value with an increase in strain rate is attributed to a higher work hardening rate (due to faster dislocation accumulation), and finer grain size at higher strain rates.

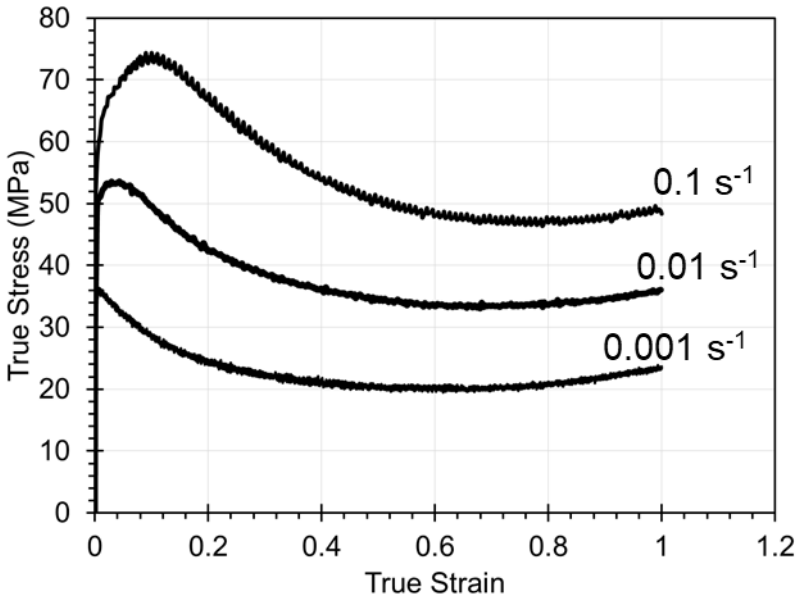

Figure 5-14 Flow stress curves of cast AZ80 samples compressed at 400 °C, at various strain rates.

5.3.2 Microstructure evolution

As described in section 5.2.2, there were no $Mg_{17}Al_{12}$ precipitates present in the material at this deformation temperature. DRX was found to take place through the grain boundary bulging mechanism at all the strain rates. This is shown for the sample deformed to a strain of 0.15 at 400 °C, 0.1 s^{-1}, in Figure 5-15 (a). Additionally, at 0.1 s^{-1}, twinning also took place at low strains, and the twins were found to be partially

recrystallized, as is shown in Figure 5-15 (b) for the sample deformed to a strain of 0.15. At higher strains, no twins could be identified in the microstructure, indicating that either the twins were fully recrystallized, or the grains in which twins were nucleated, twinned completely. The twins were again identified to be $\{10\bar{1}2\} < 10\bar{1}1 >$ tensile twins based on EBSD misorientation angle analysis (Figure 5-15 (c). In addition to DRX, CDRX was also found to be active under all the investigated deformation conditions, and a micrograph showing the same for the sample deformed at 400 °C, 0.1 s^{-1}, to a strain of 0.15, is presented in Figure 5-16.

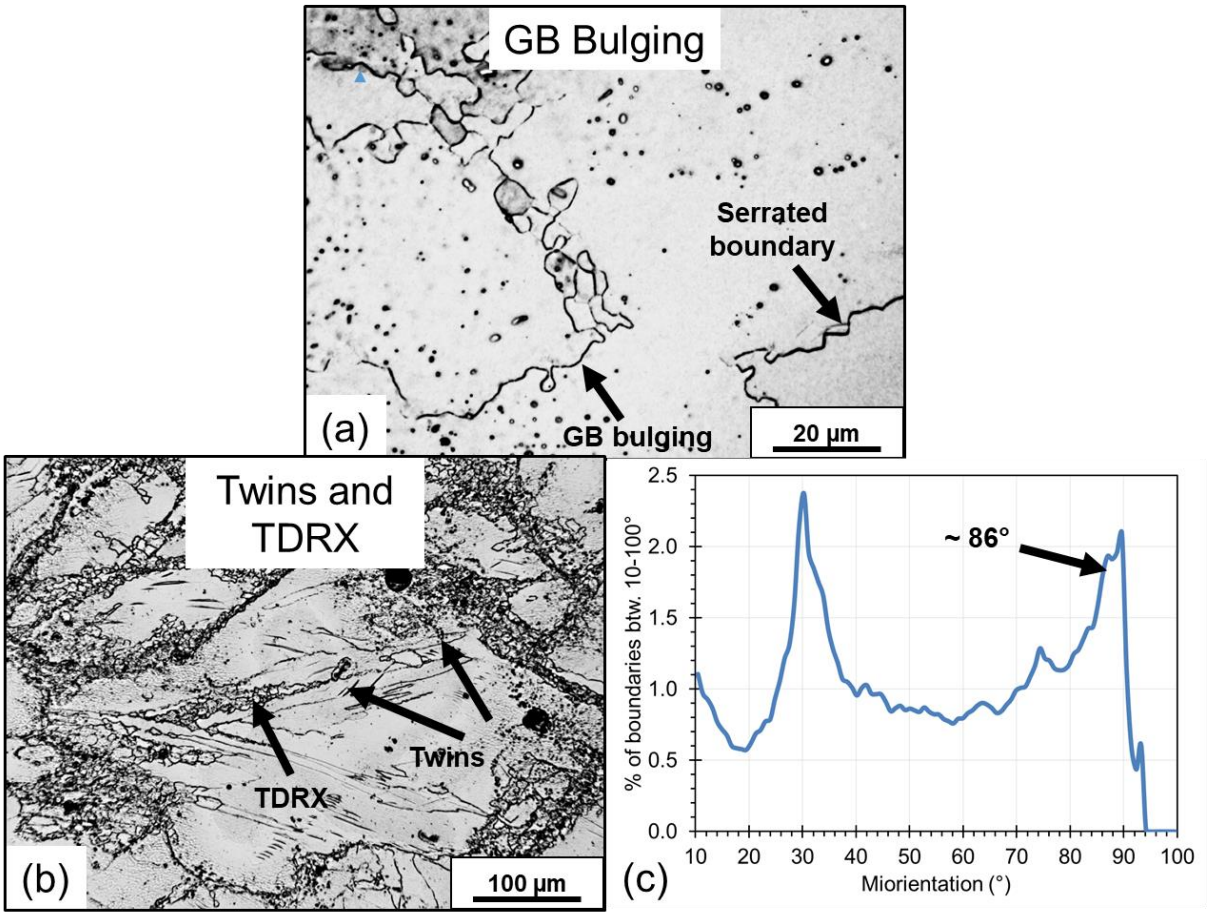

Figure 5-15 DRX mechanism for sample deformed at 400 °C, 0.1 s^{-1} to a strain of 0.15: (a) Grain boundary bulging, (b) TDRX, and (c) Misorientation angle plot for the entire scanned area (1.5 x 1.5 mm), developed using the EBSD data. A peak at ~ 86° indicates $\{10\bar{1}2\} < 10\bar{1}1 >$ *tensile twinning.*

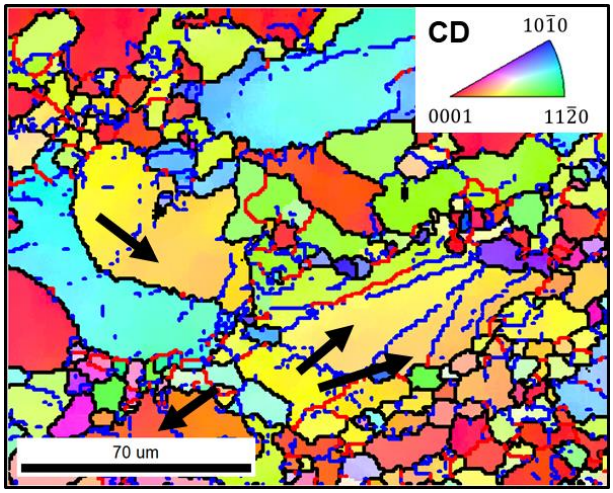

Figure 5-16 CDRX via kink band formation and grain fragmentation in the sample deformed at 400 °C, 0.1 s^{-1}, to a strain of 0.15. Compression direction is vertical. Blue lines and red lines mark the low angle boundaries, with misorientations in range of 2-5° degrees, and 5-10°, respectively, while black lines mark the grain boundaries. Arrows mark some of the kink bands observed in the microstructure.

The microstructures of the sample deformed at various strain rates to a strain of 1.0 are presented in Figure 5-17. It can be observed that the sample deformed at the lowest strain rate showed a homogeneous microstructure, with relatively coarse grains, while at increasing strain rates, the microstructure became less homogeneous, but more grain refined (grain size quantification results are presented in Figure 5-19).

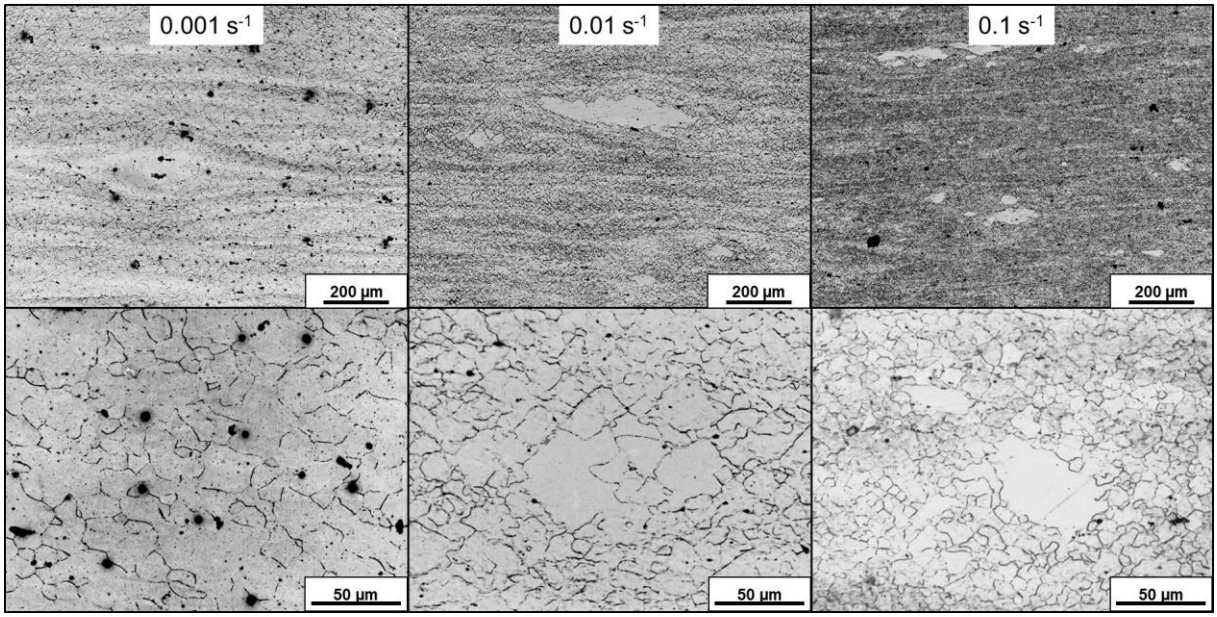

Figure 5-17 Microstructures of the samples compressed to a strain of 1.0 at various strain rates. The top row shows lower magnification micrographs, while the bottom row shows the corresponding higher magnification micrographs.

The microstructural inhomogeneity manifested more strongly at the free side surface of the samples, and is shown in Figure 5-18. This figure presents the micrographs at the top-side edge of the samples compressed to a strain of 1.0 at 400 °C, for strain rates ranging from 0.001 s^{-1} to 1 s^{-1}. The approximate location on the sample's cross-section from where these micrographs were taken is illustrated in the inset in Figure 5-18 (a). It can be seen that as the deformation strain rate increased, the side surface of the sample became less smooth, and also the microstructural heterogeneity in the sample's interior increased substantially. The sample deformed at the strain rate of 1 s^{-1} also showed presence of fracture cracks (one such crack is marked by an arrow in Figure 5-18 (a)). It is noted that at higher strain rates, non-homogenous deformation mechanisms like shear banding and twinning can become active to accommodate the imposed deformation, because slip based deformation modes might not be able to accommodate the deformation at an adequate rate. Shear bands were not investigated in the present research, however twinning was indeed observed to take place in the material at strain rates of 0.1 s^{-1} and higher. Some twins are also visible near the sample edges in the micrographs presented in Figure 5-18 (a). Prior literature on Mg AZ31 alloy indicates that fracture crack nucleation in many cases is strongly linked to the occurrence of twinning and/or shear banding in the material [19, 30, 55], and therefore it is likely that they contributed to the fracture cracking observed in the present work as well. Another possible reason for cracking is local melting of the eutectic $Mg_{17}Al_{12}$ phase (present in the material as a result of non-equilibrium solidification) at high temperatures and high strain rates, which can result in formation of a void, which can then grow into a crack as a result of tensile stresses (hoop stresses) on the sample's surface during compression (refer to the stress distribution plot in the sample presented in Appendix E) [86]. Based on the Scheil solidification phase fraction map presented in Figure 4-6 (a), local melting of the eutectic $Mg_{17}Al_{12}$ phase can take place at temperatures above ~ 400 °C.

It is noted that the heterogeneity was more pronounced near the surface, owing to the region experiencing comparatively lower strain levels than the central region, which would delay grain refinement. This interpretation is based on the strain distribution in the sample (refer to Appendix E).

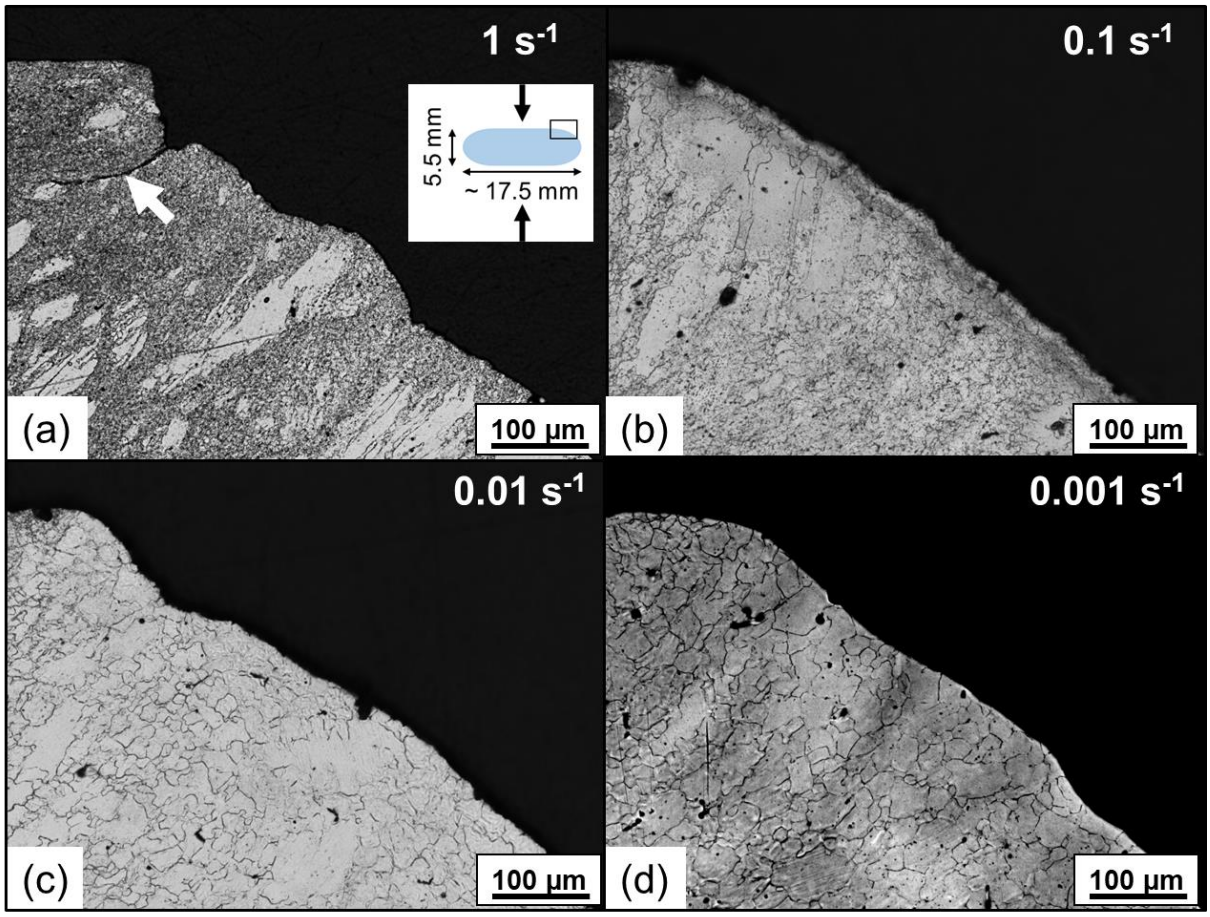

Figure 5-18 Microstructural and surface features of the samples deformed at 400 °C and different strain rates to a strain of 1.0. The white arrow in (a) marks a fracture crack. The inset image in (a) shows the approximate location on the deformed and sectioned samples where the micrographs were taken from. The vertical arrows in the inset represent the compression direction.

The microstructure quantification results for the samples compressed to strain of 1.0 at various strain rates are presented in Figure 5-19. The grain size values are based on the EBSD data. DRXed grains were determined using a GOS of ≤ 2°, as in section 5.2.2. Note that the grain size analysis is limited to the central region of the deformed samples, as was indicated in Figure 4-13 (section 4.3.1), and the grains closer to the edges, as in Figure 5-18, were not included. It can be seen from the figure that both the overall grain size and the DRX grain size decreased as the deformation strain rate increased.

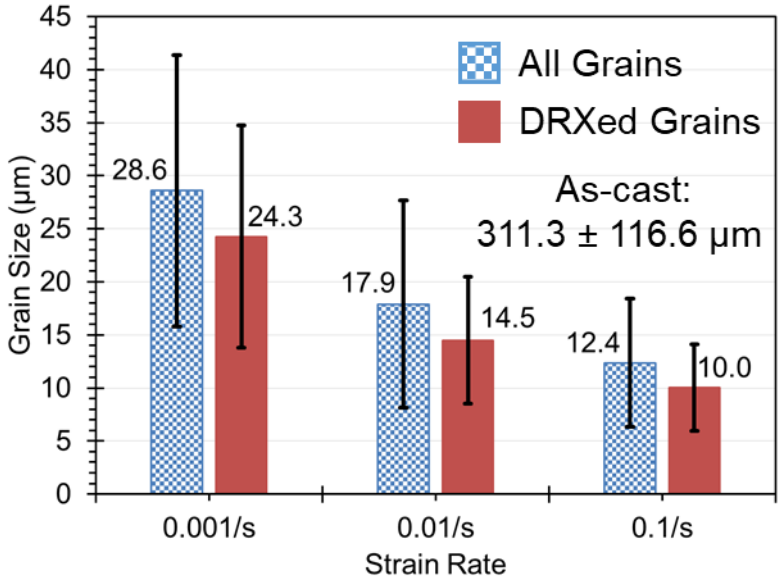

Figure 5-19 Grain size in the cast AZ80 samples deformed at 400 °C at various strain rates to a strain of 1.0. EBSD data was used to determine the grain size values of the deformed samples, while for the as-cast material, grain size was determined manually, using the optical micrographs. DRXed grains were determined based on a GOS ≤ 2° filter.

5.3.3 Texture evolution

The texture results for the samples deformed to a strain of 1.0 at various strain rates are presented in Figure 5-20. In all the cases, a near basal texture along the compression direction developed due to deformation, while the texture intensity was found to increase with an increase in the deformation strain rate.

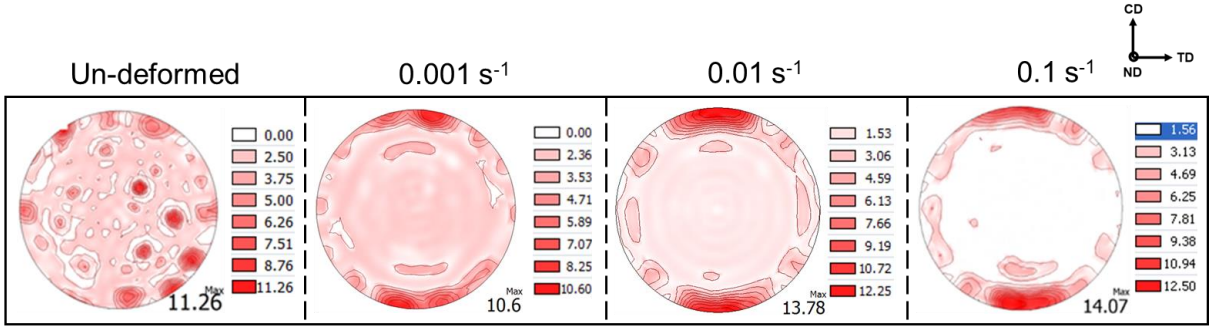

Figure 5-20 XRD macrotexture of the samples deformed to strain of 1.0 at different strain rates. Texture of the as-cast material is also provided for reference. The unit of texture intensity is "Multiples of Random Distribution (MRD)". Orientation legend: CD – Compression direction, ND – Normal direction, TD – Transverse direction.

The texture of the DRXed and non-DRXed grains for the samples deformed at the strain rates of 0.001 s^{-1} and 0.1 s^{-1} are presented in Figure 5-21. It can be seen that the textures of the DRXed and non-DRXed grains were comparable for both the strain

rates, indicating that the DRXed grains preserved the deformation texture in both the cases. As such, it can be concluded that DRXed grains in the cast AZ80 alloy deformed at strain rates in the range of 0.001 s^{-1} - 1 s^{-1} at 400 °C preserves the deformation texture.

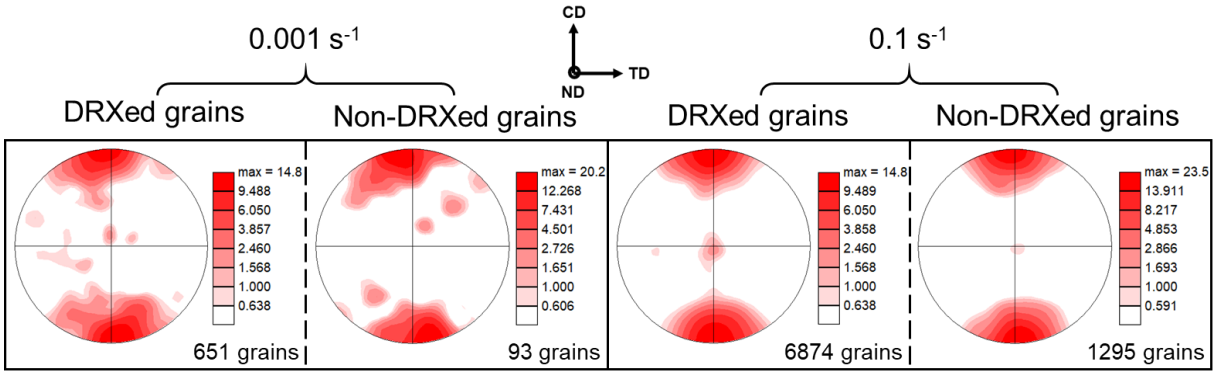

Figure 5-21 Texture of DRXed and non-DRXed grains for the samples deformed to a strain of 1.0 at 0.001 s^{-1} and 0.1 s^{-1}, calculated using the EBSD data, and a GOS ≤ 2° filter to identify the DRXed grains. The number of grains in each subset are also provided. The unit of texture intensity is "Multiples of Random Distribution (MRD)". Orientation legend: CD – Compression direction, ND – Normal direction, TD – Transverse direction.

5.3.4 Summary

The effect of deformation strain rate on the hot deformation behavior of cast AZ80 alloy was studied for strain rates ranging from 0.001 s^{-1} to 0.1 s^{-1}, at a temperature of 400 °C. The main findings of the study are summarized in the following:

1) DRX took place by grain boundary bulging mechanism at all strain rates, and in addition, TDRX also took place for the sample deformed at the strain rate of 0.1 s^{-1}. CDRX was active as a recovery and grain refinement mechanism under investigated test conditions.
2) The microstructural homogeneity decreased with an increase in the strain rate, while the overall grain size and DRX grain size decreased. The microstructural heterogeneity became especially pronounced and noticeable at the free side surface of the samples deformed at higher strain rates. The sample deformed at 1 s^{-1} even showed the presence of fracture cracks.
3) Deformation at all strain rates resulted in the development of a sharp basal texture along the compression direction, which became slightly more intense with increasing strain rates. DRXed grains preserved the deformation texture in all cases.

5.4 Effect of strain

This section describes the microstructure and texture evolution with deformation strain, for cast AZ80 alloy deformed at 400 °C at two strain rates: 0.001 s^{-1}, 0.1 s^{-1}. The corresponding flow stress curves were presented in Figure 5-14.

5.4.1 Microstructure evolution

As was described in sections 5.2.2 and 5.3.2, the material that was deformed at 400 °C, showed no presence of $Mg_{17}Al_{12}$ precipitates after the completion of deformation. It is important to understand when this dissolution took place and how. Relevant micrographs which illustrate this are presented in Figure 5-22, and correspond to the condition of the sample at various stages of the deformation process, for deformation at 400 °C, 0.1 s^{-1}: (a) as-cast material, (b) sample heated to the test temperature in Gleeble™ 3500, and held for 60 seconds, just prior to the start of compression, (c) sample deformed to a strain of 0.05, which happens to be lower than the critical strain required to initiate DRX in the material ($\varepsilon_C \sim 0.08$), (d) sample deformed to a strain of 0.15, which is a higher strain level than the critical strain, and (e) sample deformed to a strain of 0.4. It can be seen that the dissolution of precipitates was initiated during heating to and holding at the test temperature of 400 °C in Gleeble™ 3500, while the majority of the dissolution took place when the material was compressed in the strain range of 0.05 to 0.15, where simultaneous deformation and DRX occurred. The equilibrium phase fraction map predicts that the $Mg_{17}Al_{12}$ precipitates should completely dissolve in the Mg matrix at this temperature, and deformation (which creates defects in the material, and thereby aids in the diffusion process), and DRX (which, owing to formation of new fine grains, increases the specific grain boundary area, and thereby again aids in the diffusion process), are likely to have aided in the dissolution of the precipitates. Mn-Al based precipitates, on the other hand, are thermally stable at this temperature, and remained more or less intact during the course of the deformation.

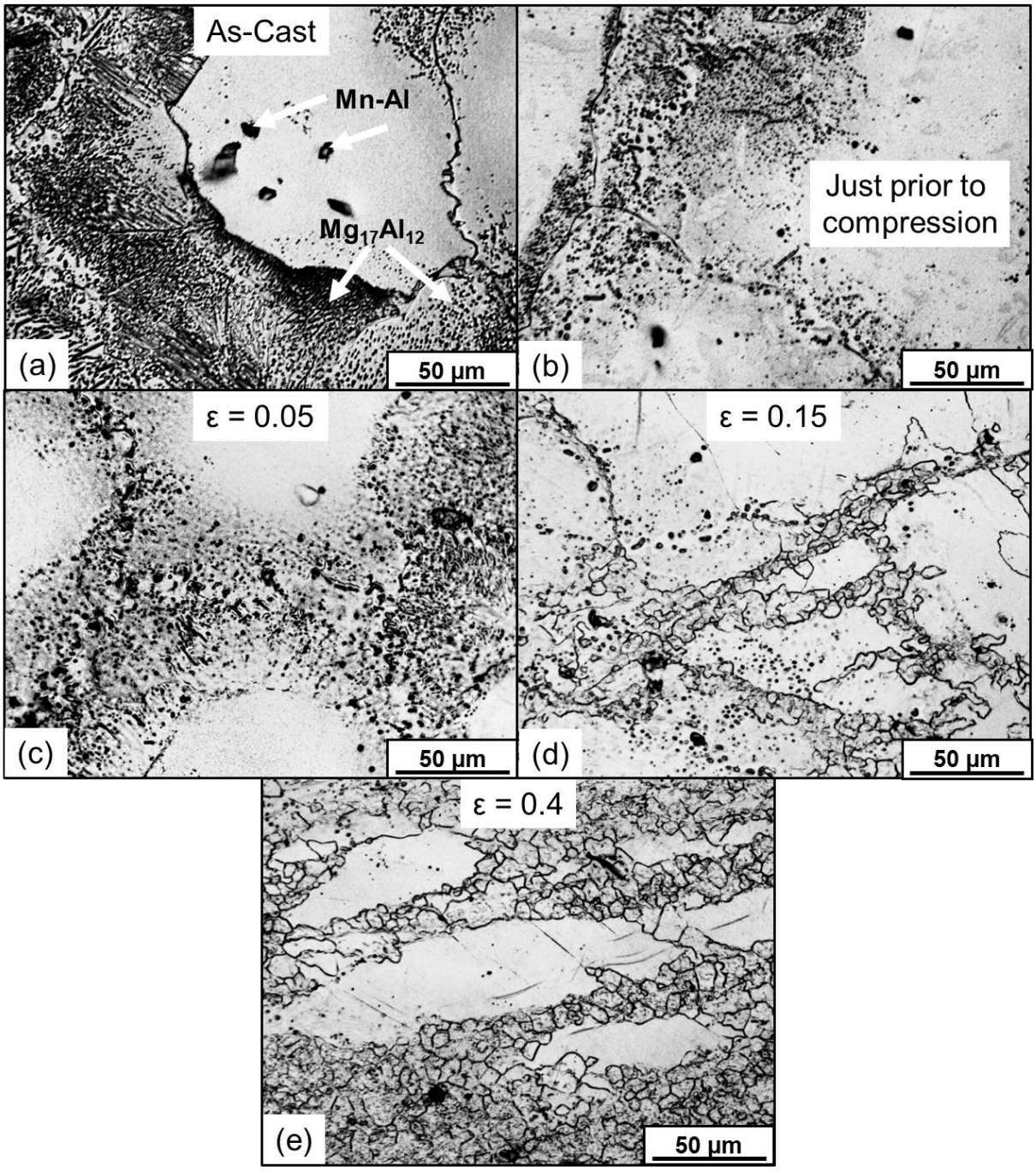

Figure 5-22 Effect of hot deformation (at 400 °C, 0.1 s^{-1}) on precipitates in cast AZ80 samples: (a) as-cast material, (b) undeformed sample after heating to 400 °C in Gleeble™ 3500 and being held at this temperature for 60 seconds, just prior to the start of compression, (c-e) sample deformed to strains of 0.05, 0.15 and 0.4, respectively.

The DRX mechanisms for deformation at 400 °C were already described in section 5.3.2, and includes DRX by grain boundary bulging mechanism at all the strain rates, and additionally TDRX at 0.1 s^{-1}. An important consideration in this regards is the critical strain level, which marks the strain at which the DRX initiates in the material.

For the sample deformed at 0.1 s^{-1}, the validity of the calculated critical strain value was tested by deforming the material to strains slightly lower and higher than the calculated critical strain for the corresponding deformation condition, and the corresponding micrographs of the deformed samples investigated for the presence of any DRXed grains. As shown in Figure 5-23, no evidence of DRX at prior grain boundaries (due to grain boundary bulging), as well as in twins (due to TDRX) could be observed for the sample strained to 0.05, while for the sample strained to 0.15, which is a higher strain level than the critical strain level, DRX at grain boundaries and twins, both, was observed. This provides some validation of our calculated critical strain value for the present material.

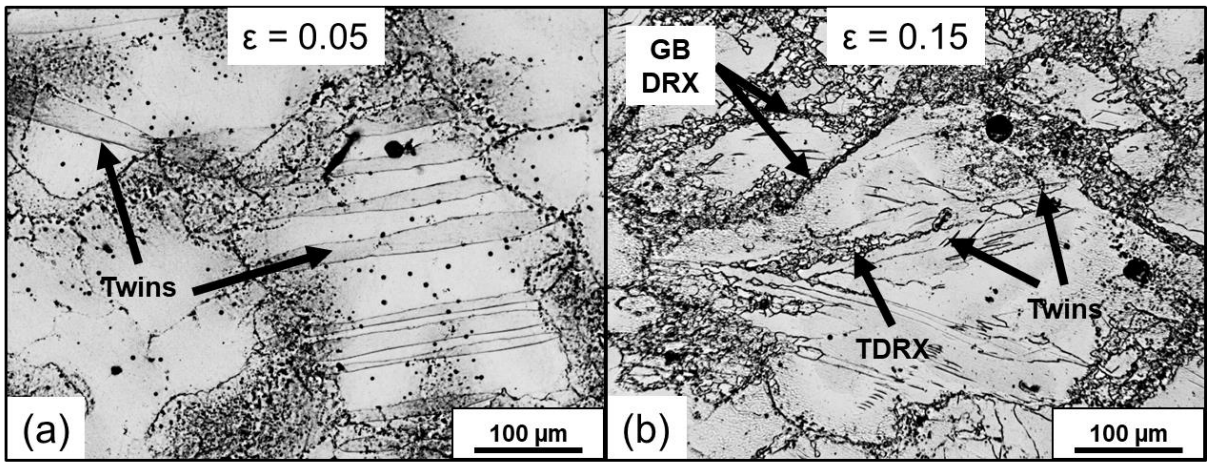

Figure 5-23 Micrographs illustrating the validity of the critical strain concept for the cast AZ80 alloy: (a) sample deformed to a strain of 0.05 at 400 °C, 0.1 s^{-1}, and (b) sample deformed to a strain of 0.15.

The microstructure evolution with strain in the range of 0.15 – 1.0 at both the strain rates is presented though the EBSD Inverse Pole Figure (IPF) maps in Figure 5-24. The compression direction in the micrographs is vertical, while the colouring scheme is with respect to the compression direction, meaning that a red coloured grain (or pixel) in the map indicates that the basal pole (i.e. the (0002) pole) of that grain or pixel is aligned parallel to the compression direction. Other colours in the IPF maps can be interpreted similarly, based on the orientation legend provided at the bottom right corner of the figure. For deformation at either strain rates, initially, a bimodal grain structure developed, with the presence of both coarse and fine grains in the microstructure. With progressive deformation, the area fraction covered by the fine grains increased, and eventually by a strain of 1.0, in both cases, a reasonably

homogeneous fine-grained microstructure developed. The microstructure at the higher strain rate was much finer compared to that at the lower strain rate, as was also described in section 5.3.2.

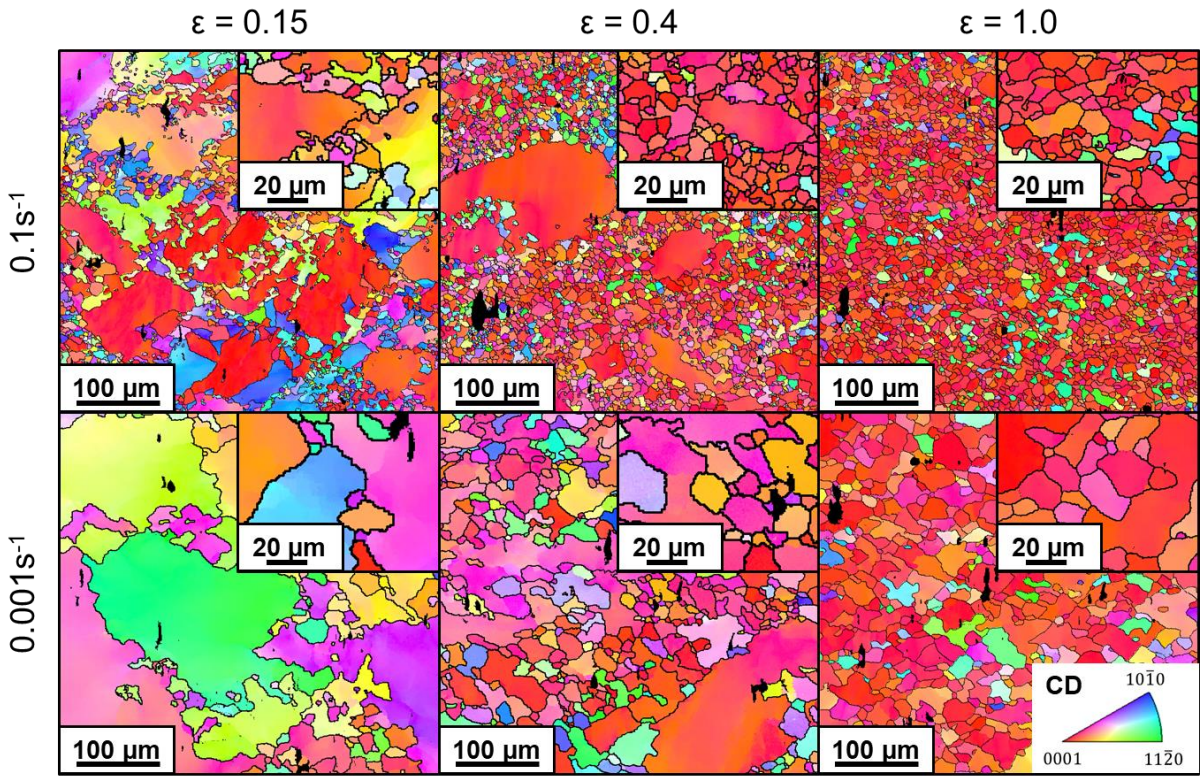

Figure 5-24 Microstructure evolution in the cast samples during hot compression at 400 °C at the two strain rates. The images in the inset show the corresponding high magnification micrographs. Compression direction is vertical.

The overall grain size values in the deformed samples are quantified in Figure 5-25. It can be seen from the figure that deformation resulted in a considerable grain refinement from the as-cast state, with a substantial portion of the refinement taking place during the initial phase of deformation to the strain of 0.4. The grain refinement is attributed to both DRX and CDRX, as described previously. It is noted that the error bars for the samples strained to 0.15 and 0.4 are not included in the figure because of the significantly bimodal nature of the microstructures, whereby the error bars were found to be comparable to the average grain size values themselves. The error bars for the samples strained to the final strain of 1.0 are small, indicating that the corresponding microstructures were relatively homogeneous.

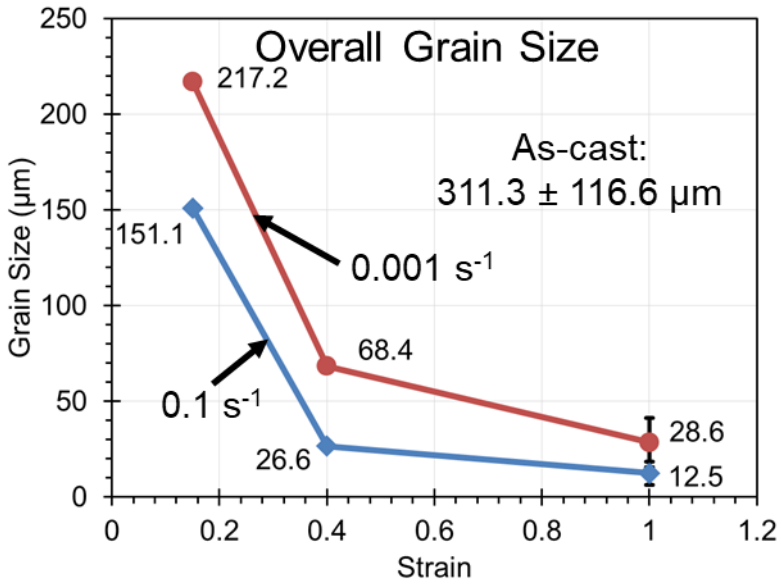

Figure 5-25 Overall grain size evolution with deformation strain for the cast AZ80 samples deformed at 400 °C, and strain rates of 0.001 s^{-1} and 0.1 s^{-1}. EBSD data was used to determine the grain size values of the deformed samples, while the grain size in the as-cast material, was determined using the optical micrographs.

It is also of interest to quantify the DRX grain size and DRX% variation in the material with deformation strain level. Previously, a GOS ≤ 2° criterion was used to identify and quantify the DRXed grains. However, a GOS criterion is typically applicable only for samples deformed to high strain levels, because for low levels of deformation, the criterion cannot distinguish between less deformed grains and DRXed grains. This is illustrated in Figure 5-26 for the current case. Figure 5-26 (a) shows the GOS distribution in the as-cast material, and indicates that almost all the grains in the starting cast material had a GOS < 2°, owing to them being not deformed. In case a purely GOS based criterion is used to identify the DRXed grains in the samples deformed to low strain levels, such as to a strain of 0.15, then besides the actual DRXed grains, many of the grains from the starting material that had not deformed appreciably by this strain level will also be included in the dataset of the DRXed grains. This problem was resolved in the current study by additionally imposing a grain size filter, of size ≤ 20 µm, for the DRXed grains (for the samples deformed at the strain rate of 0.1 s^{-1}), and is based the grain size distribution results presented in Figure 5-26 (b), which shows a strengthening of the distribution peak in between 2-20 µm, as the deformation progressed, indicating that the DRXed grains were distributed within this size range. The GOS distribution of only the grains of size ≤ 20 µm, for sample

deformed to a strain of 0.15 is plotted in Figure 5-26 (c), and their low GOS value (mostly under 2°) confirm that they represent the DRXed grains.

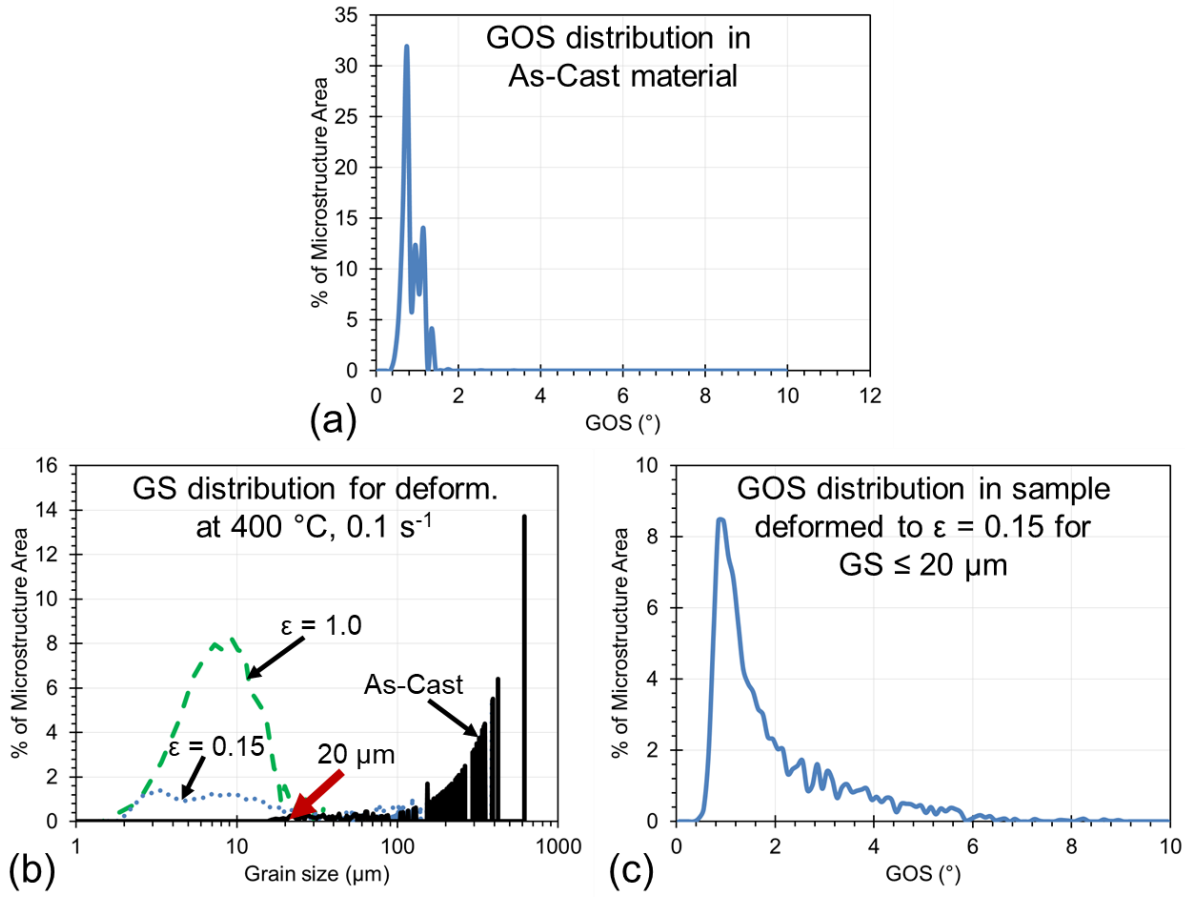

Figure 5-26 Developing a grain size based criterion to identify DRXed grains at low strain levels in the cast AZ80 sample deformed at 400 °C, 0.1 s^{-1}: (a) GOS distribution in the as-cast material, (b) Grain size distribution in the as-cast material, and samples deformed to the strains of 0.15 and 1.0, and (c) GOS distribution in sample deformed to the strain of 0.15, for only the grains which were smaller than 20 µm. GS in (b) refer to grain size.

It is noted that a comparable upper limit to the DRX grain size for the samples deformed at 0.001 s^{-1} could not be defined (because of a much wider grain size distribution in this case), and therefore no attempt has been made here to quantify the DRX grain size and fraction for the samples deformed at 0.001 s^{-1}.

The DRX quantification results for deformation at 400 °C, 0.1 s^{-1} are presented in Figure 5-27. A combined GOS and grain size criteria, as described above, was used. Considering the results, it can be seen that the DRX grain size did not vary appreciably during the course of the deformation. DRX% increased with deformation strain, up to a strain of 0.4, after which it remained essentially stable. It is noted that the DRX%

results are based on single measurements per sample, and therefore slight variations in the individual values with repeat measurements can be expected.

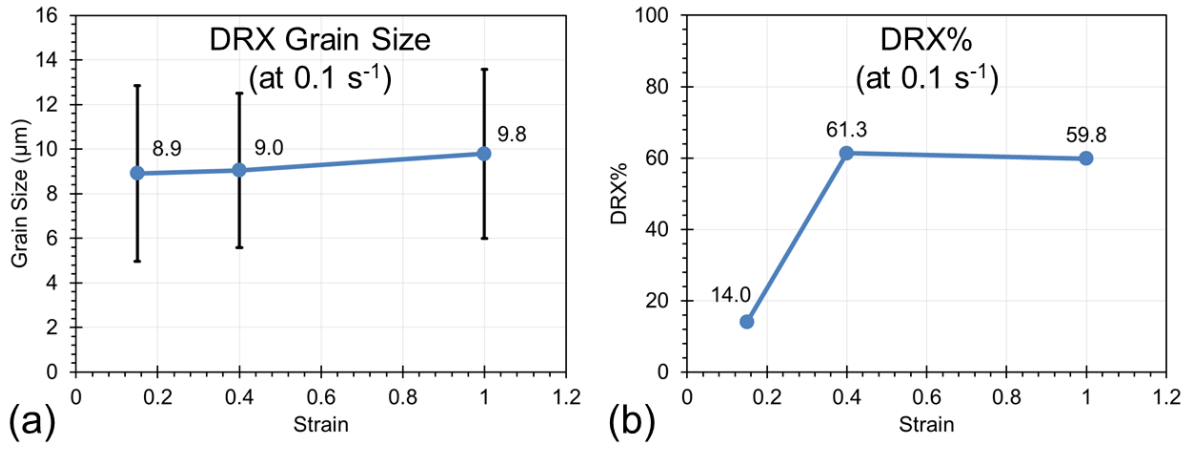

Figure 5-27 (a) DRX grain size, and (b) DRX%, in the cast AZ80 samples deformed at 400 °C, 0.1 s^{-1} to various strain levels. EBSD data was used to plot the above graphs. DRXed grains were identified using a combined criteria: GOS ≤ 2° and grain size ≤ 20 μm.

The results pertaining to the DRX grain size are in line with the existing knowledge on the subject, where the DRX grain size is reported to be independent of the deformation strain level [48, 67, 114]. With regards to the DRX%, the initial increase was due to the DRX front progressing into and consuming the non-recrystallized regions, while a saturation in the DRX% beyond a strain of 0.4 suggests that an equilibrium between deformation and DRX had developed. It is noted that the microstructure from Figure 5-24 at strain of 1.0 appeared pretty homogenous, and considering that a DRX% of ~ 60% at a strain of 1.0 might appear pretty low. This discrepancy can be understood considering the following points:

1) DRX is a dynamic phenomenon, in which new grains develop, while old DRXed grains deform, which might increase the GOS of the latter above 2°. Therefore, many such DRXed-deformed grains are not included in the calculations for DRX grain size and %, in case a GOS ≤ 2° criterion is used. As such, the DRX data presented in Figure 5-27 should be considered as more of a representative of the recently DRXed grains.

2) In addition to DRX, CDRX also took place in the material, leading to grain refinement and development of a homogeneous microstructure. These

CDRXed grains are not included in calculations of DRX% in Figure 5-27 because of the use of the GOS ≤ 2° criterion.

5.4.2 Texture evolution

The texture evolution results are presented in Figure 5-28. The texture of the as-cast material is also provided for reference. For ease in the interpretation of the results, the starting texture is divided into three components (with respect to the compression direction (CD)), viz. A, B and C (wherein A represents the grains which were oriented with their basal poles inclined 70-90° to the CD, B: grains oriented 20-70° to the CD, and C: grains oriented 0-20° to the CD). Texture evolution during deformation is dictated by the slip/twin activity, which in turn is determined by the Schmid Factor (SF) values on various slip/twin systems, and their relative CRSS ratios. It is noted that SF is simply a geometrical factor, which is used to resolve the applied (deformation) load along different deformation modes (slip/twin systems) [130]. SF varies from 0 to 0.5, with a higher value for a particular deformation mode indicating an ease in its activation. The concept of CRSS was already described in section 2.1.2. A particular deformation mode can become active only when the resolved shear stress (RSS) along the deformation mode, which is given by $RSS = SF * Applied\ stress$, becomes equal to the CRSS for that deformation mode at that temperature. The SF values and CRSS (at 400 °C) for various deformation modes of interest in the present work are presented in Figure 5-29. It is noted that SF for $\{10\bar{1}2\} < 10\bar{1}1 >$ tensile twinning is not provided in Figure 5-29 (a), but it is known that due to the polar nature of its activation, its activation is favored only for component A during a compressive loading along the CD.

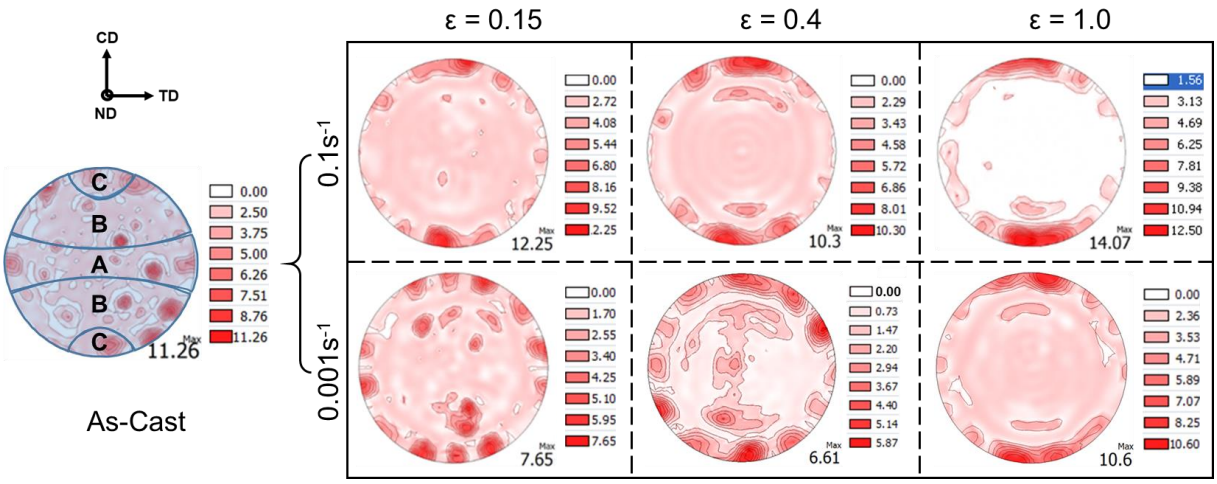

Figure 5-28 XRD macrotexture evolution in the cast AZ80 samples for deformation at 400 °C at the two strain rates. The texture of the as-cast material is divided into three components for ease in the interpretation of the results - A: grains oriented with their basal poles inclined 70-90° to the CD, B: grains oriented 20-70° to the CD, and C grains oriented 0-20° to the CD. The unit of texture intensity is "Multiples of Random Distribution (MRD)". Orientation legend: CD – Compression direction, ND – Normal direction, TD – Transverse direction.

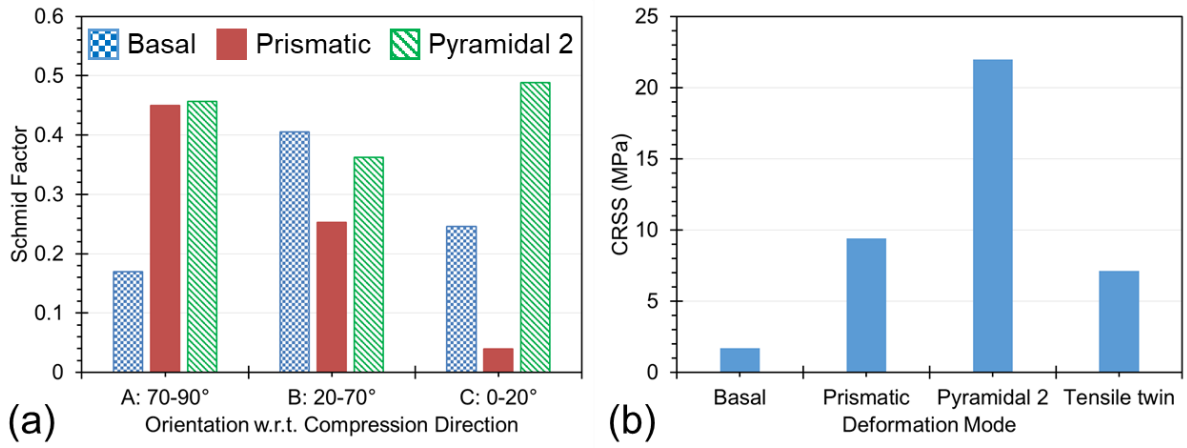

Figure 5-29 (a) Schmid factor (SF) values for the major slip modes in the as-cast material with respect to the compression direction (for interpretation of orientations A-C, refer to Figure 5-28). SF values were determined using the EBSD data. (b) CRSS values of the major deformation modes in pure Mg at 400 °C [39].

Considering the SF and CRSS values presented in Figure 5-29, it is evident that component A favors mainly the prismatic slip, and tensile twinning, component B favors mainly the basal slip, while component C favors mainly the Py2 slip, in the material during the deformation. In addition, basal slip is also likely for all the components, owing to its much lower CRSS compared to the other slip systems. With

this knowledge of potentially active deformation modes at 400 °C, the texture results presented in Figure 5-28 can now be interpreted. Considering the texture evolution at 0.1 s^{-1}, the texture rapidly changed to a sharp basal texture (along the CD) from an initial random texture in the as-cast material. Such rapid texture modification cannot take place due to slip activity, and is attributed to $\{10\bar{1}2\} < 10\bar{1}1 >$ tensile twinning in the material. Since this texture is reasonably sharp, this also indicates that twinning took place profusely, and/or entire grains in which twins got nucleated got fully twinned. During deformation beyond strain of 0.15, the texture essentially remained stable at this level. Deformation in the strain range of 0.15-1.0 is likely to have taken place through a combination of basal and Py2 slips. For deformation at 0.001 s^{-1}, twinning did not take place, which is also reflected in the corresponding texture evolution results, which show a gradual transition from the initial random texture in the as-cast material to a sharp basal texture, as the material was progressively deformed to higher strain levels. In this case, the deformation and texture evolution is attributed to mainly the basal slip activity (which results in grains to rotate towards a basal orientation, as described in section 2.1.4.1).

5.4.3 Summary

The microstructure and texture evolution with deformation strain for cast AZ80 alloy deformed at 400 °C, and strain rates of 0.001 s^{-1} and 0.1 s^{-1}, was studied. The main findings of the study are summarized in the following:

1) $Mg_{17}Al_{12}$ precipitate phase is not thermally stable in AZ80 alloy at 400 °C, and therefore dissolved into the Mg matrix during the deformation, aided by both, deformation and DRX. Mn-Al based precipitates are thermally stable, and remained more or less intact during the course of the deformation.
2) Concept of critical strain to mark the initiation of DRX in the material is found to be valid for cast AZ80 alloy, with regards to DRX through both, grain boundary bulging mechanism, as well as TDRX.
3) DRX and CDRX at both the strain rates resulted in considerable grain refinement from the as-cast state. The microstructure became reasonably homogeneous by a deformation strain of 1.0 at both the strain rates.
4) A DRX grain size of ~ 10 µm was determined for the cast AZ80 alloy deformed at 400 °C, 0.1 s^{-1}, and was found to be independent of the deformation strain

level. DRX% increased with the progress of deformation, but became saturated at around ~ 60%, by a strain of 0.4.

5) Deformation resulted in the development of a sharp basal texture at both the strain rates. At the higher strain rate, the texture development was rapid, and is attributed to the occurrence of $\{10\bar{1}2\} < 10\bar{1}1 >$ tensile twinning at low strains, while at the lower strain rate, the development was more gradual, and is attributed to deformation though mainly the basal slip.

5.5 Effect of $Mg_{17}Al_{12}$ precipitates on dynamic recrystallization in cast AZ80 alloy

The current section explores the role of $Mg_{17}Al_{12}$ precipitates on DRX in the cast AZ80 alloy. The as-cast material showed the presence of a substantial amount of $Mg_{17}Al_{12}$ precipitates, in both, the lamellar form of discontinuous precipitates (DP), and the lath form of continuous precipitates (CP). Based on the predictions from the equilibrium phase fraction map of the alloy (presented earlier in Figure 4-6), and some preliminary investigations on the microstructures of the samples deformed at 300 °C, 0.001 s^{-1}, it was determined that $Mg_{17}Al_{12}$ precipitates were present in the material for this deformation condition. The precipitates were also found to affect the microstructure evolution, including the DRX behaviour. This deformation condition was thereby chosen for more detailed analysis pertaining to the effect of DP and CP on the DRX behaviour of the alloy.

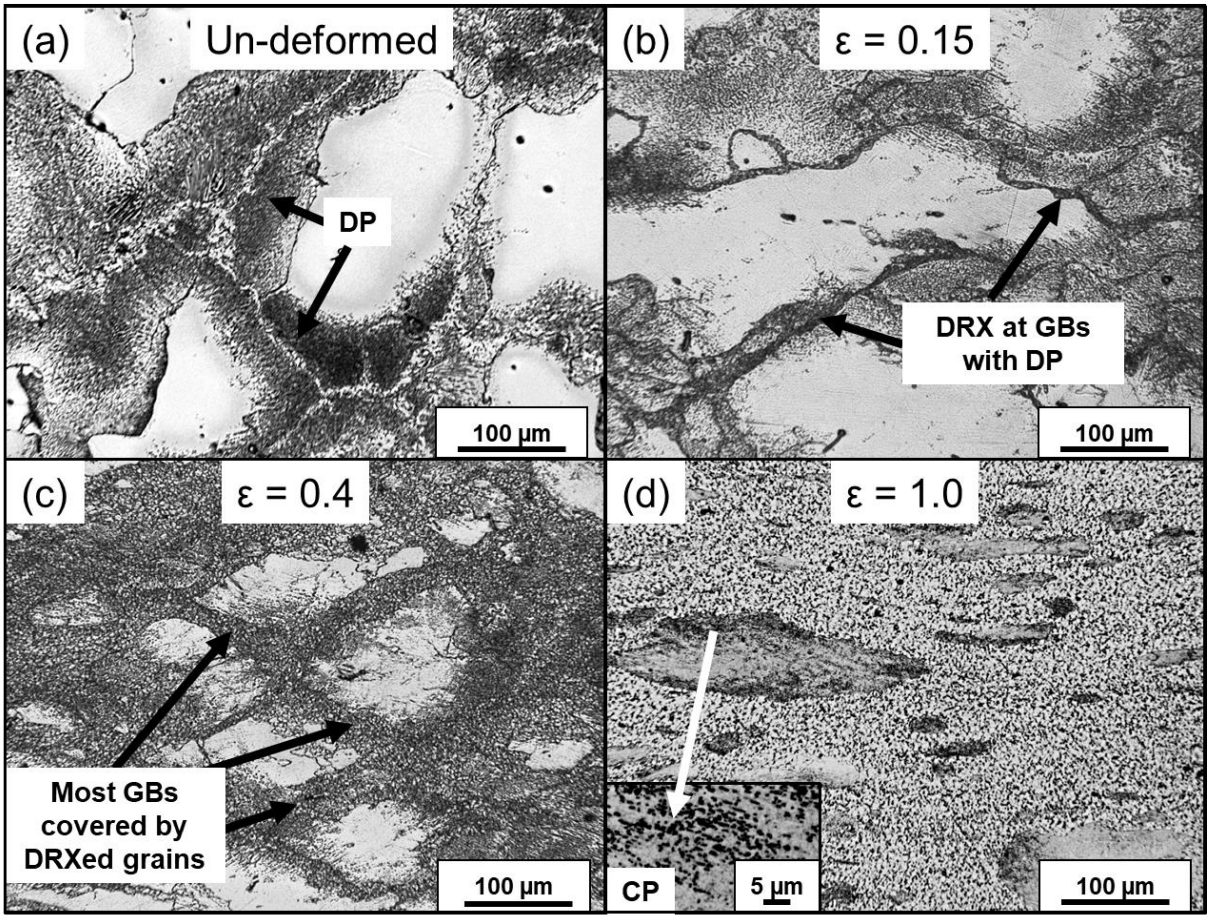

Figure 5-30 Evolution of microstructure with deformation strain at 300 °C, 0.001 s^{-1}: (a) as-cast material, and (b-d) shows micrographs of the samples deformed to strain levels of 0.15, 0.4 and 1.0, respectively.

How the DRX structure evolved and the microstructure changed with deformation at 300 °C, 0.001 s^{-1}, can be seen through the micrographs presented in Figure 5-30. Initially, the DRXed grains nucleated at the prior grain boundaries, and since the DRX grain size was much finer than the size of the starting grains, a necklace type of microstructure developed. With progressive deformation, the necklace structure broadened, progressively consuming more of the non-recrystallized regions of the prior grains. The role played by DP and CP in this is described below.

5.5.1 Role of lamellar discontinuous precipitates

As can be seen from Figure 5-30 (a), DP occupied most of the grain boundary regions in the as-cast material. Since DRX was also found to take place at the grain boundaries, it might appear that the two were related. Higher magnification micrographs, as presented in Figure 5-31, and reveal that DRX took place in both cases, when there were a substantial amount of DP present in the grain boundary region, as well as when the grain boundaries were relatively free of any precipitates.

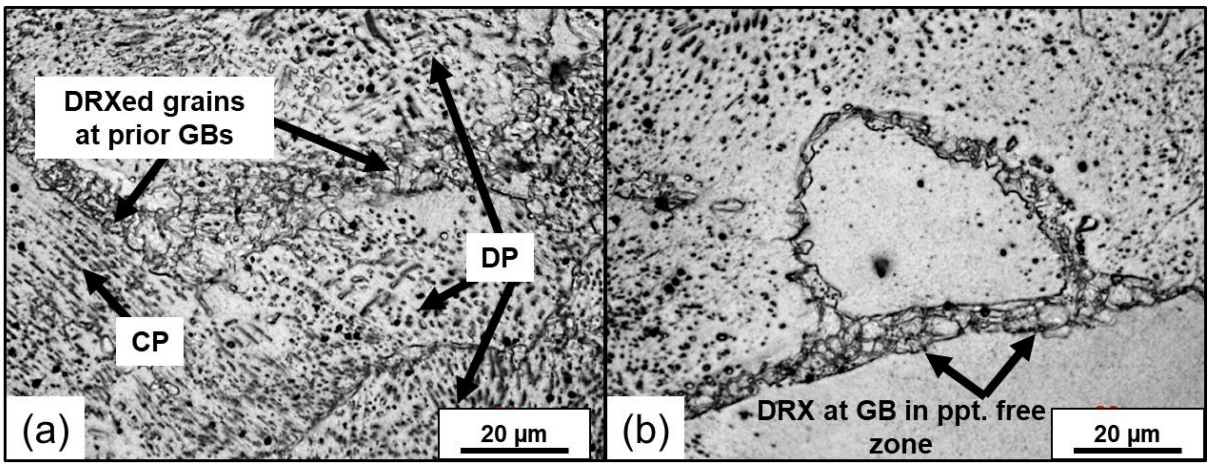

Figure 5-31 Micrographs of the cast AZ80 sample deformed at 300 °C, 0.001 s^{-1}, to a strain of 0.15, showing the occurrence of DRX at grain boundaries: (a) with, and (b) without precipitates. CP and DP in (a) refer to lath continuous precipitates, and lamellar discontinuous precipitates, respectively.

Occurrence of DRX in previously DP precipitated regions (as in Figure 5-31 (a)) suggest that DP might have promoted DRX, but considering that DRX also took place at grain boundaries independent of the presence of precipitates, it is difficult to say definitively that DP was the cause of DRX. Considering this, further evidence in support of the role of DP in promoting the DRX is desirable.

In this regards it is noted that previously Xu et al. have reported that increased DP content in a cast AZ91 alloy, as a result of pre-aging the material before hot compression tests, resulted in an increase in the DRX content from 17% to 64%, for deformation at 300 °C, 0.2 s^{-1} [24]. The role of DP in promoting the DRX is also theoretically justified considering that DP can be considered as a cluster of large particles (> 1 µm), which would promote DRX though the particle stimulated nucleation (PSN) mechanism described earlier (refer to sections 2.1.3 and 2.2.4.2). It is noted that PSN mechanism reportedly shears the $Mg_{17}Al_{12}$ precipitate particles into small fragments, which gets distributed at the boundaries of the newly DRXed grains [33], and the same observation was made in the present work as well (this is more evident in Figure 5-32 (b) and Figure 5-33). In fact, it was found that the content of DP in the material visibly decreased as the deformation progressed, with the result that for the sample deformed to the strain of 1.0, no DP precipitates were observed in the microstructure (Figure 5-30). A progressive shearing and fragmentation of DP in the material with deformation (and DRX) is a possible explanation for this. Further evidence in support of PSN at DP comes in the form of the texture results, which revealed that the DRXed grains showed a random texture (refer to Figure 5-12 in section 5.2.3), while it is noted that PSN causes texture randomization, including in AZ alloys [22, 23, 24]. It is noted that the grain boundary bulging mechanism can also potentially result in DRX texture randomization [21]. However, it was shown earlier that DRX through the grain boundary bulging mechanism actually preserved the deformation texture for the cast AZ80 alloy deformed at 400 °C, 0.001 s^{-1} (refer to section 5.2.3), and based on a prior work by Backx et al. on AZ31 alloy, this effect is expected to persist at lower temperatures [21]. As such, a random texture of the DRXed grains observed in the present work can be attributed to PSN alone, and the role of lamellar discontinuous precipitates in promoting the DRX via PSN can be inferred.

5.5.2 Role of lath continuous precipitates

Results showing the role of CP on the microstructure evolution are presented in Figure 5-32. It was observed that the DRX front advanced much more rapidly into the non-recrystallized regions at locations where relatively few or none of the CP precipitates were present ahead of the advancing DRX front. This is shown for the samples deformed to the strain of 0.15 and 1.0 in Figure 5-32 (a) and (b), respectively, and

suggests that the CP blocked the progress of the DRX front, possibly reducing the amount of DRX that could have taken place in the material if the CP were not present. Considering the submicron size and finely distributed nature of the CP particles [91, 92], their role in restraining the movement of DRX front is justified based on the Zener drag force, and the grain boundary pinning phenomena (refer to section 2.2.4.2, and equation 2.3).

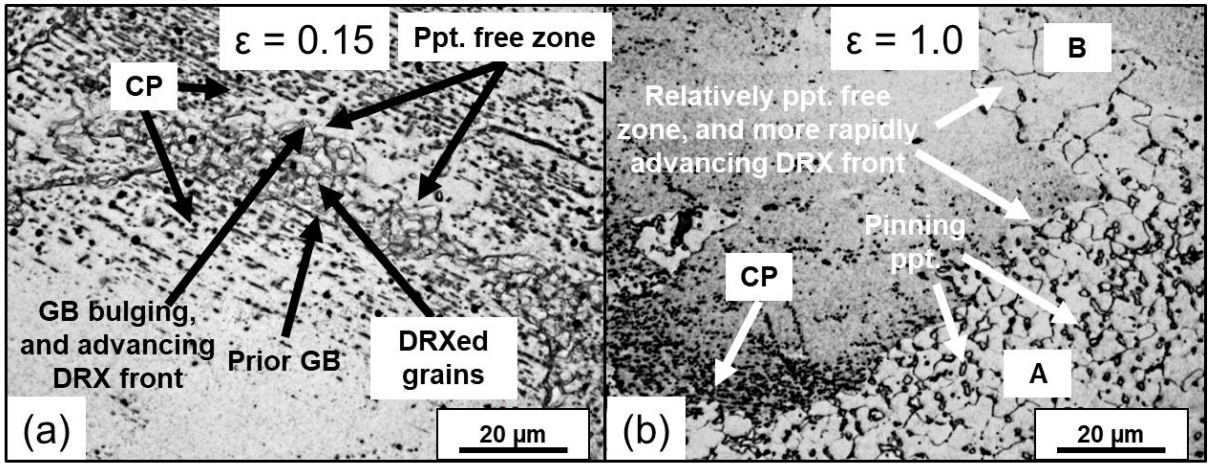

Figure 5-32 Role of CP on microstructure evolution. Both micrographs show that DRX front advanced relatively easily in the precipitate free areas, while faced resistance in propagation in regions where precipitate particles were present ahead of the moving front. (b) additionally shows particle pinning of the DRXed grains by fine $Mg_{17}Al_{12}$ precipitate particles, with more pinned DRXed grains, as in region A, being much finer, compared to the DRXed grains in the less pinned regions, as in B.

5.5.3 Precipitates pinning the boundaries of the DRXed grains

Besides pinning of the advancing DRX front by the CP particles, it was also observed that fine particles of $Mg_{17}Al_{12}$ pinned the boundaries of the DRXed grains, thereby restricting their growth, and promoting grain refinement. This is evident from Figure 5-32 (b), whereby some regions with more and less pinned DRXed grains are marked. It can be seen that the pinned grains were much finer compared to the less pinned grains. Previously Xu et al. have suggested that these fine precipitate particles gets generated from the lamellar precipitates due to their shearing as a result of deformation [33]. Since DRX takes place preferentially at the lamellar particles (via PSN), the generated fine particles get distributed at the boundaries of the newly DRXed grains, thereby pinning them. The size and morphology of these precipitates in the current work can be visualized more clearly in Figure 5-33.

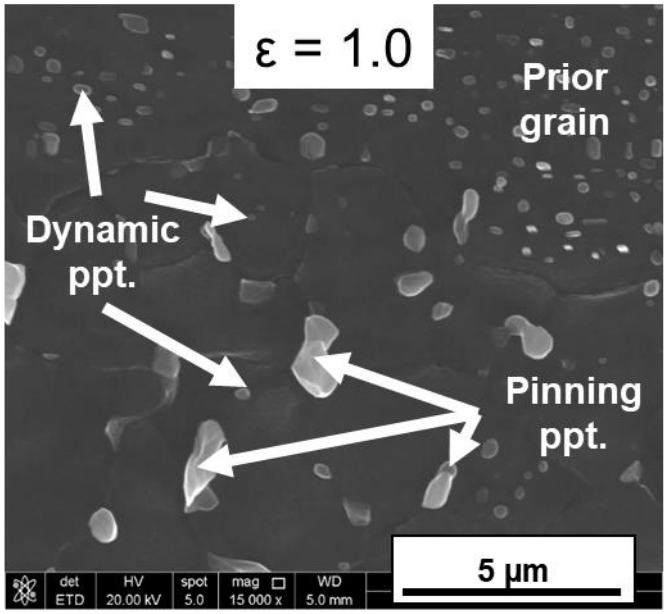

Figure 5-33 Pinning of boundaries of DRXed grains by fine $Mg_{17}Al_{12}$ precipitate particles. Also is shown dynamic precipitation of $Mg_{17}Al_{12}$ particles within prior grains and DRXed grains.

There is another way in which the pinning particles could have generated, and is related to the dynamic precipitation of $Mg_{17}Al_{12}$ precipitates as fine globular particles during the deformation itself (refer to section 2.2.4.1) [85, 97]. Dynamic precipitation is aided by an increased defect density (dislocations, voids, etc.) in the material generated due to deformation, which aids in diffusion. Figure 5-33 shows evidence of dynamic precipitation of $Mg_{17}Al_{12}$ particles in the present material during hot deformation (these particles were not present in the as-cast material, as can be seen from the corresponding micrographs presented in Figure 4-5 in section 4.1.2), in the form of small regularly shaped particles, within both, the prior grains, as well as the DRXed grains. Additionally, it is very likely that dynamic precipitation also took place at the grain boundaries of the DRXed grains, since boundaries are a preferred site for precipitation, and thereby would have acted as the pinning precipitates.

5.5.4 Summary

The role of various morphologies of the $Mg_{17}Al_{12}$ precipitates present in the as-cast material on the DRX and microstructure evolution during hot deformation at 300 °C, 0.001 s^{-1} was investigated. The main findings of the study are summarized in the following:

1) The results validate the findings of Xu et al. on cast AZ91 alloy [24], which showed that the DP promoted DRX and texture randomization via PSN during hot compression at 300 C, 0.2 s^{-1}.
2) PSN resulted in shearing/crushing of the DP particles, which got distributed at the boundaries of the newly DRXed grains, pinning them from growth, and thereby promoting further grain refinement.
3) The results indicate that the CP blocked the progress of the DRX front into non-recrystallized regions of the prior grains, possibly reducing the extent to which DRX took place in the material.
4) It was shown that dynamic precipitation took place in the material during the deformation at 300 °C.

5.6 Effect of processing history of the starting material (cast vs extruded)

This section studies and compares the effect of hot deformation on the microstructure and texture evolution when starting with two very different states of AZ80 (as-cast and as-extruded material). The hot deformation behavior of these two starting materials is compared at 400 °C at two strain rates: 0.001 s^{-1}, and 0.1 s^{-1}. The extruded material was deformed along the prior extrusion direction for this study. The results pertaining to the microstructure and texture evolution for the starting cast material were already presented in section 5.4, and are therefore not repeated here, except for some specific data.

5.6.1 Flow stress curves

The flow stress curves, critical strain values, and work hardening rate plots, of the cast and extruded samples, deformed at 400 °C in the strain rate range of 0.001 s^{-1} to 0.1 s^{-1}, are presented in Figure 5-34. Considering the flow stress data presented in Figure 5-34 (a), it can be seen that at low strain levels the cast material typically showed higher flow stress values compared to the extruded material, and is consistent with what has been reported previously in a study comparing cast and extruded AZ31 alloys in hot compression, and is attributed to a higher DRX fraction in the extruded-deformed material which promotes strain softening [67]. At higher strain levels, the flow stress curves for the cast and extruded materials converged, indicating that the flow stress values became independent of the processing history (cast/extruded) of the starting material, and is attributed to development of similar grain sizes in the two starting materials with progress of deformation (corresponding results are presented later in this section) [131].

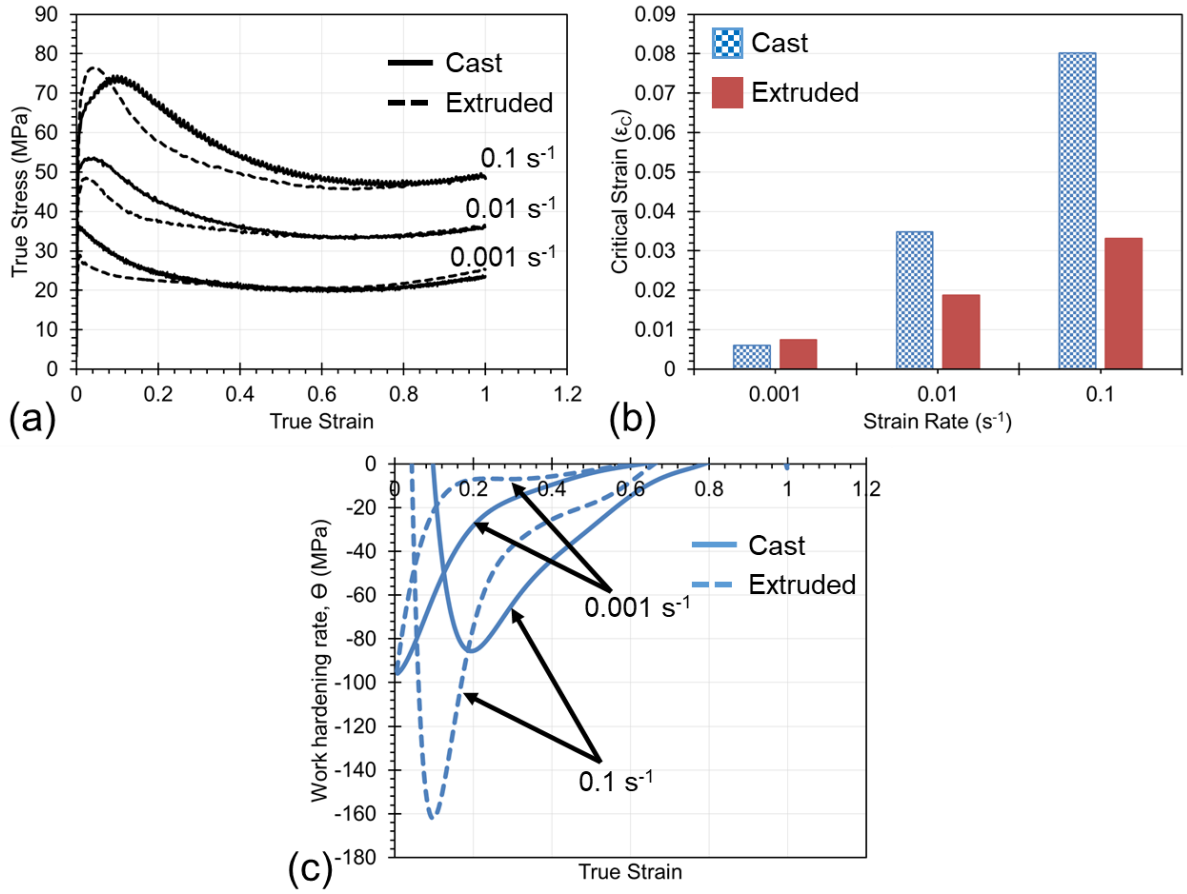

Figure 5-34 Cast AZ80 and extruded AZ80 samples deformed at 400 °C at various strain rates: (a) flow stress curves, (b) critical strain values, and (c) work hardening rate plots.

The plots in Figure 5-34 (b) and (c) suggest that the extruded material shows an earlier onset of the DRX (based on the lower ε_C values), and a faster DRX kinetics (based on the more pronounced work softening rates), compared to the cast material. These predictions are found to be consistent with the corresponding results reported in literature on the AZ31 alloy, and are validated for the current starting materials in later text.

5.6.2 Microstructure evolution

The extruded material showed the occurrence of both, DRX (though grain boundary bulging mechanism), and CDRX (via kink band formation, and development of low angle boundaries), under all the investigated deformation conditions, similar to that observed in the cast material deformed under similar deformation conditions (refer to sections 5.2.2 and 5.3.2). Figure 5-35 illustrates this for the extruded material deformed at 400 °C, 0.1 s^{-1} to a strain of 0.15.

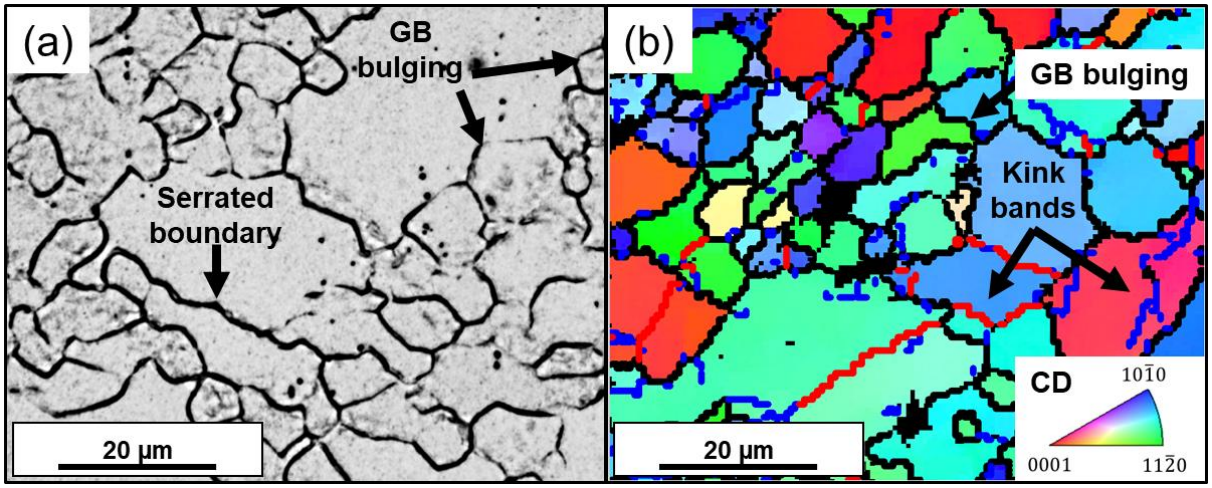

Figure 5-35 Extruded AZ80 sample deformed at 400 °C, 0.1 s^{-1} to a strain of 0.15: (a) evidence of DRX through the grain boundary bulging mechanism, and (b) evidence of CDRX through kink band formation and grain fragmentation. (a) and (b) are not from the same location on the sample. Compression direction in the micrographs is vertical. Blue lines and red lines in (b) mark the low angle boundaries, with misorientations in range of 2-5° degrees, and 5-10°, respectively, while black lines mark the grain boundaries.

The microstructure evolution in the extruded material with deformation strain at the two strain rates is presented through the micrographs in Figure 5-36. As in the cast material, deformation at the higher strain rate (0.1 s^{-1}) resulted in the development of a bimodal grain structure. The microstructure progressively got refined as the strain increased, and eventually by a strain of 1.0, a reasonably homogeneous and fine-grained microstructure was developed. There was no evidence of twinning in the extruded material, even in the samples deformed to low strain levels (ε = 0.15 and 0.4). At the lower strain rate, unlike in the corresponding cast-deformed samples, there was no appreciable change in the microstructure with progressive deformation. The microstructure remained more or less homogenous throughout the deformation process at this strain rate.

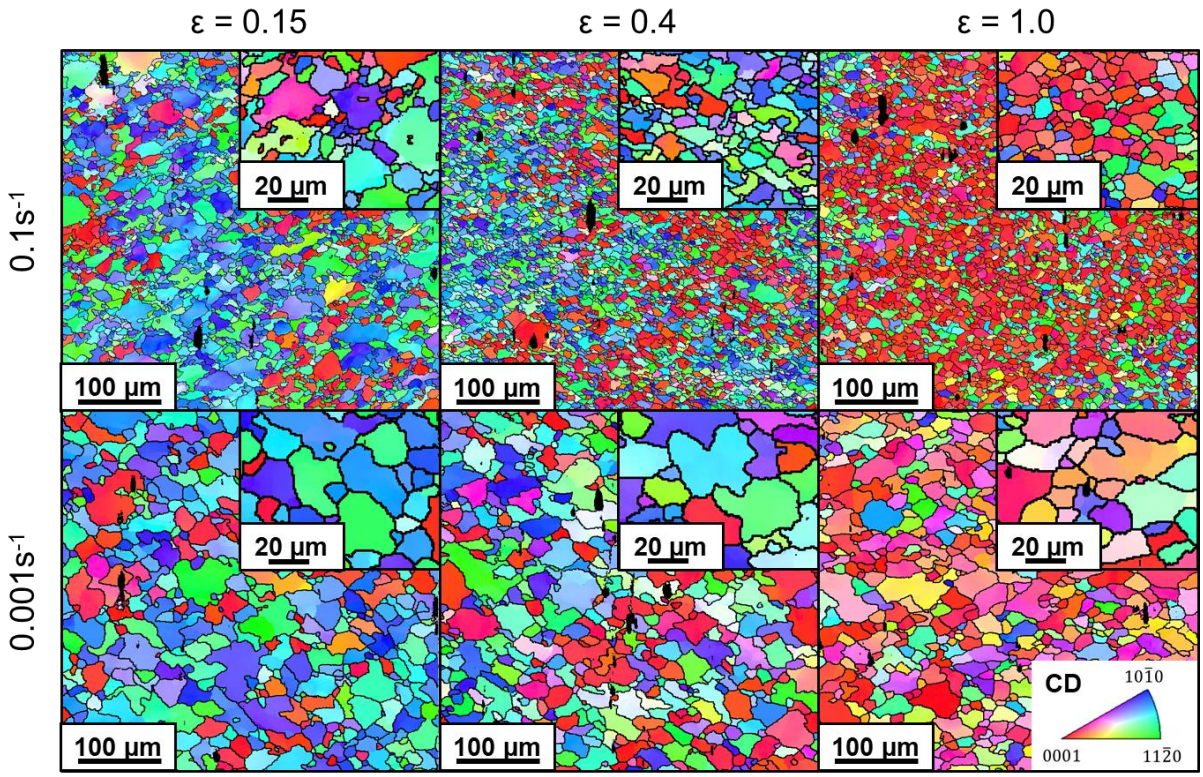

Figure 5-36 Microstructure evolution in the extruded samples during hot compression at 400 °C at the two strain rates. The images in the inset show the corresponding high magnification micrographs. Compression direction is vertical.

The microstructure analysis results are presented in Figure 5-37 and Figure 5-38. Figure 5-37 shows the evolution of the overall grain size for the cast and extruded samples with deformation strain at the two strain rates. It can be seen that at the lower strain rate (0.001 s^{-1}), the overall grain size in the extruded material did not change appreciably, unlike that in the corresponding cast-deformed samples, which showed substantial grain refinement with an increase in the deformation strain. For deformation at the higher strain rate, the extruded material also showed grain refinement with progressive deformation. The grain size beyond the strain of 0.4 at either strain rates was relatively stable for the extruded deformed samples. Another interesting observation is that at the final strain of 1.0 (which based on Figure 5-34 (c) is a higher strain level than the steady-state strain in all cases), the grain size in the cast and extruded samples was comparable.

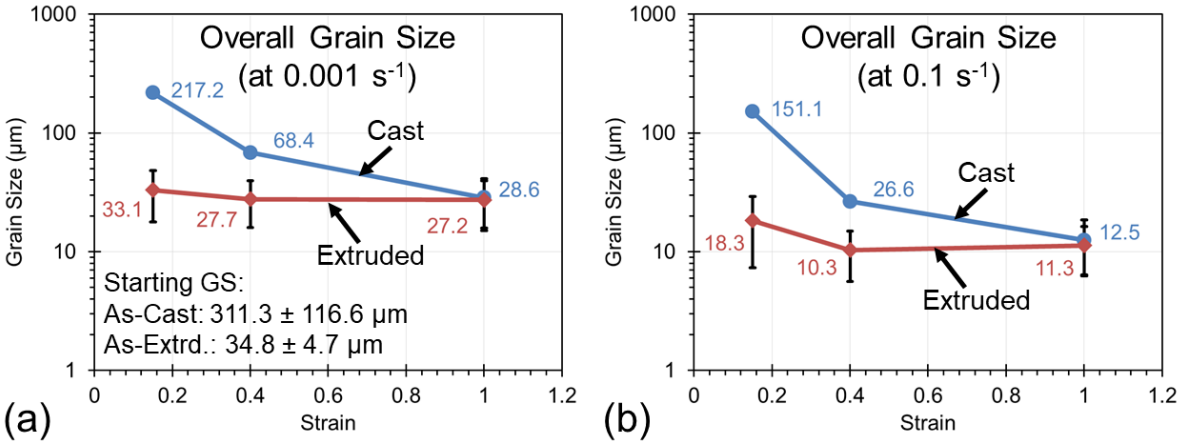

Figure 5-37 Overall grain size values in the cast and extruded AZ80 samples for deformation at: (a) 0.001 s^{-1}, and (b) 0.1 s^{-1}. EBSD data was used to determine the grain sizes in the deformed samples, while for the as-received (undeformed material), grain size values were determined using the optical micrographs.

The DRX data for the two sets of the starting samples, for deformation at the strain rate of 0.1 s^{-1}, are presented in Figure 5-38, and are based on the EBSD data. It is noted that the data pertaining to the extruded material is offset by a strain of + 0.05 (i.e. along the positive x-axis) in order to facilitate clearer visualization. In order to identify the DRXed grains, the same criteria as defined in section 5.4.1 for the strain wise evolution of the microstructure of the cast material (viz. GOS ≤ 2° and grain size ≤ 20 µm) was found to be appropriate for the extruded material as well (refer to Appendix C), and used. As in section 5.4.1, the relevant criteria for deformation at 0.001 s^{-1} could not be defined, and therefore the results at only 0.1 s^{-1} are presented in Figure 5-38. The DRX grain size was found to be independent of the deformation strain level, and interestingly was found to be comparable to that of the cast deformed samples. Since the starting cast material showed a much larger initial grain size than the starting extruded material, this conclusively shows that the DRX grain size is not a function of the starting grain size for the AZ80 alloy. Considering Figure 5-38 (b), the DRX% increased with deformation strain in both cases, while for strains beyond 0.4, the DRX% achieved a steady-state for both cast and extruded deformed samples, indicating that DRX would have likely not reached 100% even if the material was deformed to even higher strain levels. The extruded material showed higher DRX% than the cast material at all the tested strain levels. It is noted that the DRX% values presented in Figure 5-38 (b) were based on single EBSD measurement per sample, and thereby variations in the specific values can be expected with the measurement

location on the sample surface. However, the results were found to be broadly consistent with those reported earlier by Beer et al. on cast and extruded AZ31 alloys [67], and therefore are expected to reflect the general trends in DRX% when comparing the hot deformation behaviour of cast and extruded forms of the same alloy. As in this previous study, a higher DRX% in case of the extruded material is attributed to its finer grain size, which would have provided more sites (grain boundary area per unit material's volume) for the DRXed grains to nucleate on.

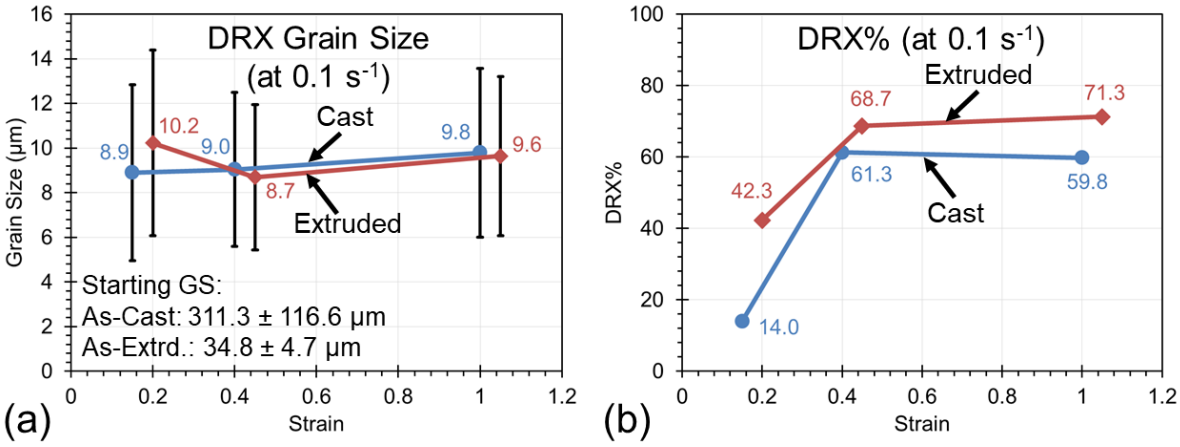

Figure 5-38 (a) DRX grain size, and (b) DRX%, for the cast and extruded AZ80 samples deformed at 400 °C, 0.1 s^{-1} to various strain levels. EBSD data was used to quantify the DRX grain size and fraction, using a GOS value of ≤ 2° and a grain size value of ≤ 20 μm to identify the DRXed grains. The data pertaining to the extruded material is offset by a strain of + 0.05 (i.e. along the positive x-axis) in order to facilitate visualization.

A noteworthy difference between the microstructures of the cast and extruded deformed samples can be observed when looking at the micrographs near the free side surface of the compressed samples. This is shown in Figure 5-39. The extruded-deformed samples showed a much smoother surface, and a more homogenous microstructure, compared to the corresponding cast-deformed samples, at all the investigated strain rates. Of special interest is the extruded sample deformed at 1 s^{-1}, which did not show any fracture cracks, unlike the corresponding cast-deformed sample. Since one of the important parameters defining a good forgeability is the ability to be forged at high strain rates, crack-free, the observations from Figure 5-39 strongly suggest the superiority of the extruded material over the cast material for forging applications. More homogenous deformation behaviour of the extruded material is attributed to its finer initial grain size, which promotes non-basal slip (refer

to section 2.2.1), and thereby makes the activation of non-homogenous deformation modes, like twinning and shear banding, less likely. As pointed out in section 5.3.2, another possible reason for crack initiation in the cast material during deformation at high temperatures and high strain rates is related to local melting of the eutectic $Mg_{17}Al_{12}$ phase present in the as-cast material, while the as-extruded material, owing to being fully recrystallized (as a result of the prior extrusion processing), is free of such low melting phase.

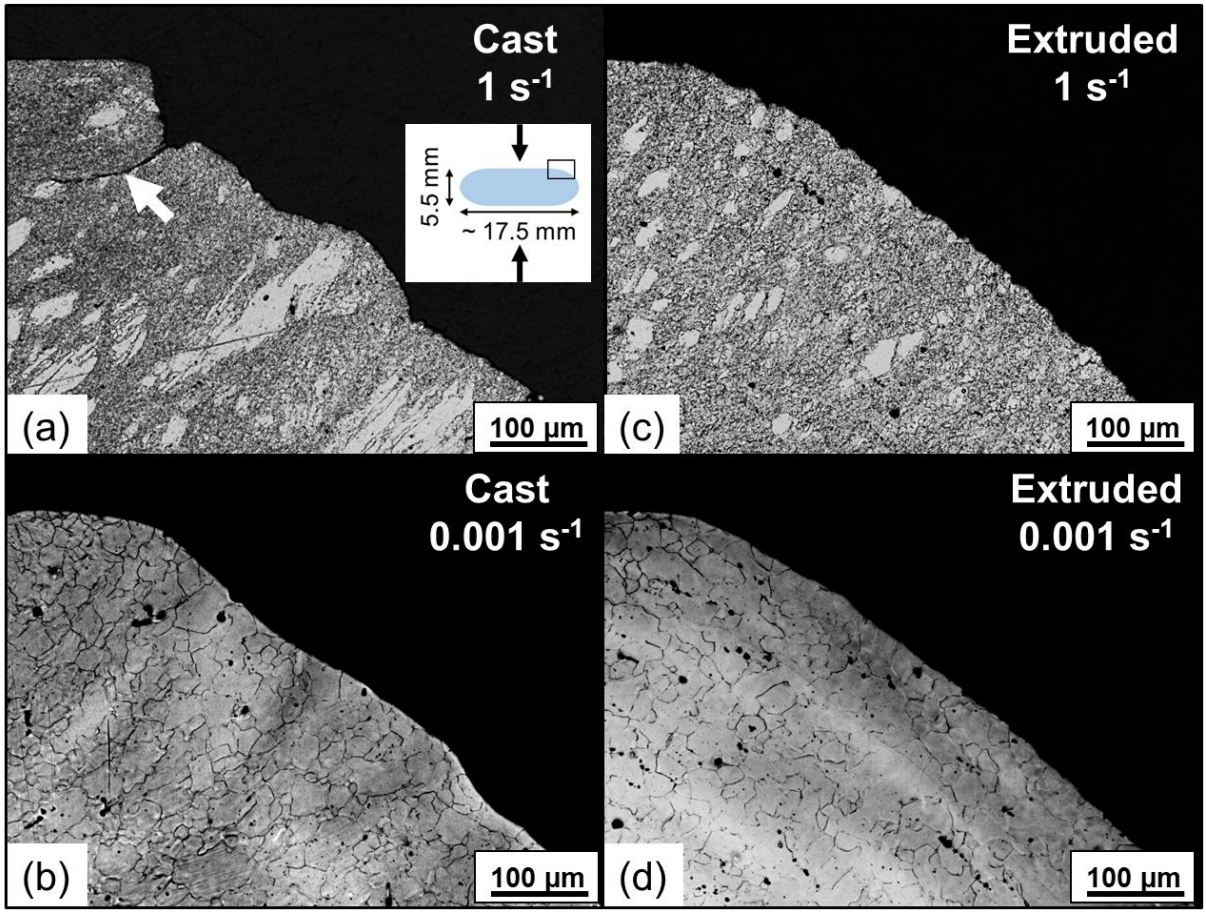

Figure 5-39 Microstructural and surface features of the cast and extruded samples deformed at 400 °C and different strain rates to a strain of 1.0. The white arrow in (a) marks a fracture crack. The inset image in (a) shows the approximate location on the deformed and sectioned samples where the micrographs were taken from. The vertical arrows in the inset image represent the compression direction.

5.6.3 Texture evolution

The texture evolution results for the extruded material are presented in Figure 5-40. For ease in the interpretation of the results, the texture of the as-extruded sample is also provided, and is divided into components A, B and C, as was done in case of the

as-cast material in section 5.4.2. It is noted that the SF values simply depend on the relative orientation of the slip planes and directions with respect to the loading direction [130]. As such, the extruded material showed comparable SF values for components A-C, as the cast material, and the corresponding data can therefore be directly referred from Figure 5-29 (section 5.4.2). Considering the SF and CRSS values, and the texture of the starting extruded material, it is evident that the majority of the grains in the starting material were oriented along the component A, which was favorable for the occurrence of prismatic slip and tensile twinning. Also, there were many grains oriented along the component C, which was favorable for the occurrence of Py2 slip.

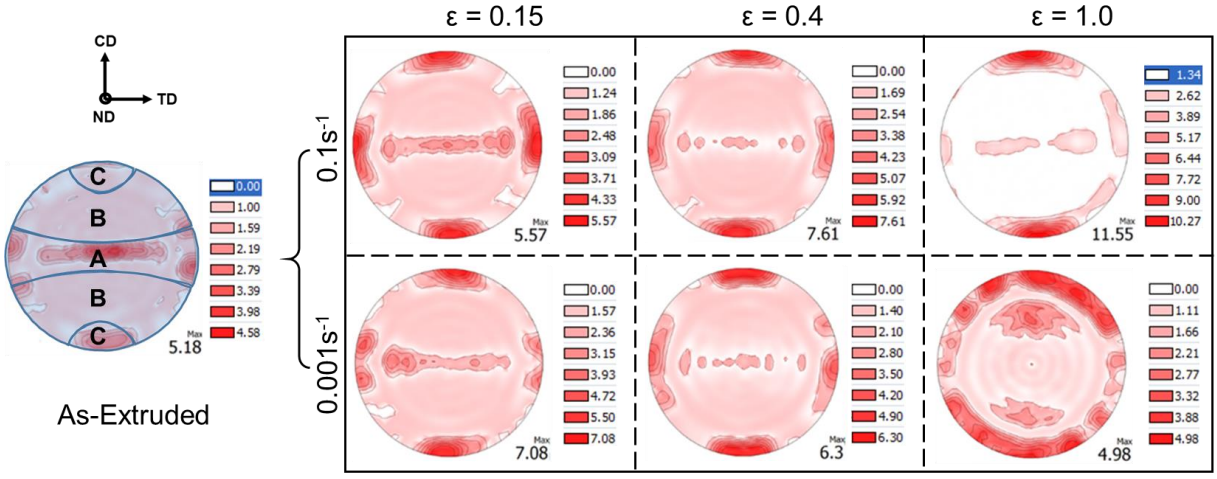

Figure 5-40 XRD macrotexture evolution in the extruded AZ80 samples for deformation at 400 °C. The texture of the as-extruded material is divided into three components for ease in the interpretation of the results - A: grains oriented with their basal poles inclined 70-90° to the CD, B: grains oriented 20-70° to the CD, and C grains oriented 0-20° to the CD. The unit of texture intensity is "Multiples of Random Distribution (MRD)". Orientation legend: CD – Compression direction, ND – Normal direction, TD – Transverse direction.

Considering the deformation of the extruded material at 0.1 s^{-1}, there was no evidence of twinning in the material, and is attributed to a relatively low grain size of the starting extruded material (which promotes non-basal slip activity, as described in section 2.2.1). The grains oriented along A thereby mainly deformed through the prismatic slip, which causes rotation of the grains about the c-axis, and also through the basal slip (owing to it much lower CRSS, despite having a relatively low SF), which causes rotation of the c-axis of the grains towards the compression direction (refer to section 2.1.4.1). The observations that component A of the starting texture were preserved to a reasonable extent during deformation even to high strain levels is a strong evidence

that prismatic slip took place for grains oriented initially along A, while the gradual sharpening of the basal texture along the compression direction (i.e. component C) provides a strong evidence that basal slip was also active, which rotated the grains initially oriented along the components A, and B, towards the component C. Since twinning did not take place, the texture evolution was much more gradual for the extruded material, compared to the cast material deformed under the same deformation conditions.

For deformation at the lower strain rate (0.001 s^{-1}), the A component was weakened during the deformation, while the C component did not strengthen. Instead, the texture became relatively diffuse, and the overall texture intensity also fell, as the deformation progressed. This indicates texture got randomized during the deformation. In order to investigate if DRX played any role in this, the texture of the DRXed and non-DRXed grains were analysed. The corresponding results are presented in Figure 5-41, which also includes the corresponding results for the extruded sample deformed at the strain rate of 0.1 s^{-1}. It is noted that in order to have a consistent criteria to determine the DRXed grains at either of the strain rates, and have it consistent with the results for the corresponding cast deformed samples (presented in section 5.3.3), a GOS ≤ 2° was used in each case (i.e. no additional upper limit to the DRX grain size was imposed, unlike what was done for the graphs presented in Figure 5-38 previously). Considering the material had already undergone a substantial amount of deformation (i.e. a strain of 1.0), the GOS criteria is deemed sufficient to distinguish between the DRXed and non-DRXed grains.

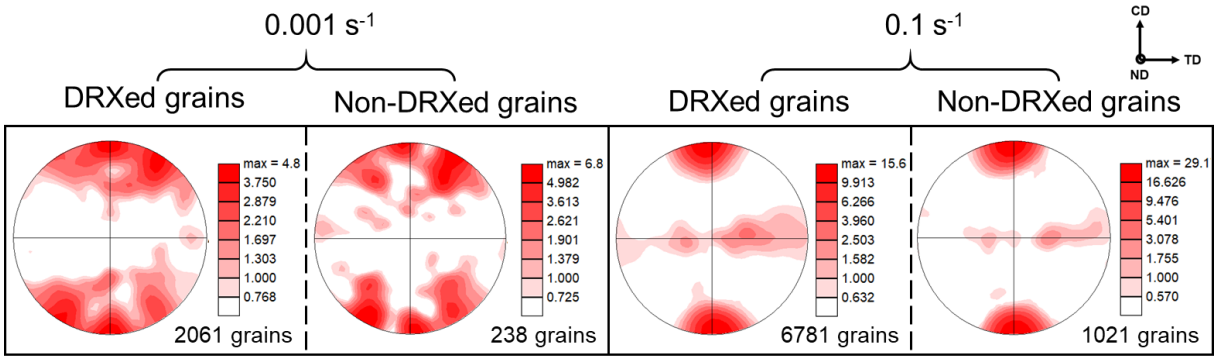

Figure 5-41 Texture of DRXed and non-DRXed grains in the extruded AZ80 samples deformed to a strain of 1.0 at 0.001 s^{-1} and 0.1 s^{-1}, calculated using the EBSD data, and a GOS ≤ 2° filter to identify the DRXed grains. The number of grains in each subset are also provided. The unit of texture intensity is "Multiples of Random Distribution (MRD)". Orientation legend: CD – Compression direction, ND – Normal direction, TD – Transverse direction.

For deformation at 0.1 s^{-1}, both the DRXed and non-DRXed grains showed a sharp basal texture, indicating that the DRXed grains preserved the deformation texture. On the other hand, for deformation at 0.001 s^{-1}, both DRXed and non-DRXed grains showed a very weak and diffuse texture. It is not clear from the present work what caused the texture randomization, however, it is proposed to have taken place through either or both of the following mechanisms:

1) DRX could have resulted in texture randomization for the extruded material for this deformation condition only. This would be supported by findings of Backx et al. on extruded AZ31 alloy, which showed that the texture randomization effect is more pronounced at lower strain rates [21].

2) Deformation at this strain rate could have resulted in a relatively slow rotation of the grains from the initial texture, and as a result, the weak texture at the strain of 1.0 might simply be a snapshot of the texture of the material which was still in transition towards a sharp basal texture. The potential role played by prismatic slip for the grains oriented along the component A in the starting material (roughly ~ 80% of the grains in the starting material were oriented as such, based on EBSD data analysis) is of special interest in this regards, since it would have prevented the grain rotation towards a sharp basal texture.

Since texture randomization is desirable for an enhanced forgeability of the material, it is of interest to investigate the above phenomenon in more detail.

It is noted that the cast material showed development of a sharp basal texture at both the strain rates, as the results in sections 5.3.3 and 5.4.2 indicated. The texture evolution in case of the non-DRXed grains was attributed to the activity of basal slip and/or $\{10\bar{1}2\} < 10\bar{1}1 >$ tensile twinning in the material during deformation, while in case of the DRXed grains, it was attributed to them preserving the deformation texture.

5.6.4 Summary

The hot deformation behaviour of the cast and extruded AZ80 alloys at 400 °C and strain rates of 0.001 s^{-1} and 0.1 s^{-1} was compared. The main findings of the study are summarized in the following:

1) The flow stress values at higher strain levels became independent of the processing history of the starting material. This was attributed to a similarity in DRX and overall grain sizes in the two starting materials at higher strain levels.
2) The extruded material showed an earlier onset of DRX, and a faster DRX kinetics, compared to the cast alloy, and also showed consistently higher DRX% at all the investigated strain levels. These observations were attributed to a finer grain size of the starting extruded material, which provides more nucleation sites for the DRXed grains.
3) The DRX grain size was found to be independent of the nature of the starting material. Since the grain size in the starting cast and extruded materials was very different, this also indicates that the starting grain size does not affect the DRX grain size for the AZ80 alloy.
4) The extruded material deformed much more homogeneously than the cast material, and did not show any presence of fracture cracks even at the highest tested strain rate of 1 s^{-1}, indicating the superiority of the extruded material over the cast material as the raw material for forging applications.
5) Extruded material showed texture randomization during deformation at 0.001 s^{-1}, with both DRXed and non-DRXed grains showing a random texture. The effect was not fully understood, however a few likely mechanisms were proposed for the same. In case of the cast material, a sharp basal texture developed with deformation at both the strain rates, as a result of the predominance of basal slip and/or $\{10\bar{1}2\} < 10\bar{1}1 >$ tensile twinning, while the DRXed grains were found to preserve the deformation texture.

5.7 Effect of texture of the starting material

This section compares the effect of texture of the starting material on the hot deformation behaviour of extruded AZ80 alloy, at 400 °C, and in the strain rate range of 0.001 – 0.1 s^{-1}. As shown earlier, the as-received extruded material showed a strong texture, with the basal poles of the grains mainly aligned perpendicular to the extrusion axis. This strong texture allowed us to study how the starting texture affected the hot deformation behaviour of the alloy by testing it in uniaxial compression with samples that were taken along and perpendicular to the extrusion axis. The samples from these two orientations are referred to as ED (for extrusion direction) and RD (for radial direction) samples in the subsequent text. Figure 5-42 (a) shows a schematic illustrating the orientation of the compression test samples with respect to the as-received extruded AZ80 rod, and Figure 5-42 (b) shows the texture of the starting material. The as-extruded material showed a fully recrystallized microstructure.

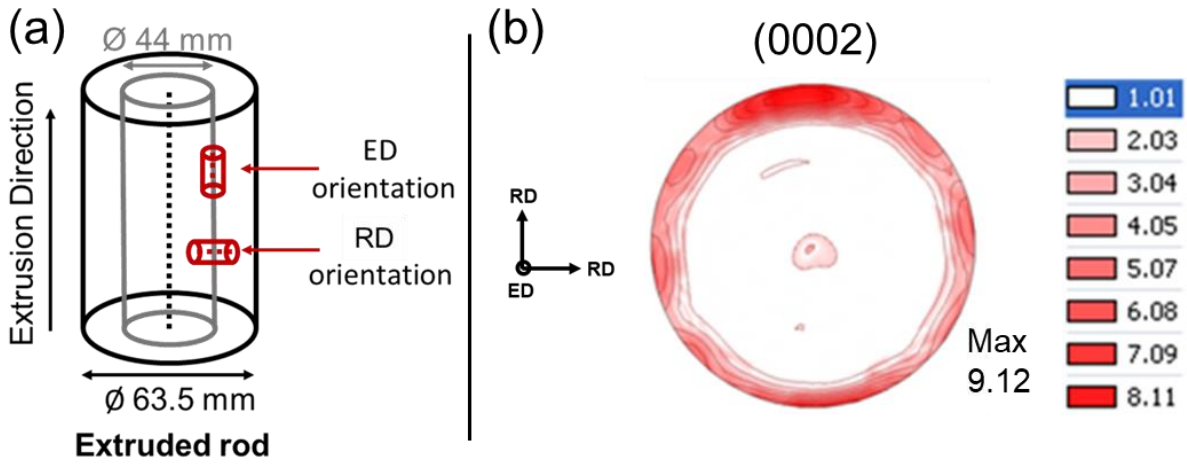

Figure 5-42 (a) Orientation of the ED and RD sets of samples with respect to the as-received extruded rod, (b) texture of the as-received material in terms of the (0002) *pole figure.*

5.7.1 Flow stress curves

The flow stress curves, critical strain values, and work hardening rate plots of the ED and RD samples are presented in Figure 5-43. Considering the flow stress curves, it can be seen that during the initial phase of the deformation, the ED samples showed slightly higher flow stress values compared to the RD samples, while the flow curves for the two sets of the samples converged at higher strain levels. The behaviour is consistent with what is previously reported for an extruded AZ31 alloy rod [132]. The

critical strain values and the work softening following the peak stress were comparable for the two starting materials, indicating comparable DRX behaviour.

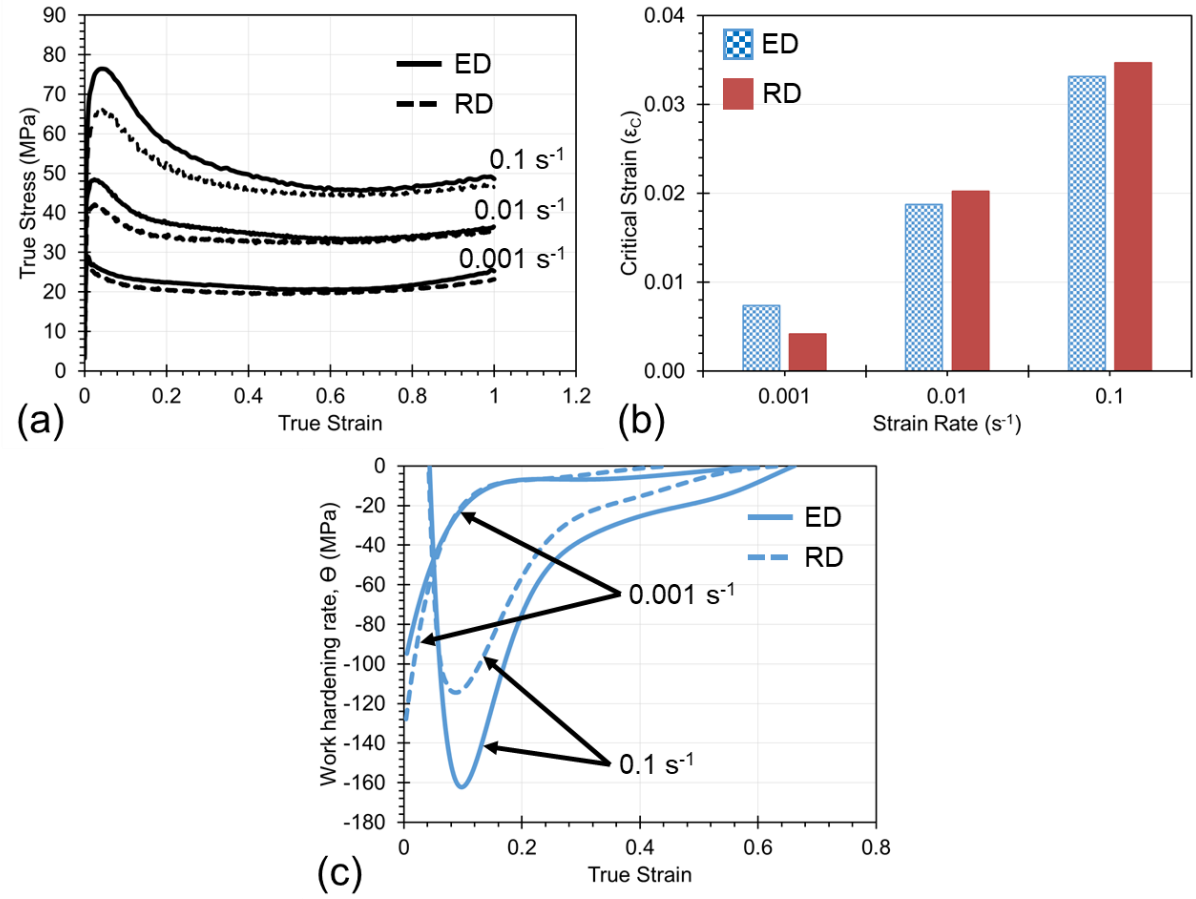

Figure 5-43 ED and RD samples compressed at 400 °C, at strain rates in the range of 0.001 s^{-1} - 0.1 s^{-1}: (a) Flow stress curves, (b) critical strain values, (c) work hardening rate plots.

5.7.2 Microstructure evolution

During hot compression, both the RD and ED samples showed DRX through the grain boundary bulging mechanism. Additionally, in both cases, CDRX was found to be active, as a grain refinement and recovery mechanism. Relevant micrographs indicating DRX and CDRX in the ED samples were presented in section 5.6.2, and since the RD samples showed comparable results, the same have not been reproduced here.

The microstructure evolution results for the two sets of samples with deformation strain are presented in Figure 5-44. The micrographs indicate that the microstructure evolution was comparable for the two sets of the samples, at both the strain rates. At 0.1 s^{-1}, a bimodal structure developed during deformation to low strain levels, which

got progressively converted to a homogenous fine-grained structure at higher strain levels. At 0.001 s^{-1}, there was no noticeable change in the microstructure of the samples as the deformation progressed.

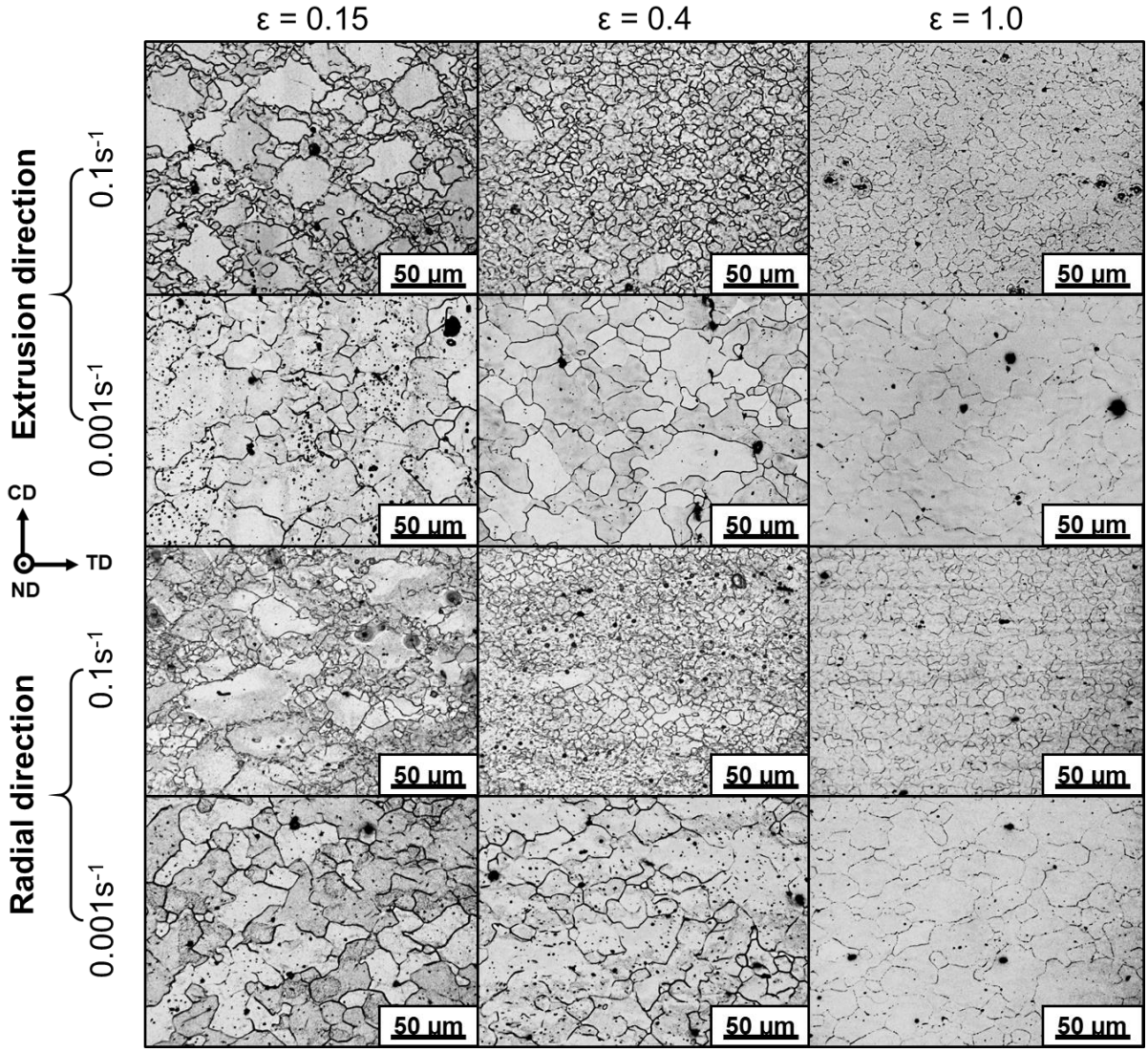

Figure 5-44 Microstructure evolution in the ED and RD samples during deformation at 400 °C, at the two strain rates.

Using EBSD data, the microstructures were quantified in terms of grain size distributions and DRX grain size.

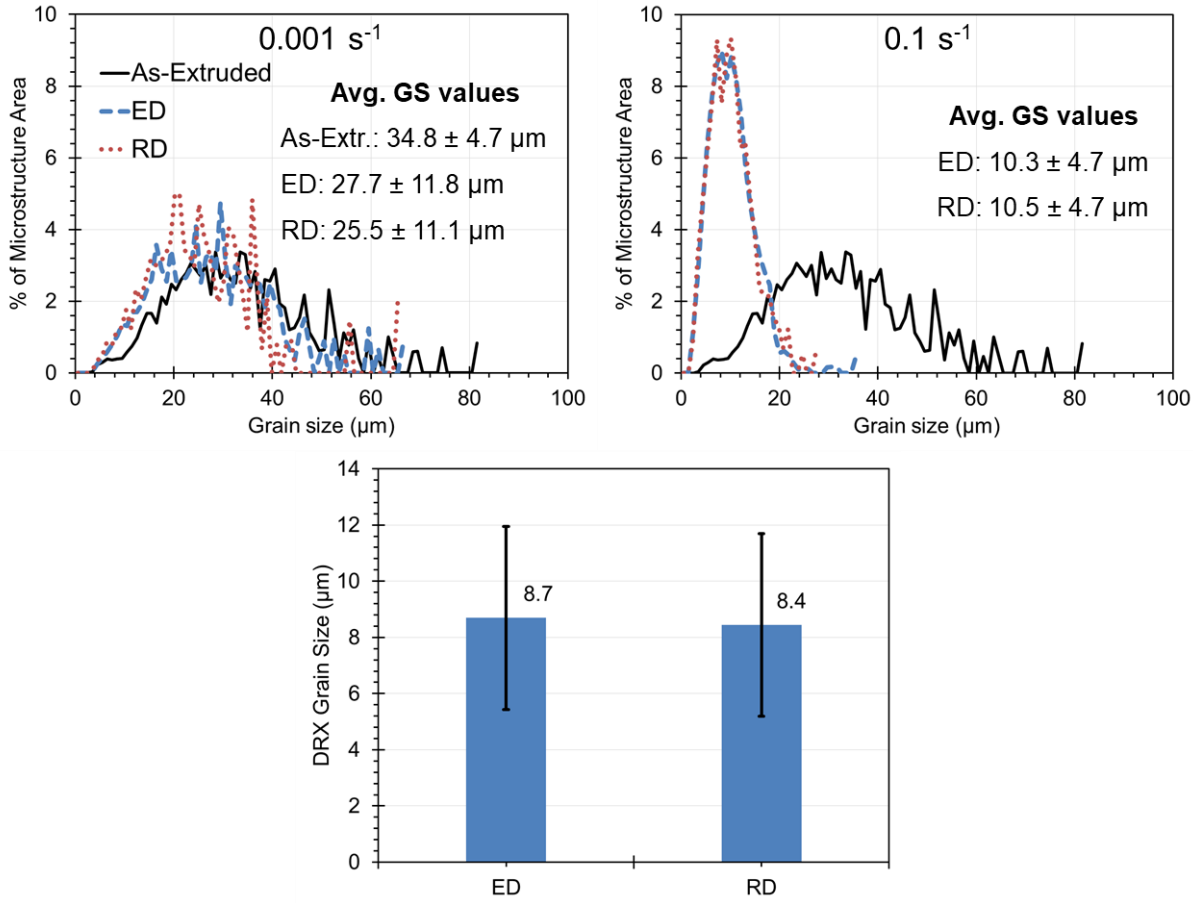

Figure 5-45 Grain size distributions in the ED and RD samples deformed at 400 °C to a strain of 0.4 at (a) 0.001 s^{-1}, and (b) 0.1 s^{-1}. (c) shows the DRX grain size values at 400 °C, 0.1 s^{-1}. EBSD data was used to develop the above plots, except for the average grain size value in the as-extruded material, which was determined using the optical micrographs.

Figure 5-45 (a) and (b) shows the grain size distribution for all the grains in the scanned area for the deformed ED and RD samples. Additionally, the grain size distribution of the as-extruded material is also provided for comparison. At either of the strain rates, the grain size distribution in ED and RD samples was comparable, strongly indicating that the microstructure evolution was independent of the starting texture. This is further validated by the similar DRX grain size values in the two cases, as shown in Figure 5-45 (c) (DRXed grains were identified using the EBSD data, by imposing a limit of GOS ≤ 2° and a grain size ≤ 20 µm, similar to what was done in sections 5.4.1 and 5.6.2 for cast and ED samples, compressed at 400 °C, 0.1 s^{-1}, respectively). The results are consistent with those reported earlier on an extruded AZ31 alloy [20]. However, it is noted that a study on an extruded ZK60 alloy showed that deformation of the material at 45° to the prior extrusion axis resulted in a lower DRX grain size and fraction compared to that for deformation along and perpendicular to the prior

extrusion axis, which the authors attributed to an ease in the occurrence of basal slip in the samples oriented at 45°, which restricted multiple slip activity in the material, and thereby the conditions for the occurrence of DRX were not as conducive [76]. Considering this latter study, it is desirable to test the deformation behaviour of the material in this orientation as well, so that a definitive statement on the role of starting texture on the DRX behaviour of the AZ80 alloy can be made.

5.7.3 Texture evolution

The texture results are presented in Figure 5-46. Results show that the texture evolution was very different for the two sets of samples. The interpretation of the results of the ED samples was provided in section 5.6.3, and is not repeated here. Considering the texture evolution of the RD samples, it can be seen that mainly a basal texture developed (along the compression direction) as the deformation progressed, at both the strain rates.

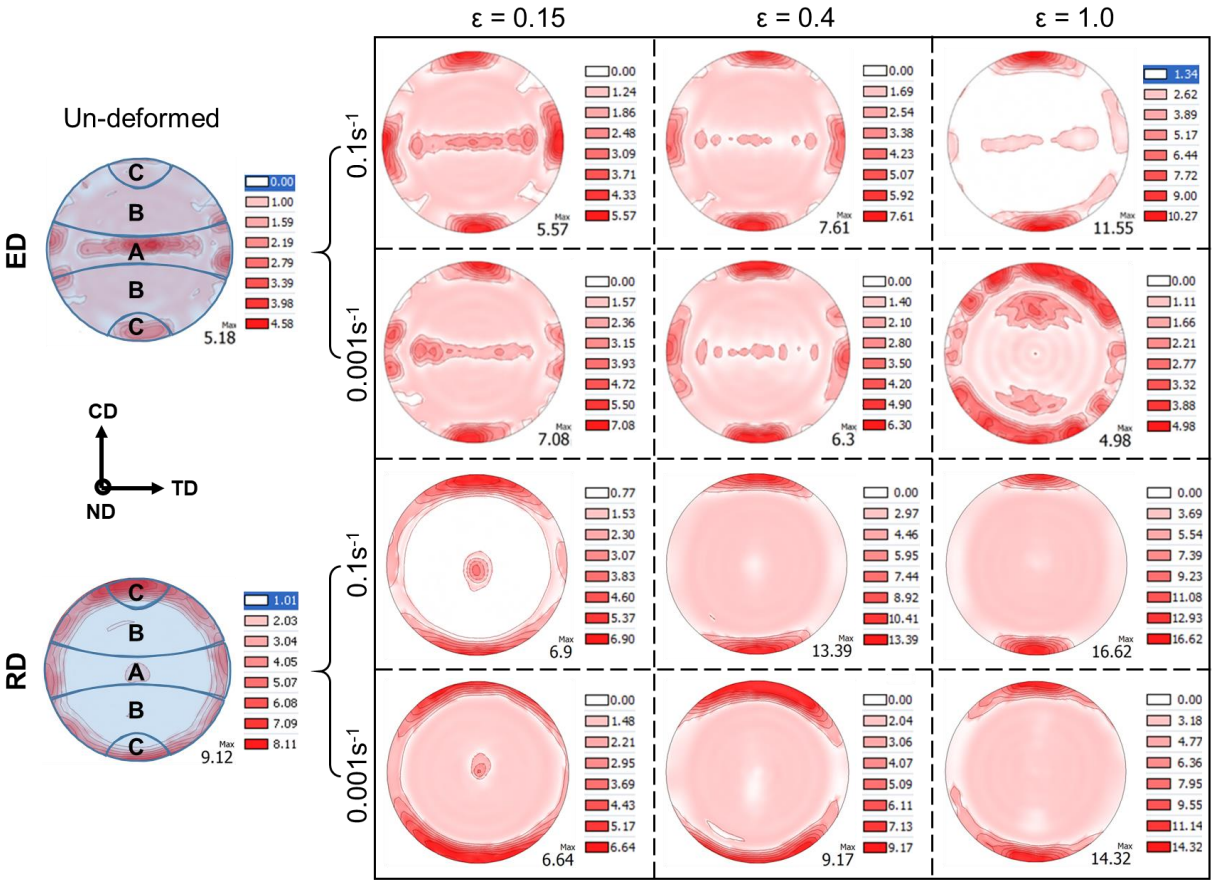

Figure 5-46 XRD macrotexture evolution with deformation strain in the ED and RD samples compressed at 400 °C at the two strain rates. The unit of texture intensity is "Multiples of Random Distribution (MRD)". Orientation legend: CD – Compression direction, ND – Normal direction, TD – Transverse direction.

One interesting observation is with regards to the texture evolution at 0.001 s^{-1}, whereby the two sets of samples showed very different behaviour: a sharp basal texture developed in case of the RD samples, while in case of the ED samples, the texture became randomized. As described in section 5.6.3, texture randomization in case of the ED samples was not fully understood, however some potential mechanisms by which it could have taken place were proposed, including: 1) texture randomization due to DRX, and/or 2) a slow rate (with respect to strain) of grain rotation due to the slip activity at the lower strain rate. Considering this latter point, the role of the significant number of grains in the starting material that were initially oriented along the A component (i.e. with their basal poles at 70-90° to the compression direction) was of special interest, because their particular orientation eased the activation of prismatic slip in them. Prismatic slip causes rotation of the grains about their c – axes [59], and thereby delays the grain rotation due to basal and Py2 slip towards a sharp basal texture. In the case of the RD samples, on the other hand, the proportion of the grains in the starting material along the component A was much less (~ 44% in the RD samples, compared to ~ 80% in the ED samples, as determined using the EBSD data). Because of a relatively low fraction of grains along the component A in the starting RD samples, the corresponding texture (i.e. the component A) did not get preserved during the deformation to any noticeable extent. Instead, many grains in the starting material were oriented along the component B (~ 46% of the grains), which favored basal slip, and thereby deformation led to the development of a basal texture in the material.

5.7.4 Anisotropy in material flow during deformation of the RD samples

The material flow behaviour for the two sets of samples was found to be very different. This is shown in Figure 5-47 (a), where it can be seen that the ED samples deformed symmetrically, while the RD samples showed a preferential flow of material perpendicular to the prior extrusion axis. The direction of the preferred material flow in case of the RD samples was determined using carefully scribed samples to keep track of the prior extrusion direction. Previously, similar results have been reported on extruded AZ31 and ZK60 alloys by other authors [73, 133].

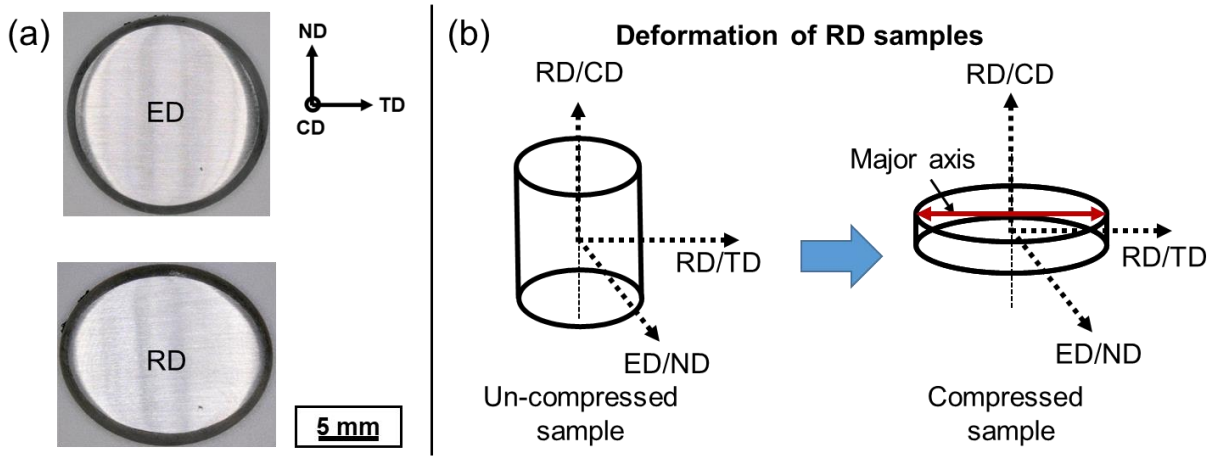

Figure 5-47 (a) Shape of the compressed samples as viewed from the compression axis for deformation at 400 °C, 0.1 s^{-1} to a strain of 1.0, (b) Schematic illustrating the direction of preferred material flow (in the RD samples) with respect to the prior extrusion axis of the material. Orientation legend – ED: Extrusion direction, RD: Radial direction, CD: Compression direction, ND: Normal direction, TD: Transverse direction. In A/B in (b), A refers to the orientation axes prior to the deformation, while B refers to the orientation axes after the deformation.

The observations can be explained based on the starting texture of the RD oriented samples. The components of the texture in the starting material were analyzed using EBSD and are plotted in Figure 5-48. It can be seen from the figure that component C was distributed symmetrically about the compression direction while components A and B were not. It is noted that in uniaxial compression the applied stress field is symmetric and there is no lateral barrier to material flow. Considering this, and noting that the grains along the component C were symmetrically distributed about the CD, they will result in a symmetric material flow during compression. On the other hand, based on a similar reasoning, an asymmetric distribution of grains along components A and B will result in an asymmetric material flow.

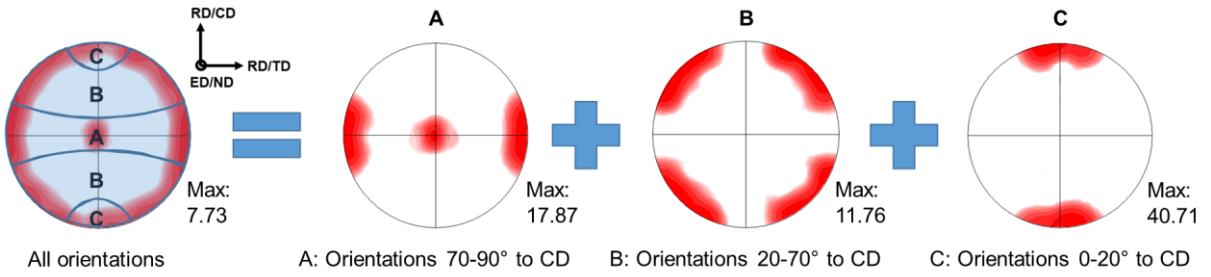

Figure 5-48 Separating the texture of the starting RD samples into various sub-components based on their orientations with respect to the CD. The unit of texture intensity is "Multiples of Random Distribution (MRD)". Orientation legend same as in Figure 5-47.

It is noted that in the case of the starting ED samples, the texture distribution was symmetric with respect to the CD (see Figure 5-49), and therefore the material deformed symmetrically during the compression tests.

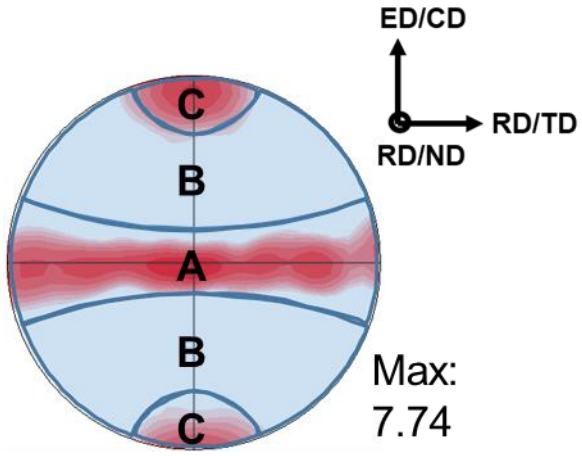

Figure 5-49 Texture of the starting ED samples w.r.t the CD. The texture is symmetric with respect to the CD. The unit of texture intensity is "Multiples of Random Distribution (MRD)". Orientation legend same as in Figure 5-47.

Asymmetry in material flow can be quantified by defining a parameter based on the shape of the deformed sample. This is called *anisotropy ratio (AR)* in the present work and is defined below.

$$\text{Anisotropy ratio (AR)} = {}^{Major\ diameter}/_{Minor\ diameter}$$

AR values closer to 1 indicate a more isotropic material flow behaviour. AR values of the RD samples deformed at 400 °C at a strain rate of 0.1 s^{-1}, to various strain levels, are presented in Figure 5-50. It can be seen from the figure that AR values increased when deformation strain increased from 0.15 to 0.4, while remained stable for deformation to higher strain levels. This evolution in AR values with deformation strain can be correlated to the corresponding evolution of the texture of the deformed samples (Figure 5-47). The corresponding texture results indicate that for deformation of the RD samples at 400 °C, 0.1 s^{-1}, the starting texture rapidly rotated towards a sharp basal texture, and once this texture got developed (by a strain of 0.4), it remained relatively steady with further deformation. This sharp basal texture along the CD is akin to the texture component C in Figure 5-48, and was also symmetrically distributed about the CD. Therefore, a material with this texture is expected to deform

symmetrically. It can, therefore, be deduced that the RD samples compressed at 400 °C, 0.1 s^{-1} deformed asymmetrically until a strain of 0.4 (because of the presence of asymmetric texture components in the starting material), and once this sharp basal texture (with symmetric distribution about the CD) developed, the material deformed symmetrically for deformation thereafter, resulting in relatively stable AR values.

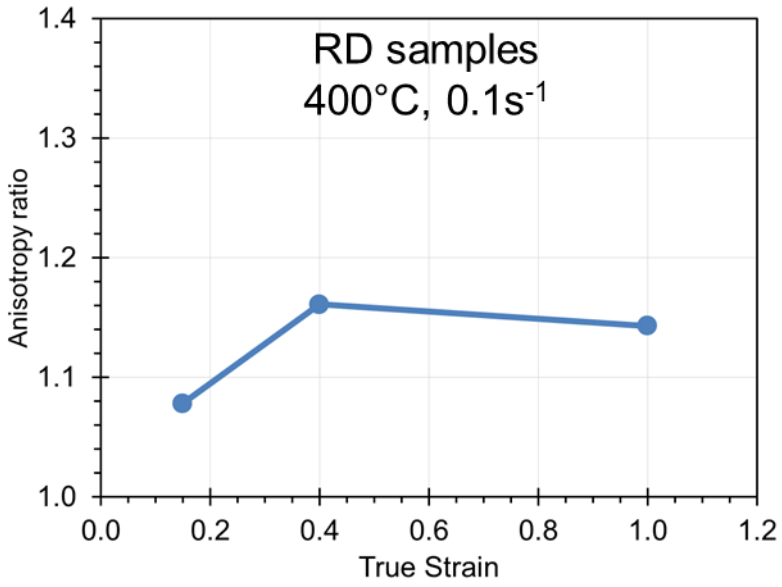

Figure 5-50 Variations in AR values with deformation strain, for deformation of the RD samples at 400 °C, 0.1 s^{-1}.

It is noted that for the deformed ED samples, any variations in the dimensions of the cross-section of the samples were within the limits of measurement accuracy, and therefore anisotropy in deformation of the ED samples is considered negligible.

5.7.5 Summary

The effect of starting texture on the hot deformation behaviour of a textured extruded AZ80 rod, along and perpendicular to the prior extrusion axis, was studied at 400 °C, and strain rates ranging from 0.001 s^{-1} to 0.1 s^{-1}. The main findings of the study are summarized in the following:

1) There was no noticeable effect of the starting texture on the microstructure evolution (including the recrystallization behaviour) for the two chosen starting textures (ED and RD samples) at both the tested strain rates (0.001 s^{-1} and 0.1 s^{-1})

2) Texture evolution at 400 °C, 0.001 s^{-1} was very different for the two sets of samples, with the ED samples showing texture randomization, while the RD samples showing the development of a sharp basal texture. The results for ED samples were not fully understood, but one of the major reason seemed to be a predominant activation of prismatic slip for the majority of the grains in the starting material, which would have prevented/delayed the development of a sharp basal texture during the deformation. In contrast, a substantial fraction of the grains in the starting RD samples were oriented favourably for the occurrence of basal slip, which led to the development of a sharp basal texture in the RD samples due to the deformation.
3) RD samples showed a preferential flow of material perpendicular to the prior extrusion axis during deformation, which resulted in the formation of an elliptical cross-section of the deformed samples (as viewed from the CD). This was attributed to the presence of asymmetric texture components in the starting material. Starting ED samples, on the other hand, had symmetric texture distribution about the CD, and therefore deformed symmetrically about it. The anisotropy in the material flow of the RD samples was quantified by defining a parameter called the Anisotropy Ratio (AR). Evolution of AR with deformation strain was successfully correlated to the evolution of texture of the corresponding sample for deformation at 400 °C, 0.1 s^{-1}.

5.8 Cast AZ80 vs cast AZ31

Most of the available literature on hot deformation behaviour of AZ alloys pertains to the AZ31 alloy. It is of interest to investigate how the AZ80 used in the present work compares to the AZ31 alloy. The current section explores the same for deformation of cast AZ80 and AZ31 alloys at 400 °C, and strain rates ranging from 0.001 – 0.1 s^{-1}. The particular test temperature was chosen because of dissolution of $Mg_{17}Al_{12}$ precipitates in the Mg matrix, so that the results can be interpreted in terms of the Al content in solid solution in the two alloys.

5.8.1 Flow stress curves

The flow stress data for the two alloys are presented in Figure 5-51 (a), while the corresponding critical strain values, and work hardening rate plots (peak strain onwards) are presented in Figure 5-51 (b) and (c), respectively. Considering the flow curves in Figure 5-51 (a), it can be seen that during the initial phase of deformation the flow stress values of the cast AZ80 alloy were much higher compared to the cast AZ31 alloy. It is noted that owing to a random texture in both the starting materials, yielding and flow stress values during the initial phase of deformation are expected to have been controlled by the basal slip [81]. As it was described in section 2.2.3, increasing the Al content in solid solution in Mg increases the CRSS values for various deformation modes, including that for the basal slip, and therefore the higher flow stress values in case of the AZ80 alloy are justified.

Following the peak in the flow stress curve, AZ80 alloy showed a much more pronounced softening than the AZ31 alloy, resulting in its flow stress value becoming comparable to (and even lower than) that of the corresponding AZ31 sample, at higher strain levels. Based on the reasoning provided in the previous paragraph, with regards to the effect of Al content on CRSS, this might seem counterintuitive. A higher flow stress value of AZ31 alloy in this case be explained on the basis of its finer grain size (as a result of deformation and DRX) compared to that in the AZ80 alloy, at higher strain levels, which resulted in a higher Hall-Petch hardening of the deformation modes in case of the former, and likely compensated for the higher solid solution hardening effect in case of the latter.

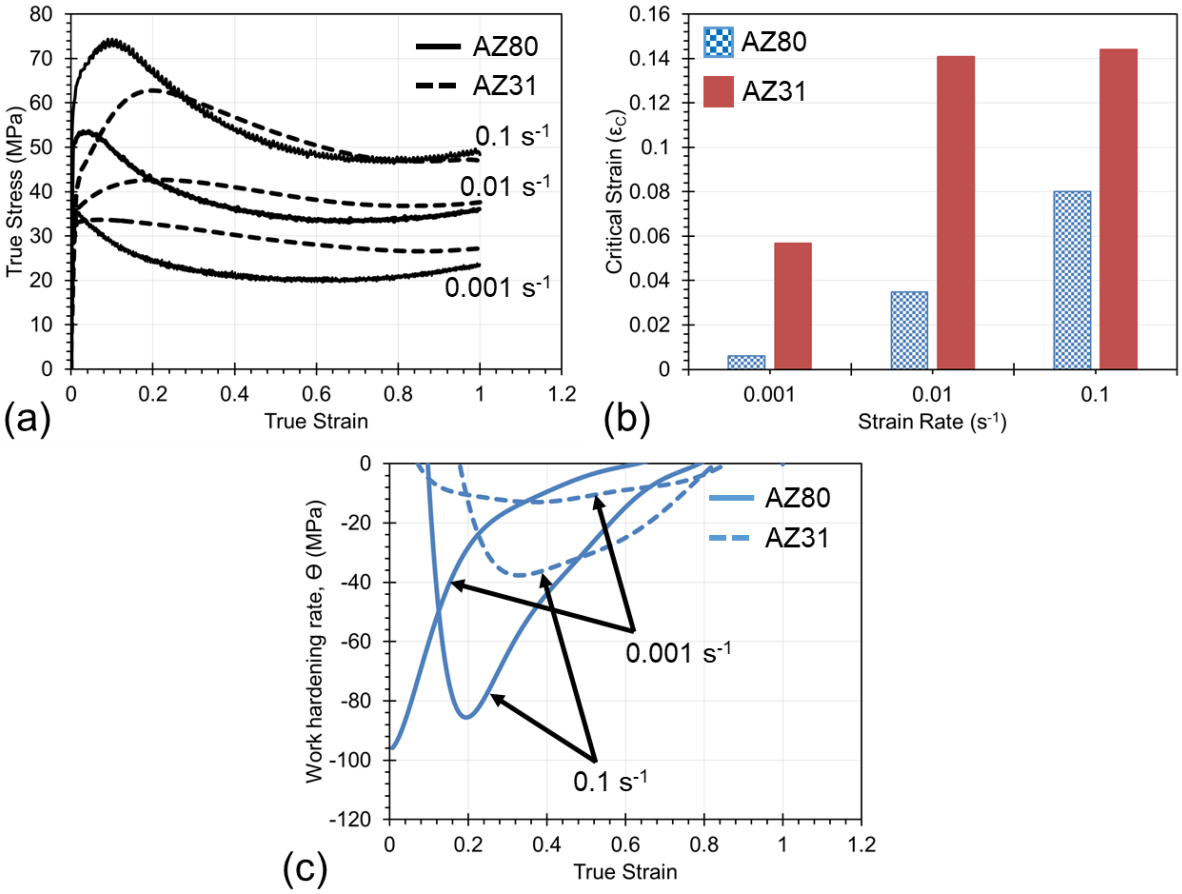

Figure 5-51 Cast AZ80 and AZ31 alloys deformed at 400 °C, at strain rates in the range of 0.001 s^{-1} to 0.1 s^{-1}: (a) flow stress curves, (b) critical strain values, (c) work hardening rate plots.

It is further noted that the AZ80 alloy showed consistently lower critical strain values for DRX initiation than the AZ31 alloy, and also showed a more pronounced work softening rate following the peak stress, indicating faster DRX kinetics in it. Both these aspects were validated in the present work, as the results provided in the following section shows.

5.8.2 Microstructure evolution

It was shown previously that for deformation at 400 °C the cast AZ80 alloy recrystallized through the grain boundary bulging mechanism at both the strain rates (0.001 s^{-1} and 0.1 s^{-1}), and additionally through the TDRX mechanism at the higher strain rate. In the case of the AZ31 alloy, similar mechanisms were observed, as shown in Figure 5-52, which shows the micrographs of the AZ31 samples deformed at 400 °C, 0.1 s^{-1} to a strain of 0.15. Twinning was observed for the AZ31 only for

deformation at 0.1 s^{-1}, as in the case of the AZ80 alloy, and as Figure 5-52 (a) shows, twins might have played a role in DRX. No attempt has been made in the current work to specifically study TDRX in either of the alloys, while it is noted that in samples deformed to higher strain levels, twins were not observed in either of the alloys. The AZ31 alloy additionally showed the presence of many coarse precipitate particles, as can also be seen in the micrographs in Figure 5-52. The particles were present in the corresponding as-cast material as well (refer to Figure 4-1 - Figure 4-3 in section 4.1.1). Since these particles were coarse (> 1 μm), and did not deform during the course of the deformation, they could have played a part in DRX through the PSN mechanism [51]. As the micrograph in Figure 5-52 (a) shows, there were indeed some locations were grains were found to recrystallize in the vicinity of such particles. However it was not ascertained in the present work if those grains indeed recrystallized through PSN, or through any other active DRX mechanism (for e.g. the DRXed grains shown in Figure 5-52 (a) could have equivalently recrystallized through the TDRX mechanism instead). It is interesting to note that a strain value of 0.15 is just slightly higher than the critical strain required to initiate DRX in the AZ31 alloy at 0.1 s^{-1} (ε_C ~ 0.14). Considering this, a very small amount of DRX in the material was expected for the samples deformed to a strain of 0.15, which the micrographs presented in Figure 5-52 indeed attest to.

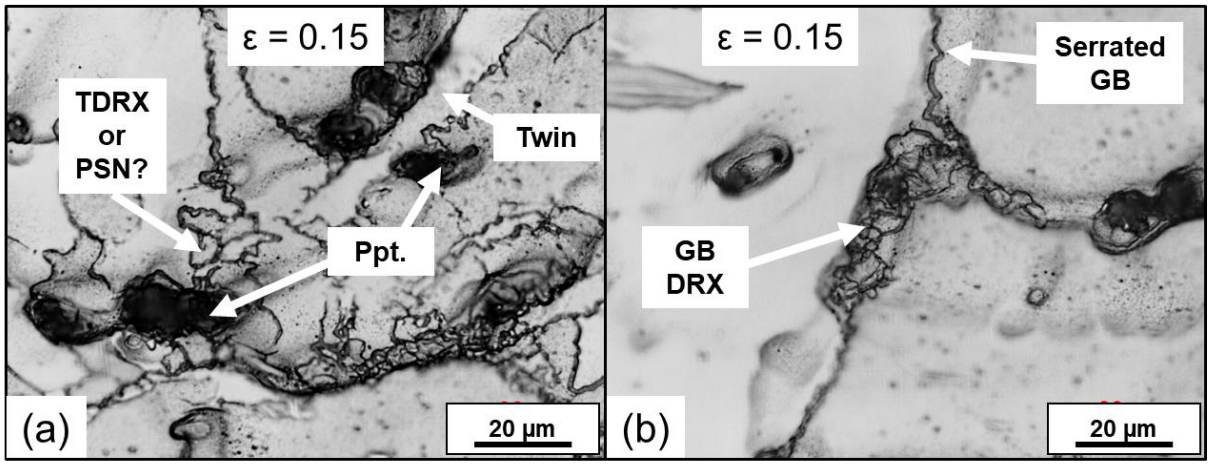

Figure 5-52 Micrographs of the cast AZ31 sample deformed at 400 °C, 0.1 s^{-1} to a strain of 0.15: (a) shows DRX through TDRX and/or PSN, while (b) shows DRX through the grain boundary serration and bulging mechanism.

The AZ31 alloy also showed grain refinement through the CDRX mechanism. This is shown in Figure 5-53, for the sample deformed at 400 °C, 0.001 s^{-1} to a strain of 1.0,

through the EBSD IPF map. The black regions in the IPF map were poorly indexed regions, and were removed from the analysis during the pre-processing of the data. EBSD was done for the AZ31 alloy only for the samples deformed to a strain of 1.0 at both the strain rates.

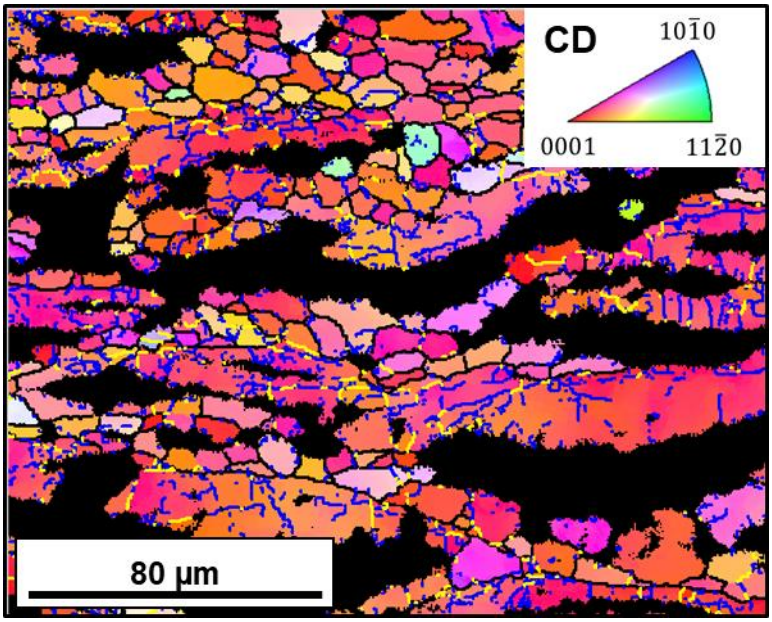

Figure 5-53 CDRX via grain fragmentation in cast AZ31 sample deformed at 400 °C, 0.1 s^{-1} to a strain of 1.0

The microstructure evolution results for the two starting alloys for deformation at 0.001 s^{-1} and 0.1 s^{-1} are presented in Figure 5-54 and Figure 5-55, respectively. For both the alloys, and at both the strain rates, DRX (and CDRX) resulted in the development of a bimodal grain structure at low strain levels. With an increase in the deformation strain level, the area covered by the fine grains increased. At all the tested strain levels, and for both the strain rates, samples of the AZ80 alloy showed a higher fraction of the fine grains compared to the corresponding samples of the AZ31 alloy. While the microstructure of the deformed samples of the AZ80 alloy became reasonably homogenous by a deformation strain of 1.0, those of the AZ31 alloy still showed a considerable bimodality.

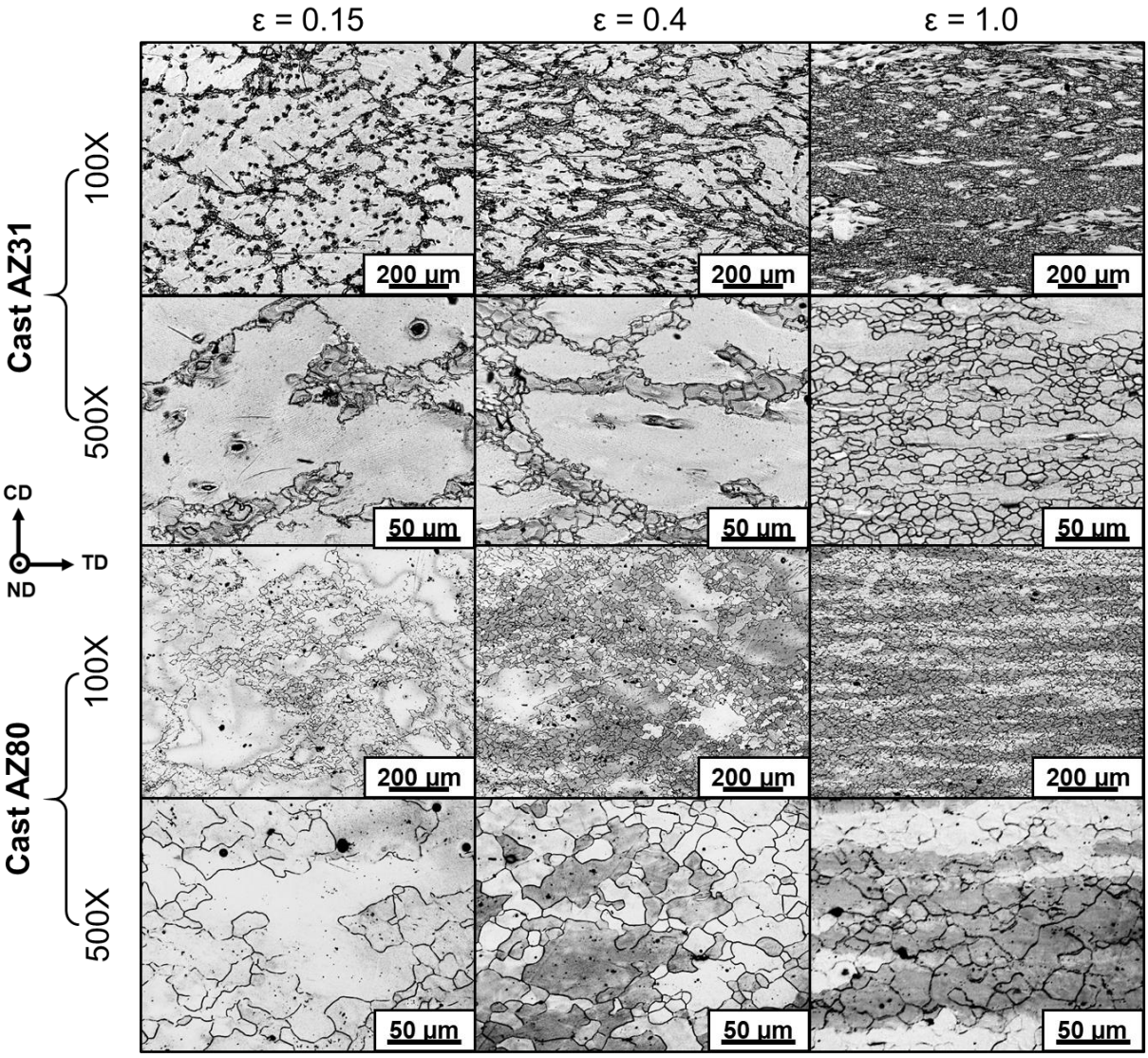

Figure 5-54 Microstructure evolution in the cast AZ31 and AZ80 samples during deformation at 400 °C, 0.001 s^{-1}.

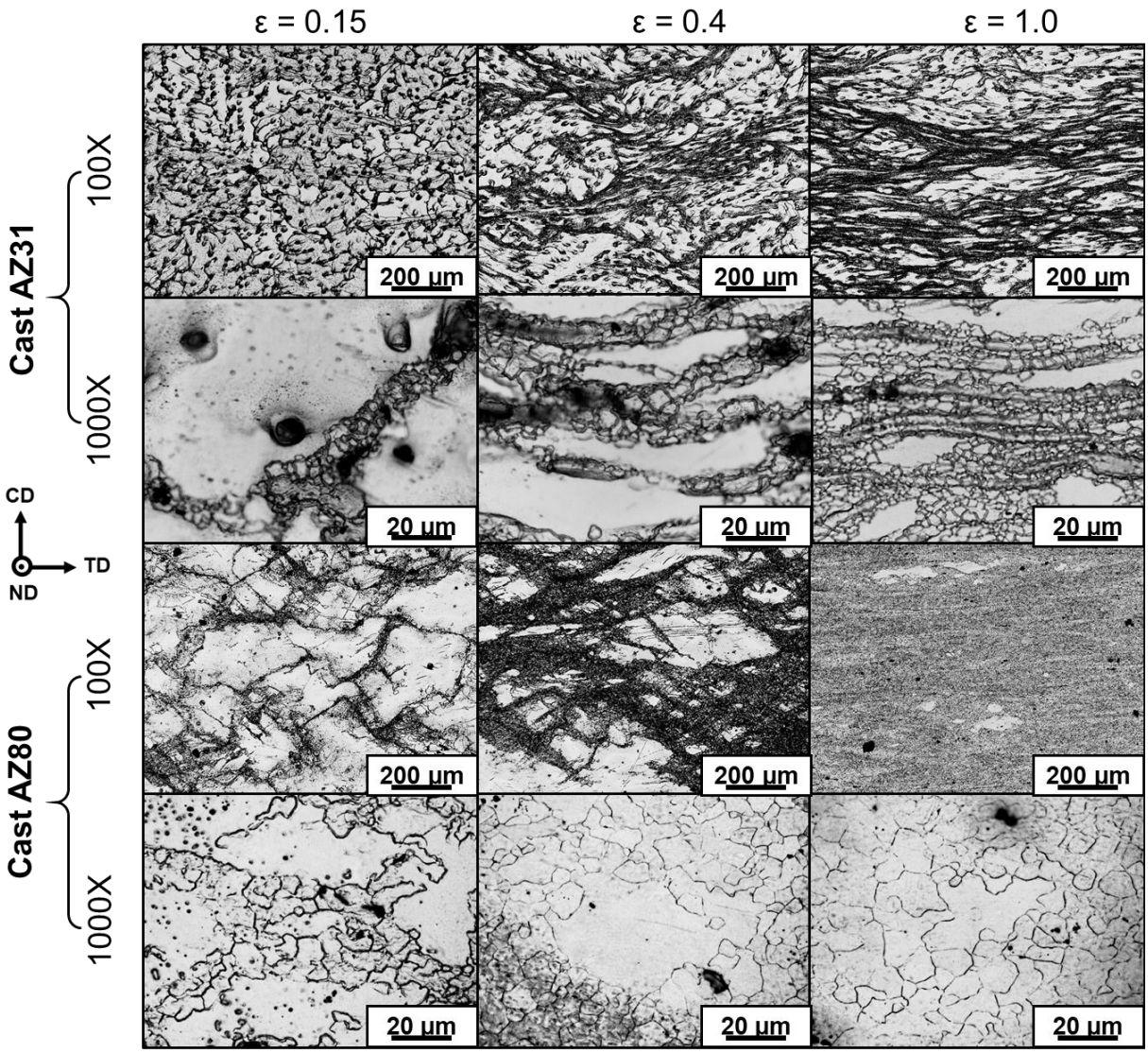

Figure 5-55 Microstructure evolution in the cast AZ31 and AZ80 samples during deformation at 400 °C, 0.1 s^{-1}.

The DRX grain sizes are analysed in Figure 5-56. The quantification is based on the EBSD data, using a GOS ≤ 2° to determine the DRXed grains. It can be seen that the DRX grain size in AZ31 alloy was much finer compared to the DRX grain size in the AZ80 alloy.

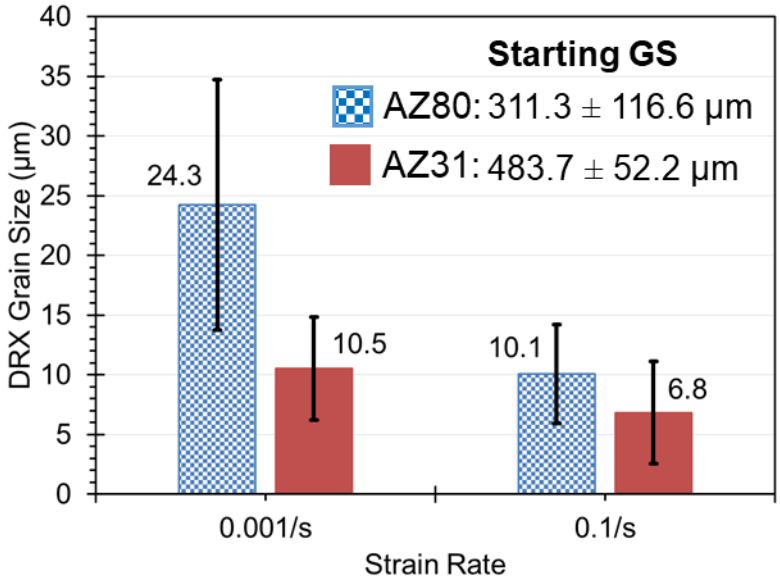

Figure 5-56 DRX grain size in the cast AZ80 and AZ31 samples deformed to a strain of 1.0 at 400 °C, at the two strain rates. EBSD data was used to determine the DRX grain size (using a GOS ≤ 2° filter), while the grain size of the as-cast alloys was determined using the optical micrographs. GS refers to grain size.

No attempt has been made in the present work to quantify the DRX% because of the significantly in-homogenous nature of the microstructure of the deformed samples of the AZ31 alloy, for which DRX% results will vary greatly with measurement location on the sample surface. It is noted that EBSD was done only once per sample, at the central location (refer to Figure 4-13), considering the limited availably of equipment and resources, and therefore averaging of the results from multiple measurements to get an average DRX% was not possible. However, based on the optical micrographs presented in Figure 5-54 and Figure 5-55, the results can be qualitatively analysed and indicate that the AZ80 alloy showed a much higher DRX% compared to the AZ31 alloy at both the strain rates, and all the strain levels.

Prior literature indicates that increasing the Al content in the material decreases the DRX grain size and DRX% [82, 84]. However, just the opposite trends in both DRX% and grain size were observed in the present work. The current results are more in line with those reported by Zhang et al. on the effect of increasing Zn content on the DRX% and DRX grain size in Mg-x%Zn-1%Mn alloy (with Zn content varying from 4 to 8 wt.%) [134]. However these latter authors did not give any explanation with regards to the trends they reported, and it is therefore desirable to further investigate these peculiar observations from a more fundamental perspective.

5.8.3 Texture results

The texture results for the AZ31 samples deformed to a strain of 1.0 are presented in Figure 5-57. It is noted that even the bulk texture was obtained using the EBSD in this case. Comparable results for the cast AZ80 samples were presented in section 5.3.3.

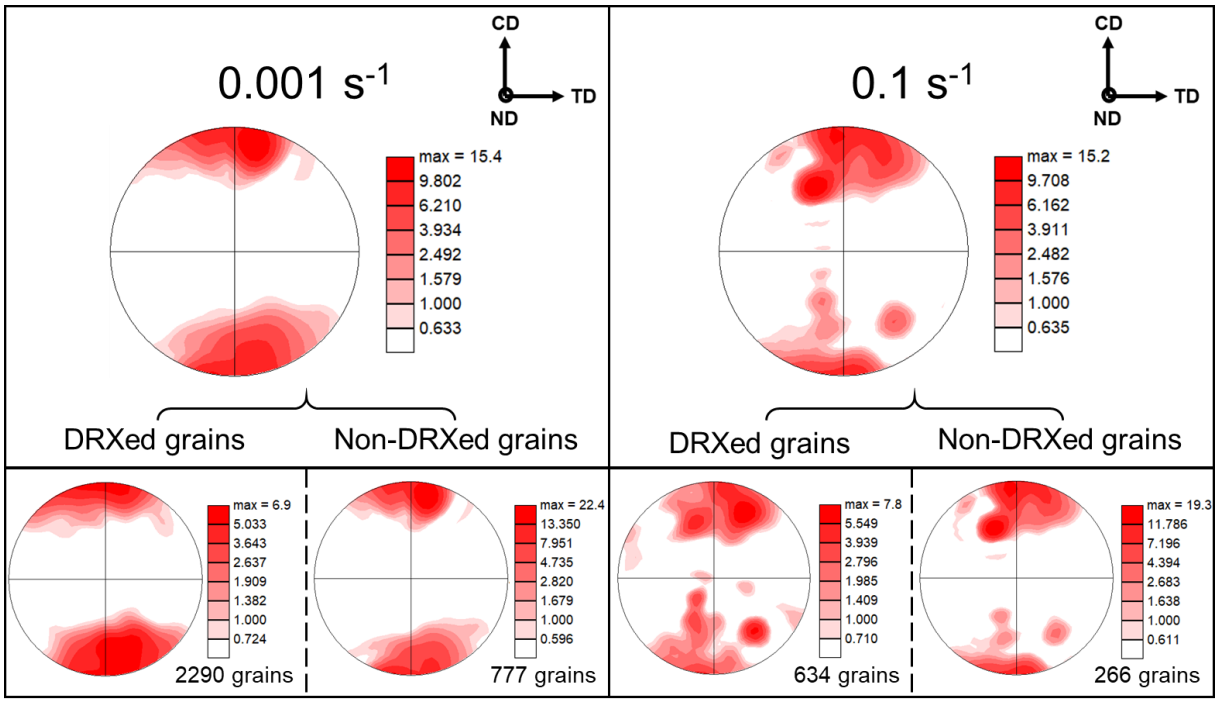

Figure 5-57 Texture of the cast AZ31 samples deformed at 400 °C at the two strain rates to a strain of 1.0. EBSD data was used to determine the textures. A GOS ≤ 2° filter was used to separate DRXed and non-DRXed grains. The number of grains in each subset are also provided. The unit of texture intensity is "Multiples of Random Distribution (MRD)". Orientation legend: CD – Compression direction, ND – Normal direction, TD – Transverse direction.

The bulk texture results show that for deformation at either of the strain rates, a sharp basal texture developed in the deformed AZ31 samples, and the results are comparable to those of the corresponding deformed AZ80 samples. Considering the texture of the DRXed and deformed grains for the AZ31 samples, it is interesting to note the much weaker intensities shown by the DRXed grains, compared to the corresponding deformed grains, at either of the strain rates, strongly suggesting that DRX resulted in texture randomization in the AZ31 alloy. These results are very different from those of the corresponding cast deformed samples, for which it was found that the DRXed grains preserved the deformation texture. Since in both the AZ31 and AZ80 alloys, DRX mainly occurred by the grain boundary bulging mechanism (for deformation at 400 °C), the current results indicate that the texture of

the DRXed grains depends not just on the deformation conditions and the DRX mechanism, but also on the alloy composition.

5.8.4 Summary

The hot deformation behaviour of the cast AZ80 and AZ31 alloys was compared for deformation at 400 °C and strain rates in the range of 0.001 s^{-1} to 0.1 s^{-1}. The main findings of the study are summarized in the following:

1) The AZ80 alloy showed higher flow stress values compared to the AZ31 alloy during the initial phase of deformation, owing to a higher solid solution strengthening effect (due to Al) on the CRSS for the basal slip in case of the AZ80 alloy. At higher strain levels, the trend reversed, owing to a higher Hall-Petch hardening effect in case of the AZ31 alloy, due to the development of a finer grain size in it, as result of deformation and DRX.
2) The AZ80 alloy showed an earlier onset of DRX and a more rapid DRX kinetics compared to the AZ31 alloy. The AZ80 alloy showed both, a large DRX grain size, and a higher DRX%, compared to the AZ31 alloy. By strain of 1.0, a homogenous microstructure developed in case of the AZ80 alloy, while that of the AZ31 alloy still showed a considerable bimodality.
3) DRX caused texture randomization in case of the AZ31 alloy, while preserved the deformation texture in case of the AZ80 alloy. The underlying reason behind this is not known from the present results.

5.9 Discussion

The purpose of this section is to present a holistic view of the experimental results and describe how they fit into the context of the current literature on this topic. To understand the hot deformation behaviour of AZ80, the first step was to test the various starting materials in uniaxial compression under a variety of deformation conditions. Successful compression tests were done for most of the deformation conditions, however for certain conditions either the sample could not be compressed successfully in a repeatable way, or the deformed sample showed surface cracking. The results are summarized in the Table 5-2. The data in the table is based solely on the surface condition of the samples after deformation and any visual observations of cracking. Similar behaviour was observed for extruded material deformed along and perpendicular to the prior extrusion axis (i.e. ED and RD samples), and therefore their data is subsumed under a single heading **Extr.** (for Extruded material). The green tick marks represent the conditions for which successful and repeatable compression tests could be done, without any evidence of surface cracking. The orange tick marks for the cast material indicate the conditions for which compression tests were successful, however there was evidence of surface cracking. An example is given in Figure 5-58 (a) of surface cracking observed in cast material deformed at 350 °C, 1 s^{-1}. This cracking was attributed to the presence of hoop stresses at the sample surface, which opens up any micro cracks present in the material, while local melting of eutectic $Mg_{17}Al_{12}$ phase is expected to have contributed to development of some of these microcracks.

It was not possible to compress the extruded material uniformly, and in a repeatable way for deformation at 300 °C, 1 s^{-1}, which is indicated in Table 5-2 by a red cross. Figure 5-58 (b-c) shows an example of the shape of the sample obtained after compression of the ED sample at 300 °C, 1 s^{-1}. Multiple repeat tests were conducted for this deformation condition, but the sample deformed differently every time, indicating that the tests were not repeatable, and the measured flow stress data not reliable. The extruded material exhibited similar tendency for deformation under nearby deformation conditions, viz. 300 °C, 0.1 s^{-1}, and 350 °C , 1 s^{-1}, though for these cases, successful compression could be performed for a majority of the repeat tests, and therefore the corresponding conditions are marked by orange tick marks (instead of red crosses).

Table 5-2 Compression test matrix showing conditions for which successful compression tests could be done, in a repeatable way, and without any evidence of visible surface cracking. For interpretation of various tick marks and crosses, refer to the description in the main body of the text.

	300 °C		350 °C		400 °C		450 °C	
	Cast	Extr.	Cast	Extr.	Cast	Extr.	Cast	Extr.
1 s^{-1}	✓	✗	✓	✓	✓	✓	✓	✓
0.1 s^{-1}	✓	✓	✓	✓	✓	✓	✓	✓
0.01 s^{-1}	✓	✓	✓	✓	✓	✓	✓	✓
0.001 s^{-1}	✓	✓	✓	✓	✓	✓	✓	✓

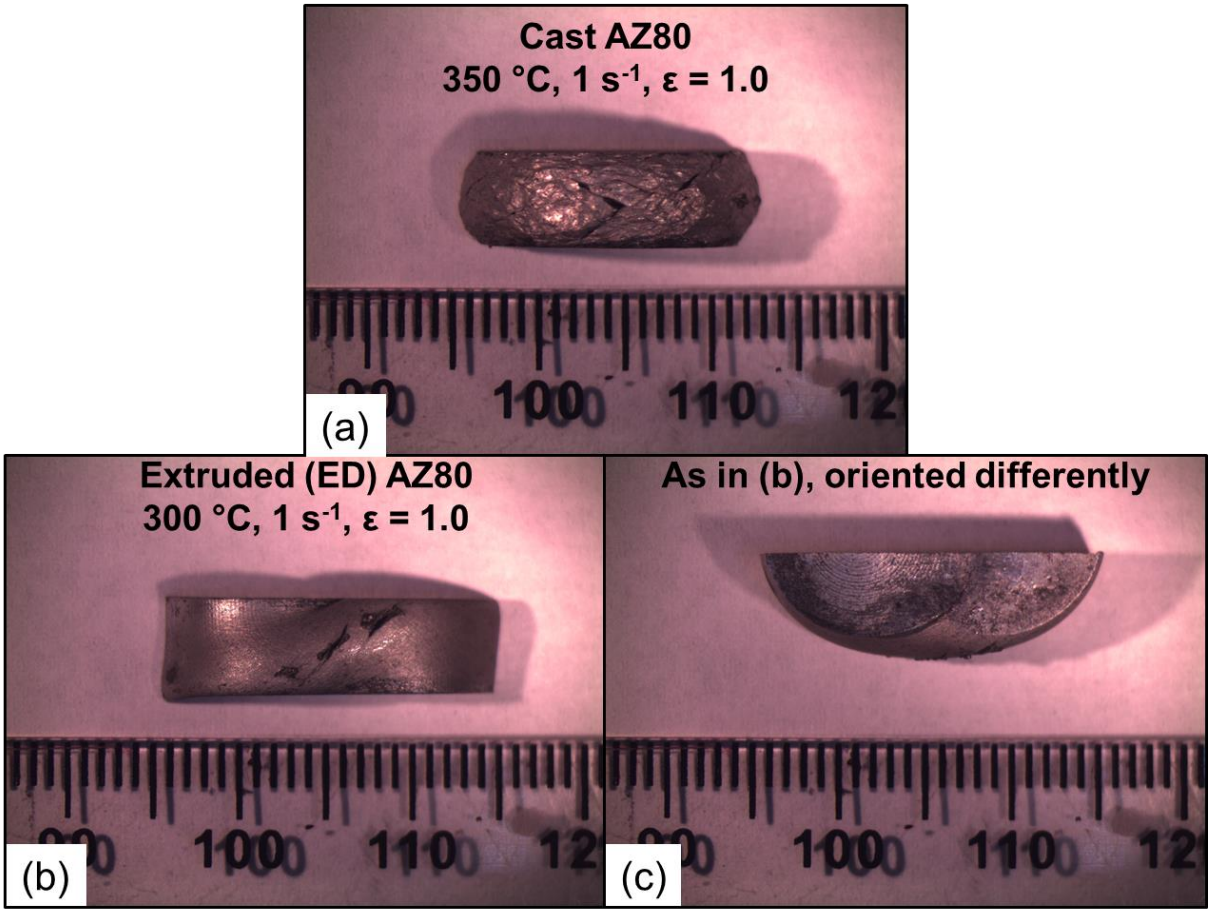

Figure 5-58 Pictures of samples compressed to a strain of 1.0: (a) Cast AZ80 sample deformed at 350 °C, 1 s^{-1}, (b) and (c) Extruded (ED) AZ80 sample deformed at 300 °C, 1 s^{-1}. (b) and (c) are images of the same sample taken from different perspectives.

Prior in-house work on cast AZ31 alloy by some of our colleagues indicate that surface cracking due to local melting of eutectic $Mg_{17}Al_{12}$ phase can be prevented by imparting a homogenization treatment to the material prior to hot compression [86, 135]. Such treatment results in the development of an equilibrium microstructure, and thereby it is expected to shift the temperature of localized melting in the AZ80 alloy from ~ 400 °C to about 480 °C (refer to Figure 4-6). It is also noted that cracking was promoted due to the presence of hoop stresses on the free surface of the samples (refer to Appendix E), and close die forging, which provides for compressive stresses even near the surface of the deforming sample, is expected to prevent, or at least delay this cracking [136]. It is noted that close die forging is more relevant for industrial forging applications.

It is also of interest to see how the flow stress values obtained in the present work compare to those published in the literature. Figure 5-59 compares the data from the present work, with those on cast and extruded (ED) AZ80 alloys reported by other researchers. The data reported in these studies (as well as in the present work) was uncorrected for any temperature rise or friction and barrelling effects during deformation. The comparison is made at a fixed strain of 0.2, with the effect of deformation conditions (temperature and strain rate) subsumed under the single Z parameter (Zener-Hollomon parameter), determined with an activation energy (Q) of 135 kJ/mol, in terms of a power law dependence. A strain of 0.2 was chosen for this comparison because the difference in the flow stress values of the cast and extruded material (that were tested in the present work) was quite pronounced at this strain level (refer to Figure 5-34 (a)). It is noted that the cast material from [137] used in comparison in Figure 5-59 (a) was actually homogenized (at 420 °C for 20 hrs) prior to the compression tests, however since no alternative reliable data source for non heat treated cast AZ80 alloy was found, the data from [137] itself was used.

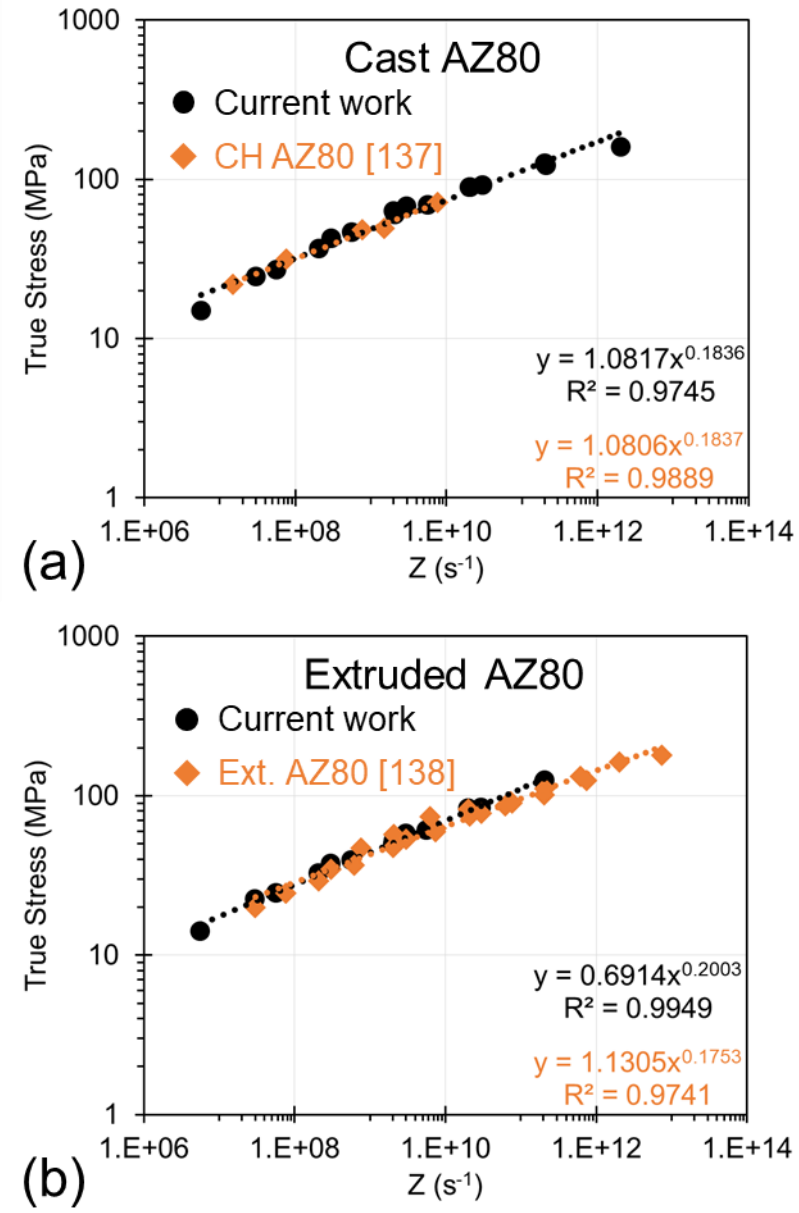

Figure 5-59 Comparison of flow stress data determined in the present work with that published in literature previously: (a) Cast AZ80 alloy. CH refers to Cast-Homogenized state of the starting material from reference [137], (b) Extruded AZ80 alloy, deformed along prior extrusion direction. Comparison is with [138]. Z refers to the Zener-Holloman parameter, calculated using the temperature and strain rate values, and an activation energy of 135 kJ/mol.

It can be seen from Figure 5-59 that the current data matches that found in the literature quite closely, validating the flow stress data obtained in the present work. Another interesting thing to note is that the flow stress values of cast and cast homogenized AZ80 are pretty similar, indicating that homogenization do not affect the flow stress value of this alloy (in hot deformation). It is noted that this similarity (between the flow stress values of cast and cast homogenized AZ80 alloy) might exist

only for the deformation till low strain levels, as the work by Wu et al. on cast and cast homogenized AZ61 indicates [139].

Detailed characterization of the microstructure and texture of the deformed samples was done only for a subset of the deformation test matrix presented earlier. Specifically, the effect of deformation temperature on the microstructure and texture evolution was studied only for the cast material, at temperatures of 300 °C – 400 °C, at a fixed strain rate of 0.001 s^{-1}. This temperature range also corresponded to a change in the precipitation behaviour of the $Mg_{17}Al_{12}$ precipitates in the material, with the precipitates being present, and in multiple morphologies, for deformation at 300 °C, while the precipitates getting quickly dissolved, as a result of deformation and DRX, for deformation at 400 °C. The effect of strain rate (in the range of 0.001 s^{-1} to 0.1 s^{-1}) was studied again only for the cast material, at a fixed temperature of 400 °C (where the precipitates rapidly dissolve in the α-Mg matrix, such that the results can be interpreted based solely on the effect of the strain rate). Under all these conditions the evolution of microstructure and texture with deformation strain was also studied, so that a correlation between these state parameters (of the material) can be established with the observed flow stress curves. EBSD was extensively used to identify the twin types in the material, and also to separate the datasets of the DRXed grains and non-DRXed grains, which were then used to calculate the DRX grain size, and compare the texture of the DRXed and non-DRXed grains.

The results indicate that DRX took place for all the deformation conditions tested, while the DRX mechanism, grain size and fraction were found to be dependent on the employed deformation conditions, as was also expected based on prior literature on the subject [35, 47]. Though the DRX fraction was not quantified, DRX grain size was found to refine with a lowering of the deformation temperature or an increment in the deformation strain rate, but was found to be independent of the deformation strain level. Similar trends have been reported previously for AZ31 and AZ91 alloys by various researchers [23, 48]. The DRX mechanism changed with deformation conditions, with particle stimulated nucleation (PSN) at the lamellar $Mg_{17}Al_{12}$ precipitates being the dominant DRX mechanism for deformation at 300 °C, while at 400 °C DRX took place only by the grain boundary bulging mechanism. DRX through PSN resulted in texture randomization, while through the grain boundary bulging mechanism resulted in preservation of the deformation texture. The observed role of

various morphologies of $Mg_{17}Al_{12}$ precipitates in microstructure development and DRX, viz. of lamellar precipitates in promoting DRX, of lath precipitates in restricting the progress of the DRX front into the non-DRXed regions, and of the fine precipitate particles at the boundaries of the DRXed grains in pinning of the DRX grain growth, for deformation at 300 °C, 0.001 s^{-1}, validates similar findings on cast AZ91 alloy deformed in uniaxial compression at 300 °C (at various strain rates) [24, 33].

Further, comparison was made between the hot deformation behaviour of cast and extruded material so as to investigate the role of processing history of the starting material on the microstructure and texture evolution during hot deformation. The study was considered important to shed some light on whether it is advantageous to use cast or wrought raw material for forging applications. The results show that development of a homogeneous microstructure is more rapid in the extruded material, owing to a finer initial grain size, and also due to it experiencing a higher DRX fraction (which is again linked to the its finer initial grain size). A finer initial grain size also prevented activation of inhomogeneous deformation mechanisms, like shear banding, and twinning, until (at least) a relatively high strain rate of 0.1 s^{-1}. Coarse grained cast material, showed twinning, and fracture cracking, at high strain rates (shear banding was not investigated in the present work). Cast material was also prone to surface cracking during deformation at high temperatures and high strain rates due to hoop stresses, and the presence of low melting eutectic $Mg_{17}Al_{12}$ phase in the material. Both these factors indicate a superior forgeability of the extruded material over the cast material for open die forging applications. It is noted that work by some other colleagues in the same research project also indicate that post forge mechanical properties, including monotonic tensile/compressive, and cyclic (fatigue) properties of the extruded forged material is superior to the corresponding cast forged material [12]. Another result of academic interest from the study was a similarity in the DRX grain size of the cast and extruded deformed samples, which based on the differences in the grain sizes of the starting materials indicated that the DRX grain size of the AZ80 alloy is independent of the grain size of the starting material. Deformation and DRX resulted in the development of similar grain sizes in both materials, despite large differences of the grain sizes in the starting materials. This also resulted in the convergence of flow stress curves for the two materials at high strain levels ($\varepsilon \sim 0.6$).

A study investigating the effect of starting texture on the hot deformation behaviour of the alloy was also performed by deforming the sharply textured as-extruded material along and perpendicular to the prior extrusion axis. It was determined that the DRX grain size and fraction were independent of the chosen starting orientations of the alloy. The results support similar findings previously reported by Al-Samman et al. on an extruded AZ31 alloy [20]. However, another study, on ZK60, suggests that for compression of the extruded material at 45° to the prior extrusion axis (an orientation that was not tested in the present work, but tested by Al-Samman et al. for the AZ31 alloy [20]), the DRX grain size and fraction might be lower compared to that for deforming the material along and perpendicular to the prior extrusion axis, owing to an ease in occurrence of basal slip in the former, which makes microstructural conditions less conducive for occurrence of DRX [76]. Considering this study, it becomes important to investigate the deformation behaviour of the extruded material along this orientation, so that a definitive statement on the role of texture on the deformation behaviour of the AZ80 alloy can be made. Another important way the effect of starting texture manifested during hot deformation was in terms of the material flow anisotropy, whereby it was determined that presence of asymmetrically distributed texture components along the loading axis results in a preferential flow of material along certain directions during deformation.

It was also of academic interest to compare the hot deformation behaviour of the AZ80 alloy with the most studied member of the AZ family, viz. the AZ31 alloy. To this end, hot compression tests were performed at 400 °C (so that $Mg_{17}Al_{12}$ precipitates did not affect the deformation behaviour of the AZ80 alloy, and the comparison could be made solely on the basis of a solid solutioning effect) at various strain rates. The AZ80 alloy showed higher grain size values and higher DRX fraction compared to the AZ31 alloy, resulting in the development of a homogenous microstructure at a deformation strain of 1.0, while the AZ31 alloy showed a bimodal microstructure. Since a homogenous structure is desirable for superior fatigue life of the forged component, this suggests superior forgeability of AZ80 over AZ31. Prior literature also suggests that with an increase in Al content, the material shows less tendency towards activation of non-homogeneous deformation mechanisms like shear banding and twinning, which might further indicate the superiority of high Al content AZ alloys for forging applications involving high deformation levels [84]. However, it is noted that the observations of

coarser DRX grain size and higher DRX fraction for AZ alloys with higher Al content (which is the AZ80 alloy in the present case) are not aligned with those reported in literature previously [82, 84], and therefore warrants further investigation. Another interesting result was in terms of the texture of the DRXed grains, whereby DRXed grains for the AZ31 alloy were found to be randomly oriented, while for the AZ80 alloy were found to preserve the deformation texture. The underlying reason behind why the orientations of the DRXed grains in the two alloys showed so different behaviour is not clear from the present work.

6 Conclusions and Future work

6.1 Conclusions

The current research is part of a Natural Sciences and Engineering Research Council of Canada's Automotive Partnership Canada grant, aimed at forging an industrial scale control arm for a Ford Fusion car. This research was experimental in nature and focused on exploring the hot deformation behaviour of cast and extruded AZ80 alloys under typical industrial forging conditions. Particular emphasis was placed on trying to understand the DRX mechanisms that occur at different temperatures and strain rates as well as the textures that evolve during hot deformation. The main findings of the research are summarised in the following:

1) In cast AZ80 alloy, $Mg_{17}Al_{12}$ precipitates were found to play an important role in the microstructure and texture evolution during deformation at 300 °C. The results indicated that the presence of these precipitates as lamellar discontinuous precipitates promoted DRX and texture randomization via PSN, while the presence of these precipitates as lath continuous precipitates restricted the occurrence of DRX in the material by blocking the progress of DRX front into the non-DRXed regions. This opens up the possibility of microstructure engineering for this alloy, whereby DRX, grain refinement, and texture randomization in the material can be promoted by giving the material a suitable heat treatment, and hence desired precipitate structure, prior to forging.
2) During hot deformation, both DRX and CDRX (i.e. recovery) processes led to significant grain refinement under all the investigated deformation conditions. DRX grain size was finer for deformation at lower temperatures and/or higher strain rates. DRX grain size was found to be independent of the grain size of the starting material, but using a finer grain sized starting material promoted the occurrence of DRX in the material during deformation (i.e. resulted in higher DRX%, compared to a coarser grained material deformed under same conditions).
3) The starting texture did not affect the microstructure evolution (including the DRX behaviour), but did affect the texture evolution, with texture randomization observed to be taking place only in case of compression of the extruded material along the prior extrusion direction, and only at the lowest tested strain

rate of 0.001 s^{-1} (at 400 °C). Additionally, an asymmetric distribution of the texture in the starting material about the compression axis was found to result in an anisotropic flow of the material (about the compression axis) during the deformation.

One of the main objectives of the current research was to determine the conditions which can potentially enhance the forgeability of the material. Forgeability in the present work is defined as the ability of the material to be deformed at high strain rates to large strains, without showing any cracking, and development of a fine grained and homogeneous microstructure, and a random texture distribution, as a result of deformation. With regards to this, the main recommendations for selecting the material and deformation conditions for forging can be summarised as follows:

1) The extruded AZ80 alloy showed better forgeability than the cast AZ80 alloy, owing to the propensity of the latter towards fracture cracking, especially at higher deformation strain rates. This was attributed to a coarser grain size of the starting cast material. It is suggested that casting techniques, which results in a faster solidification of the material (and hence resulting in a more refined microstructure), might be found useful to enhance the forgeability of the cast material. Also, local melting of eutectic $Mg_{17}Al_{12}$ phase for deformation at high temperatures and strain rates could have contributed to fracture cracking in case of deformation of the cast material. A suitable homogenization treatment prior to hot deformation, is expected to be beneficial in this regards.
2) Grain refinement and texture randomization is possible for deformation at 300 °C, whereby $Mg_{17}Al_{12}$ precipitates are present as DP, and promote DRX and texture randomization via PSN. However the resultant microstructure is bimodal (study was done only for the cast AZ80 alloy), and might not be desirable for many fatigue critical applications. It may however be possible to alleviate this problem by providing a suitable heat treatment to the starting material, in order to saturate the microstructure with lamellar DP, prior to its hot deformation, which would enhance occurrence of DRX in the material.
3) Deformation of the extruded AZ80 alloy at 400 °C, 0.1 s^{-1}, resulted in the development of a homogenous and fine grained microstructure. However, deformation under this condition resulted in the development of a sharp basal

texture in the material (by a strain of 1.0), which might severely limit to what extent the material can withstand any further deformation before fracture (in case higher deformation levels are desired).

6.2 Future Work

Based on the analysis of the current results, and those available from the literature, a few areas were identified for which additional research is desirable in order to further the knowledgebase for these alloys. These are highlighted in the following:

1) Cast material showed propensity to crack from the sample side surface at 400 °C, at high strain rates. A potential reason for this is related to local melting of the eutectic $Mg_{17}Al_{12}$ phase, which is present in the as-cast material. A suitable homogenization treatment prior to hot deformation, is expected to be beneficial in this regards [86, 135]. An annealing treatment of ~ 20 hrs at 420 °C is recommended for complete homogenization of the material from the as-cast state (for AZ80 alloy) [87].
2) Prior literature indicates that high propensity of deformation twinning at higher strain rates can enhance the occurrence of DRX in the material [43, 140]. This can be advantageous for forging applications since both high DRX% and high strain rates are desirable. Such an affect has been previously reported for the cast AZ91 alloy [43], however no comparable study on cast AZ80 alloy is currently available. It is therefore desirable to study this, and based on the referred study on cast AZ91 [43], studying this effect at 300 °C, at strain rate of 1 s^{-1} is proposed for the cast AZ80 alloy.
3) The current research showed that lamellar DP promotes DRX and texture randomization, while lath CP blocks the progress of DRX in the material. The current results validate similar findings reported earlier by Xu et al. on cast AZ91 alloy [24]. However, as in the case of the study by Xu et al., a direct observation of PSN at lamellar DP, and of fragmentation of lamellar DP in the DRXed regions, which results in the formation of the pinning precipitates, has eluded the present work as well, and therefore a more systematic study to actually observe this is desirable. The current author proposes the following experimental approach: i) Solution treating the starting material to dissolve away all the precipitates, resulting in the development of a chemically homogeneous material (at 420 °C, for 20 hours [87]), ii) peak aging the solution treated samples at temperatures where (majorly) lamellar DP precipitation takes place in the material (at 150-200 °C [92]), and iii) hot deforming these samples at a single deformation condition (at temperatures lower than 350 °C,

because at higher temperatures the precipitates dissolve away in the matrix), and studying the microstructure and texture evolution with deformation strain, with high resolution SEM, TEM (Transmission Electron Microscopy) and EBSD.

4) Previously, few authors have shown for deformed AZ31 alloy, that static recrystallization (SRX), which is recrystallization taking place after deformation during annealing at high temperatures, can result in development of a homogeneous microstructure (from an initial bimodal state) [141]. Depending on the deformation conditions, and the annealing temperature, the duration of annealing required for development of a homogenous microstructure can be as short as a few seconds. To date, there is no literature available on the SRX behaviour of the hot deformed AZ80 alloy, and therefore it needs to be explored. It is especially desirable to study this for the cast material, for the deformation conditions which results in development of a bimodal microstructure: viz. low temperatures and/or high strain rates. Based on the referred study on AZ31 alloy [141], it is proposed to anneal the samples deformed under these conditions in the temperature range of 300 °C - 400 °C for 1 s to 10,000 s, and study the evolution of microstructure.
5) A bimodal microstructure developed in the cast AZ80 alloy for deformation at 300 °C, at a strain rate of 0.001 s^{-1}. Though for certain fatigue critical applications, such microstructure is not desirable, for certain applications requiring both high strength and ductility of the material, such bimodal microstructures are considered desirable [142, 143]. Of special interest are harmonic microstructures, whereby the fine grained and coarse grained regions in the microstructure are periodically arranged. Owing to the nature of the DRX process in the present material at 300 °C, whereby DRX takes place preferentially at the lamellar $Mg_{17}Al_{12}$ precipitates, which are present at the prior grain boundaries, and whose content (i.e. spread in the grain interior) can be altered by prior heat treatment [24], the material offers a unique route to develop precisely tailored (i.e. desirable extent of fine grained and coarse grained regions) harmonic microstructures. It is of interest to explore this route for developing precisely tailored bimodal microstructure using this approach for this material.

References

[1] N. H. T. S. Administration. [Online]. Available: http://www.nhtsa.gov/staticfiles/rulemaking/pdf/cafe/2017-2025_CAFE-GHG_Supplemental_NOI07292011.pdf.

[2] R. Kuziak, R. Kawalla and S. Waengler, "Advanced high strength steels for automotive industry," *Archives of Civil and Mechanical Engineering,* vol. 8, no. 2, pp. 103-117, 2008.

[3] M. W. Andure, S. C. Jirapure and L. P. Dhamande, "Advance Automobile Material for Light Weight Future – A Review," in *International Conference on Benchmarks in Engineering Science and Technology ICBEST 2012*, 2012.

[4] K. U. Kainer, Magnesium Alloys and Technology, WILEY-VCH Verlag GmbH & Co. KGaA, 2003.

[5] H. E. Friedrich and B. L. Mordike, Magnesium Technology – Metallurgy, Design Data, Applications, Springer, 2006.

[6] M. Kleiner, M. Geiger and A. Klaus, "Manufacturing of Lightweight Components by Metal Forming," *CIRP Annals,* vol. 52, no. 2, pp. 521-542, 2003.

[7] A. A. Luo, "Magnesium casting technology for structural applications," *Journal of Magnesium and Alloys,* vol. 1, no. 1, pp. 2-22, 2013.

[8] M. K. Kulekci, "Magnesium and its alloys applications in automotive industry," *The International Journal of Advanced Manufacturing Technology,* vol. 39, no. 9, p. 851–865, 2008.

[9] Reports, Green Car, "Magnesium The Next Material For Lighter, More Efficient Cars," 19 December 2013. [Online]. Available: https://www.greencarreports.com/news/1089227_magnesium-the-next-material-for-lighter-more-efficient-cars. [Accessed 14 July 2019].

[10] J. Hirsch and T. Al-Samman, "Superior light metals by texture engineering: Optimized aluminum and magnesium alloys for automotive applications," *Acta Materialia,* vol. 61, no. 3, pp. 818-843, 2013.

[11] A. Gryguc, S. K. Shaha, S. B. Behravesh, H. Jahed, M. Wells, B. Williams and X. Su, "Monotonic and cyclic behaviour of cast and cast-forged AZ80 Mg," *International Journal of Fatigue,* vol. 104, pp. 136-149, 2017.

[12] A. Gryguc, S. B. Behravesh, S. K. Shaha, H. Jahed, M. Wells, B. Williams and X. Su, "Low-cycle fatigue characterization and texture induced ratcheting behaviour of forged AZ80 Mg alloys," *International Journal of Fatigue,* vol. 116, pp. 429-438, 2018.

[13] D. Toscano, S. K. Shaha, B. Behravesh, H. Jahed and B. Williams, "Effect of Forging on Microstructure, Texture, and Uniaxial Properties of Cast AZ31B Alloy," *Journal of Materials Engineering and Performance,* vol. 26, no. 7, p. 3090–3103, 2017.

[14] D. Toscano, S. K. Shaha, B. Behravesh, H. Jahed and B. Williams, "Effect of forging on the low cycle fatigue behavior of cast AZ31B alloy," *Materials Science and Engineering: A,* vol. 706, pp. 342-356, 2017.

[15] D. Toscano, S. K. Shaha, B. Behravesh, H. Jahed, B. Williams and X. Su, "Influence of Low Temperature Forging on Microstructure and Low Cycle Fatigue Behavior of Cast AZ31B Mg Alloy," in *Magnesium Technology 2018*, 2018.

[16] S. M. H. Karparvarfard, S. K. Shaha, S. B. Behravesh, H. Jahed and B. W. Williams, "Microstructure, texture and mechanical behavior characterization of hot forged cast ZK60 magnesium alloy," *Journal of Materials Science & Technology,* vol. 33, no. 9, pp. 907-918, 2017.

[17] S. M. H. Karparvarfard, S. K. Shaha, S. B. Behravesh, H. Jahed and B. W. Williams, "Fatigue life improvement of cast ZK60 Mg alloy through low temperature closed-die forging for automotive applications," in *MATEC Web Conferences - 12th International Fatigue Congress (FATIGUE 2018)*, 2018.

[18] S. M. H. Karparvarfard, S. K. Shaha, S. B. Behravesh, H. Jahed and B. W. Williams, "Fatigue characteristics and modeling of cast and cast-forged ZK60 magnesium alloy," *International Journal of Fatigue,* vol. 118, pp. 282-297, 2019.

[19] T. Al-Samman and G. Gottstein, "Room temperature formability of a magnesium AZ31 alloy: Examining the role of texture on the deformation mechanisms," *Materials Science and Engineering A,* vol. 488, no. 1-2, pp. 406-414, 2008.

[20] T. Al-Samman and G. Gottstein, "Dynamic recrystallization during high temperature deformation of magnesium," *Materials Science and Engineering A,* vol. 490, no. 1-2, pp. 411-420, 2008.

[21] P. Backx and L. Kestens, "Dynamic Recrystallization during Compression of Mg-3%Al-1%Zn," *Materials Science Forum,* Vols. 495-497, pp. 633-638, 2005.

[22] X. Li, F. Jiao, T. Al-Samman and S. G. Chowdhury, "Influence of second-phase precipitates on the texture evolution of Mg–Al–Zn alloys during hot deformation," *Scripta Materialia,* vol. 66, no. 3-4, pp. 159-162, 2012.

[23] S. W. Xu, N. Matsumoto, S. Kamado, T. Honma and Y. Kojima, "Effect of Mg17Al12 precipitates on the microstructural changes and mechanical properties of hot compressed AZ91 magnesium alloy," *Materials Science and Engineering A,* vol. 523, no. 1-2, pp. 47-52, 2009.

[24] S. W. Xu, N. Matsumoto, S. Kamado, T. Honma and Y. Kojima, "Effect of pre-aging treatment on microstructure and mechanical properties of hot compressed Mg–9Al–1Zn alloy," *Materials Science and Engineering A,* vol. 517, no. 1-2, pp. 354-360, 2009.

[25] W. F. Hosford, Mechanical Behaviour of Materials, Cambridge University Press, 2009.

[26] G. Gottstein, "Recovery, Recrystallization, Grain Growth," in *Physical Foundations of Materials Science*, Springer Verlag, 2004, pp. 303-356.

[27] M. H. Yoo, "Slip, twinning, and fracture in hexagonal close-packed metals," *Metallurgical and Materials Transactions A,* vol. 12, no. 3, p. 409–418, 1981.

[28] G. Taylor and H. Quinney, "The plastic distortion of metals," *Philosophical Transactions of the Royal Society A,* vol. 230, no. 681-693, pp. 323-362, 1931.

[29] M. R. Barnett, "Twinning and the ductility of magnesium alloys: Part I: “Tension” twins," *Materials Science and Engineering A,* vol. 464, no. 1-2, pp. 1-7, 2007.

[30] M. R. Barnett, "Twinning and the ductility of magnesium alloys: Part II. “Contraction” twins," *Materials Science and Engineering A,* vol. 464, no. 1-2, pp. 8-16, 2007.

[31] T. Al-Samman, "Magnesium – The Role of Crystallographic Texture, Deformation Conditions and Alloying Elements on Formability," RWTH Aachen University, Aachen, 2008.

[32] M. R. Barnett, Z. Keshavarz, A. G. Beer and X. Ma, "Non-Schmid behaviour during secondary twinning in a polycrystalline magnesium alloy," *Acta Materialia,* vol. 56, no. 1, pp. 5-15, 2008.

[33] S. W. Xu, S. Kamado, N. Matsumoto, T. Honma and Y. Kojima, "Recrystallization mechanism of as-cast AZ91 magnesium alloy during hot compressive deformation," *Materials Science and Engineering A,* vol. 527, no. 1-2, pp. 52-60, 2009.

[34] M. D. Nave and M. R. Barnett, "Microstructures and textures of pure magnesium deformed in plane-strain compression," *Scripta Materialia,* vol. 51, no. 9, pp. 881-885, 2004.

[35] O. Sitdikov and R. Kaibyshev, "Dynamic Recrystallization in Pure Magnesium," *Materials Transactions,* vol. 42, no. 9, pp. 1928-1937, 2001.

[36] O. Sitdikov, R. Kaibyshev and T. Sakai, "Dynamic Recrystallization Based on Twinning in Coarse-Grained Mg," 2003.

[37] M. R. Barnett, "A Taylor model based description of the proof stress of magnesium AZ31 during hot working," *Metallurgical and Materials Transactions A,* vol. 34, pp. 1799-1806, 2003.

[38] W. B. Hutchinson and M. R. Barnett, "Effective values of critical resolved shear stress for slip in polycrystalline magnesium and other hcp metals," *Scripta Materialia,* vol. 63, no. 7, pp. 737-740, 2010.

[39] A. Chapuis and J. H. Driver, "Temperature dependency of slip and twinning in plane strain compressed magnesium single crystals," *Acta Materialia,* vol. 59, no. 5, pp. 1986-1994, 2011.

[40] J. Koike, T. Koboyashi, T. Mukai, H. Watanabe, M. Suzuki, K. Maruyama and K. Higashi, "The activity of non-basal slip systems and dynamic recovery at room temperature in fine-grained AZ31B magnesium alloys," *Acta Materialia,* vol. 51, no. 7, pp. 2055-2065, 2003.

[41] T. Walde and H. Riedel, "Modeling texture evolution during hot rolling of magnesium alloy AZ31," *Materials Science and Engineering A,* vol. 443, no. 1-2, pp. 277-284, 2007.

[42] Q. Dai, D. Zhang and X. Chen, "On the anisotropic deformation of AZ31 Mg alloy under compression," *Materials & Design,* vol. 32, no. 10, pp. 5004-5009, 2011.

[43] L. Liu and H. Ding, "Study of the plastic flow behaviors of AZ91 magnesium alloy during thermomechanical processes," *Journal of Alloys and Compounds,* vol. 484, no. 1-2, pp. 949-956, 2009.

[44] F. J. Humphreys and M. Hatherly, "Recrystallization of Single-Phase Alloys," in *Recrystallization and Related Annealing Phenomena*, Second, Ed., Elsevier, 2004, pp. 215-267.

[45] S. E. Ion, F. J. Humphreys and S. H. White, "Dynamic recrystallisation and the development of microstructure during the high temperature deformation of magnesium," *Acta Metallurgica,* vol. 30, no. 10, pp. 1909-1919, 1982.

[46] X. Yang, H. Miura and T. Sakai, "Dynamic Evolution of New Grains in Magnesium Alloy AZ31 during Hot Deformation," *Materials Transactions,* vol. 44, no. 1, pp. 197-203, 2003.

[47] A. Galiyev, R. Kaibyshev and G. Gottstein, "Correlation of plastic deformation and dynamic recrystallization in magnesium alloy ZK60," *Acta Materialia,* vol. 49, no. 7, pp. 1199-1207, 2001.

[48] S. M. Fatemi-Varzaneh, A. Zarei-Hanzaki and H. Beladi, "Dynamic recrystallization in AZ31 magnesium alloy," *Materials Science and Engineering A,* vol. 456, no. 1-2, pp. 52-57, 2007.

[49] F. Humphreys and M. Hatherly, "The Deformed State," in *Recrystallization and Related Annealing Phenomena*, Second ed., Elsevier, 2004, pp. 11-65.

[50] H. Miura, M. Ito, X. Yang and J. J. Jonas, "Mechanisms of grain refinement in Mg–6Al–1Zn alloy during hot deformation," *Materials Science and Engineering A,* vol. 538, pp. 63-68, 2012.

[51] R. D. Doherty, D. A. Hughes, F. J. Humphreys, J. J. Jonas, D. J. Jensen, M. E. Kassner, W. E. King, T. R. McNelley, H. J. McQueen and A. D. Rollett, "Current issues in recrystallization: a review," *Materials Science and Engineering A,* vol. 238, no. 2, pp. 219-274, 1997.

[52] J. D. Robson, D. T. Henry and B. Davis, "Particle effects on recrystallization in magnesium–manganese alloys: Particle-stimulated nucleation," *Acta Materialia,* vol. 57, no. 9, pp. 2739-2747, 2009.

[53] F. J. Humphreys and M. Hatherly, "Recrystallization of Two-Phase Alloys," in *Recrystallization and Related Annealing Phenomena*, Second ed., Elsevier, 2004, pp. 285-319.

[54] S. L. Couling, J. F. Pashak and L. Sturkey, "Unique deformation and aging characteristics of certain magnesium-base alloys," *Transactions of American Society for Metals,* vol. 51, pp. 94-107, 1959.

[55] M. R. Barnett, M. D. Nave and C. J. Bettles, "Deformation microstructures and textures of some cold rolled Mg alloys," *Materials Science and Engineering A,* vol. 386, p. 205–211, 2004.

[56] Y. B. Chun and C. H. J. Davies, "Texture effects on development of shear bands in rolled AZ31 alloy," *Materials Science and Engineering A,* vol. 556, pp. 253-259, 2012.

[57] D. K. Sun, C. P. Chang and P. W. Kao, "Microstructural study of strain localization in hot compressed Mg–3Al–1Zn alloy," *Materials Science and Engineering A,* vol. 527, no. 26, pp. 7050-7056, 2010.

[58] University of Cambridge, "Geometry during slip," Dissemination of IT for the Promotion of Materials Science (DoITPoMS), [Online]. Available: https://www.doitpoms.ac.uk/tlplib/slip/geometry_during_slip.php.

[59] S. R. Agnew, M. H. Yoo and C. N. Tomé, "Application of texture simulation to understanding mechanical behavior of Mg and solid solution alloys containing Li or Y," *Acta Materialia,* vol. 49, no. 20, pp. 4277-4289, 2001.

[60] T. Al-Samman, X. Li and S. G. Chowdhury, "Orientation dependent slip and twinning during compression and tension of strongly textured magnesium AZ31 alloy," *Materials Science and Engineering A,* vol. 527, no. 15, pp. 3450-3463, 2010.

[61] J. d. Valle and O. A. Ruano, "Influence of texture on dynamic recrystallization and deformation mechanisms in rolled or ECAPed AZ31 magnesium alloy," *Materials Science and Engineering A,* vol. 487, no. 1-2, pp. 473-480, 2008.

[62] M. R. Barnett, Z. Kehsavarz, A. G. Beer and D. Atwell, "Influence of grain size on the compressive deformation of wrought Mg–3Al–1Zn," *Acta Materialia,* vol. 52, no. 17, pp. 5093-5103, 2004.

[63] N. Stanford and M. R. Barnett, "Solute strengthening of prismatic slip, basal slip and {10-12} twinning in Mg and Mg–Zn binary alloys," *International Journal of Plasticity,* vol. 47, p. 165–181, 2013.

[64] B. Raeisinia and S. R. Agnew, "Using polycrystal plasticity modeling to determine the effects of grain size and solid solution additions on individual deformation mechanisms in cast Mg alloys," *Scripta Materialia,* vol. 63, no. 7, p. 731–736, 2010.

[65] B. Raeisinia, S. R. Agnew and A. Akhtar, "Incorporation of Solid Solution Alloying Effects into Polycrystal Modeling of Mg Alloys," *Metallurgical and Materials Transactions A,* vol. 42, no. 5, p. 1418–1430, 2011.

[66] M. R. Barnett, A. G. Beer, D. Atwell and A. Oudin, "Influence of grain size on hot working stresses and microstructures in Mg–3Al–1Zn," *Scripta Materialia,* vol. 51, no. 1, pp. 19-24, 2004.

[67] A. G. Beer and M. R. Barnett, "Microstructural Development during Hot Working of Mg-3Al-1Zn," *Metallurgical and Materials Transactions A,* vol. 38, no. 8, p. 1856–1867, 2007.

[68] C. M. Sellars, "Recrystallization of metals," *Metals Forum,* vol. 4, pp. 75-80, 1981.

[69] H. Watanabe, H. Tsutsui, T. Mukai, K. Ishikawa, Y. Okanda, M. Kohzu and K. Higashi, "Grain Size Control of Commercial Wrought Mg-Al-Zn Alloys Utilizing Dynamic Recrystallization," *Materials Transactions,* vol. 42, no. 7, pp. 1200-1205, 2001.

[70] R. Gehrmann, M. M. Frommert and G. Gottstein, "Texture effects on plastic deformation of magnesium," *Materials Science and Engineering A,* vol. 395, no. 1-2, pp. 338-349, 2005.

[71] M. R. Barnett, "Influence of deformation conditions and texture on the high temperature flow stress of magnesium AZ31," *Journal of Light Metals,* vol. 1, no. 3, pp. 167-177, 2001.

[72] B. H. Lee, S. H. Park, S.-G. Hong, K.-T. Park and C. S. Lee, "Role of initial texture on the plastic anisotropy of Mg–3Al–1Zn alloy at various temperatures," *Materials Science and Engineering A,* vol. 528, no. 3, p. 1162–1172, 2011.

[73] T. W. Wong, A. Hadadzadeh and M. A. Wells, "High temperature deformation behavior of extruded AZ31B magnesium alloy," *Journal of Materials Processing Technology,* vol. 251, pp. 360-368, 2018.

[74] K. P. Rao, Y. V. R. K. Prasad and K. Suresh, "Materials modeling and simulation of isothermal forging of rolled AZ31B magnesium alloy: Anisotropy of flow," *Materials & Design,* vol. 32, no. 5, pp. 2545-2553, 2011.

[75] D. Kobold, T. Pepelnjak, G. Gantar and K. Kuzman, "Analysis of Deformation Characteristics of Magnesium AZ80 Wrought Alloy under Hot Conditions," *Journal of Mechanical Engineering,* vol. 56, no. 12, pp. 823-832, 2010.

[76] R. O. Kaibyshev, B. K. Sokolov and A. M. Galiyev, "The Influence of Crystallographic Texture on Dynamic Recrystallization," *Textures and Microstructures,* vol. 32, no. 1-4, pp. 47-63, 1999.

[77] M. R. Barnett, "Quenched and Annealed Microstructures of Hot Worked Magnesium AZ31," *Materials Transactions,* vol. 44, no. 4, pp. 571-577, 2003.

[78] M. Wang, R. Xin, B. Wang and Q. Liu, "Effect of initial texture on dynamic recrystallization of AZ31 Mg alloy during hot rolling," *Materials Science and Engineering A,* vol. 528, no. 6, p. 2941–2951, 2011.

[79] N. V. Dudamell, I. Ulacia, F. Gálvez, S. Yi, J. Bohlen, D. Letzig, I. Hurtado and M. T. Pérez-Prado, "Influence of texture on the recrystallization mechanisms in an AZ31 Mg sheet alloy at dynamic rates," *Materials Science and Engineering A,* vol. 532, p. 528– 535, 2012.

[80] A. Akhtar and E. Teghtsoonian, "Substitutional solution hardening of magnesium single crystals," *Philosophical Magazine,* vol. 25:4, pp. 897-916, 1972.

[81] C. H. Cáceres and D. M. Rovera, "Solid solution strengthening in concentrated Mg–Al alloys," *Journal of Light Metals,* vol. 1, no. 3, pp. 151-156, 2001.

[82] A. K. Mahato, "The effect of composition and temperature on the deformation behaviour of magnesium-aluminium binary alloys," Deakin University, Victoria, 2016.

[83] J. D. Robson, "Effect of Rare-Earth Additions on the Texture of Wrought Magnesium Alloys: The Role of Grain Boundary Segregation," *Metallurgical and Materials Transactions A,* vol. 45, no. 8, p. 3205–3212, 2014.

[84] F. Guo, D. Zhang, H. Wu, L. Jiang and F. Pan, "The role of Al content on deformation behavior and related texture evolution during hot rolling of Mg-Al-Zn alloys," *Journal of Alloys and Compounds,* vol. 695, pp. 396-403, 2017.

[85] F. Guo, D. Zhang, X. Yang, L. Jiang and F. Pan, "Strain-induced dynamic precipitation of Mg17Al12 phases in Mg–8Al alloys sheets rolled at 748 K," *Materials Science and Engineering A,* vol. 636, pp. 516-521, 2015.

[86] T. W. Wong, A. Hadadzadeh, M. J. Benoit and M. A. Wells, "Impact of homogenization heat treatment on the high temperature deformation behavior of cast AZ31B magnesium alloy," *Journal of Materials Processing Technology,* vol. 254, pp. 238-247, 2018.

[87] I. A. Yakubtsov, B. J. Diak, C. A. Sager, B. Bhattacharya, W. D. MacDonald and M. Niewczas, "Effects of heat treatment on microstructure and tensile deformation of Mg AZ80 alloy at room temperature," *Materials Science and Engineering A,* vol. 496, no. 1-2, pp. 247-255, 2008.

[88] L. Jiang, D. Zhang, X. Fan, F. Guo, G. Hu, H. Xue and F. Pan, "The effect of Sn addition on aging behavior and mechanical properties of wrought AZ80 magnesium alloy," *Journal of Alloys and Compounds,* vol. 620, pp. 368-375, 2015.

[89] D. Duly, J. P. Simon and Y. Brechet, "On the competition between continuous and discontinuous precipitations in binary Mg-Al alloys," *Acta Metallurgica et Materialia,* vol. 43, no. 1, pp. 101-106, 1995.

[90] K. N. Braszczyńska-Malik, "Discontinuous and continuous precipitation in magnesium–aluminium type alloys," *Journal of Alloys and Compounds,* vol. 477, no. 1-2, pp. 870-876, 2009.

[91] S. Celotto, "TEM study of continuous precipitation in Mg–9 wt%Al–1 wt%Zn alloy," *Acta Materialia,* vol. 48, no. 8, pp. 1775-1787, 2000.

[92] W.-J. Lai, Y.-Y. Li, Y.-F. Hsu, S. Trong and W.-H. Wang, "Aging behaviour and precipitate morphologies in Mg–7.7Al–0.5Zn–0.3Mn (wt.%) alloy," *Journal of Alloys and Compounds,* vol. 476, no. 1-2, pp. 118-124, 2009.

[93] T. Y. Kwak and W. J. Kim, "Hot compression behavior of the 1 wt% calcium containing Mg–8Al–0.5Zn (AZ80) alloy fabricated using electromagnetic casting technology," *Materials Science & Engineering A,* vol. 615, p. 222–230, 2014.

[94] D. A. Porter, K. E. Easterling and M. Y. Sherif, Phase Transformations in Metals and Alloys, CRC Press, 2009.

[95] J. B. Clark, "Age hardening in a Mg-9 wt.% Al alloy," *Acta Metallurgica,* vol. 16, no. 2, pp. 141-152, 1968.

[96] H. R. Abedi, A. Zarei-Hanzaki, M. B. Biucki and M. Emamy, "Evaluating the room temperature mechanical properties of age hardened AZ80 magnesium alloy using shear punch testing method," *Materials Science and Engineering A,* vol. 606, pp. 360-369, 2014.

[97] P. Changizian, A. Zarei-Hanzaki and H. Abedi, "On the recrystallization behavior of homogenized AZ81 magnesium alloy: The effect of mechanical twins and γ precipitates," *Materials Science and Engineering A,* vol. 558, pp. 44-51, 2012.

[98] J. D. Robson, N. Stanford and M. R. Barnett, "Effect of precipitate shape on slip and twinning in magnesium alloys," *Acta Materialia,* vol. 59, no. 5, pp. 1945-1956, 2011.

[99] S. R. Agnew, R. P. Mulay, F. J. P. III, C. A. Calhoun, J. J. Bhattacharyya and B. Clausen, "In situ neutron diffraction and polycrystal plasticity modeling of a Mg–Y–Nd–Zr alloy: Effects of precipitation on individual deformation mechanisms," *Acta Materialia,* vol. 61, no. 10, pp. 3769-3780, 2013.

[100] J. Wang and N. Stanford, "Investigation of precipitate hardening of slip and twinning in Mg5%Zn by micropillar compression," *Acta Materialia,* vol. 100, pp. 53-63, 2015.

[101] J. F. Nie, "Effects of precipitate shape and orientation on dispersion strengthening in magnesium alloys," *Scripta Materialia,* vol. 48, no. 8, pp. 1009-1015, 2003.

[102] F. Wang, J. J. Bhattacharyya and S. R. Agnew, "Effect of precipitate shape and orientation on Orowan strengthening of non-basal slip modes in hexagonal crystals, application to magnesium alloys," *Materials Science and Engineering A,* vol. 666, pp. 114-122, 2016.

[103] M. R. Barnett, D. Atwell and A. G. Beer, "Grain Size in Mg Alloys: Recrystallization and Mechanical Consequences," *Materials Science Forum,* Vols. 558-559, pp. 433-440, 2007.

[104] E. I. Poliak and J. J. Jonas, "A one-parameter approach to determining the critical conditions for the initiation of dynamic recrystallization," *Acta Materialia,* vol. 44, no. 1, pp. 127-136, 1996.

[105] E. I. Poliak and J. J. Jonas, "Initiation of Dynamic Recrystallization in Constant Strain Rate Hot Deformation," *ISIJ International,* vol. 43, no. 5, pp. 684-691, 2003.

[106] J. J. Jonas, X. Quelennec, L. Jiang and É. Martin, "The Avrami kinetics of dynamic recrystallization," *Acta Materialia,* vol. 57, no. 9, pp. 2748-2756, 2009.

[107] G. R. Stewart, A. M. Elwazri, S. Yue and J. J. Jonas, "Modelling of dynamic recrystallisation kinetics in austenitic stainless and hypereutectoid steels," *Materials Science and Technology,* vol. 22, no. 5, pp. 519-524, 2006.

[108] G.-Z. Quan, Y. Shi, Y.-X. Wang, B.-S. Kang, T.-W. Ku and W.-J. Song, "Constitutive modeling for the dynamic recrystallization evolution of AZ80

magnesium alloy based on stress-strain data," *Materials Science and Engineering A,* vol. 528, no. 28, pp. 8051-8059, 2011.

[109] B.-J. Lv, J. Peng, D.-W. Shi, A.-T. Tang and F.-S. Pan, "Constitutive modeling of dynamic recrystallization kinetics and processing maps of Mg–2.0Zn–0.3Zr alloy based on true stress–strain curves," *Materials Science and Engineering A,* vol. 560, pp. 727-733, 2013.

[110] A. Dehghan-Manshadi, M. R. Barnett and P. D. Hodgson, "Recrystallization in AISI 304 austenitic stainless steel during and after hot deformation," *Materials Science and Engineering A,* vol. 485, no. 1-2, pp. 664-672, 2008.

[111] C. M. Sellars and J. A. Whiteman, "Recrystallization and Grain Growth in Hot Rolling," *Metal Science,* vol. 13, no. 3-4, pp. 187-194, 1979.

[112] J. Wang, J. Chen, Z. Zhao and X.-y. Ruan, "Dynamic Recrystallization Behavior of Microalloyed Forged Steel," *Journal of Iron and Steel Research, International,* vol. 15, no. 3, pp. 78-81, 91, 2008.

[113] M. R. Barnett, "Hot working microstructure map for magnesium AZ31," *Material Science Forum,* vol. 426–432, p. 515–520, 2003.

[114] J. P. Sah, G. J. Richardson and C. M. Sellars, "Grain-Size Effects during Dynamic Recrystallization of Nickel," *Metal Science,* vol. 8, no. 1, pp. 325-331, 1974.

[115] T. Sakai and J. J. Jonas, "Overview no. 35 Dynamic recrystallization: Mechanical and microstructural considerations," *Acta Metallurgica ,* vol. 32, no. 2, pp. 189-209, 1984.

[116] J. C. Tan and M. J. Tan, "Dynamic continuous recrystallization characteristics in two stage deformation of Mg–3Al–1Zn alloy sheet," *Materials Science and Engineering A,* vol. 399, no. 1-2, pp. 124-132, 2003.

[117] Z. Zhang, Q. Le and J. Cui, "Structure and mechanical properties of AZ31 magnesium alloy billets by different hot-top semi-continuous casting technology," *Rare Metals,* vol. 30, pp. 414-418, 2011.

[118] GLEEBLE, "GLEEBLE® 3500-GTC SYSTEM," [Online]. Available: https://www.gleeble.com/products/gleeble-systems/gleeble-3500.html. [Accessed 14 July 2019].

[119] T. V. Padfield, "Metallography and Microstructures of Magnesium and Its Alloys," in *ASM Handbook Volume 9 - Metallography and Microstructures*, G. F. V. Voort, Ed., ASM International, 2004, pp. 801-815.

[120] A. J. Schwartz, M. Kumar, B. L. Adams and D. P. Field, Eds., Electron Backscatter Diffraction in Materials Science, Second ed., Springer, 2000.

[121] Max-Planck-Institut für Eisenforschung GmbH, "Electron backscatter diffraction - EBSD," [Online]. Available: https://www.mpie.de/3077954/EBSD. [Accessed 14 July 2019].

[122] EDAX, OIM Analysis v8, EDAX, 2016.

[123] J. Liu, Z. Cui and C. Li, "Modelling of flow stress characterizing dynamic recrystallization for magnesium alloy AZ31B," *Computational Materials Science,* vol. 41, no. 3, pp. 375-382 , 2008.

[124] H. Watanabe, T. Mukai, M. Kohzu, S. Tanabe and K. Higashi, "Effect of temperature and grain size on the dominant diffusion process for superplastic flow in an AZ61 magnesium alloy," *Acta Materialia,* vol. 47, no. 14, pp. 3753-3758, 1999.

[125] W. -J. Kim, S. W. Chung, C. C. S. and D. Kum, "Superplasticity in thin magnesium alloy sheets and deformation mechanism maps for magnesium alloys at elevated temperatures," *Acta Materialia,* vol. 49, no. 16, pp. 3337-3345, 2001.

[126] K. Hirai, H. Somekawa, Y. Takigawa and K. Higashi, "Superplastic forging with dynamic recrystallization of Mg–Al–Zn alloys cast by thixo-molding," *Scripta Materialia,* vol. 56, no. 3, pp. 237-240, 2007.

[127] H. J. Frost and M. F. Ashby, Deformation-Mechanism Maps: The Plasticity and Creep of Metals and Ceramics, Pergamon Press, Oxford, 1982, p. 44.

[128] S. S. Vagarali and T. G. Langdon, "Deformation mechanisms in h.c.p. metals at elevated temperatures—II. Creep behavior of a Mg-0.8% Al solid solution alloy," *Acta Metallurgica,* vol. 30, no. 6, pp. 1157-1170 , 1982.

[129] C. D. Barrett, A. Imandoust, A. L. Oppedal, K. Inal, M. A.Tschopp and H. E. Kadiri, "Effect of grain boundaries on texture formation during dynamic recrystallization of magnesium," *Acta Materialia ,* vol. 128, pp. 270-283 , 2017.

[130] G. Gottstein, "Mechanical Properties," in *Physical Foundations of Materials Science*, Springer, 2004, pp. 197-302.

[131] B. Derby, "The dependence of grain size on stress during dynamic recrystallisation," *Acta Metallurgica et Materialia,* vol. 39, no. 5, pp. 955-962, 1991.

[132] X. Yang, H. Miura and T. Sakai, "Dynamic nucleation of new grains in magnesium alloy during hot deformation," *Materials Science Forum,* Vols. 419-422, pp. 515-520, 2003.

[133] A. Hadadzadeh, M. A. Wells, S. K. Shaha, H. Jahed and B. W. Williams, "Role of compression direction on recrystallization behavior and texture evolution

during hot deformation of extruded ZK60 magnesium alloy," *Journal of Alloys and Compounds,* vol. 702, p. 274–289, 2017.

[134] Z. Ding-fei, G.-l. Shi, X.-b. Zhao and F.-g. Qi, "Microstructure evolution and mechanical properties of Mg-x% Zn-1% Mn (x= 4, 5, 6, 7, 8, 9) wrought magnesium alloys," *Transactions of Nonferrous Metals Society of China,* vol. 21, no. 1, pp. 15-25, 2011.

[135] T. W. Wong, "High Temperature Forging of AZ31B Magnesium Alloy," University of Waterloo, Waterloo, Ontario, Canada, 2016.

[136] P. Skubisz, J. Sinczak and S. Bednarek, "Forgeability of Mg–Al–Zn magnesium alloys in hot and warm closed die forging," *Journal of Materials Processing Technology,* vol. 177, pp. 210-213, 2006.

[137] F. Ju, Z. Xia, B. Diak, O. Ojo, W. MacDonald and M. Niewczas, "Modeling and simulation of Mg AZ80 alloy forging behaviour," *SAE International,* 2007.

[138] Z. Su, L. Wan, C. Sun, Y. Cai and D. Yang, "Hot deformation behavior of AZ80 magnesium alloy towards optimization of its hot workability," *Materials Characterization,* vol. 122, pp. 90-97, 2016.

[139] H.-y. Wu, J.-c. Yang, F.-j. Zhu and H.-c. Liu, "Hot deformation characteristics of as-cast and homogenized AZ61 Mg alloys under compression," *Materials Science and Engineering A,* vol. 550, p. 273– 278 , 2012.

[140] S. Mandal, M. Jayalakshmi, A. K. Bhaduri and V. S. Sarma, "Effect of Strain Rate on the Dynamic Recrystallization Behavior in a Nitrogen-Enhanced 316L(N)," *Metallurgical and Materials Transactions A,* vol. 45, no. 12, p. 5645–5656, 2014.

[141] A. G. Beer and M. R. Barnett, "Microstructure evolution in hot worked and annealed magnesium alloy AZ31," *Materials Science and Engineering A,* vol. 485, no. 1-2, pp. 318-324, 2008.

[142] D. Orlov, H. Fujiwara and K. Ameyama, "Obtaining Copper with Harmonic Structure for the Optimal Balance of Structure-Performance Relationship," *Materials Transactions,* vol. 54, no. 9, p. 1549 to 1553, 2013.

[143] S. Asqardoust, A. Z. Hanzaki, H. R. Abedi, T. Krajnak and P. Minárik, "Enhancing the strength and ductility in accumulative back extruded WE43 magnesium alloy through achieving bimodal grain size distribution and texture weakening," *Materials Science and Engineering A,* vol. 698, pp. 218-229, 2017.

Appendix A

XRD phase analysis results on the as-received starting materials

The XRD phase identification results on the starting alloys are presented in this section.

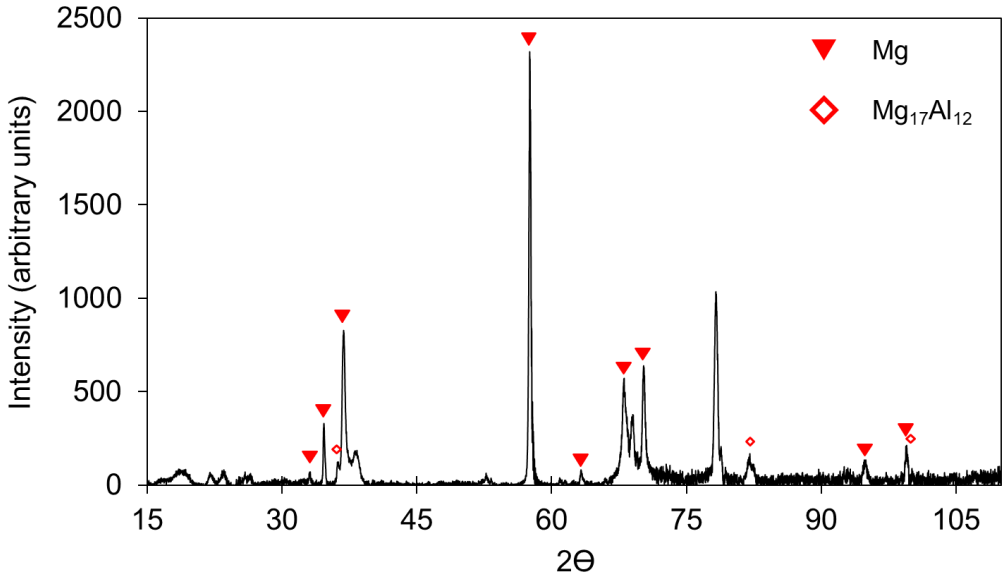

Figure A-1 XRD phase identification analysis of cast AZ31 alloy

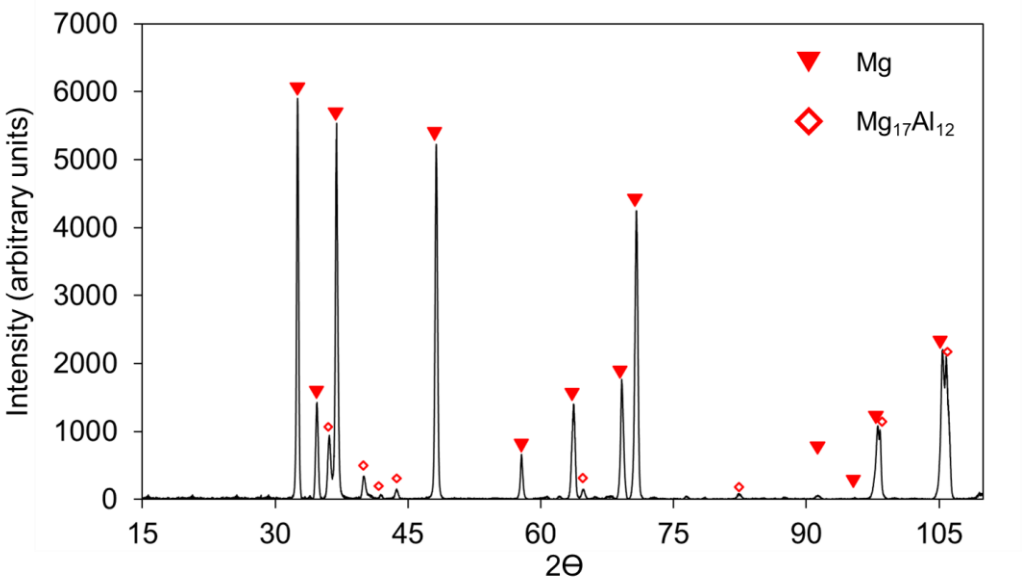

Figure A-2 XRD phase identification analysis of cast AZ80 alloy

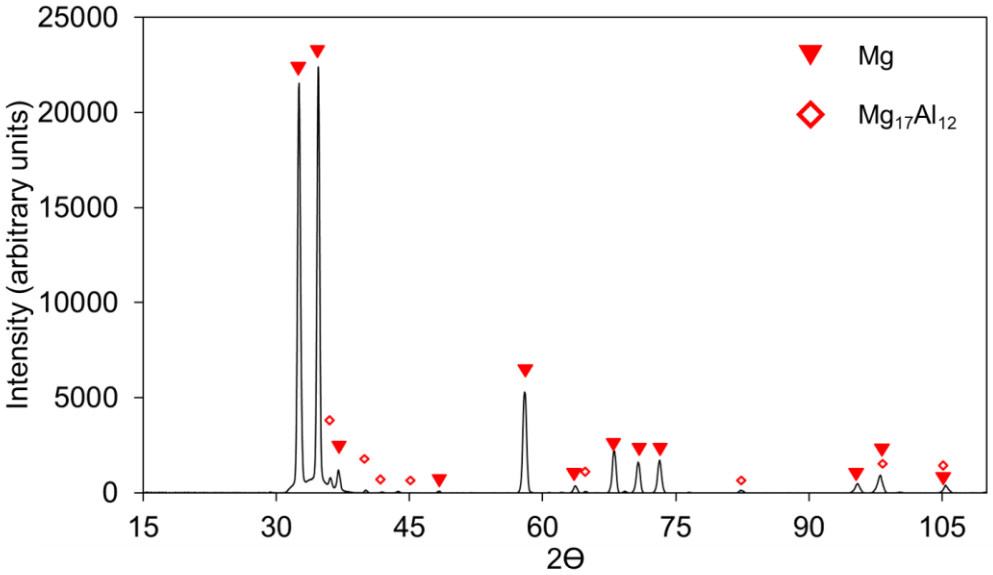

Figure A-3 XRD phase identification analysis of extruded AZ80 alloy

Appendix B

Grain size determination

This section shows the methodology used to calculate the average grain size from optical micrographs, and how it relates to the average grain size of the same material determined using the EBSD data. The line intercept method is illustrated in Figure B-1 and Table B-1, taking the example of as-extruded AZ80 material. It is noteworthy that the average line intercept value is typically scaled by a factor of 1.74 to determine the actual grain size value (i.e. $d = 1.74 * L$, where d is the equivalent grain diameter, while L is the average intercept length), in order to account for the three dimensional nature of the grains [69].

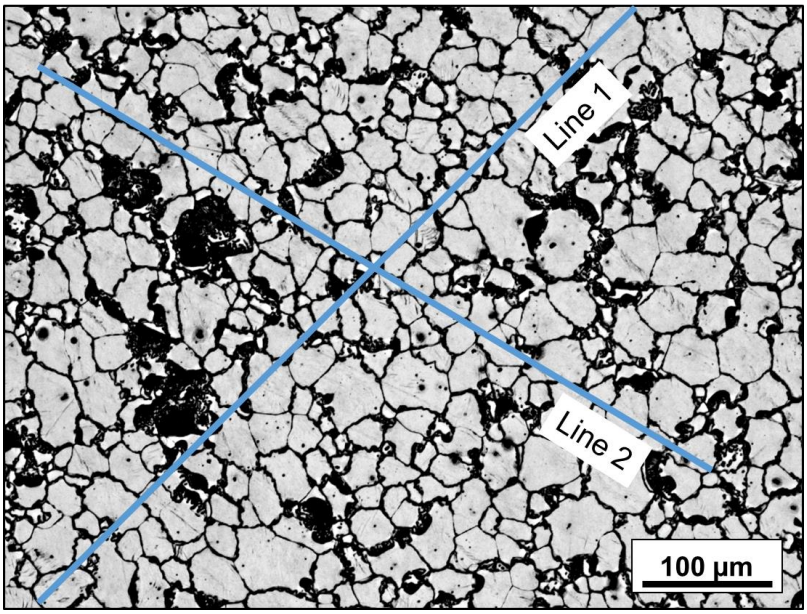

Figure B-1 Optical micrograph of the as-received extruded AZ80 alloy. Straight lines were drawn to intersect as many grains as possible. The number of grains intercepted by them were determined and average intercept length calculated.

Table B-1 Calculations for the average grain size based on the line intercept measurements. L represent average intercept length per grain, while d represents equivalent grain diameter. Average and standard deviation calculations were performed on d.

Line #	Length (µm)	# Intercepts	# Grains	L (µm)	d (µm)= 1.74 * L
1	648.8	36.5	35.5	18.3	**31.8**
2	604.4	31	30	20.1	**35.0**
Average Grain Size					**33.4 ± 1.6 µm**

In the current work, the optical micrographs were used for the grain size calculations only for the as-received materials, while for the deformed samples, grains sizes were determined from the EBSD data, automatically using the specific grain size tool. The grain size determined using the optical micrographs is based on intercepting at least 100 grains, while that using the EBSD data is based on measuring at least 500 grains. The grain size values determined using the two methods on the same sample are compared in Table B-2. The average grain size values are similar, while the standard deviation value is significantly larger in case of the EBSD data.

Table B-2 Average grain size value in the as-received extruded material determined using the two methods described above.

Optical Micrographs	34.8 ± 4.7 µm
EBSD	33.6 ±14.4 µm

Appendix C

Additional grain size criterion to identify DRXed grains in less deformed samples of extruded AZ80 alloy

The GOS distribution in the as-extruded material is presented in Figure C-1 (a), and indicates that most of the grains had a GOS less than 1°. Thereby, using a purely GOS based criterion will create issues with correctly identifying the DRXed grains in less deformed samples. As in the case of the cast material, it was determined that for deformation at 400 °C, 0.1 s^{-1}, new grains got generated within the grain size range of 2-20 µm (Figure C-1 (b)), which suggested that the DRX grains had size smaller than 20 µm. Considering this, a combined criteria of GOS ≤ 2°, and grain size ≤ 20 µm was used to identify the DRXed grains in the extruded deformed samples (as in the case of the cast deformed samples). For deformation at 0.001 s^{-1}, at the same temperature, the grain size distribution was very wide (Figure C-1 (c)), and comparable to the distribution in the starting material, and therefore a suitable upper limit to the DRX grain size could not be determined. Therefore the DRX quantification is limited to the strain rate of 0.1 s^{-1}.

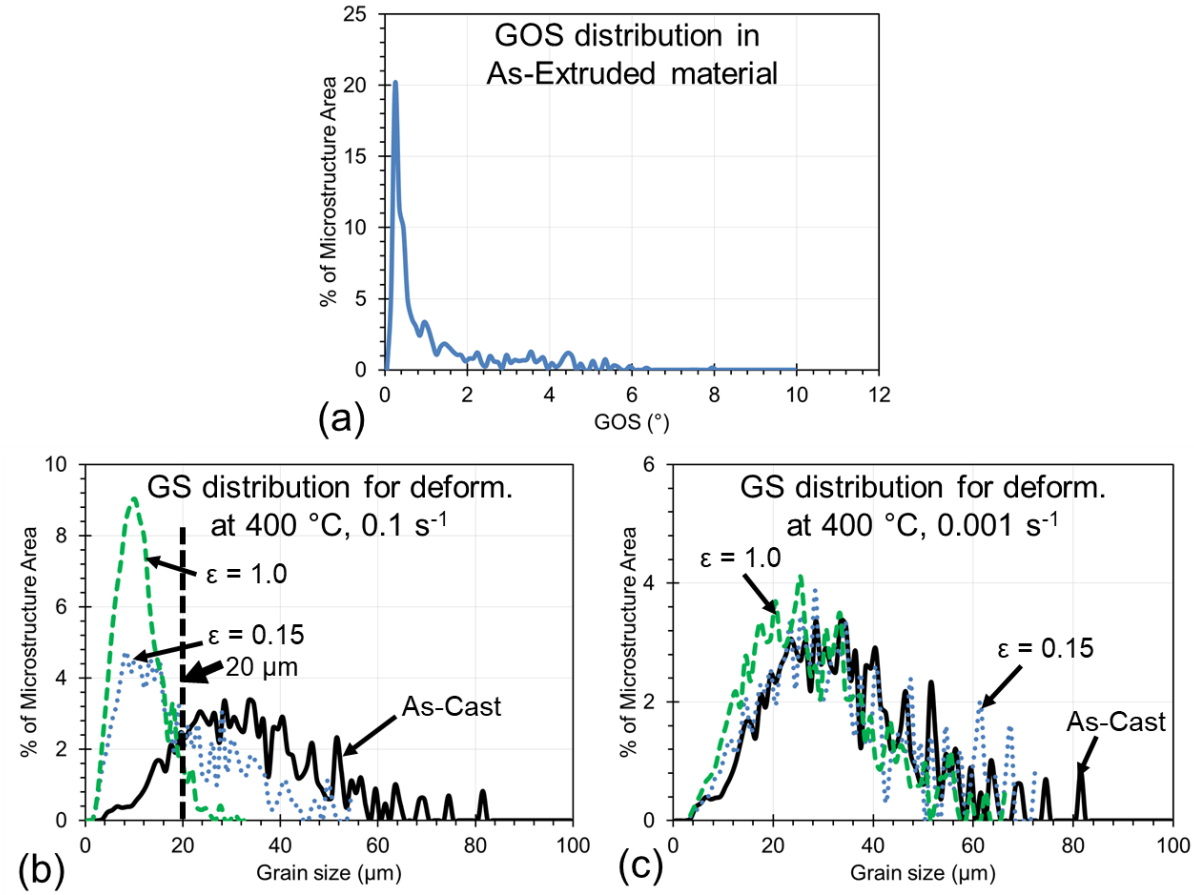

Figure C-1 Developing a grain size based criterion to identify DRXed grains at low strain levels in the extruded AZ80 samples (ED) deformed at 400 °C: (a) GOS distribution in the as-extruded material, (b) Grain size distribution in the ED samples deformed at 0.1 s^{-1}, (c) Grain size distribution in the ED samples deformed at 0.001 s^{-1}. EBSD data was used to generate all the above plots. GS in (b-c) refer to grain size.

Appendix D

Flow stress data for all tested conditions

The flow stress data for the different starting materials for all the tested deformation conditions are presented in this section.

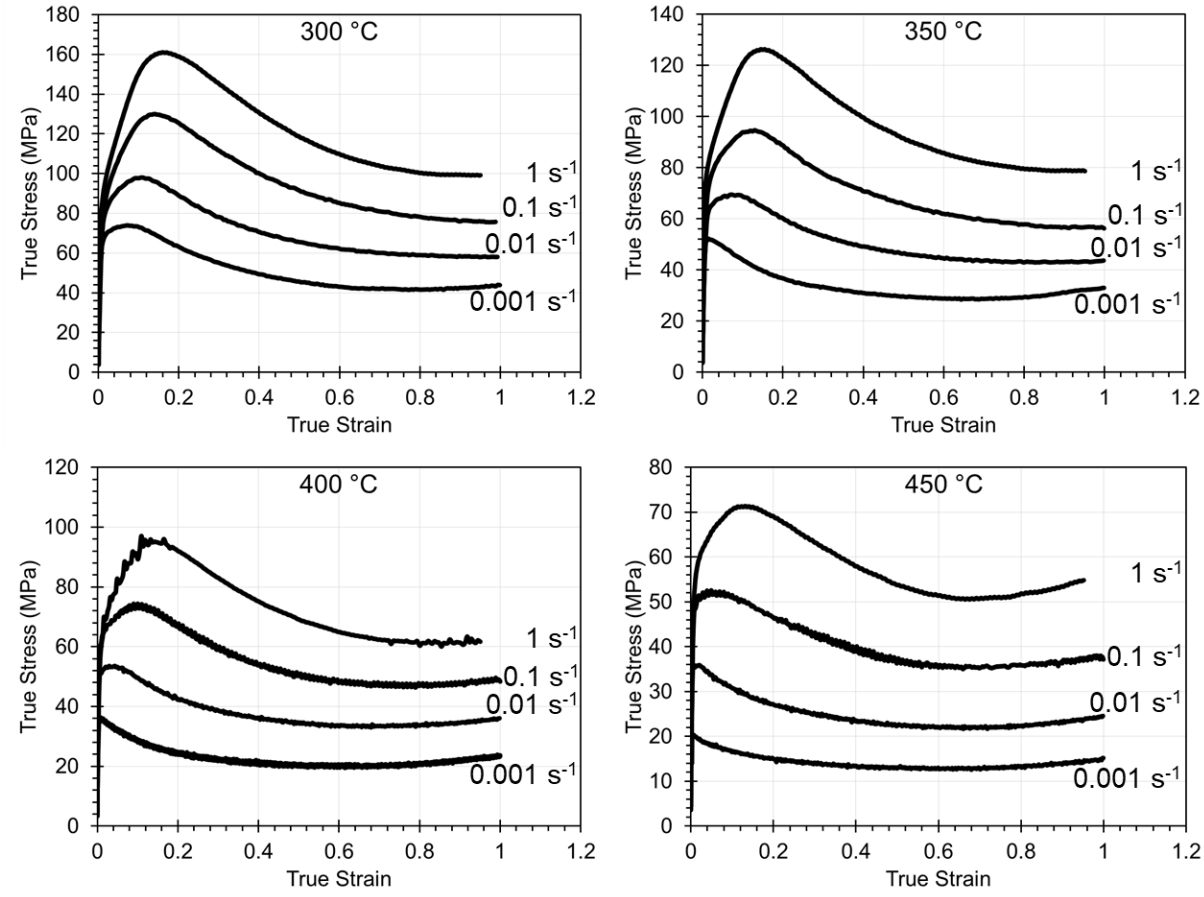

Figure D-1 Flow stress curves of the cast AZ80 alloy

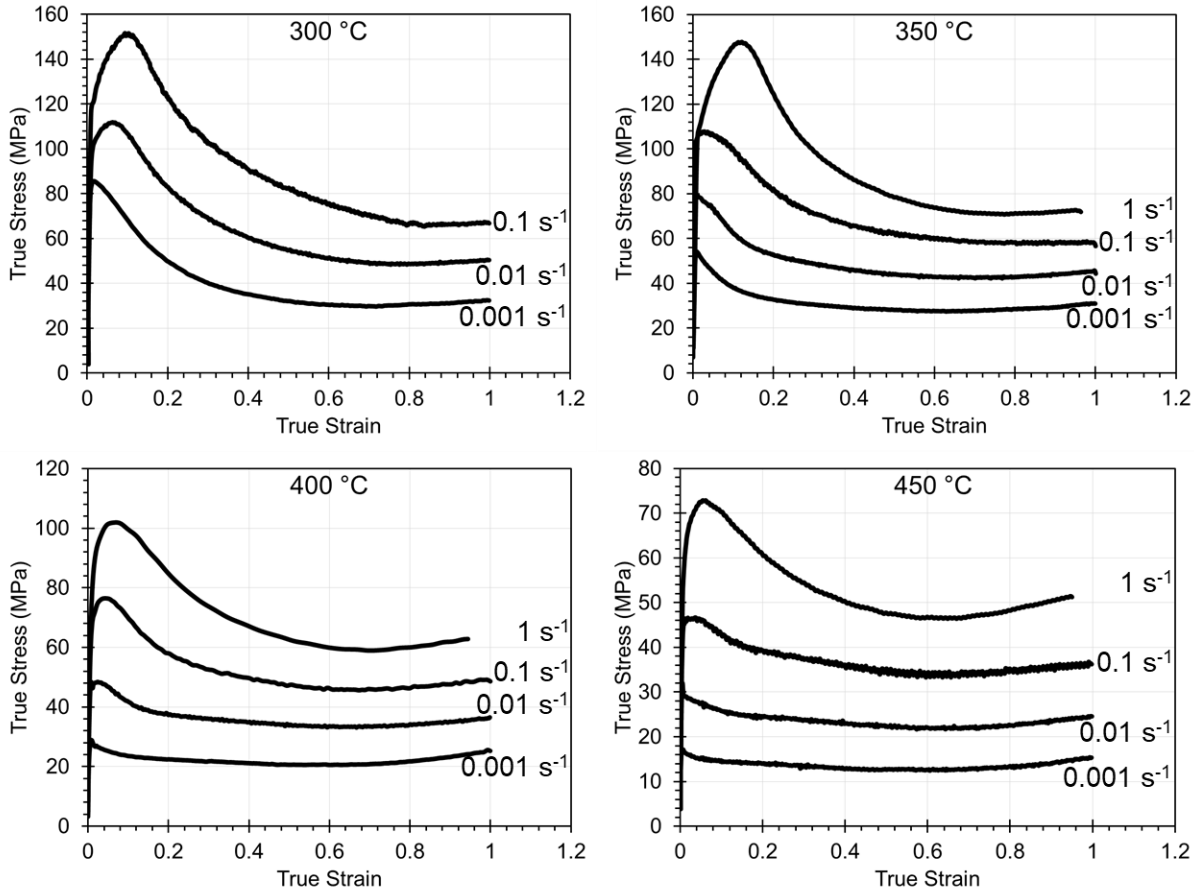

Figure D-2 Flow stress curves of the extruded AZ80 alloy deformed in compression along the prior extrusion direction

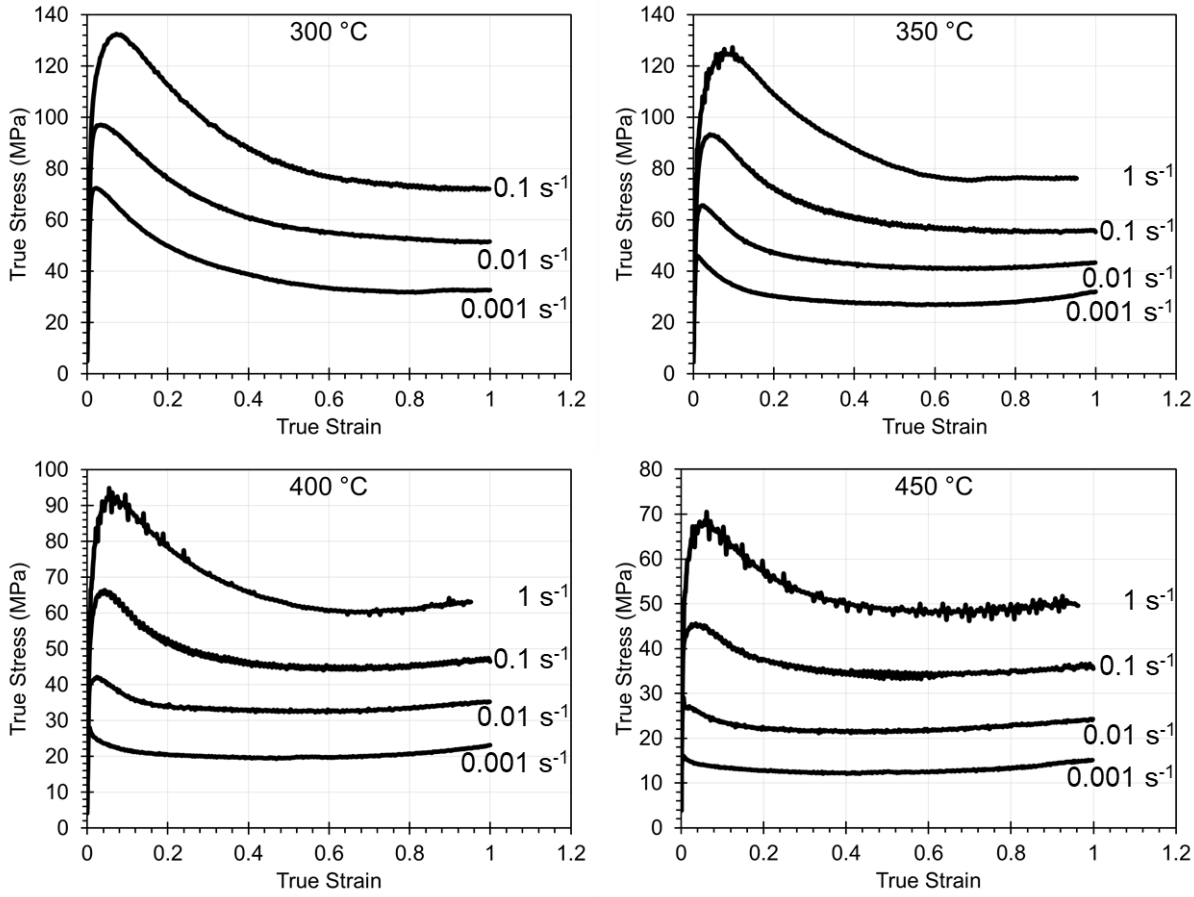

Figure D-3 Flow stress curves of the extruded AZ80 alloy deformed in compression perpendicular to the prior extrusion direction (i.e. along the radial direction)

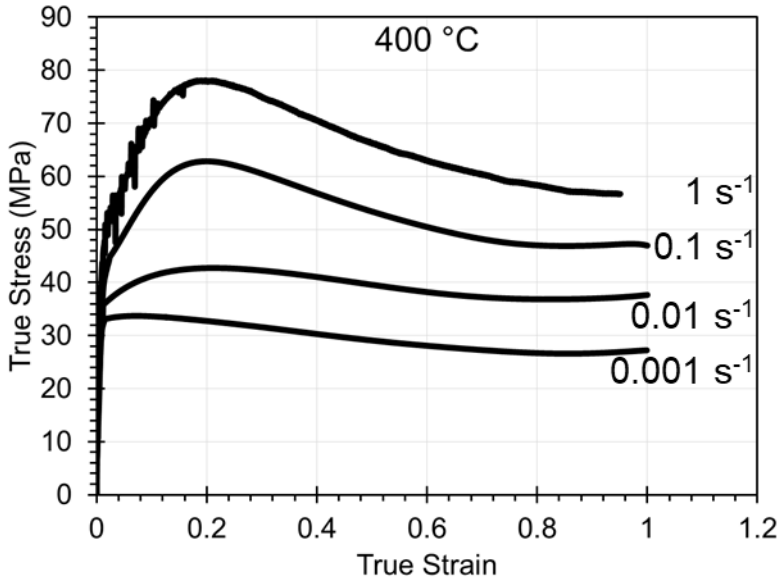

Figure D-4 Flow stress curves of the cast AZ31 alloy. Tests were not performed at other temperatures.

Appendix E

This section presents the effective strain distribution, and principal stress distributions in an extruded (ED) sample compressed at 400 °C, 0.01 s^{-1}, to a strain of 1.0, obtained using an in-house developed DEFORM 3D finite element model (FEM) for the same. The flow stress data were provided by me, while the model was developed and simulations were run by another student on the same project, Tharindu Kodippili.

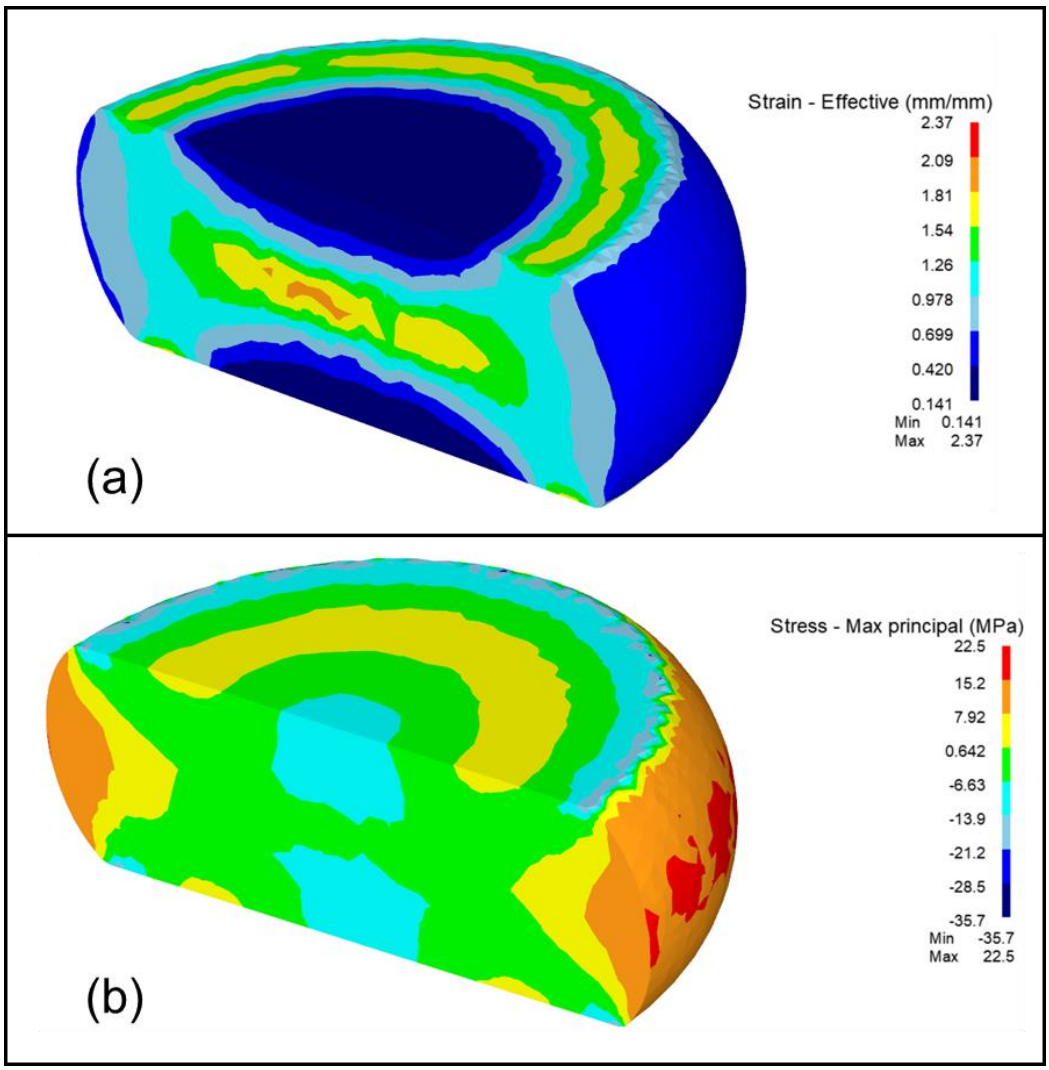

Figure E-1 Distribution of (a) effective strain, and (b) principal stress, in an extruded (ED) sample deformed in uniaxial compression at 400 °C, 0.01 s^{-1}, to a strain of 1.0, obtained using a DEFORM 3D FEM model. Positive values in (b) indicate net tensile stresses, while negative values indicate net compressive stresses. Courtesy: Tharindu Kodippili, University of Waterloo.

Appendix F

This section provides the Proportional–Integral–Derivative (PID) controller settings for the Gleeble™ 3500 that were used in the present work. The file corresponds to compression at 400 °C, 0.1 s^{-1}, but the same PID settings were consistently used for tests at other deformation conditions as well.

```
set lastruntime to 0sec
// tl: 1 sl:3
// system setup...
set strokelimit to -150.00mm
set forcelimit to 50000kgf
set maxangle to 110deg
set forcelevelmax to 50000kgf
set forcelevelmin to 50000kgf
set limTC to 3
set limTemp to 8001C
set ticoef to 1.0
set rampterm to 30000pct  // original rampterm=20000pct
set ramiterm to 0pct
set ramdterm to 200pct     // original ramdterm=400pct
set forceKp to -0.50pct
set forceKi to -0.0005pct

// end of system setup.

// tl: 2 sl:21
// stress/strain setup...
set strainmode to 1
set strainsrc to LGauge.index
set strainX0 to 15.000mm
set strVolume to 10.000mm*10.000mm*0.7853975*15.000mm
// end of stress/strain setup.
// tl: 3 sl:29
acquire Force LGauge PRam PTemp Strain Stress Stroke TC1
// tl: 4 sl:31
// sr = 0.1
// tl: 5 sl:33

// tl: 6 sl:35

// tl: 7 sl:37
set pump to on
delay 1sec
set mechanical to on
delay 1sec
set setuprun to on
delay 1sec
set heat to on
delay 500msec
set thermal to on
set lastruntime to systime
```

```
// tl: 8 sl:49

// tl: 9 sl:51
sample at 10.0Hz
// tl: 10 sl:53
ramp Force to -0.5000kN in 10.0000sec &
ramp TC1 to 0.0000C in 10.0000sec
// tl: 11 sl:56
ramp Force to -0.3000kN in 80.0000sec &
ramp TC1 to 400.0000C in 80.0000sec
// tl: 12 sl:59
ramp Force to -0.3000kN in 60.0000sec &
ramp TC1 to 400.0000C in 60.0000sec
// tl: 13 sl:62
sample at 500.0Hz
// tl: 14 sl:64
zero Force
zero LGauge
delay 50msec
// tl: 15 sl:68

// tl: 16 sl:70
ramp Strain to -1.0000 in 10.0000sec &
ramp TC1 to 400.0000C in 10.0000sec
// tl: 17 sl:73
ramp Strain to -1.0000 in 0.1000sec &
ramp TC1 to 0.0000C in 0.1000sec
// tl: 18 sl:76
set Quench1 to on
// tl: 19 sl:78
ramp Strain to -1.0000 in 8.0000sec &
ramp TC1 to 0.0000C in 8.0000sec
// tl: 20 sl:81
set Quench1 to off
// tl: 21 sl:83
sample off
set thermal to off
delay 200msec
set heat to off
set tc1 to 0C
set mechanical to off
set setuprun to off
if hypress
    set hypress to off
    delay 4.0sec
end
delay 2sec
set pump to off
delay 1sec
set stroke to 0cm
if torsionflag
    set torsion to 0rev
else
    set wedge to 0cm
end
```